
LHC EFFECTIVE MODEL FOR OPTICS CORRECTIONS

Measurements and corrections of high-order non-linear optics

Dissertation
zur Erlangung des Doktorgrades
der Naturwissenschaften

Vorgelegt beim Fachbereich Physik
der Johann Wolfgang Goethe-Universität
in Frankfurt am Main

von
MAËL LE GARREC
aus Obernai, Elsäss, Frankreich.

Frankfurt am Main 2024
(D30)

Vom Fachbereich Physik der Johann Wolfgang Goethe-Universität als Dissertation
angenommen.

Dekan:

Gutachter:

Datum der Disputation:

Abstract

This thesis investigates the crucial role of higher-order magnetic fields and non-linear optics in the stability and performance of particle accelerators, focusing on the Large Hadron Collider (LHC) at CERN. The control of non-linear optics, which deals with the interaction of charged particle beams with complex magnetic fields such as sextupolar, octupolar, decapolar, and so on, is essential for managing beam dynamics. The LHC, as the world's most powerful accelerator, provides a unique opportunity to study these high-order effects, serving as a testbed for future accelerator designs.

These higher-order fields significantly affect the beam's dynamic aperture and lifetime, especially at injection energy, where precise correction of magnetic field errors is required. Managing these challenges is not only vital for optimizing LHC performance but also for guiding the design and operation of next-generation machines.

A key contribution of this work is the development of correction methods for Resonance Driving Terms (RDTs), a critical factor in beam lifetime and dynamic aperture limitations. New corrective strategies for RDTs have led to notable improvements in beam lifetime and dynamic aperture at both injection and top energy operation. This thesis also addresses the discrepancies observed between experimental measurements and models of beam observables.

These findings highlight the importance of precise modeling and correction of non-linear magnetic fields, offering insights that will benefit both the LHC and future high-energy particle accelerators.

Extended Summary

The Large Hadron Collider (LHC) at CERN, situated in a 27-kilometer tunnel beneath the Swiss-French border, is the world's largest and most powerful particle accelerator. Its primary mission is to recreate the conditions of the universe just moments after the Big Bang, enabling scientists to explore the fundamental forces and particles that constitute the cosmos. This remarkable facility accelerates protons and heavy ions to nearly the speed of light before colliding them with immense energy, providing profound insights into the building blocks of matter and the fundamental interactions that govern our universe. The LHC represents not only a monumental engineering achievement but also a crucial tool for advancing our understanding of high-energy physics.

Operating such a complex and powerful machine requires overcoming numerous technical challenges, particularly in maintaining the precise control and stability of its particle beams. One significant challenge lies in managing the effects of higher-order magnetic fields, which often arise from field errors in the magnets used to guide and focus the particle beams. These field errors can profoundly impact beam dynamics and its lifetime. Addressing these challenges is essential to ensuring that the LHC operates effectively and continues to produce valuable scientific results. Furthermore, non-linear optics control is crucial for the success of future accelerators like the HL-LHC and FCC, which will increasingly rely on high-order non-linear optics corrections to achieve their performance targets. The following extended summary synthesizes findings from three detailed studies investigating various aspects of higher-order multipole effects and their implications on the LHC's beam dynamics.

This thesis employs the Hamiltonian formalism to describe particle motion in the transverse planes under the influence of various multipole fields. In non-linear lattices, the complexity of beam dynamics increases significantly, necessitating the use of advanced mathematical tools such as Lie Algebra and Poisson Brackets to accurately characterize non-linear effects. The study derives explicit higher-order non-linear transfer maps and provides a comprehensive summary of multipole combinations. These non-linearities in the lattice lead to complex

phenomena such as high-order chromaticity, amplitude detuning, chromatic amplitude detuning, and resonances driven by Resonance Driving Terms (RDTs), all of which are thoroughly derived and supported by detailed measurement techniques.

Optics measurements are conducted using a wide range of techniques and software tools. Turn-by-turn data acquisition via Beam Position Monitors (BPMs) is emphasized as a crucial method for evaluating beam optics, where an AC-dipole excites the beam, and the resulting oscillations are analyzed using Fourier transforms to extract tunes and identify resonances. Further treatment is done via the oscillation amplitudes and the magnitude of spectral lines to retrieve linear and non-linear observables such as the phase advance, beta function, dispersion, coupling, orbit, and RDTs. Chromaticity measurements involve inducing momentum offsets by varying the RF frequency and observing the corresponding tune shifts.

To advance the understanding of high-order non-linear fields, new measurement and analysis methods have been developed. One such tool, the Non-Linear Chromaticity GUI, simplifies the process of analyzing and correcting chromaticity during operation. Additionally, a novel response matrix approach has been introduced, enabling efficient direct corrections of Resonance Driving Terms (RDTs) in the LHC. This marks a shift from empirical correction adjustments to a more quantitative and systematic method. These techniques have proven effective in correcting several key observables, as discussed throughout this thesis. The development of these methods has been crucial in reducing commissioning time, enabling a greater focus on high-order multipoles, from octupoles to decatetrapoles, some of which have never been studied before. These investigations were further facilitated by improvements in the collimator sequence, allowing the exploration of a higher action and momentum offsets. Additionally, enhancements in dynamic aperture, as presented in this thesis, provided the required amplitudes to probe these higher-order effects more effectively.

The first chapter explores the origins and consequences of skew octupolar fields within the LHC. These fields significantly influence the dynamic aperture of the accelerator, a parameter that defines the amplitudes within which the particle beam remains stable. Skew octupolar correctors are installed around key detectors, such as ATLAS and CMS, to manage these fields and mitigate their effects on beam stability. The study focuses on measuring these fields with optics designed for top energy, at 6.8 TeV per particle. Corrections were performed using a response matrix based approach, a different method than what was used a few years prior, marking a shift from empirical corrections to a more quantitative and systematic approach for the first time in the LHC. This method effectively addresses skew octupolar RDTs using the available corrector magnets, although its performance is limited by the absence of one corrector, which constrains the achievable correction strength. Consequently, the RDTs of interest, f_{1012} and f_{1210} , can either be effectively corrected or maintained at a constant level depending on the corrector configuration.

Additionally, the study investigates the unexpected influence of Landau octupoles on skew octupolar RDTs at injection energy, at 450 GeV per particle. Landau octupoles, which are powerful magnets used at injection energy to introduce damping through a tune spread, generated a significant shift in skew octupolar RDTs during measurements under various powering configurations. Skew octupolar resonances have previously been identified as a source of emittance growth in the presence of electron clouds. The more intuitive explanation for the generation of skew fields by normal multipoles had been the misalignments of these octupoles, specifically roll errors. However, simulations indicate that octupole misalignments have minimal impact on skew octupolar fields. Instead, coupling has been identified as a crucial factor. The combination of coupling and the strong powering of Landau octupoles at injection energy is expected to be a major contributor to skew octupolar RDTs. Therefore, precise modeling of coupling is essential for predicting the behavior of skew octupolar RDTs. Accurate modeling and correction of skew octupolar fields in the LHC are essential to suppress resonances and improve both the beam's dynamic stability and lifetime.

The second chapter focuses on decapolar fields in the LHC, particularly at injection energy. As the FCC is expected to rely on precise control of decapolar fields, their accurate study in the LHC is essential to increase confidence in its design and operational strategies. Consequently, this study addresses previously observed discrepancies between measurements and models related to third-order chromaticity, a critical parameter that describes how particles with an energy deviation experience different oscillation frequencies than the reference particle. Accurate control of chromaticity is vital for maintaining beam stability. The introduction of previously unobserved observables, has provided a clearer understanding of these discrepancies. Among these observables are the bare chromaticity, which represents the chromaticity of the machine without any correctors powered on to observe the bare influence of field errors, and chromatic amplitude detuning, a detuning function of both momentum deviations and oscillation amplitudes. Several approaches to measuring the same fields help clarify the various contributions. The research reveals that the decay of the decapolar component in the main dipoles is a significant factor contributing to these discrepancies. When the LHC was designed, this decay was deemed too small to be significant and thus was not included in the magnetic error tables used for simulation. However, as the machine's parameters are pushed further each year and the effects of higher-order fields become better understood, it becomes clear that accurate control and modeling of these fields are necessary.

For the first time in the LHC, measurements and corrections of the decapolar Resonance Driving Term f_{1004} were carried out at injection energy. Corrections are based on a response matrix approach, effectively implementing combined corrections of third-order chromaticity, chromatic amplitude detuning, and RDT f_{1004} , leading to a 3% improvement in beam lifetime. Conversely, deliberately degrading the RDT alone resulted in a 10% decrease in beam lifetime,

underscoring the importance of this resonance corrections for stable beam operation. The study also explored how sextupoles and octupoles interact to generate decapolar-like fields. It was found that sextupoles, both alone and in combination with Landau octupoles, produce a substantial f_{1004} decapolar RDT when powered to small currents. Therefore, in an operational context, decapolar resonances, largely generated by strong octupoles, would benefit from adapted corrections. These findings suggest that further advancements in correction methods could lead to even greater improvements in beam lifetime.

The third chapter investigates very-high-order fields in the LHC, specifically dodecapolar and decatetrapolar fields. Using a newly implemented collimation setup and custom post-processing techniques, this study successfully observed these higher-order fields. Studies were conducted to estimate the effect of the non-linearity of the momentum compaction factor on the chromaticity function during its computation from the RF frequency. The results indicate that while the momentum compaction factor shows a second order in the LHC, its effects on the resulting chromaticity are negligible even at large momentum offsets. Several chromaticity measurements with varying configurations of octupolar and decapolar corrections then revealed the presence of fourth and fifth-order terms ($Q^{(4)}$ and $Q^{(5)}$). These measurements consistently identified these higher-order terms with similar values, demonstrating their robustness. Additionally, it is emphasized that accurately characterizing the lower-order terms requires good measurement of these higher-order terms. The study identifies, through simulations, dodecapolar and decatetrapolar fields as primary contributors to these higher-order effects, originating from field errors in the main dipoles and quadrupoles. The LHC's field error model appears to be in relative agreement with the measurements once the decay of decatetrapolar components is considered.

For the first time at injection energy, the dodecapolar Resonance Driving Term f_{0060} was measured. This measurement shows clear repeatability, even when performed with different configurations of octupolar and decapolar corrections. The measured values were found to be in good agreement with the model. The research concludes that further investigations are needed to address limitations in the measurement range of the chromaticity function and to refine estimates of higher-order chromaticity terms. Additionally, studying the impact of lower-order multipoles on the dodecapolar RDT and its effect on beam lifetime would be valuable for optimizing the LHC's performance.

In summary, the research detailed in these studies underscores the critical importance of understanding and managing higher-order multipole effects in the LHC. Skew octupolar fields, decapolar fields, and other higher-order fields have a significant impact on the beam's dynamic aperture and lifetime. Developing and implementing advanced measurement techniques and correction methods is essential for enhancing the understanding of non-linear optics. The insights gained from these studies are crucial for optimizing the LHC's performance.

As particle accelerators continue to evolve, the challenges associated with higher-order multipole components will persist. Ongoing research in this field is vital for addressing these challenges and ensuring that future accelerators achieve the precision required for new scientific discoveries. The lessons learned from the LHC's experience with the complex interactions of multipole fields will inform the design and operation of next-generation accelerators, such as the HL-LHC and FCC, which will increasingly rely on precise non-linear optics control. These advancements will ensure that these accelerators remain at the forefront of exploring fundamental questions about the universe.

The work presented in these chapters represents a significant contribution to the field of accelerator physics by offering practical solutions for current operational challenges and paving the way for future advancements.

Zusammenfassung

Der Large Hadron Collider (LHC) am CERN, der sich in einem 27 Kilometer langen Tunnel unter der Grenze zwischen der Schweiz und Frankreich befindet, ist der größte und leistungsstärkste Teilchenbeschleuniger der Welt. Seine Hauptaufgabe besteht darin, die Bedingungen des Universums unmittelbar nach dem Urknall nachzubilden, um Wissenschaftler*innen die Erforschung der fundamentalen Kräfte und Teilchen zu ermöglichen, die das Universum ausmachen. Diese bemerkenswerte Anlage beschleunigt Protonen und schwere Ionen nahezu auf Lichtgeschwindigkeit, bevor sie mit enormer Energie kollidieren, was tiefgreifende Einblicke in die Bausteine der Materie und die grundlegenden Wechselwirkungen, die unser Universum bestimmen, liefert. Der LHC stellt nicht nur eine monumentale ingenieurtechnische Leistung dar, sondern ist auch ein wesentliches Instrument zur Förderung unseres Verständnisses der Hochenergiephysik.

Der Betrieb einer derart komplexen und leistungsfähigen Maschine erfordert die Bewältigung zahlreicher technischer Herausforderungen, insbesondere in Bezug auf die präzise Steuerung und Stabilität der Teilchenstrahlen. Eine wesentliche Herausforderung besteht darin, die Auswirkungen höherer magnetischer Felder zu beherrschen, die häufig durch Feldfehler in den Magneten entstehen, die zur Führung und Fokussierung der Teilchenstrahlen verwendet werden. Diese Feldfehler können die Strahldynamik und die Strahllebensdauer erheblich beeinflussen. Die Bewältigung dieser Herausforderungen ist entscheidend, um den LHC effektiv zu betreiben und weiterhin wertvolle wissenschaftliche Ergebnisse zu erzielen. Darüber hinaus ist die Kontrolle nichtlinearer Optiken von entscheidender Bedeutung für den Erfolg zukünftiger Beschleuniger wie den HL-LHC und den FCC, die zunehmend auf nichtlineare Korrekturen höherer Ordnung angewiesen sein werden, um ihre Leistungsziele zu erreichen. Die folgende erweiterte Zusammenfassung fasst die Ergebnisse aus drei detaillierten Studien zusammen, die verschiedene Aspekte der höheren Multipol-Effekte und deren Auswirkungen auf die Strahldynamik des LHC untersuchen.

Diese Dissertation verwendet den Hamiltonschen Formalismus, um die Teilchenbewegung

Zusammenfassung

in den transversalen Ebenen unter dem Einfluss verschiedener Multipolfelder zu beschreiben. In nichtlinearen Gittern steigt die Komplexität der Strahldynamik erheblich an, weshalb fortschrittliche mathematische Werkzeuge wie die Lie-Algebra und Poisson-Klammern notwendig sind, um nichtlineare Effekte genau zu charakterisieren. Die Arbeit leitet explizite nichtlineare Übertragungsabbildungen höherer Ordnung her und bietet eine umfassende Zusammenfassung von Multipolkombinationen. Diese Nichtlinearitäten im Gitter führen zu komplexen Phänomenen wie hoher Chromatizität, Amplitudentuning, chromatischem Amplitudentuning und Resonanzen, die durch Resonanzanregungsbegriffe (RDTs) getrieben werden. All diese Phänomene werden ausführlich abgeleitet und durch detaillierte Messtechniken unterstützt.

Optikmessungen werden mit einer Vielzahl von Techniken und Software-Tools durchgeführt. Die turn-by-turn-Datenerfassung über Beam Position Monitors (BPMs) wird als entscheidende Methode zur Bewertung der Strahloptik hervorgehoben, bei der ein AC-Dipol den Strahl anregt und die resultierenden Oszillationen mittels Fourier-Transformationen analysiert werden, um Tunes zu extrahieren und Resonanzen zu identifizieren. Eine weiterführende Analyse erfolgt über die Oszillationsamplituden und die Größe der Spektrallinien, um lineare und nichtlineare Observablen wie Phasenvorschub, Betafunktion, Dispersion, Kopplung, Orbit und RDTs zu bestimmen. Chromatizitätsmessungen beinhalten das Induzieren von Impulsabweichungen durch Änderung der HF-Frequenz und die Beobachtung der entsprechenden Tune-Verschiebungen.

Um das Verständnis nichtlinearer Felder höherer Ordnung zu verbessern, wurden neue Mess- und Analysemethoden entwickelt. Eines dieser Werkzeuge, das Non-Linear Chromaticity GUI, vereinfacht den Prozess der Analyse und Korrektur der Chromatizität während des Betriebs. Zusätzlich wurde ein neues Ansatzverfahren mit Antwortmatrizen eingeführt, das effiziente direkte Korrekturen der Resonanzanregungsbegriffe (RDTs) im LHC ermöglicht. Dies stellt einen Übergang von empirischen Korrekturanpassungen hin zu einer quantitativeren und systematischeren Methode dar. Diese Techniken haben sich als effektiv bei der Korrektur mehrerer wichtiger Observablen erwiesen, wie im Laufe dieser Dissertation erörtert wird. Die Entwicklung dieser Methoden war entscheidend für die Reduzierung der Inbetriebnahmezeit, was einen stärkeren Fokus auf höhere Multipole, von Oktupolen bis hin zu Dekatetrapolen, ermöglichte – einige davon wurden zuvor nie untersucht. Diese Untersuchungen wurden zudem durch Verbesserungen in der Kollimatorschaltung erleichtert, die die Erforschung größerer Aktionen und Impulsabweichungen ermöglichen. Darüber hinaus trugen die in dieser Dissertation vorgestellten Verbesserungen der dynamischen Apertur dazu bei, die erforderlichen Amplituden bereitzustellen, um diese höherordnigen Effekte effektiver zu untersuchen.

Das erste Kapitel untersucht die Ursprünge und Auswirkungen schiefer Oktupolfelder

innerhalb des LHC. Diese Felder beeinflussen erheblich die dynamische Apertur des Beschleunigers, ein Parameter, der die Amplituden definiert, innerhalb derer der Teilchenstrahl stabil bleibt. Schiefe Oktupolkorrekturen sind um wichtige Detektoren wie ATLAS und CMS installiert, um diese Felder zu steuern und ihre Auswirkungen auf die Strahlstabilität zu mindern. Die Studie konzentriert sich darauf, diese Felder mit Optiken zu messen, die für die Höchstenergie von 6,8 TeV pro Teilchen ausgelegt sind. Korrekturen wurden mithilfe eines antwortmatrixbasierten Ansatzes durchgeführt, was eine andere Methode darstellt als die, die einige Jahre zuvor verwendet wurde. Dies markiert einen Übergang von empirischen Korrekturen zu einem quantitativeren und systematischeren Ansatz für den LHC. Diese Methode adressiert effektiv schiefe Oktupol-RDTs unter Verwendung der verfügbaren Korrektormagnete, obwohl ihre Leistung durch das Fehlen eines Korrektors eingeschränkt ist, was die erreichbare Korrekturstärke begrenzt. Folglich können die von Interesse stehenden RDTs, f_{1210} und f_{1012} je nach Korrektorkonfiguration entweder effektiv korrigiert oder auf einem konstanten Niveau gehalten werden.

Darüber hinaus untersucht die Studie den unerwarteten Einfluss von Landau-Oktupolen auf die schiefen Oktupol-RDTs bei Einspeiseenergie von 450 GeV pro Teilchen. Landau-Oktupole, die bei Einspeiseenergie als leistungsstarke Magnete eingesetzt werden, um durch eine Tune-Verbreiterung Dämpfung einzuführen, erzeugten während der Messungen unter verschiedenen Einspeisekonfigurationen eine signifikante Verschiebung der schießen Oktupol-RDTs. Schiefe Oktupolresonanzen wurden zuvor als eine Quelle für Emittanzwachstum in Gegenwart von Elektronenwolken identifiziert. Die intuitivere Erklärung für die Erzeugung schiefer Felder durch normale Multipole war die Fehljustierung dieser Oktupole, insbesondere Rollfehler. Simulationen zeigen jedoch, dass Fehljustierungen von Oktupolen einen minimalen Einfluss auf schiefe Oktupolfelder haben. Stattdessen wurde die Kopplung als ein entscheidender Faktor identifiziert. Die Kombination aus Kopplung und der starken Einspeisung von Landau-Oktupolen bei Einspeiseenergie wird als Hauptursache für die schießen Oktupol-RDTs angesehen. Daher ist eine präzise Modellierung der Kopplung unerlässlich, um das Verhalten der schießen Oktupol-RDTs vorherzusagen. Eine genaue Modellierung und Korrektur der schießen Oktupolfelder im LHC sind entscheidend, um Resonanzen zu unterdrücken und sowohl die dynamische Stabilität als auch die Lebensdauer des Strahls zu verbessern.

Das zweite Kapitel konzentriert sich auf Dekapolfelder im LHC, insbesondere bei Einspeiseenergie. Da beim FCC eine präzise Kontrolle der Dekapolfelder erwartet wird, ist ihre genaue Untersuchung im LHC entscheidend, um das Vertrauen in das Design und die Betriebsstrategien zu erhöhen. Folglich behandelt diese Studie zuvor beobachtete Diskrepanzen zwischen Messungen und Modellen in Bezug auf die chromatische Aberration dritter Ordnung, einen kritischen Parameter, der beschreibt, wie Teilchen mit einer Energieabweichung

Zusammenfassung

unterschiedliche Oszillationsfrequenzen als das Referenzteilchen erfahren. Eine genaue Kontrolle der Chromatizität ist entscheidend für die Aufrechterhaltung der Strahlstabilität. Die Einführung zuvor nicht beobachteter Observablen hat ein klareres Verständnis dieser Diskrepanzen ermöglicht. Zu diesen Observablen gehören die nackte Chromatizität, die die Chromatizität der Maschine ohne aktivierte Korrektoren darstellt, um den unmittelbaren Einfluss von Feldfehlern zu beobachten, sowie das chromatische Amplitudentuning, eine Tuningfunktion sowohl von Impulsabweichungen als auch von Oszillationsamplituden. Mehrere Ansätze zur Messung derselben Felder helfen, die verschiedenen Beiträge zu klären. Die Forschung zeigt, dass der Abfall der dekapolaren Komponente in den Hauptdipolen ein signifikanter Faktor ist, der zu diesen Diskrepanzen beiträgt. Als der LHC entworfen wurde, wurde dieser Abfall als zu gering erachtet, um signifikant zu sein, und wurde daher nicht in den Magnetfehlertabellen berücksichtigt, die für Simulationen verwendet wurden. Mit der zunehmenden Beanspruchung der Maschinenparameter und dem besseren Verständnis der Auswirkungen höherer Felder wird jedoch deutlich, dass eine genaue Kontrolle und Modellierung dieser Felder notwendig ist.

Erstmals im LHC wurden Messungen und Korrekturen des dekopolaren Resonance Driving Term f_{1004} bei Einspeiseenergie durchgeführt. Die Korrekturen basieren auf einem antwortmatrixbasierten Ansatz, der die kombinierten Korrekturen der chromatischen Aberration dritter Ordnung, des chromatischen Amplitudentunings und des RDT f_{1004} effektiv umsetzt, was zu einer Verbesserung der Strahlaufzeit um 3% führt. Im Gegensatz dazu führte die absichtliche Verschlechterung des RDT allein zu einem Rückgang der Strahlaufzeit um 10

Das dritte Kapitel untersucht sehr-hochordentliche Felder im LHC, speziell dodecapolare und decatetrapolare Felder. Mit einer neu implementierten Kollimationssanordnung und benutzerdefinierten Nachbearbeitungstechniken konnte diese Studie erfolgreich diese höherordentlichen Felder beobachten. Es wurden Studien durchgeführt, um den Effekt der Nichtlinearität des Impulskompaktierungsfaktors auf die Chromatizitätsfunktion während ihrer Berechnung aus der RF-Frequenz zu schätzen. Die Ergebnisse zeigen, dass der Impulskompaktierungsfaktor zwar im LHC eine zweite Ordnung aufweist, seine Auswirkungen auf die resultierende Chromatizität jedoch vernachlässigbar sind, selbst bei großen Impulsabweichungen. Mehrere Chromatizitätsmessungen mit unterschiedlichen Konfigurationen von oktupolarer und dekpolarer Korrektur offenbarten dann das Vorhandensein von vierten und fünften Ordnungsbegriffen ($Q^{(4)}$ und $Q^{(5)}$). Diese Messungen identifizierten konsistent diese höherordentlichen Terme mit ähnlichen Werten, was ihre Robustheit demonstriert. Darüber hinaus wird betont, dass eine genaue Charakterisierung der niedrigeren Ordnungen eine gute Messung dieser höherordentlichen Terme erfordert. Die Studie identifizierte durch Simulationen dodecapolare und decatetrapolare Felder als primäre Beiträge zu diesen höherordentlichen Effekten, die aus Feldfehlern in den Hauptdipolen und Quadrupolen stammen. Das Modell

der Feldfehler des LHC scheint relativ gut mit den Messungen übereinzustimmen, wenn der Abfall der decatetrapolaren Komponenten berücksichtigt wird.

Für die erste Messung bei Einspeiseenergie wurde der dodepolare Resonance Driving Term f_{0060} gemessen. Diese Messung zeigt eine klare Wiederholbarkeit, selbst wenn sie mit unterschiedlichen Konfigurationen von oktupolarer und dekpolarer Korrektur durchgeführt wird. Die gemessenen Werte wurden als gut mit dem Modell übereinstimmend befunden. Die Forschung kommt zu dem Schluss, dass weitere Untersuchungen erforderlich sind, um die Einschränkungen im Messbereich der Chromatizitätsfunktion anzugehen und die Schätzungen höherordentlicher Chromatizitätsbegriffe zu verfeinern. Darüber hinaus wäre es wertvoll, den Einfluss niedrigerer Multipole auf den dodepolaren RDT und dessen Auswirkungen auf die Strahllaufzeit zu untersuchen, um die Leistung des LHC zu optimieren.

Zusammenfassend unterstreicht die in diesen Studien detaillierte Forschung die kritische Bedeutung des Verständnisses und der Steuerung höherordentlicher Multipoleffekte im LHC. Schiefe Oktupolfelder, Dekapolfelder und andere höherordentliche Felder haben einen signifikanten Einfluss auf die dynamische Apertur und die Lebensdauer des Strahls. Die Entwicklung und Implementierung fortschrittlicher Messmethoden und Korrekturmethoden ist entscheidend für das Verständnis der nichtlinearen Optik. Die aus diesen Studien gewonnenen Erkenntnisse sind entscheidend für die Optimierung der Leistung des LHC.

Da sich Teilchenbeschleuniger weiterhin entwickeln, werden die Herausforderungen im Zusammenhang mit höheren Multipolen bestehen bleiben. Laufende Forschung in diesem Bereich ist von entscheidender Bedeutung, um diese Herausforderungen zu bewältigen und sicherzustellen, dass zukünftige Beschleuniger die für neue wissenschaftliche Entdeckungen erforderliche Präzision erreichen. Die aus den Erfahrungen des LHC mit den komplexen Wechselwirkungen von Multipolfeldern gewonnenen Erkenntnisse werden das Design und den Betrieb künftiger Beschleuniger, wie HL-LHC und FCC, die zunehmend auf eine präzise Kontrolle der nichtlinearen Optik angewiesen sein werden, informieren. Diese Fortschritte werden sicherstellen, dass diese Beschleuniger an der Spitze der Erforschung fundamentaler Fragen zum Universum bleiben.

Die in diesen Kapiteln präsentierte Arbeit stellt einen bedeutenden Beitrag zum Bereich der Beschleunigerphysik dar, indem sie praktische Lösungen für aktuelle Betriebsherausforderungen bietet und den Weg für zukünftige Fortschritte ebnet.

Acknowledgements

Ok, so this is the place where I get to talk about my life and where you'll be looking for you name to see what I've got to say about you. This would need to be a blog post given how many things I want to say, so it will be *relatively* brief. Let's start first by saying that I'm incredibly happy to have done this thesis at CERN, which I honestly found quite fun. Not only because the subject was interesting, but also because I have been surrounded by kind, caring and smart people through all these years.

To give a little perspective, I have originally studied computer science at EPITA (École Pour l'Informatique et les Techniques Avancées) in Paris and earned an engineering degree in that field. Nothing really predestined me to work in any field related to physics, let alone to do a PhD on accelerator physics, but here we are! After my degree, I applied for a trainee position at CERN, basically working on software development for optics measurements and corrections. After two years of training, I was proposed with a PhD on the topics I've been learning, which I gladly accepted. This is how I embarked on a 3-year journey about accelerator physics. For this, I would never be thankful enough to Rogelio Tomas, who recruited and trusted me for that first contract, without which my life would probably be vastly different. I am also immensely grateful to Ewen Maclean, who has been a fantastic supervisor, even probably the best I've had yet to meet. He has always been present to help with me accelerator concepts in a very intelligible manner. Being kind, following up with my studies and always proposing new ideas made me feel like a complete member of the OMC team. On the university side, at Goethe-Universität Frankfurt, I would like to thank Giuliano Franchetti for his guidance and ideas about this thesis.

Through my now five years at CERN, I have had the privilege to meet incredible people who changed not only my career path but also who I am for the best. And even if it sounds a bit weird, I am incredibly happy you have all been there.

Upon starting my very first contract, I was paired with Max Mihailescu and Sébastien Joly in an office, all three beginning our journey at CERN. I am very thankful to Max for having been a good friend during his short stay here, and for his insights on mathematics. I consider myself remarkably lucky to have met Sébastien, who probably should be listed as a supervisor here given how much he helped me when I struggled to learn the basics of accelerator physics. I would also like to thank

Acknowledgements

Michael Hofer and Félix Carlier, who were there to answer my countless questions, be it when I started or even now at the end of my PhD. Closely related to my thesis subject were Félix Soubelet and Joschua Dilly who greatly helped me in various ways. Thanks a lot as well to Jacqueline Keintzel and Frank Zimmerman, to have given me the opportunity to work for a month at KEK in Japan, and expand my knowledge of lepton accelerators.

Many thanks to all the members of the OMC team who were great colleagues, be it in the office or during barely-legal night and week-end shifts in the control room. Specifically, I would like to thank Wietse Van Goethem, Leon Van Riesen-Haupt, Elena Fol, Andreas Wegscheider, Vittorio Ferrentino and Tobias Persson. Talking about the control room, I want to thank the LHC operation team and specifically Michi Hostettler for our conversations and his deep knowledge of CERN and the LHC.

CERN being a vast laboratory, I had the pleasure to meet remarkable people who I enjoyed to be around. I cannot detail how much you all mean to me as this is already quite long, but you get the idea. For this, thanks a lot to Sofia, Christophe, David, Jean-Baptiste, Lisa, Joanna, Roxana, Dora, Joséphine, Jack, Ellie, Tirsi, Kostas, Björn, Christian, Laura, Roland, Luca, Wainer, Tiziana and Pierre.

This thesis would not have been possible without the support of people from outside of CERN. Namely I would like to thank my IRC friends, bonswouar, WhatIsGoingDown, pankkake, ShameOnYou, href and bishop. Special thanks to a large friend group I have always loved to be part of, *la crème de la crème de la cataphilie*. Thanks a ton as well to Clotilde, Matthias, Alpha, Paul, Antoine, Nicolas, Youness, Ksenia, Gérard, Vivien, Baptiste, Félix, Benjamin, Fabian and Tsu for everything that happened during those years, making them memorable. I would like to thank a lot my parents and family who have always been there to support me in every possible way, no matter my decisions. Thanks Antje, Michel, and Yoann.

*Il faut savoir douter où il faut,
se soumettre où il faut,
croire où il faut.*

BLAISE PASCAL

Contents

Abstract	iii
Extended Summary	v
Zusammenfassung	xi
Acknowledgements	xvii
Glossary	xxv
1. Introduction	1
1.1. Motivations /	1
1.2. Thesis Outline /	2
2. Concepts of Accelerator Physics	3
2.1. Particle Accelerators /	3
2.1.1. The CERN Complex /	4
2.1.2. The Large Hadron Collider /	5
2.2. Magnetic Fields /	8
2.2.1. Nomenclature /	8
2.2.2. Multipole Expansion /	9
2.2.3. Beam Rigidity and Normalization /	11
2.2.4. Hamiltonian /	12
2.2.5. Harmonics /	12
2.3. Coordinate Systems /	13
2.3.1. Linear Lattice /	14
2.3.2. Non-Linear Lattice /	18
2.4. Examples of Maps /	24
2.4.1. Non-Linear Transfer of a Single Sextupole /	24
2.4.2. Non-Linear Transfer of Two Sextupoles /	26
2.5. Observables /	27
2.5.1. Dispersion /	27
2.5.2. β -function /	28

2.5.3. Coupling / 29	
2.6. Detuning Effects / 30	
2.6.1. Chromaticity / 30	
2.6.2. Amplitude Detuning / 32	
2.6.3. Chromatic Amplitude Detuning / 32	
2.6.4. Feed-Down / 33	
2.7. Resonances / 34	
2.7.1. Tune Diagram / 34	
2.7.2. Frequency Spectrum / 36	
3. Optics Measurements and Corrections	37
3.1. Beam Instrumentation / 37	
3.1.1. Beam Position Monitors / 37	
3.1.2. Collimators / 38	
3.1.3. Beam Loss Monitors / 38	
3.1.4. Beam Current Transformer / 39	
3.1.5. BBQ System / 39	
3.1.6. AC-Dipole / 39	
3.2. Optics Measurements / 40	
3.2.1. Tools and Softwares / 40	
3.2.2. Turn-by-Turn Signal / 41	
3.2.3. Chromaticity / 44	
3.3. Correction Principles / 45	
3.3.1. Response Matrix / 46	
3.3.2. Global Trims for Chromaticity / 47	
4. Skew Octupolar Fields	49
4.1. Introduction / 49	
4.2. Response Matrix Based RDT Corrections at Top Energy / 50	
4.2.1. Measurement / 50	
4.2.2. Response Matrix and Corrections / 51	
4.3. Skew-Octupolar RDT driven by Landau Octupoles / 57	
4.3.1. Misalignments / 58	
4.3.2. Linear Coupling / 59	
4.4. Summary / 63	
5. Decapolar Fields	65
5.1. Introduction / 65	
5.2. Response of correctors / 66	

5.3. Bare Chromaticity /	69
5.4. Chromatic Amplitude Detuning /	71
5.5. Accounting for Decay /	73
5.6. Resonance Driving Terms /	78
5.6.1. Measurement and correction /	79
5.6.2. Feed-Up Contributions /	84
5.6.3. Feed-Down Contributions /	90
5.7. Summary /	90
6. Higher Order Fields	93
6.1. Introduction /	93
6.2. Chromaticity /	94
6.2.1. Procedure /	94
6.2.2. Measurements /	99
6.3. Model Estimates /	105
6.4. Dodecapolar RDT /	110
6.5. Summary /	113
7. SuperKEKB Studies	115
7.1. Introduction /	115
7.2. Measurement Techniques for Linear Optics /	116
7.2.1. Closed Orbit Distortion /	116
7.2.2. Turn-by-Turn /	117
7.2.3. OMC3 Graphical User Interface /	117
7.3. Optics Observations /	118
7.3.1. Beta-Beating /	119
7.3.2. Amplitude Detuning /	123
7.3.3. Resonance Driving Terms /	125
7.3.4. Chromaticity /	127
7.4. Summary /	129
8. Conclusions	131
List of Figures	133
List of Tables	139

Appendices	143
A. Hamiltonians and Transfer Maps	145
A.1. Hamiltonians of Elements / 145	
A.2. Transfer Maps / 146	
A.2.1. Generic Effective Hamiltonian of Two Elements / 146	
A.2.2. Transfer Map of Two Sextupoles / 149	
A.2.3. Transfer Map of a Sextupole and Octupole / 151	
A.2.4. Transfer Map of a Skew Quadrupole and Octupole / 152	
B. Chromatic Amplitude Detuning	153
B.1. Derivations / 153	
B.1.1. Principle / 154	
B.1.2. Sextupole / 155	
B.1.3. Octupole / 156	
B.1.4. Decapole / 157	
B.1.5. Dodecapole / 158	
B.2. PTC Validation / 159	
C. Resonance Driving Terms	161
C.1. Expressions / 161	
C.2. Frequency Spectrum Lines / 162	
C.3. Amplitude, Resonances and Lines / 164	
Bibliography	171
List of Publications	179
Curriculum Vitæ	183

Glossary

Nomenclature

AC-Dipole Dipole magnet capable of generating variable oscillating fields. Used to increase the transverse amplitude via forced oscillations for optics measurements.

Amplitude detuning Tune shift dependent on the amplitude of transverse oscillations. Corrected via octupoles.

Aperture Physical aperture, i.e. where the beam can pass, of an element in the accelerator.

Beam Short for "Particle beam". Beam 1 and Beam 2 refer to either of the two beams travelling in opposite directions in the LHC.

Beta-beating Relative difference of the beta function between measurement and model. Often expressed in percents: $(\beta_{meas.} - \beta_{mdl})/\beta_{mdl} \cdot 100$.

Beta-function Twiss parameter β as a function of s , the longitudinal position. Related to the amplitude of transverse oscillations of the beam and its size.

Chromatic Amplitude Detuning Tune shift dependent on both the amplitude of transverse oscillations and the momentum offset. Corrected via decapoles.

Chromaticity Tune shift dependent on the momentum offset. Corrected via sextupoles to the first order.

Closed orbit Path of the reference particle through the accelerator, closing back on itself.

Coupling Coupling of a particle's motion in the transverse planes. Corrected via skew quadrupoles to the first, linear, order.

Crosstalk Unwanted magnetic interference between adjacent magnetic circuits.

Drift Drift space, a field-free region.

Dynamic Aperture Maximum region in phase space where particle motion remains stable over time, beyond which particles may be lost.

Feed-down Lower-order-like effects induced by a particle passing off-center through a multipole.

Feed-up Higher-order-like effects induced by a combination of lower-order multipoles.

Landau Octupole Strong octupoles present in the LHC to introduce Landau Damping. The tune spread created via amplitude detuning helps suppress the coherent instabilities of many particles.

MAD-X Current version of the Methodical Accelerator Design framework developed in BE-ABP. Used for beam dynamics simulations.

Online Refers to actions, often corrections, performed in the control room during measurements, where time is limited. Opposed to *offline*.

Acronyms

BBQ	Base Band Tune – Precise tune measurement system consisting of a pick-up and filters.
BCH	Baker-Campbell-Hausdorff theorem – Formula for the combination of exponentials in a Lie algebra, $e^X \cdot e^Y = e^Z$.
BPM	Beam Position Monitor – Instrumentation used to retrieve both position and intensity of the beam via its induced electric field.
IP	Interaction Point – Center of the straight sections of the LHC. Beams collides in four of them where they cross (IP1, 2, 5, 8).
IR	Insertion Region – Part of the straight sections, between the dispersion suppressors. The IP is located at its center.
LHC	Large Hadron Collider – Largest and most powerful particle collider in the world.
LSA	LHC Software Architecture – Software used to operate the particle accelerators at CERN. Based on an online database to manage high and low level parameter settings.
MAD-X	Methodical Accelerator Design – Current version of the framework developed in BE-ABP. Used for beam dynamics simulations.
MD	Machine Development – Dedicated studies aimed at improving the accelerator parameters or testing new operational configurations.
PTC	Polymorphic Tracking Code – Framework used by MAD-X to perform calculations in the non-linear regime.
RDT	Resonance Driving Term – Coefficients related to the strength of a resonance.

RF Radio Frequency – Shorthand for the acceleration system of the accelerator.

Symbols

$B\rho$	Magnetic rigidity – Quantifies the ability of a field to deviate a particle [Tm].
J_n	Skew magnetic field strength – Skew field component of a multipole of order n , normalized to the magnetic rigidity [m^{-n}].
$J_{x,y}$	Action – Phase space coordinate in the Courant-Snyder normalization [m].
K_n	Normal magnetic field strength – Normal field component of a multipole of order n , normalized to the magnetic rigidity [m^{-n}].
Q	Tune – Number of betatron oscillations per turn in a circular accelerator [1].
$Q^{(n)}$	Chromaticity of order n – Orders up to three are generally denoted Q' , Q'' and Q''' [1].
$[,]$	Poisson brackets operator – Commonly used in accelerator physics as commutator in the Lie algebra.
α_c	Momentum compaction factor – Characterizes the change of particles' path length with the momentum offset [1].
β^*	β -function at a given IP [m].
δ	Momentum offset – Deviation of a particle's momentum relative to the reference one [1].
f_{jklm}	Resonance Driving Term – Specific term related to a multipole of order $n=j+k+l+m$ [$m^{-n/2}$].
$ C^- $	Minimum tune separation – Global quantification of the linear coupling [1].

Introduction

1.1. Motivations

Optics control in accelerators is a key factor for optimizing the performance and stability of high-energy particle colliders like the Large Hadron Collider (LHC). As accelerators push the boundaries of operational parameters, the influence of higher-order magnetic fields becomes more pronounced, requiring precise corrections to ensure optimal performance. Addressing non-linearities, which arise from magnetic field errors, is crucial not only for the LHC's current operations but also for future collider designs.

The LHC acts as a central testbed for investigating higher-order non-linearities that directly influence beam stability, dynamic aperture, and beam lifetime. Correcting these non-linearities is crucial for sustaining high performance in the LHC and for informing the design of future machines. This research is driven by the need to develop advanced beam-based techniques for measuring and correcting these higher-order effects, shifting from traditional empirical methods to more precise and quantitative approaches. Accurately quantifying the fields present in the LHC is essential for achieving a comprehensive understanding of the machine. Such confidence in managing non-linear dynamics is vital for the development and operation of future accelerators like the High Luminosity LHC (HL-LHC) and the Future Circular Collider (FCC).

A key issue highlighted during the LHC's Run 2 is the observed discrepancy at injection energy between the measured third-order chromaticity Q''' and the predictions made by existing models. The magnetic measurements of the LHC's magnets, conducted during its construction phase, have served as the foundation for simulations, beam steering, and non-linear correction computations. However, this discrepancy suggests the presence of previously unaccounted-for field errors not captured by the initial magnetic measurements. Identifying and addressing these unknown sources of higher-order magnetic errors is crucial for improving the LHC's operational parameters, particularly during beam injection, to ensure optimal performance and stability.

This thesis aims to address these challenges by developing improved methods for characterizing

higher-order magnetic fields, such as decapolar components, and their impact on beam dynamics. Through direct, quantitative approaches, the research seeks to refine correction strategies and better understand the interplay of non-linear magnetic fields. These advancements will contribute not only to enhancing the LHC's performance but also to informing the design and operation of future high-energy colliders.

1.2. Thesis Outline

The thesis starts by giving the motivations for this thesis work, as well as its outline, in Chapter 1. Key concepts of accelerator physics are presented in Chapter 2. The CERN accelerator complex and the LHC are then detailed. Measurement and correction techniques are presented in Chapter 3.

The first results chapter, Chapter 4 examines the skew octupolar fields which have been shown to limit the dynamic aperture, especially during beam excitation with the AC-Dipole. A response matrix method was developed to correct skew octupolar Resonance Driving Terms (RDTs) at top energy. The study also explores the influence of Landau octupoles on skew octupolar RDTs at injection energy, revealing the importance of accurate coupling modeling in predicting these effects.

The second chapter, Chapter 5, delves into the decapolar fields at injection energy, addressing discrepancies between measurements and model predictions of third-order chromaticity. Through a series of novel measurements and simulations, including the introduction of chromatic amplitude detuning, the research identifies the decay of the decapolar component in the main dipoles as a key factor in these discrepancies. Corrective strategies were developed for decapolar RDTs, leading to measurable improvements in beam lifetime and stability.

The third chapter, Chapter 6, builds up on the achievements of the decapolar corrections and focuses on the measurement and analysis of dodecapolar and decatetrapolar fields, made possible by improved dynamic aperture, measurement techniques and refinements in post-processing. The study successfully measures higher-order chromaticity terms and dodecapolar RDTs, demonstrating their significant contribution to the overall field errors and allowing the first ever benchmarking of these effects in the LHC. The findings underscore the need for further investigation into these higher-order fields and their impact on beam dynamics to optimize the LHC's performance.

The final chapter, Chapter 7, which serves as a supplementary section, explores the application of optics measurement techniques employed at CERN to the SuperKEKB rings (HER and LER) at KEK in Tsukuba, Japan. This study is the outcome of a one-month secondment as part of the EAJADE collaboration.

Finally, conclusions for these studies are drawn in Chapter 8.

Concepts of Accelerator Physics

2.1. Particle Accelerators

Particle accelerators have come a long way since their invention in the 20th century, when they could only reach a few MeV of energy using electric fields [1]. Today, they achieve much higher energies, up to the TeV range, allowing for more detailed investigations into particle physics.

One of the major milestones in accelerator development was the shift to circular accelerators, known as synchrotrons. By the 1970s, machines like the ISR at CERN could accelerate particles to 62 GeV using beams from the Proton Synchrotron (PS) [2], enabling significant advances in particle physics experiments.

As accelerators have evolved, so has the need for better control of particle beams. Managing beam stability and lifetime has become crucial, especially in modern machines like the LHC.

Considerable advancements have been made in both radiofrequency acceleration technologies, collimation, superconducting magnets and beam dynamics to keep beams stable and on track, even at high energies. These improvements are not only important for physics research but are also used in medical and industrial fields.

In modern accelerators, precise beam control is necessary to ensure efficient and accurate collisions. Correcting beam optics has moved from being just a theoretical exercise to an essential part of operations. This has led to a shift away from empirical methods, where trial and error were common, towards more direct, quantitative approaches that provide a detailed and accurate correction of beam dynamics. These advancements not only improve performance but also play a key role in designing future accelerators with better stability and efficiency.

2. Concepts of Accelerator Physics

2.1.1. The CERN Complex

CERN is a large laboratory located on the border of France and Switzerland, near Geneva. Although well-known for discoveries in particle physics, studies are also conducted on medical applications, biology, radiation hardness or material science. Several accelerators are part of the accelerator complex, as illustrated in Fig. 2.1. A large number of fixed target experiments exist, whose beams are delivered by various accelerators depending on their needs. These experiments are often renewed¹.

The largest part of the CERN accelerator complex is the LHC. The LINAC4, PSB, PS and SPS accelerators serve as pre-injectors to the LHC.

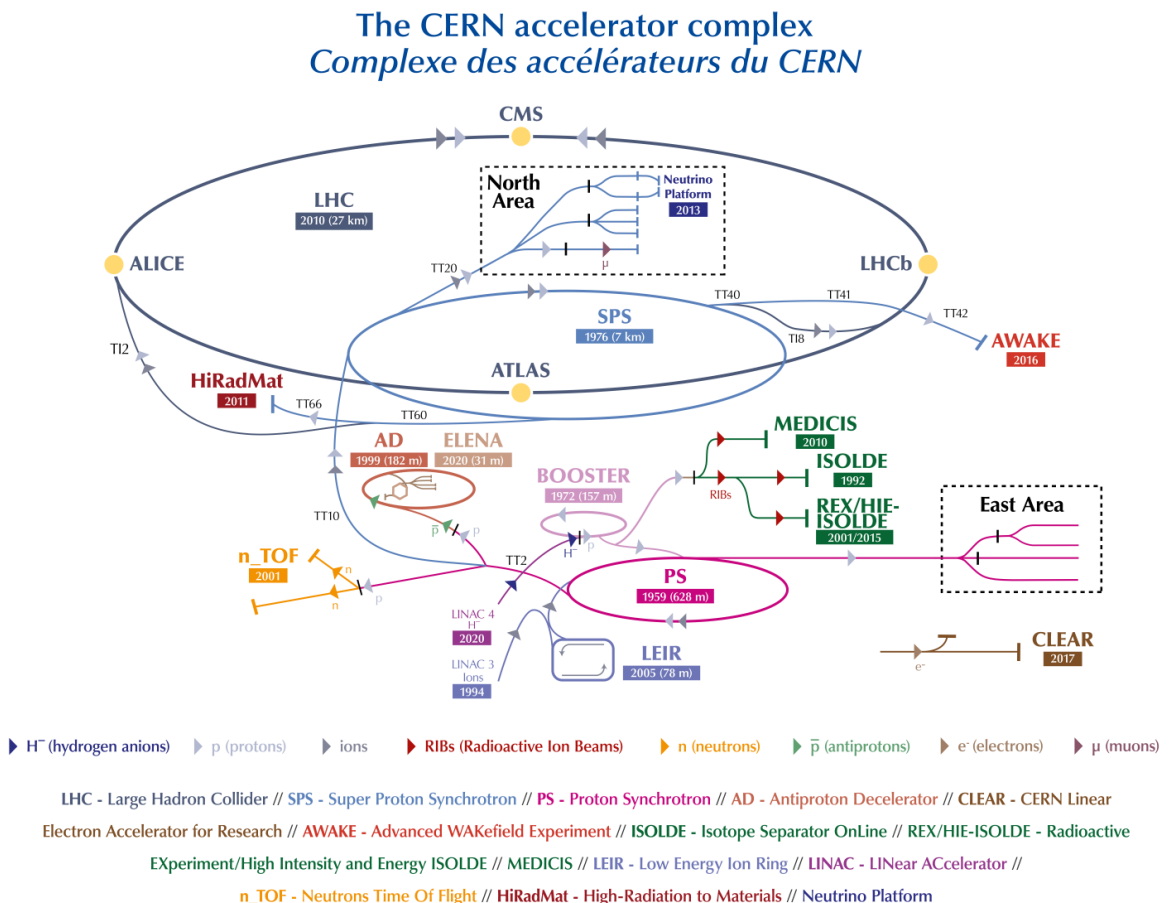


Figure 2.1.: Schematic illustration of the accelerator complex at CERN. Most accelerators are both used as injectors for the LHC or to provide beams to fixed target experiments [3].

¹Up to date information can be found on <https://home.cern/science/experiments>.

2.1.2. The Large Hadron Collider

The Large Hadron Collider (LHC) is a circular particle accelerator primarily designed to collide protons for fundamental particle physics research. It can also occasionally collide ions such as oxygen or lead for specific studies. At the time of writing, in 2024, it holds several records, such as being the largest and most powerful accelerator in the world, at nearly 27 km long. The LHC is composed of two beam pipes, capable of accelerating two particle beams from an injection energy of 450 GeV to an energy of 6,800 GeV, before colliding them in four detectors: ATLAS, CMS, Alice and LCHb.

Well-publicized, the LHC is often depicted via its superconducting dipole magnets, housed in blue cryostats, aimed at cooling the coils. Figure 2.2 shows a 3D cut of such magnets. The LHC is mostly composed of these *main* dipoles, holding 1,232 of them, each about 14 meters long. Particles in the LHC travel at nearly the speed of light (99.9999905%), completing roughly 11,200 turns around the tunnel each second. To generate the intense magnetic fields needed to deflect such high-momentum particles, currents of approximately 12,000 amperes are supplied to the magnets. However, conventional materials like copper would overheat and melt under this current load, necessitating the use of superconducting materials such as niobium-titanium (NbTi).



Figure 2.2.: 3D cut of a main LHC dipole [4]. Both beam pipes can be seen surrounded by the coils, strongly clamped by the yokes.

Straight Sections and Arcs

The LHC is not a perfect circle. It is indeed composed of height *straight* sections, called the *Insertion Regions* (IRs) where detectors or specific instrumentation are placed. Connecting those sections, the *arcs* are where the majority of the magnets and their correctors are located, along with some instrumentation like beam position monitors. Figure 2.3 shows the arcs as well as the purpose of each straight section, housing either specific instrumentation or detectors.

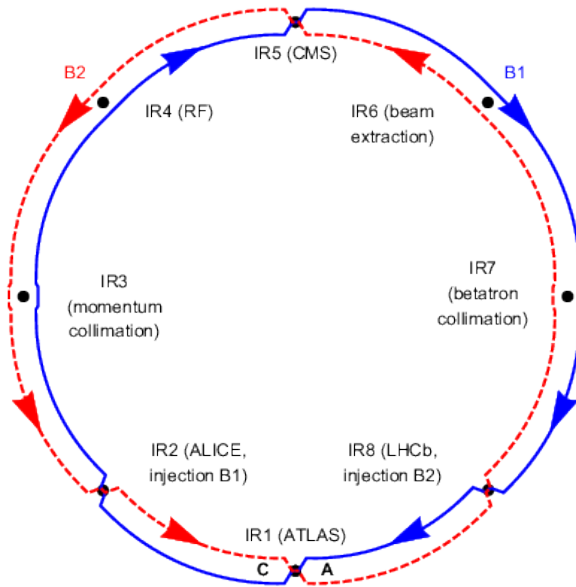


Figure 2.3.: Schematic of the LHC layout.

Arc Cells

Each arc is made up of 23 cells. Magnets are organized in a standard FODO structure (see Section 2.3.1), as shown in Fig. 2.4. *Dipoles* are responsible for bending the trajectory of the particles. Their associated correctors, the orbit correctors, mitigate any possible drift in the path. *Quadrupoles* are used to control the beam size along the ring. Their effect is focusing in one plane and defocusing in the other. Their associated correctors control the frequency of oscillations of the beam (see tune, Section 2.3.1) and possible field imperfections. *Sextupoles* correct chromaticity, a misfocus from quadrupoles due to particles having a different momentum than the reference particle. *Octupoles* are used to stabilize the beam by introducing Landau Damping [5]. The associated correctors correct higher-order chromaticity effects as well as amplitude-dependant tune shifts. *Decapoles* correctors aim at correcting an even higher chromaticity order.

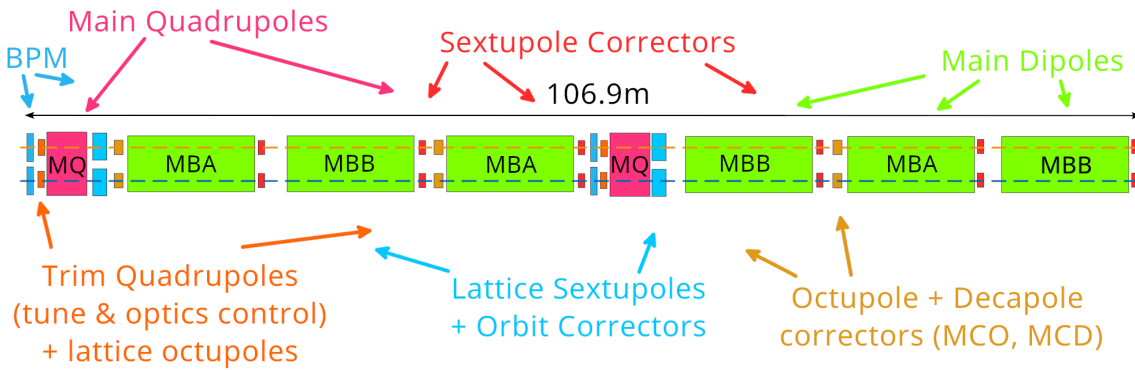


Figure 2.4.: Schematic of an LHC Arc cell [6].

Cycles

During the operation of the LHC, the machine goes through several states, each defined for specific scenarios [7].

A common example is the operational cycle of the LHC, illustrated in Fig. 2.5. Initially, the magnets are pre-cycled [8] without any beam circulating, to ensure a reproducible magnetic state. Their current is then increased to accept particles at the injection energy of 450GeV. To verify the machine's proper functioning, a probe bunch of reduced intensity is first injected, at around 10^{10} particles. The number of bunches and their intensity are then gradually increased to obtain the desired scheme needed for collisions, which varies throughout the year based on experimental demands. The number of bunches and their intensity can be adjusted as needed to ensure the machine's safety. A common scheme in 2024 is to inject about 2350 bunches, with around $1.5 \cdot 10^{11}$ particles in each bunch, for collisions. Optics measurements, due to their destructive nature, typically use between one and three *pilot* bunches at a lower intensity of 10^{10} particles.

The current in the magnets is then increased along with adjustments in the phase and voltage of the RF system to accelerate the particles to an energy of 6.8 TeV. During this ramp, the beam is initially squeezed at the Interaction Points. However, further squeezing is limited by the detectors' resolution, which is insufficient to accurately reconstruct a large number of collision events simultaneously. Collisions then start, while levelling the β^* at the ATLAS and CMS experiments relative to the remaining beam intensity, ensuring optimal performance of the detectors.

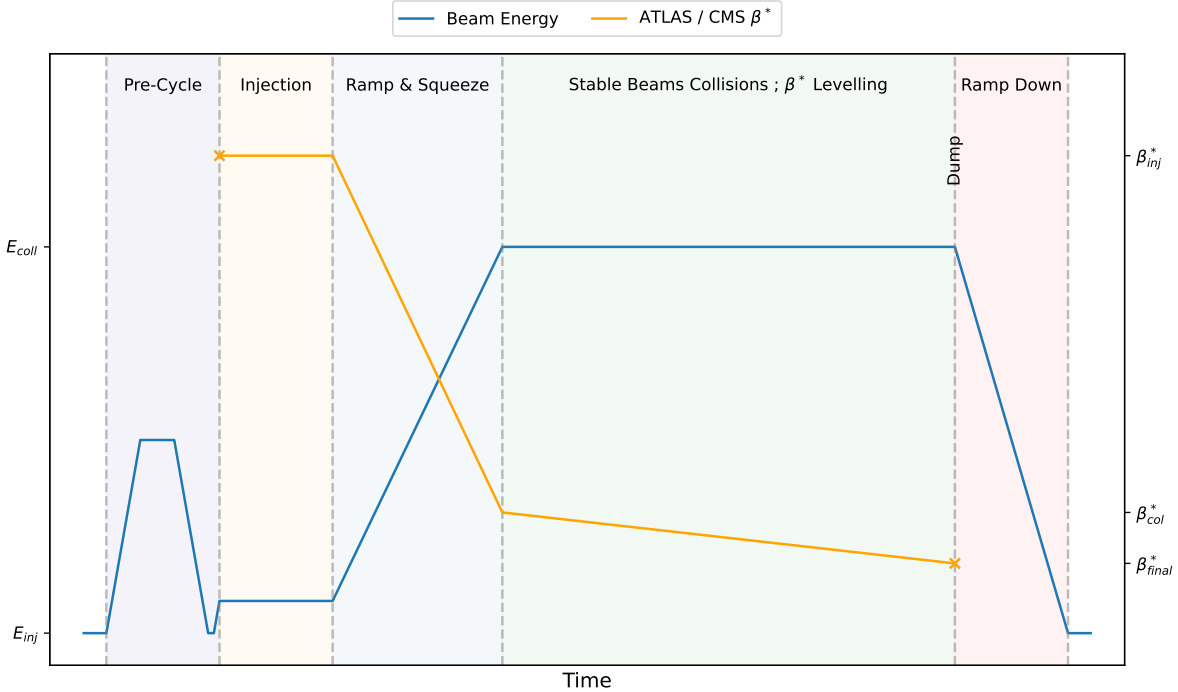


Figure 2.5.: Simplified illustration of a standard LHC cycle. Adapted from [9].

2.2. Magnetic Fields

2.2.1. Nomenclature

Several notations coexist to denote magnetic fields. In this thesis, the *European Convention* [10] is used for field indices, as shown in Table 2.1. MAD-X, and MAD-NG, however, use the *American Convention*.

Multipole	Index	MAD-X
Dipole	1	0
Quadrupole	2	1
Sextupole	3	2
Octupole	4	3
Decapole	5	4
Dodecapole	6	5
Decatetrapole	7	6
Decahexapole	8	7

Table 2.1.: Relation between the field indices used in this thesis and multipoles.

As such, unless explicitly stated, quantities such as the magnetic strength b and normalized strength K presented latter will be expressed with the notation used in the first column. A schematic representation of magnets up to dodecapole, order 6, is given in Fig. 2.6.

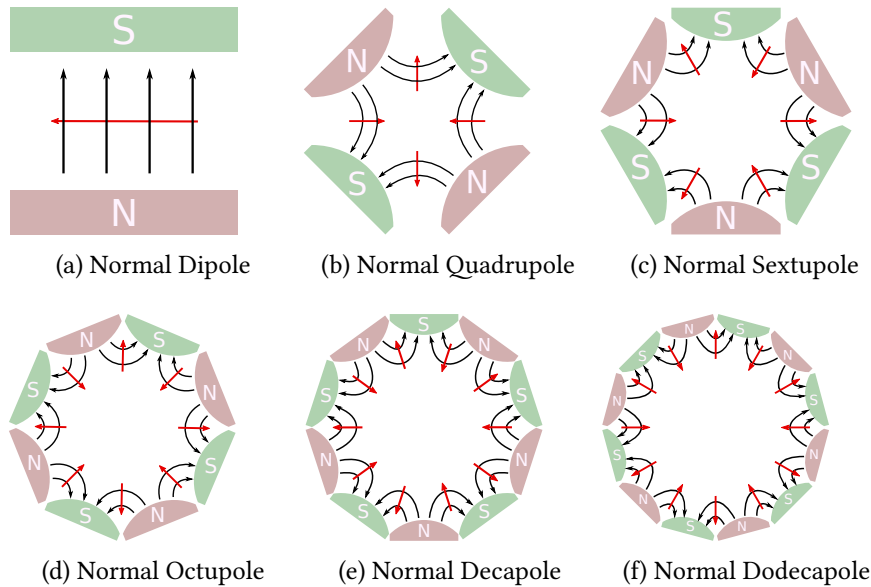


Figure 2.6.: Schematics of magnetic multipoles. In black the magnetic field lines, which extend also to the inner part of the magnets, but drawing them there has been omitted for clarity of the figure. Red arrows indicate the direction of force on a positive charge moving out of the page towards the reader. Courtesy of Joschua Dilly [10].

2.2.2. Multipole Expansion

In order to force the particles to form a closed orbit, they are subjected to magnetic fields that deflect their trajectories. The force exerted on a charged particle via electromagnetic fields is the Lorentz force \vec{F} [11],

$$\vec{F} = \frac{d\vec{p}}{dt} = q(\vec{E} + \vec{v} \times \vec{B}), \quad (2.1)$$

where \vec{p} is the momentum of the particle, q its charge, \vec{v} its velocity, \vec{E} the electric field and \vec{B} the magnetic field. With particles close to the speed of light, it becomes apparent that magnetic fields are dominant in the resulting force and are thus used to act on the particles trajectories. The guiding magnetic field in the transverse planes x and y can be described using a *multipole expansion*, where the components of the magnetic field can be written as a series of terms corresponding to different orders of multipoles. The multipole expansion is then given in terms of the normal and skew field

gradients \mathcal{B} and \mathcal{A} with multipoles of order n [12],

$$B_y + iB_x = \sum_{n=1}^{\infty} (\mathcal{B}_n + i\mathcal{A}_n) (x + iy)^{n-1}. \quad (2.2)$$

The normal and skew field gradients \mathcal{B} and \mathcal{A} for a multipole of order n can then be calculated from this complex field,

$$\mathcal{B}_n + i\mathcal{A}_n = \frac{1}{(n-1)!} \cdot \left. \frac{\partial^{n-1} (B_y + iB_x)}{\partial(x+iy)^{n-1}} \right|_{x=0, y=0}. \quad (2.3)$$

For instance, expanded up to octupoles, the magnetic field acting on the horizontal plane reads,

$$B_y = \underbrace{B_{y0}}_{\text{dipole}} + \underbrace{\frac{\partial B_y}{\partial x} \cdot x}_{\text{quadrupole}} + \underbrace{\frac{1}{2!} \frac{\partial^2 B_y}{\partial x^2} \cdot x^2}_{\text{sextupole}} + \underbrace{\frac{1}{3!} \frac{\partial^3 B_y}{\partial x^3} \cdot x^3}_{\text{octupole}} + \dots \quad (2.4)$$

An ideal magnet would often produce either a sole normal or skew field. However, this is not applicable to real-life magnets that are imperfect, due to design and manufacturing constraints. Field errors are thus introduced, relative to the main field of the ideal 2N-pole magnet at a reference radius r_{ref} , as shown in Eq. (2.5). The coefficients of the normal and skew relative field errors, referred to as a_n and b_n , are dimensionless but often given in units of 10^{-4} .

$$B_y + iB_x = \begin{cases} \mathcal{B}_N \cdot \sum_{n=1}^{\infty} (b_n + ia_n) \left(\frac{x+iy}{r_{ref}} \right)^{n-1}, & \text{for normal magnets} \\ \mathcal{A}_N \cdot \sum_{n=1}^{\infty} (b_n + ia_n) \left(\frac{x+iy}{r_{ref}} \right)^{n-1}, & \text{for skew magnets} \end{cases} \quad (2.5)$$

The total normal and skew field components of order n for an imperfect 2N-pole magnet is thus given by the following equation:

$$\begin{aligned} \mathcal{B}_n &= \mathcal{B}_N \cdot \frac{b_n}{r_{ref}^{n-1}}, \\ \mathcal{A}_n &= \mathcal{A}_N \cdot \frac{a_n}{r_{ref}^{n-1}}. \end{aligned} \quad (2.6)$$

The unit of the field is relative to the multipole order n : [Tm $^{1-n}$].

2.2.3. Beam Rigidity and Normalization

Beam Rigidity

In order to bend particles to form a ring, the force acting on the particles given by the Lorentz force must be equal to the centrifugal force [11, 13]:

$$q(\vec{E} + \vec{v} \times \vec{B}) = \frac{mv^2}{\rho}, \quad (2.7)$$

with q the charge of the particle, \vec{E} and \vec{B} respectively the electric and magnetic field strengths, \vec{v} the velocity of the particle, m its mass and ρ the radius of the circular path. The beam rigidity is a quantification of the ability of a magnetic field to bend the trajectory of a particle. It is derived from the previous equation and relates the magnetic field B , the radius of curvature ρ to the momentum p and charge q of the particle. By neglecting the electrical force and using $p = mv$,

$$\begin{aligned} qvB &= \frac{mv^2}{\rho}, \\ \rightarrow qB &= \frac{p}{\rho}, \\ \rightarrow B\rho \quad [\text{T.m}] &= \frac{p}{q}. \end{aligned} \quad (2.8)$$

The beam rigidity can also be expressed via the momentum in GeV. The usual approximation is then given by,

$$B\rho \approx 3.33 \cdot pc. \quad (2.9)$$

It is of interest when designing an accelerator to set the maximum field as well as the required radius of curvature for a specific momentum and particle. An interesting metric of an accelerator is also its *filling factor*, or percentage of dipoles in the machine. It can be calculated via the radius of curvature: $f = \rho/r$. A low filling factors means more space for other magnets, collimators, beam instrumentation, etc.

Field Normalization

The Beam Rigidity is also used as a way to normalize magnetic field strengths in particle accelerators where the momentum of the particle changes (i.e. acceleration or deceleration). The normalized Normal and Skew magnetic strengths K and J for a multipole of order n are thus given by [12] the following,

$$\begin{aligned} K_n &= \frac{q}{p}(n-1)!\mathcal{B}_n, \\ J_n &= \frac{q}{p}(n-1)!\mathcal{A}_n, \end{aligned} \quad (2.10)$$

with p the momentum of the particle, q its charge and \mathcal{B} and \mathcal{A} the field gradients.

2.2.4. Hamiltonian

The Hamiltonian describing the motion of relativistic particles in static electromagnetic fields is given by [14],

$$H = c\sqrt{(\mathbf{p} - q\mathbf{A})^2 + m^2c^2} + q\phi. \quad (2.11)$$

where ϕ is the scalar potential, \mathbf{A} the vector potential, q , \mathbf{p} and m respectively the charge, canonical momentum and mass of the particle and c the celerity of light.

After having changed this Hamiltonian to be dependent on curved coordinates, introduced in the next section, the motion in the transverse planes for a given multipole of order n (other than dipoles) can be described by the following [14],

$$\begin{aligned} H &= \frac{q}{p}\Re\left[\sum_{n>1}(\mathcal{B}_n + i\mathcal{A}_n)\frac{(x+iy)^n}{n}\right] \\ &= \Re\left[\sum_{n>1}(K_n + iJ_n)\frac{(x+iy)^n}{n!}\right]. \end{aligned} \quad (2.12)$$

Quite often, when studying the effect of a magnet on the beam, only one component is required, and the sum can thus be dropped. The normal and skew fields can also be isolated in order to consider their sole effect as shown in the following,

$$\begin{aligned} N_n &= \frac{1}{n!}K_n\Re[(x+iy)^n], \\ S_n &= -\frac{1}{n!}J_n\Im[(x+iy)^n]. \end{aligned} \quad (2.13)$$

2.2.5. Harmonics

The magnetic fields in the LHC are generated by the coils of its magnets. However, real-world magnets never produce a perfect, single field as desired. Instead, some field errors, known as *allowed harmonics*, naturally arise due to the geometric symmetries of the coils. As a result, the main dipoles of the

LHC can generate fields resembling those of sextupoles, decapoles, decatetrapoles, and so on [15]. Additionally, manufacturing imperfections contribute to field errors beyond the allowed ones, an example being octupolar errors seen in the LHC dipoles.

During the design of the LHC, the main dipoles have been identified to generate significant field errors. Magnetic measurements of those various fields were thus taken and magnetic tables built based on real-life magnets nowadays installed in the machine. Those magnetic tables, computed for each LHC configuration by *WISE* [16] are used by simulation softwares. Predictions of field errors and compensating strength for the correctors is computed by the Field Description for the LHC (*FiDeL*, [17]). *FiDeL* is used in the LHC control system in operation to compensate the field errors depending on the current configuration of the machine.

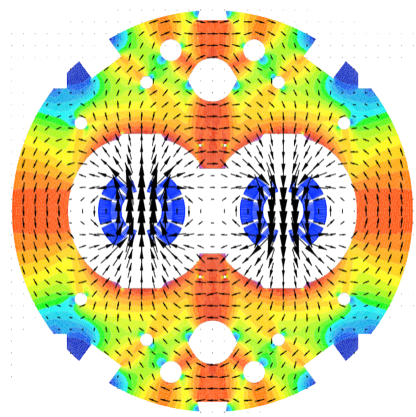


Figure 2.7.: Magnetic field in a dipole magnet [15].

2.3. Coordinate Systems

In circular accelerators, particle dynamics are represented using a traveling coordinate system. A reference orbit is determined by the lattice and its magnet strengths, forming the *optics*. In the case of a synchrotron, like the LHC, the reference orbit is also called the closed orbit.

The Frenet-Serret coordinate system moves along the ring on the reference orbit. The coordinates are then transverse: x and y , and longitudinal in the direction of travel: s . Figure 2.8 shows those coordinates.

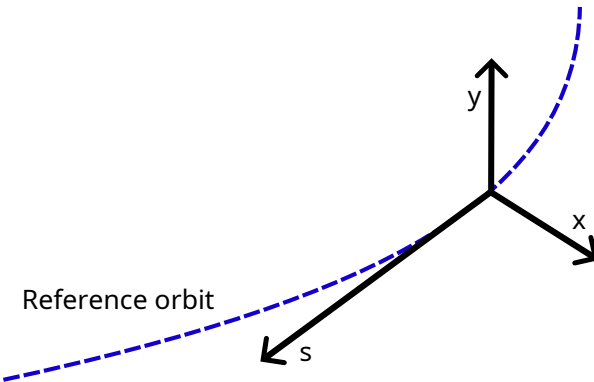


Figure 2.8.: Frenet-Serret coordinate system, commonly used in accelerator physics. The system moves along the reference orbit.

This coordinate system is widely used to simply describe either an element's or a particle's position in the accelerator. Without any explicit mention, those are coordinates used in this thesis. It is frequent to use the variable z to refer to either x or y in equations. In order to describe the motion of particles through a lattice, different coordinate systems can be used. To better describe the motion of particles through a lattice, various coordinate systems can be employed. First, the formalism for a linear lattice will be introduced, followed by an explanation of how motion in a machine with non-linear elements can be characterized.

Linear optics refers to the regime where the forces acting on particles, such as those from dipoles and quadrupoles, are directly proportional to the particle's displacement from the reference trajectory, resulting in simple, predictable motion described by linear equations and transfer matrices. Non-linear optics, on the other hand, involves higher-order magnetic elements like sextupoles and octupoles, where the forces are non-linear with respect to displacement. This leads to more complex particle motion, which can result in phase-space distortions and chaotic trajectories.

2.3.1. Linear Lattice

Courant-Snyder Parameters

A circular accelerator is composed of many multipoles of different orders. A very basic design only requires dipoles and quadrupoles in order to operate. Dipoles are used to bend the particles in order to form the ring, whereas quadrupoles are used to focus the beam to a focal point, similar to light optics. Those elements can be arranged in a particular order, to form a FoDo cell. Such cells present an alternating placement of focusing and defocusing quadrupoles with dipoles in between, as shown in Fig. 2.9, and are usually repeated many times along the ring.

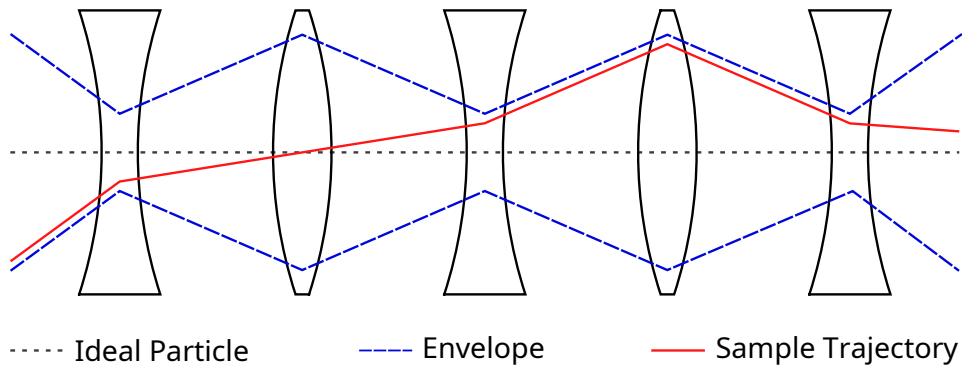


Figure 2.9.: Line composed of FoDo cells, a basic cell present in most accelerators, composed of a Focusing and a Defocusing quadrupole. The envelope is a factor of the β -function and the action J .

A lattice composed of only dipoles and quadrupoles, is referred to as a *linear* lattice. In a synchrotron, a circular particle accelerator, particles undergo transverse and longitudinal oscillations. Taking into account those oscillations, the phase-space ellipse of a particle at a position s in the ring can be described with a new system: the Courant-Snyder parameters, also known as Twiss parameters or the *optics functions* [18], as shown in Fig. 2.10.

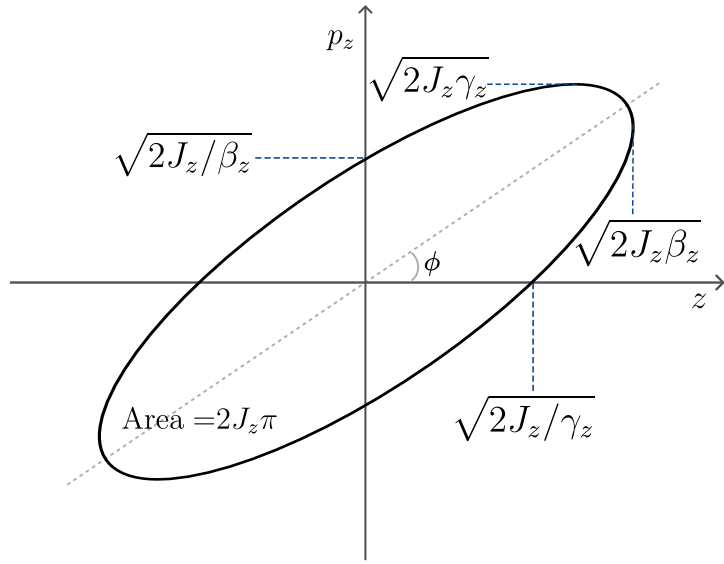


Figure 2.10.: Phase-space ellipse of a linear machine, parametrized by the Courant-Snyder parameters α , β and γ .

J , the action, is invariant of linear motion at a given energy and describes the amplitude of oscillations. It is related to the other quantities by:

$$J_z = \frac{1}{2}(\gamma_z \cdot z^2 + 2\alpha_z p_z \cdot z + \beta_z p_z^2). \quad (2.14)$$

The action can be related to the area in phase space, called the single particle emittance: $\epsilon = 2J$. As the β parameter varies along the ring, it is referred to as the β -function and is related to the amplitude of the oscillations. Thus, the smaller is the β -function, the smaller is also the envelope of the beam. The number of oscillations per turn is called the *tune*, and is closely related to the β -function:

$$Q_{x,y} = \frac{1}{2\pi} \oint \frac{1}{\beta_{x,y}(s)} ds. \quad (2.15)$$

It is common to express the position of a particle using *action-angle* variables, allowing to switch between the Courant-Snyder parameters and the Frenet-Serret system:

$$\begin{aligned} z &= \sqrt{2J_z\beta_z} \cos \phi_z \\ p_z &= -\sqrt{\frac{2J_z}{\beta_z}} (\sin \phi_z + \alpha_z \cos \phi_z). \end{aligned} \quad (2.16)$$

Normalized Coordinates

In order to simplify the description of the linear motion in a ring, a transformation can be applied to the previously seen coordinates. Figure Fig. 2.11 shows a phase-space described in both coordinates. The new coordinates, \hat{z} , and \hat{p}_z , are then expressed as factors of the α and β functions:

$$\begin{pmatrix} \hat{z} \\ \hat{p}_z \end{pmatrix} = \begin{pmatrix} \frac{1}{\sqrt{\beta_z}} & 0 \\ \frac{\alpha_z}{\sqrt{\beta_z}} & \sqrt{\beta_z} \end{pmatrix} \begin{pmatrix} z \\ p_z \end{pmatrix}. \quad (2.17)$$

This allows to describe the motion as a simple rotation, the new coordinates being only dependent on the invariant J_z and the phase ϕ_z :

$$\begin{aligned} \hat{z} &= \sqrt{2J_z} \cos(\phi_z), \\ \hat{p}_z &= \sqrt{2J_z} \sin(\phi_z). \end{aligned} \quad (2.18)$$

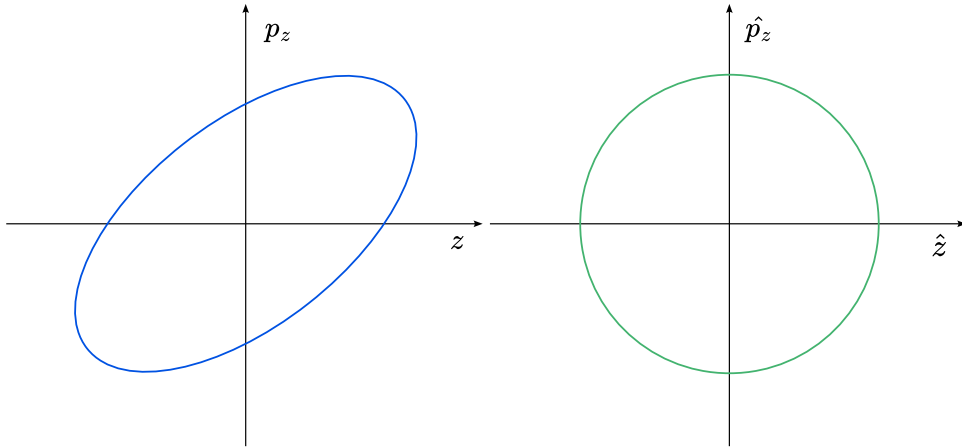


Figure 2.11.: Phase space described in both regular and normalized coordinates

Linear Transfer Maps

The final position of a particle after passing through an accelerator element can be described using *transfer maps*. In the case of linear optics, these maps take the form of matrices. Importantly, these maps should be symplectic, meaning they preserve the area of phase space, ensuring that the particle's motion is accurately represented. Symplecticity guarantees that key properties of the beam, such as its emittance, remain consistent, which is crucial for maintaining the stability and integrity of particle trajectories in the accelerator. For a matrix M and positions z at the initial location and s , the general formula reads [19]:

$$\begin{pmatrix} z \\ z' \end{pmatrix}_s = M \cdot \begin{pmatrix} z \\ z' \end{pmatrix}_0 \quad (2.19)$$

This formalism assumes that the magnetic field is constant along the element in the longitudinal direction. Basic elements such as drifts, dipoles, quadrupoles can then be described by a simple 2×2 matrix:

$$M_{drift} = \begin{pmatrix} 1 & L \\ 0 & 1 \end{pmatrix}, \quad (2.20)$$

$$M_{dipole} = \begin{pmatrix} \cos(L/\rho) & \rho \sin(L/\rho) \\ -1/\rho \sin(L/\rho) & \cos(L/\rho) \end{pmatrix}, \quad (2.21)$$

$$M_{focusing\ quad.} = \begin{pmatrix} \cos(\sqrt{k_2}L) & 1/\sqrt{k_2} \sin(\sqrt{k_2}L) \\ -\sqrt{k_2} \sin(\sqrt{k_2}L) & \cos(\sqrt{k_2}L) \end{pmatrix}, \quad (2.22)$$

$$M_{defocusing\ quad.} = \begin{pmatrix} \cosh(\sqrt{|k_2|}L) & 1/\sqrt{|k_2|} \sinh(\sqrt{|k_2|}L) \\ \sqrt{|k_2|} \sinh(\sqrt{|k_2|}L) & \cosh(\sqrt{|k_2|}L) \end{pmatrix}, \quad (2.23)$$

where L is the length of the element, ρ the radius of curvature of the orbit and k_2 the normalized strength of quadrupoles. In the case of quadrupoles, a focusing matrix should be used in the horizontal plane for focusing quadrupoles, where defocusing matrices should be used in the vertical plane. The opposite goes for defocusing quadrupoles.

Transfer matrices can be combined together to describe a larger group of elements, as the FoDo cell seen previously. Its transfer matrix can then be expressed as:

$$M_{FoDo} = M_{focusing\ quad.} \cdot M_{drift} \cdot M_{defocusing\ quad.} \cdot M_{drift}. \quad (2.24)$$

For a closed machine, a full revolution can be described by a so-called *one-turn map*, being the transfer matrix of the whole machine, denoted \mathcal{M} . Such a map can potentially contain thousands of elements.

2.3.2. Non-Linear Lattice

So far, Courant-Snyder parameters were a good way to describe the distribution of positions and velocities of particles in the transverse plane. One caveat of using this formalism is that it is restrained to linear optics and does not address non-linear elements, like octupoles. These elements generate forces that are not directly proportional to a particle's displacement from the reference trajectory. Effects such as resonances or those arising from an arrangement of several multipoles together can be described by the concepts introduced in this section. An overview of the needed mathematical tools is first given, before introducing maps.

Lie Algebra

One way to describe non-linear effects is to introduce Lie Algebra [20], a powerful algebra able to describe transformations, symmetries and their associated conserved quantities. The Lie algebra is a vector space, denoted \mathfrak{g} , equipped with a binary operation called the *Lie bracket* and denoted $[x, y]$ for two vectors x and y . Any vector space equipped with a Lie bracket (or commutator) satisfying the following conditions is called a Lie algebra:

- Bilinearity:

$$\begin{aligned} [ax + by, z] &= a[x, z] + b[y, z], \\ [z, ax + by] &= a[z, x] + b[z, y], \quad \forall x, y, z \in \mathfrak{g} \text{ and } a, b \text{ scalars} \end{aligned} \tag{2.25}$$

- Alternativity:

$$[x, x] = 0, \quad \forall x \in \mathfrak{g} \tag{2.26}$$

- Anticommutativity:

$$[x, y] = -[y, x], \quad \forall x, y \in \mathfrak{g} \tag{2.27}$$

- The Jacobi identity:

$$[x, [y, z]] + [y, [z, x]] + [z, [x, y]] = 0, \quad \forall x, y, z \in \mathfrak{g} \tag{2.28}$$

The *Lie bracket*, plays a central role in the Lie algebra. It describes how dynamical variables evolve under infinitesimal symplectic transformations.

Poisson Brackets

In accelerator physics, following the Hamiltonian formalism and classical mechanics, the commutator is represented by the *Poisson brackets*, which satisfy the necessary conditions for describing particle motion [20, 21]. Poisson brackets are used to express continuous symmetries, conserved quantities, and the time evolution of dynamical variables within the system.

Let's consider position and momentum coordinates $q_1 \cdots q_n$ and $p_1 \cdots p_n$ of a 2n-dimensional phase space. Usually, those would be x, y, p_x and p_y for transverse coordinates. The Poisson brackets of two functions f and g is then defined by:

$$[f, g] = \sum_{i=1}^n \frac{\partial f}{\partial q_i} \frac{\partial g}{\partial p_i} - \frac{\partial f}{\partial p_i} \frac{\partial g}{\partial q_i}. \tag{2.29}$$

The evolution of coordinates and momenta in time is described by Hamilton's equations of motion, which can be naturally expressed with Poisson brackets:

$$\begin{aligned} \frac{\partial H}{\partial p_i} = \frac{dq_i}{dt} &= [q_i, H] \\ -\frac{\partial H}{\partial q_i} = \frac{dp_i}{dt} &= [p_i, H]. \end{aligned} \tag{2.30}$$

Lie Operator

Given a function f , a differential operator called *Lie operator* is defined, and is closely related to the previously seen Poisson bracket:

2

$$:f := \sum_{i=1}^n \frac{\partial f}{\partial q_i} \frac{\partial}{\partial p_i} - \frac{\partial f}{\partial p_i} \frac{\partial}{\partial q_i}. \quad (2.31)$$

The action of this operator on a function g is equivalent to the Poisson brackets, as in:

$$:f:g = [f, g]. \quad (2.32)$$

A particular power series of this Lie operator can now be defined, called *Lie transformation*:

$$\begin{aligned} e^{:f:}g &= \sum_{l=0}^{\infty} \frac{1}{l!} :f: ^l g \\ &= g + [f, g] + \frac{1}{2!} [f, [f, g]] + \dots . \end{aligned} \quad (2.33)$$

Non-Linear Transfer Maps

As introduced in Section 2.3.1, the dynamics of a particle beam in a circular accelerator can be described by *transfer maps*. A symplectic *One Turn Map* \mathcal{M} that includes N non-linear elements is defined [20] as:

$$\mathcal{M} = e^{:h_N:} \cdot e^{:h_{N-1}:} \cdots e^{:h_1:} \cdot \mathcal{R} \quad (2.34)$$

where \mathcal{R} is a matrix describing the linear motion over one turn and the h_i terms representing the Hamiltonian of each non-linear elements of the machine. Via the Baker-Campbell-Hausdorff (BCH) theorem [22, 23], previous Lie transformations can be combined and simplified via Eq. (2.35) and Eq. (2.36). Further orders can be found and computed via [23].

$$e^{:h_1:} \cdot e^{:h_2:} = e^{:h:} \quad (2.35)$$

with

$$\begin{aligned}
 h &= h_1 + h_2 && \Rightarrow 1^{\text{st}} \text{ order} \\
 &+ \frac{1}{2}[h_1, h_2] && \Rightarrow 2^{\text{nd}} \text{ order} \\
 &+ \frac{1}{12}[h_1, [h_1, h_2]] - \frac{1}{12}[h_2, [h_1, h_2]] && \Rightarrow 3^{\text{rd}} \text{ order} \\
 &+ \dots
 \end{aligned} \tag{2.36}$$

The one turn map is thus expressed as a single Lie transformation:

$$\mathcal{M} = e^{h:} \cdot \mathcal{R}. \tag{2.37}$$

In most cases, where the non-linear perturbations are small, the above series converges quickly and only the first order of Eq. (2.36) is used [24]. The resulting expression is then more elegant, being a simple sum of the Hamiltonians of the N non-linear elements:

$$\mathcal{M} = e^{h_1 + h_2 + \dots + h_N:} \cdot \mathcal{R}. \tag{2.38}$$

It is though to be noted that in this thesis experimental measurements show the evidence of higher order contributions. In order to fully understand the combined effect of multipoles, the BCH expansion needs to be expended further than the first two terms.

When transporting coordinates from one point to another, the length of the elements must be taken into account:

$$\begin{aligned}
 e^{LH:}x_0 &= x_1, \\
 e^{LH:}p_0 &= p_1.
 \end{aligned} \tag{2.39}$$

Normal Form

As non-linearities are introduced in the machine, the phase-space becomes distorted, resulting in J_z no longer being an invariant of motion. The previously seen normalization does not work anymore and the phase-space is no longer a simple circle. A new normalization is then introduced, called the *normal form*, with complex coordinates ζ , depending on new action and angle coordinates I_z and ψ_z :

$$\zeta_{z,\pm} = \sqrt{2I_z}e^{\mp i\psi_z}. \tag{2.40}$$

An exaggerated vision of such a phase-space in Courant-Snyder, normalized, and normal form coordinates can be seen in Fig. 2.12.

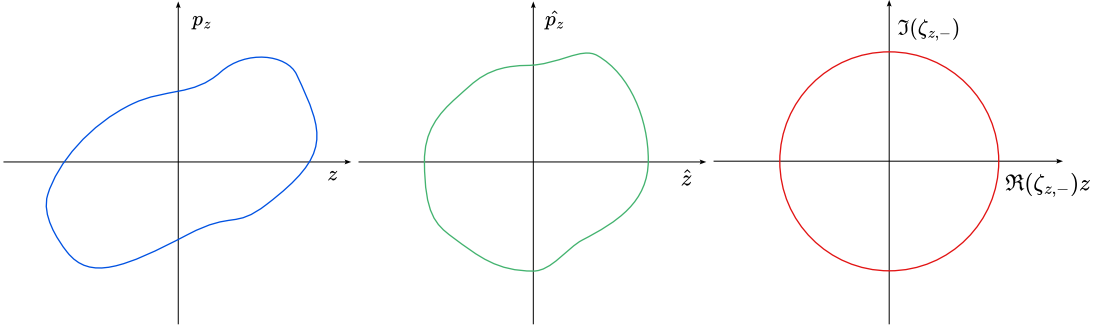


Figure 2.12.: Exaggerated phase space distorted by non-linearities described in regular (left), normalized (middle) and normal form (right) coordinates.

The map defined previously in Eq. (2.37) can be rewritten in order to retrieve an invariant of motion I_z by introducing a generating function F :

$$\tilde{\mathcal{M}} = e^{-F} \mathcal{M} e^{F} \quad (2.41)$$

Such a generating function includes all the non-linearities, simplifying the calculations. Going back and forth from normalized to normal forms coordinates is then straightforward, as depicted in Fig. 2.13. The hamiltonian H is now only dependent on the action I_z .

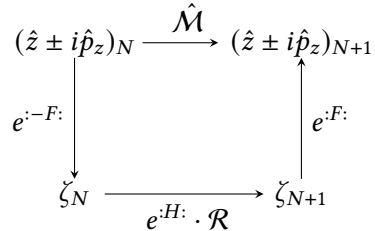


Figure 2.13.: A one turn map from turn N to $N+1$ solved using a generating function F , transforming to normal form coordinates ζ , applying the linear rotation R and transforming back to normalized coordinates.

The function F is defined as

$$F = \sum_{jklm} f_{jklm} \zeta_{x,+}^j \zeta_{x,-}^k \zeta_{y,+}^l \zeta_{y,-}^m, \quad (2.42)$$

where f_{jklm} are the so-called Resonance Driving Terms (RDTs). The summation $jklm$ is done over all the combinations of j, k, l and m with $j + k + l + m = n$ for a multipole of order n , as shown in

Eq. (2.43):

$$\sum_{jklm} = \sum_{j=0}^n \sum_{k=0}^n \sum_{l=0}^n \sum_{m=0}^n ; \quad j+k+l+m = n. \quad (2.43)$$

The expression of the resonance driving terms is given by the global hamiltonian term h_{jklm} by

$$f_{jklm} = \frac{h_{jklm}}{1 - e^{i2\pi[(j-k)Q_x + (l-m)Q_y]}}, \quad (2.44)$$

where this coefficient is a summation over the hamiltonian terms of elements w in the lattice,

$$h_{jklm} = \sum_w h_{w,jklm} e^{i[(j-k)\Delta\phi_x + (l-m)\Delta\phi_y]}. \quad (2.45)$$

The expression of $h_{w,jklm}$ is itself derived from the general hamiltonian of Eq. (2.12) by applying a multinomial expansion on the coordinates [25] as shows Eq. (2.46). Derivations and more information on resonance driving terms can be found in Appendix C.

$$h_{w,jklm} = -\Re \left[\frac{K_{w,n} + iJ_{w,n}}{j!k!l!m!2^{j+k+l+m}} i^{l+m} \beta_{w,x}^{\frac{j+k}{2}} \beta_{w,y}^{\frac{l+m}{2}} \right] \quad (2.46)$$

Transforming from the normal form coordinates back to the original normalized coordinates can be done using the right side of Fig. 2.13. Which is written, to second order, as:

$$\begin{aligned} h_z^\pm &= e^{iF} \cdot \zeta_z^\pm \\ &\simeq \zeta_z^\pm + [F, \zeta_z^\pm] + \frac{1}{2!} [F, [F, \zeta_z^\pm]]. \end{aligned} \quad (2.47)$$

Using this equation to the first order and Eq. (2.40), the normalized coordinates can be expressed after N turns in Eq. (2.48).

$$\begin{aligned} (x - ip_x)(N) &= \sqrt{2I_x} e^{i(2\pi Q_x N + \psi_{x_0})} - \\ &\quad 2i \sum_{jklm} j f_{jklm} (2I_x)^{\frac{j+k-1}{2}} (2I_y)^{\frac{l+m}{2}} e^{i[(1-j+k)(2\pi Q_x N + \psi_{x_0}) + (m-l)(2\pi Q_y N - \psi_{y_0})]} \\ (y - ip_y)(N) &= \sqrt{2I_y} e^{i(2\pi Q_y N + \psi_{y_0})} - \\ &\quad 2i \sum_{jklm} l f_{jklm} (2I_x)^{\frac{j+k}{2}} (2I_y)^{\frac{l+m-1}{2}} e^{i[(k-j)(2\pi Q_x N + \psi_{x_0}) + (1-l+m)(2\pi Q_y N - \psi_{y_0})]}. \end{aligned} \quad (2.48)$$

This equation highlights the contribution of the non-linear elements to the motion of the particles.

Spectral lines arising from these contributions are discussed in Section 2.7.2. It is though to be observed that some f_{jklm} terms will not contribute to the motion in a given plane due to the dependence on j or l .

2.4. Examples of Maps

It is important to remember that two expansions are used when creating non linear transfer maps. When referring to the order of a map, it is the order of the BCH formula, used to combine Hamiltonians, that is referred to. The Lie transformation to transport the coordinates themselves is usually only taken to the first order.

2.4.1. Non-Linear Transfer of a Single Sextupole

Here, we are interested on the effect of a single sextupole on the regular frenet-serret coordinates x , y , p_x and p_y . Let's consider a sextupole with strength K_3 and a normal field,

$$H_3 = \frac{1}{6}K_3(x^3 - 3xy^2). \quad (2.49)$$

A transfer map, from longitudinal coordinate s_0 to s_1 , consisting of only this element is the following:

$$\begin{pmatrix} x \\ p_x \\ y \\ p_y \end{pmatrix}_{s_1} = e^{L:H_3:} \begin{pmatrix} x \\ p_x \\ y \\ p_y \end{pmatrix}_{s_0}, \quad (2.50)$$

where L is the length of the multipole. Using Eq. (2.33) to expand the Lie transformation to the first order, it can be rewritten as

$$\begin{aligned} e^{L:H_3:}x &= x + [L \cdot H_3, x], \\ e^{L:H_3:}p_x &= p_x + [L \cdot H_3, p_x], \\ e^{L:H_3:}y &= y + [L \cdot H_3, y], \\ e^{L:H_3:}p_y &= p_y + [L \cdot H_3, p_y]. \end{aligned} \quad (2.51)$$

Applying the poisson bracket of Eq. (2.29) on x or y yields 0, as neither the Hamiltonian nor x and y are dependent on p_x and p_y .

$$\begin{aligned}
 [L \cdot H_3, x] &= \overbrace{\frac{\partial(L \cdot H_3)}{\partial x} \frac{\partial x}{\partial p_x}}^0 - \overbrace{\frac{\partial(L \cdot H_3)}{\partial p_x} \frac{\partial x}{\partial x}}^0 + \underbrace{\frac{\partial(L \cdot H_3)}{\partial y} \frac{\partial x}{\partial p_y}}_0 - \underbrace{\frac{\partial(L \cdot H_3)}{\partial p_y} \frac{\partial x}{\partial y}}_0 \\
 &= 0.
 \end{aligned} \tag{2.52}$$

The poisson bracket applied on p_x or p_y though evaluates to a non-zero value, as the momentum is present in $p_{x,y}$ while x, y are present in the Hamiltonian:

$$\begin{aligned}
 [L \cdot H_3, p_x] &= \frac{\partial(L \cdot H_3)}{\partial x} \frac{\partial p_x}{\partial p_x} - \underbrace{\frac{\partial(L \cdot H_3)}{\partial p_x} \frac{\partial p_x}{\partial x}}_0 + \underbrace{\frac{\partial(L \cdot H_3)}{\partial y} \frac{\partial p_x}{\partial p_y}}_0 - \underbrace{\frac{\partial(L \cdot H_3)}{\partial p_y} \frac{\partial p_x}{\partial y}}_0 \\
 &= \frac{1}{2} K_3 L (x^2 - y^2)
 \end{aligned} \tag{2.53}$$

The same method is used for p_y . The final form of the transfer map Eq. (2.50) is then the following:

$$\begin{pmatrix} x \\ p_x \\ y \\ p_y \end{pmatrix}_{s_1} = \begin{pmatrix} 1 & & & \\ & 1 + \left(\frac{1}{2p_x} K_3 L (x^2 - y^2) \right) & & \\ & & 1 & \\ & & & 1 - \left(\frac{1}{p_y} K_3 L x y \right) \end{pmatrix} \begin{pmatrix} x \\ p_x \\ y \\ p_y \end{pmatrix}_{s_0}. \tag{2.54}$$

It is not necessary to go higher than the first order, as the second order of the expansion of the Lie transformation is 0 ; p_x is indeed not present in the result of the first poisson bracket:

$$\begin{aligned}
 \frac{1}{2!} [L \cdot H_3, [L \cdot H_3, p_x]] &= \frac{1}{2!} \left[L \frac{1}{6} K_3 (x^3 - 3xy^2), \left[L \frac{1}{6} K_3 (x^3 - 3xy^2), p_x \right] \right] \\
 &= \frac{1}{2!} \left[L \frac{1}{6} K_3 (x^3 - 3xy^2), \frac{1}{2} K_3 L (x^2 - y^2) \right] \\
 &= \frac{1}{2!} \cdot 0 \\
 &= 0
 \end{aligned} \tag{2.55}$$

2.4.2. Non-Linear Transfer of Two Sextupoles

We saw previously that a single sextupole only acts as a sextupole when it is alone in the transfer map, which is expected. Let's now consider two sextupoles whose hamiltonians are denoted H_1 and H_2 .

Creating a map consisting of only two sextupoles does not make much sense, as it finally results in one sextupole as their coordinates are the same. Instead, a drift is added between the two elements. The Hamiltonian of a drift of length L_D is given by [26],

$$D = -\frac{L_D}{2}(p_x^2 + p_y^2). \quad (2.56)$$

The application of the lie transformation on the canonical coordinates is then very simple, as no higher orders arise ($[D, [D, x]] = 0$):

$$\begin{aligned} e^{:D:}x &= x + L_D p_x, \\ e^{:D:}p_x &= p_x. \end{aligned} \quad (2.57)$$

The transfer map of such a line is then the following,

$$\mathcal{M} = e^{:Z:} = e^{:H_2:} \cdot e^{D:H_1:}, \quad (2.58)$$

describing the evolution of coordinates from a longitudinal position s_0 to s_1 ,

$$\begin{pmatrix} x \\ p_x \\ y \\ p_y \end{pmatrix}_{s_1} = \mathcal{M} \cdot \begin{pmatrix} x \\ p_x \\ y \\ p_y \end{pmatrix}_{s_0} \quad (2.59)$$

In order to combine those elements, the BCH formula from Eq. (2.36) is used, presented here to the third order for two elements,

$$Z = \underbrace{H_2 + H_1}_{\text{First order}} + \underbrace{\frac{[H_2, H_1]}{2}}_{\text{Second order}} + \underbrace{\frac{[H_2, [H_2, H_1]]}{12} - \frac{[H_1, [H_2, H_1]]}{12}}_{\text{Third order}} \quad (2.60)$$

First Order To the first order, the resulting effective hamiltonian is only the summation of two sextupoles.

Second Order The drift added to change the coordinates of H_1 allows the poisson bracket to evaluate to a non-zero value. Octupolar-like terms indeed appear in the effective hamiltonian. From this, it can be inferred that two sextupoles will interact together and introduce effects like amplitude detuning, second order chromaticity and RDTs. Details of the derivation can be found in Appendix A.

Third Order To the third order, even higher orders such as decapolar-like effects appear. Such effects include the third order chromaticity, chromatic amplitude detuning and RDTs.

Remark It is to be noted that while sextupoles do introduce higher-order terms, these are often designed to be small in comparison to those brought by the actual higher-order multipoles, making them thus often negligible. Such is the case in the LHC.

2.5. Observables

2.5.1. Dispersion

Treating a beam as a single particle having the design momentum p_0 leads to a machine with no apparent ill effect related to that momentum. However, when considering a particle beam where each particle follows a distribution in momentum, a few effects arise from this deviation, called the *momentum offset*, δ . It is defined as a relative difference to the design momentum:

$$\delta = \frac{p - p_0}{p_0}. \quad (2.61)$$

Those effects are referred to as *chromatic aberrations*. The first and most important to consider is the *dispersion*. Dispersion results from a particle with a momentum offset being deflected differently by the dipoles compared to a particle at the design momentum. Figure 2.14 shows an example of deflection. The particle is still subject to the other properties of the lattice, but with a different orbit, described by the dispersion function in Eq. (2.62).

$$\begin{aligned} D_x(s) &= \frac{\Delta x(s)}{\delta} \\ D_y(s) &= \frac{\Delta y(s)}{\delta}. \end{aligned} \quad (2.62)$$

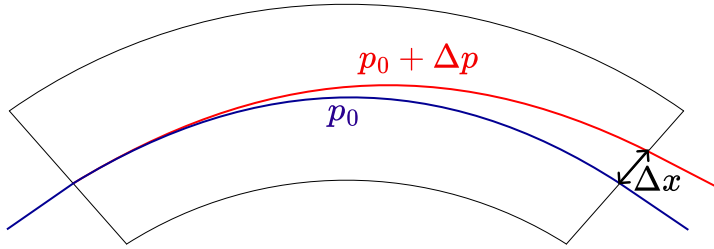


Figure 2.14.: Particles with a momentum offset will be deflected differently by dipoles. This offset in position can be described by the dispersion function.

Momentum Compaction Factor In synchrotrons, particles with a deviation in momentum with respect to the reference particle will experience a different path length due to the bending of the dipoles. This effect is characterized by the *momentum compaction factor* [11],

$$\alpha_c = \frac{\Delta C/C}{\delta}, \quad (2.63)$$

relating the circumference of the ring C to the momentum offset δ . A positive momentum compaction factor indicates a longer path traveled by particles with a positive momentum offset, and vice versa.

The momentum compaction factor can also be broken down into orders as an infinite sum, where the constant term is often referred to as the first order,

$$\alpha_c = \underbrace{\alpha_{c,0}}_{\text{Constant term}} + \underbrace{\sum_{i \geq 1} \alpha_{c,i} \delta^i}_{\text{Linear and non linear terms}}. \quad (2.64)$$

In the LHC, the contribution from the non constant terms is negligible [27]. Further details can be found in Section 6.2.1.

2.5.2. β -function

As seen previously in Section 2.3.1, the β -function is related to the amplitude of oscillations of the beam. Figure 2.15 shows how the β -function oscillates along the ring due to quadrupoles focusing and defocusing properties. The β -function is an important quantity found as a factor in several other observables that will be described later in this thesis.

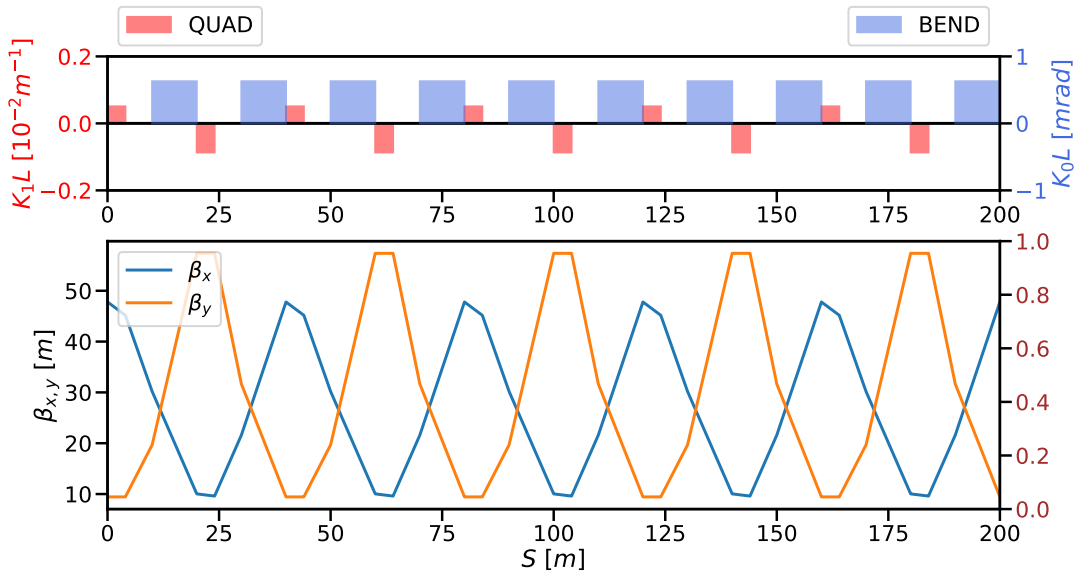


Figure 2.15.: Evolution of the β -function along the lattice. Horizontal and vertical beatings are usually opposite given the focusing and defocusing properties of quadrupoles in each plane.

A difference in β -function compared to the design leads to possibly unstable and larger beams, degrading its properties and making it harder to control. The relative difference in β -function is called the beta-beating, expressed in percents:

$$\beta\text{-beating [\%]} = \frac{\beta_z(s) - \beta_z(s)_{model}}{\beta_z(s)_{model}}. \quad (2.65)$$

2.5.3. Coupling

In a perfect scenario, the particle motion of each transverse plane is independent, or *uncoupled*. In practice, this transverse motion can be altered by some magnetic elements, giving rise to *betatron coupling* where the motion of each plane is not independent anymore. Such elements can be quadrupoles, mounted with a roll error introducing skew-quadrupolar fields, which are the main source of linear coupling in the LHC [9]. Field imperfections, solenoids and feed-down from higher orders can also contribute to coupling.

The resonances $Q_x + Q_y$ and $Q_x - Q_y$, called the *sum* and *difference* resonances, are mainly excited by skew quadrupoles. When coupling is present in the machine, the former may lead to unstable motion while the latter introduces an periodic exchange of emittance between the planes, keeping it stable. They can be characterized by the RDTs f_{1010} and f_{1001} .

Effects of normal multipoles start showing their skew counterpart (and vice versa) as the motion of transverse planes become coupled. This is demonstrated in Chapter 4 with octupoles.

2.6. Detuning Effects

2

2.6.1. Chromaticity

Chromaticity is the tune change ΔQ relative to the momentum offset δ . Chromaticity can be described by a Taylor expansion, given by

$$Q(\delta) = Q_0 + Q' \delta + \frac{1}{2!} Q'' \delta^2 + \frac{1}{3!} Q''' \delta^3 + O(\delta^4). \quad (2.66)$$

Or, more generally, rewritten as a sum to include all orders up to n :

$$Q(\delta) = Q_0 + \sum_{i=1}^n \frac{1}{i!} Q^{(i)} \delta^i. \quad (2.67)$$

The first order of the chromaticity expansion, Q' , is generally simply referred to as *chromaticity*, sometimes as *linear chromaticity*. The other terms are thus referred to as *non-linear chromaticity*.

The chromaticity change induced by a single element of order n and length L can be derived from the Hamiltonian of Eq. (2.12), averaging over the phase variables and differentiating relative to the actions $J_{x,y}$ and the momentum offset δ :

$$\Delta Q_{x,y}^{(n)} = \frac{\partial^n Q_{x,y}}{\partial^n \delta} = \frac{1}{2\pi} \int_L \left\langle \frac{\partial^{(n+1)} H}{\partial J_{x,y} \partial^n \delta} \right\rangle ds. \quad (2.68)$$

Detailed derivations are provided in [28], and an example is presented in the following section.

Linear Chromaticity from Sextupoles The first order chromaticity Q' is contributed to by sextupoles in the presence of off-momentum particles. The normal field of a sextupole, following Eq. (2.13) is given by

$$\mathcal{N}_3(x, y) = \frac{1}{3!} (x^3 - 3xy^2). \quad (2.69)$$

As the momentum offset δ introduces a change in orbit via dispersion [29], a variable change can be operated on both x and y , as shown in Eq. (2.70). In this thesis, vertical dispersion will be though neglected.

$$\begin{aligned} x &\rightarrow x + \Delta x = x + D_x \delta \\ y &\rightarrow y + \Delta y = y + D_y \delta \end{aligned} \quad (2.70)$$

The positions x and y can once be replaced, using the twiss parameters, giving the full expression:

$$\begin{aligned} \mathcal{N}_3(x + \Delta x, y) = & \frac{1}{6} K_3 \left[\left(\sqrt{2J_x\beta_x} \cos \phi_x \right)^3 \right. \\ & + 3 \left(\sqrt{2J_x\beta_x} \cos \phi_x \right)^2 D_x \delta \\ & + 3 \left(\sqrt{2J_x\beta_x} \cos \phi_x \right) D_x^2 \delta^2 \\ & + D_x^3 \delta^3 \\ & - 3 \left(\sqrt{2J_x\beta_x} \cos \phi_x \right) \left(\sqrt{2J_y\beta_y} \cos \phi_y \right)^2 \\ & \left. - 3D_x \delta (\sqrt{2J_y\beta_y} \cos \phi_y)^2 \right] \end{aligned} \quad (2.71)$$

Averaging over the phase variables removes any odd cosine:

$$\begin{aligned} \langle \mathcal{N}_3(x + \Delta x, y) \rangle = & \frac{1}{6} K_3 \left(3J_x\beta_x D_x \delta \right. \\ & + D_x^3 \delta^3 \\ & \left. - 3D_x \delta J_y \beta_y \right) \end{aligned} \quad (2.72)$$

The chromaticity can then be obtained by differentiating relative to the action $J_{x,y}$ to retrieve the tune, and finally by the momentum offset δ , as presented in Eq. (2.73). In the presence of second order dispersion [29], sextupoles will generate some amount of Q'' , usually negligible in the LHC.

$$\begin{aligned} \Delta Q'_x &= \frac{1}{2\pi} \int_L \frac{\partial^2 \langle \mathcal{N}_3 \rangle}{\partial J_x \partial \delta} ds \quad ; \quad \Delta Q'_y &= \frac{1}{2\pi} \int_L \frac{\partial^2 \langle \mathcal{N}_3 \rangle}{\partial J_y \partial \delta} ds \\ &= \frac{1}{2\pi} L \frac{1}{2} K_3 \beta_x D_x && = -\frac{1}{2\pi} L \frac{1}{2} K_3 \beta_y D_x \\ &= \frac{1}{4\pi} K_3 L \beta_x D_x && = -\frac{1}{4\pi} K_3 L \beta_y D_x \end{aligned} \quad (2.73)$$

Non-Linear Chromaticity Higher orders of the chromaticity function are described in [28] and follow the same logic as for the linear chromaticity from sextupoles. A general formula can be found for the chromaticity of order n , $n > 2$, relating a chromaticity of order n with a multipole of order $n+2$:

$$\begin{aligned}\Delta Q_x^{(n)} &= \frac{1}{4\pi} K_{n+2} L \beta_x D_x^n \\ \Delta Q_y^{(n)} &= - \frac{1}{4\pi} K_{n+2} L \beta_x D_x^n\end{aligned}\tag{2.74}$$

2.6.2. Amplitude Detuning

Amplitude detuning is a tune shift induced by the amplitude of oscillations of a particle. This detuning is directly related to the single particle emittance and can be described via a Taylor expansion around the emittance of both planes, ϵ_x and ϵ_y . Equation (2.75) shows this expansion up to the second order. Further expansions can be found in [28].

$$\begin{aligned}Q_z(\epsilon_x, \epsilon_y) &= Q_{z0} + \left(\frac{\partial Q_z}{\partial \epsilon_x} \epsilon_x + \frac{\partial Q_z}{\partial \epsilon_y} \epsilon_y \right) \\ &\quad + \frac{1}{2!} \left(\frac{\partial^2 Q_z}{\partial \epsilon_x^2} \epsilon_x^2 + 2 \frac{\partial^2 Q_z}{\partial \epsilon_x \partial \epsilon_y} \epsilon_x \epsilon_y + \frac{\partial^2 Q_z}{\partial \epsilon_y^2} \epsilon_y^2 \right) + \dots\end{aligned}\tag{2.75}$$

The first order terms of amplitude detuning are generated by octupoles, and to some extent by sextupoles when considering their higher order contributions. Those higher contributions are usually measurable but small compared to the ones of normal octupoles in the LHC. Further derivations can be found in Appendix B.

2.6.3. Chromatic Amplitude Detuning

Similar to amplitude detuning, *chromatic amplitude detuning* is a tune shift induced by the amplitude of oscillations of a particle but with an additional dependence on the momentum offset. This effect can be described by a Taylor expansion around the emittance of both planes ϵ_x , ϵ_y , and the momentum offset δ . Equation (2.76) shows this expansion up to the second order. Both the emittance ϵ and the action J can be seen to describe the chromatic amplitude detuning as terms are interchangeable with $\epsilon_{x,y} = 2J_{x,y}$. This expansion being more general than the ones of chromaticity or amplitude detuning, is it to be expected to retrieve those terms here as well.

$$\begin{aligned}
Q_z(\epsilon_x, \epsilon_y, \delta) = & Q_{z0} + \left[\frac{\partial Q_z}{\partial \epsilon_x} \epsilon_x + \frac{\partial Q_z}{\partial \epsilon_y} \epsilon_y + \frac{\partial Q_z}{\partial \delta} \delta \right] \\
& + \frac{1}{2!} \left[\frac{\partial^2 Q_z}{\partial \epsilon_x^2} \epsilon_x^2 + \frac{\partial^2 Q_z}{\partial \epsilon_y^2} \epsilon_y^2 + \frac{\partial^2 Q_z}{\partial \delta^2} \delta^2 \right. \\
& \quad \left. + 2 \frac{\partial^2 Q_z}{\partial \epsilon_x \partial \epsilon_y} \epsilon_x \epsilon_y + 2 \frac{\partial^2 Q_z}{\partial \epsilon_x \partial \delta} \epsilon_x \delta + 2 \frac{\partial^2 Q_z}{\partial \delta \partial \epsilon_y} \delta \epsilon_y \right] \\
& + \dots
\end{aligned} \tag{2.76}$$

Sextupolar contributions To the first order of the expansion, the only term coming from sextupoles is the linear chromaticity, seen previously in Section 2.6.1.

Octupolar contributions To the first order, the amplitude detuning terms $\frac{\partial Q_z}{\partial \epsilon_x} \epsilon_x$ and $\frac{\partial Q_z}{\partial \epsilon_y} \epsilon_y$ are contributed to by octupoles. The second order chromaticity Q'' appears when expanding to the second order.

Decapolar contributions The terms highlighted in orange, in Eq. (2.77), are the terms contributed to the first order by decapoles. Terms depending on both the emittance and the momentum offset are present, as well as the third order chromaticity Q''' . Further derivations can be found in Appendix B.

$$\begin{aligned}
Q_z(\epsilon_x, \epsilon_y, \delta) = & Q_{z0} + \left[\frac{\partial Q_z}{\partial \epsilon_x} \epsilon_x + \frac{\partial Q_z}{\partial \epsilon_y} \epsilon_y + \frac{\partial Q_z}{\partial \delta} \delta \right] \\
& + \frac{1}{2!} \left[\frac{\partial^2 Q_z}{\partial \epsilon_x^2} \epsilon_x^2 + \frac{\partial^2 Q_z}{\partial \epsilon_y^2} \epsilon_y^2 + \frac{\partial^2 Q_z}{\partial \delta^2} \delta^2 \right. \\
& \quad \left. + 2 \frac{\partial^2 Q_z}{\partial \epsilon_x \partial \epsilon_y} \epsilon_x \epsilon_y + 2 \frac{\partial^2 Q_z}{\partial \epsilon_x \partial \delta} \epsilon_x \delta + 2 \frac{\partial^2 Q_z}{\partial \delta \partial \epsilon_y} \delta \epsilon_y \right] \\
& + \frac{1}{3!} \left[\frac{\partial^3 Q_z}{\partial \delta^3} \delta^3 + \frac{\partial^3 Q_z}{\partial \epsilon_x^3} \epsilon_x^3 + \frac{\partial^3 Q_z}{\partial \epsilon_y^3} \epsilon_y^3 + \dots \right]
\end{aligned} \tag{2.77}$$

2.6.4. Feed-Down

When a particle passes off-center through a magnet, an effect called *feed-down* appears. Feed-down is a lower order contribution created by either mis-aligned magnets or an off-center orbit of the beam. A particle with an orbit offset will then experience the main field of the magnet and effects similar to those of lower order multipoles. The combined contributions of multipoles up to order P on a field of order n is given by the following and greatly detailed in [10]:

$$(K_n + iJ_n)^{w/feed-down} = \sum_{p=0}^P (K_{n+p} + iJ_{n+p}) \frac{(\Delta x + i\Delta y)^p}{p!} \quad (2.78)$$

Opposed to feed-down is feed-up, the higher order effects introduced by combinations of multipoles. This effect is though not a consequence of the beam position in a given field. This effect is explained in great details in Appendix A.

2.7. Resonances

2.7.1. Tune Diagram

The resonances discussed in this thesis are related to the optics of the accelerator. Such resonances create unstable motion and can lead to loosing particles.

Figure 2.16a shows a tune diagram where the fractional part of tunes Q_x and Q_y can be related to resonance lines excited by multipoles up to decapoles ($n = 5$). It becomes apparent that the diagram fills quickly when considering further orders, as shows Fig. 2.16b. Thankfully, the higher the multipole order, the weaker the resonances usually are as their introduced perturbations are usually smaller. This makes choosing a working point possible, even if some particles are hitting resonance lines.

When considering the resonance driving terms f_{jklm} from Eq. (2.44), it can be noted that the term diverges for particular tune values. This leads to a disproportionate increase in particles position in phase-space, eventually leading to loosing them. Resonant conditions due to the tunes can thus be described by the following condition:

$$(j - k)Q_x + (l - m)Q_y = p \quad , \quad j, k, l, m, p \in \mathbb{Z}. \quad (2.79)$$

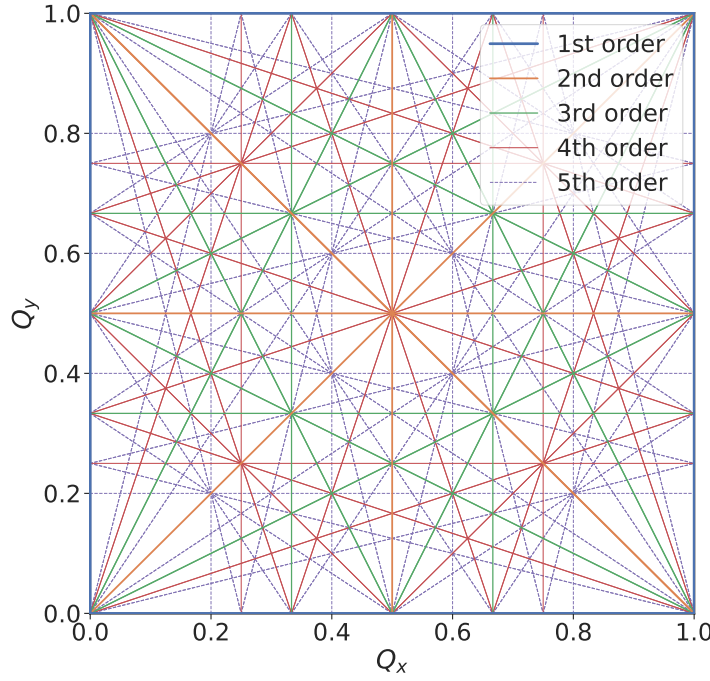
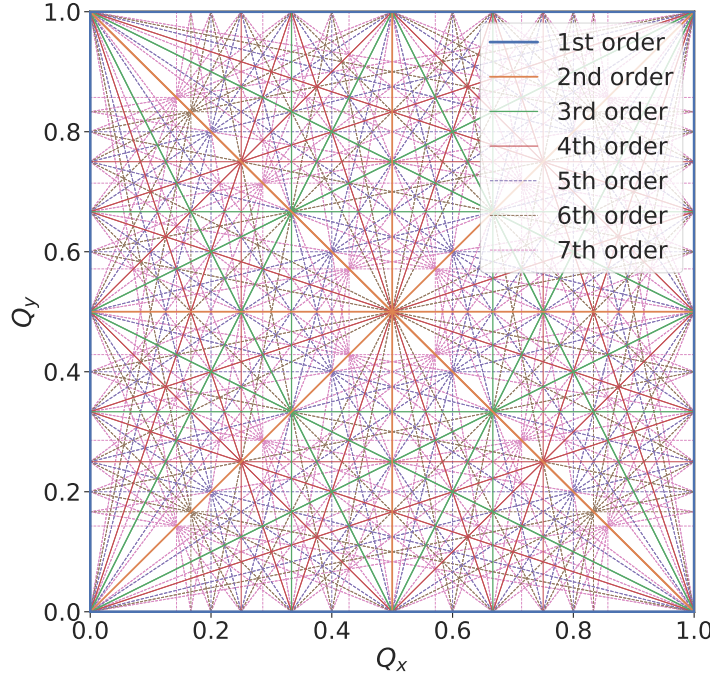
(a) Resonances lines up to decapoles ($n \leq 5$).(b) Resonances lines up to decatetrapole ($n \leq 7$).

Figure 2.16.: Tune diagram with resonance lines excited by different multipole orders. The working point is chosen in an area where few lines are present. When considering higher orders, it becomes apparent that the beam will inevitably hit several resonances.

2.7.2. Frequency Spectrum

As seen in Eq. (2.48), resonance driving terms have an impact on the transverse motion of a particle. This means that performing a FFT on the turn-by-turn signal will reveal spectral lines linked to specific resonance driving terms. Each RDT f_{jklm} can thus be observed in either one or both the frequency spectrums of the horizontal and vertical planes, at multiples of $Q_x \pm Q_y$. Equation (2.80) shows where those lines would appear:

$$\begin{aligned} H_{jklm} &\quad \text{at } (1 - j + k)Q_x + (m - l)Q_y \quad ; \quad j \neq 0 \\ V_{jklm} &\quad \text{at } (k - j)Q_x + (1 - l + m)Q_y \quad ; \quad l \neq 0. \end{aligned} \quad (2.80)$$

The RDT f_{3000} coming from sextupoles can for example be seen in the horizontal spectrum at $(1 - 3 + 0)Q_x + (0 - 0)Q_y = -2Q_x$. For a value $Q_x = 0.27$, the line is seen at 0.46. No line can be seen in the vertical spectrum due to $l = 0$. Detailed tables of such lines for RDTs up to order 6 can be found in Appendix C.

The amplitude of each line will depend on the action I_z and the amplitude of the RDT [30]:

$$\begin{aligned} |H_{f_{jklm}}| &= 2j(2I_x)^{\frac{j+k-1}{2}}(2I_y)^{\frac{l+m}{2}}|f_{jklm}| \\ |V_{f_{jklm}}| &= 2l(2I_x)^{\frac{j+k}{2}}(2I_y)^{\frac{l+m-1}{2}}|f_{jklm}|. \end{aligned} \quad (2.81)$$

By reworking the previous Eq. (2.81), it can be seen that RDTs are factors of the line amplitude and the actions I_x and I_z :

$$\begin{aligned} |f_{jklm}| &= \frac{|H_{f_{jklm}}|}{2j(2I_x)^{\frac{j+k-1}{2}}(2I_y)^{\frac{l+m}{2}}} \\ |f_{jklm}| &= \frac{|V_{f_{jklm}}|}{2l(2I_x)^{\frac{j+k}{2}}(2I_y)^{\frac{l+m-1}{2}}}. \end{aligned} \quad (2.82)$$

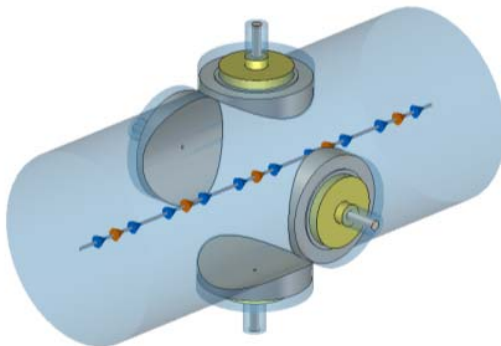
In practice, an approximation of $J = I$ is done. The RDT is then related to the fit of the line amplitude versus the action.

Optics Measurements and Corrections

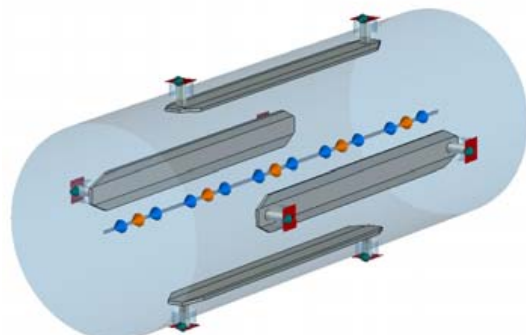
3.1. Beam Instrumentation

3.1.1. Beam Position Monitors

Beam Position Monitors (BPMs) are one of the most utilized and essential elements of beam diagnostics in particle accelerators. In the LHC, most of the BPMs are dual plane, and thus composed of four electrodes, distributed as two per plane. The BPM system consists of over than 550 BPMs per beam, positioned along the ring, in the arcs and the IPs. The most common type, the *curved-button*, shown in Fig. 3.1a, is typically placed near quadrupoles [31].



(a) Button "BPM" type BPM of the LHC [31].



(b) Stripline "BPMSW" type BPM of the LHC [31].

Other pickups such as the *stripline*, shown in Fig. 3.1b, albeit more complex and expensive, offer a better signal to noise ratio and are capable of identifying the direction of the beam [31]. Such features

3. Optics Measurements and Corrections

are essential for the LHC, were both beams travel through the same aperture at the IPs.

3.1.2. Collimators

Collimators are a crucial part of the LHC. Their purpose is to protect the machine against beam losses and clean the outer parts of the beam [32]. The energy of the beams in the LHC is high enough to not only quench the magnets, but to also damage the elements. At injection energy, with a low intensity pilot bunch, the consequences of a loss are less severe.

3

3.1.3. Beam Loss Monitors

Beam Loss Monitors are detectors mounted on various elements of the accelerator, such as magnets or collimators, to detect abnormal losses of particles. They play a crucial role in the protection of the machine, triggering a dump when losses exceed the threshold set for their respective element. BLMs use ionization chambers, working on the same principle as simple Geiger counters: a tube filled with gas, in presence of a high voltage [33]. A picture of BLMs mounted on the LHC is given in Fig. 3.2.

Dashboards in the control room are regularly used to monitor the losses along the ring when performing optics measurements, as those prove to often be destructive. An example of such a dashboard is given in Fig. 3.3.



Figure 3.2.: Beam Loss Monitors (BLM), in yellow, on the LHC [33].

3.1. Beam Instrumentation

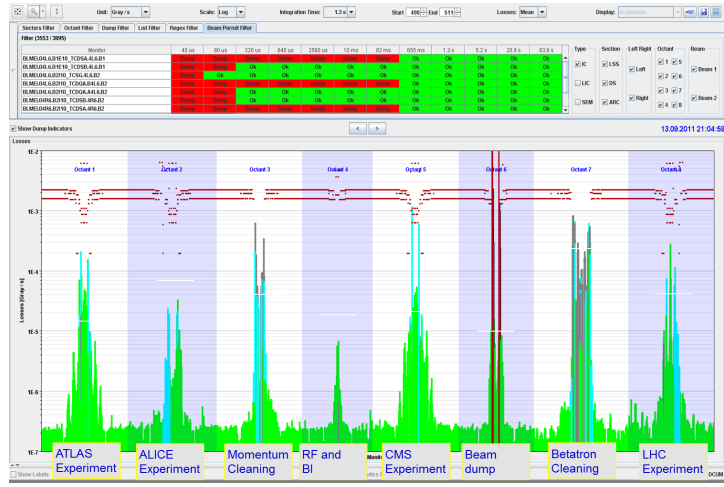


Figure 3.3.: Graphical interface used in the CERN Control Center (CCC) for instantaneous losses in the LHC [33]. Different parts of the accelerator have varying dump thresholds.

3.1.4. Beam Current Transformer

The Beam Current Transformer (BCT) is a device used to measure the intensity of a particle beam by detecting the current induced by the moving charge of the beam as it passes through the coil of the BCT. The beam effectively acts as a primary coil and induces a current in the secondary coil of the transformer. The BCTs are designed to be able to measure intensities from pilot bunches of $8\mu\text{A}$ to total beams of more than 860mA [34]. During optics measurements, beam intensity is often closely monitored to ensure data quality, as certain observables may not be detectable at low intensities.

3.1.5. BBQ System

The Base-Band Tune (BBQ) system in the LHC is designed to measure the beam's tune via its turn-by-turn signal. It operates by detecting and analyzing the signals of diode peak-detectors [35, 36]. The system further implements processing hardware and software, transmitting the acquired data to the control and logging systems. The system can operate with no explicit excitation, relying on the residual beam oscillations, or by using tune kickers or frequency sweeps [35].

3.1.6. AC-Dipole

The AC dipole of the LHC is a crucial component for optics studies. Its primary function is to excite the beam into large coherent oscillation, achieved by applying a sinusoidally oscillating dipole field [37]. By ramping up and down adiabatically the amplitude, large coherent oscillations can be produced

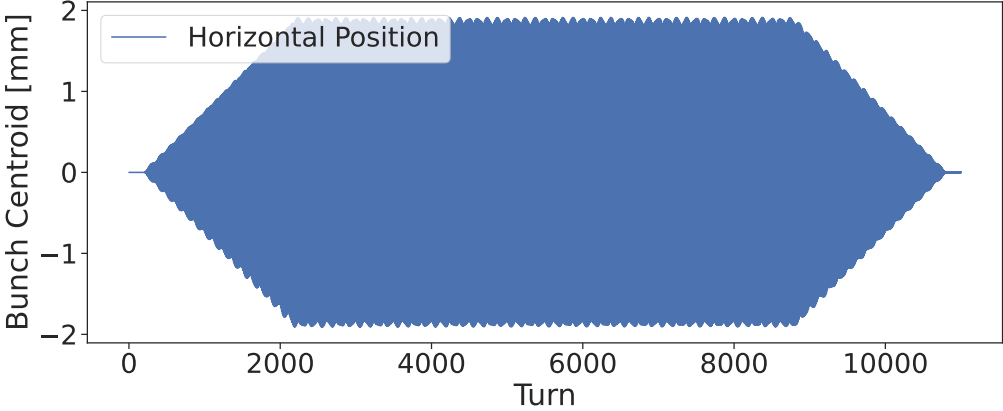


Figure 3.4.: Simulated turn by turn data with an AC-Dipole first ramping up then down.

without any decoherence or emittance growth. Figure 3.4 shows an example of a simulation made with an AC-Dipole. Exciting the beam to large amplitudes make the study of linear optics, such as beta-beating easier, and that of non linear optics such as resonances possible.

The AC-Dipole is set to oscillate at a frequency Q_d , different from the natural tune of the machine Q and thus introduces systematic effects that needs to be compensated during the optics analysis. The transverse position of a particle under the influence of the AC-Dipole, at turn number n and observation point s , is given by [38–40]:

$$z(s, n) = \frac{BL}{4\pi\rho\delta_z} \cdot \sqrt{\beta_z(s)\beta_{z,0}} \cdot \cos(2\pi Q_{d,z}n + \phi_z(s) + \phi_{z,0}), \quad (3.1)$$

where B is the amplitude of the oscillating magnetic field, L the length of the AC-Dipole, $B\rho$ the magnetic rigidity, δ the difference between Q_d and Q , β and β_0 the beta function at the observed point and the AC-Dipole, ϕ and ϕ_0 the phase advance at the observed point and of the AC-Dipole.

3.2. Optics Measurements

To perform optics measurements, several tools and techniques are used. This section details the various implemented methods to measure specific observables.

3.2.1. Tools and Softwares

In order to perform the measurements, analysis and simulations presented in this thesis, various tools and softwares have been developed, used and contributed to.

Optics simulations have been done mainly in MAD-X [41] and PTC. MAD-NG [42] and Xsuite [43] have also been explored for specific tasks such as free RDT simulations and GPU tracking.

Analysis of chromaticity measurements are done via a newly developed graphical interface [44] written in Python. This tool makes cleaning of the raw signal data, its analysis and results export more reliable and easier. Overall, analysis of turn-by-turn measurements is supported by a large panel of libraries written by the Optics Measurements and Corrections (OMC) team, in Python and Java [45].

3.2.2. Turn-by-Turn Signal

One of the key data acquisition methods for optics measurements in the LHC is turn-by-turn acquisition, where beam position is collected on a per-turn basis. This process involves exciting the beam using an AC-Dipole to induce forced oscillations. Typically, a pilot bunch is used for this purpose, containing a reduced intensity of 10^{10} protons, compared to the standard operational bunch intensity of 10^{11} . The lower intensity allows for larger amplitude oscillations, enabling more precise measurements while ensuring the safety of the machine and minimizing the risk of damaging components.

A spectral analysis is then performed via a *FFT* on the signal, making apparent the driven tunes from the AC-Dipole, the transverse tunes and the possible resonance lines, as shown in Fig. 3.5.

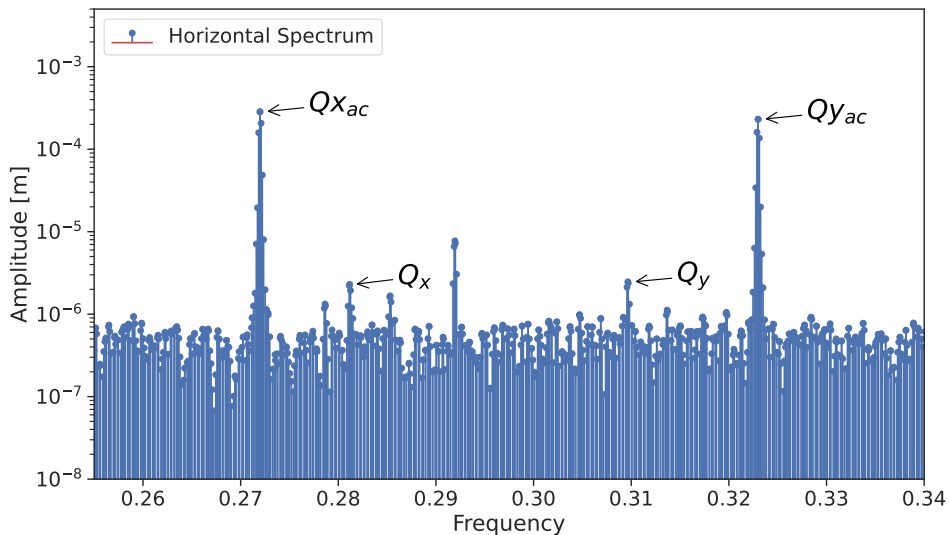


Figure 3.5.: Horizontal frequency spectrum of a turn-by-turn measurement in the LHC. The *driven* tunes of the AC-Dipoles have the highest amplitudes while the natural tune can be seen close to it. Other lines are often created by resonances.

From these oscillations and spectral lines, the optics observables, such as β -beating, dispersion, coupling, and resonance driving terms, can be reconstructed [46]. These key quantities provide valuable

insights into the beam's dynamics and will be detailed further in the following sections.

Betatron Phase The betatron phase can be determined at a given BPM by performing an FFT on the turn-by-turn data. The angle of the main peak, the tune, is then taken to obtain the phase. The phase advance between two BPMs is simply their phase difference.

β -Beating The β -beating can be reconstructed via the phase advance between BPMs. The computation involves using a model created via a simulation software such as MAD-X. The *beta*-function at a given BPM can be calculated from the measured phases of 3 BPMs denoted i, j, k [47],

$$\beta(s_i) = \beta^{model}(s_i) \cdot \frac{\cot(\Delta\phi_{i,j}) + \cot(\Delta\phi_{i,k})}{\cot(\Delta\phi_{i,j}^{model}) + \cot(\Delta\phi_{i,k}^{model})} \quad (3.2)$$

with $\Delta_{i,j}$ being the phase advance between BPMs i and j . Using specific phase advances between BPMs enhances the precision of the β -function measurement. This approach can also be extended to use an arbitrary number N of BPMs [48, 49]. The measurement of the β -function via phase advance is independent from BPM calibration and relies solely on the accuracy of the phase measurement.

Dispersion To retrieve the linear dispersion, turn-by-turn measurements are performed at certain momentum offsets. This allows the computation of the dispersion via the shift in mean orbit Δz and the momentum offset δ ,

$$D_z = \frac{\Delta z}{\delta}. \quad (3.3)$$

In the LHC, measurements are typically taken at ± 100 Hz, corresponding to a momentum offset $\delta \approx \pm 0.7$.

Action The action in a given plane and BPM, located at position s is calculated from the amplitude \mathcal{A} of the main peak in the frequency spectrum, which corresponds to the tune, along with the beta-function at that BPM derived from the model,

$$2J_{BPM} = \frac{\mathcal{A}_{BPM}^2}{\beta_{model,BPM}}. \quad (3.4)$$

This method of action computation is directly influenced by BPM calibration errors [50]. The overall action is then the average over n BPMs:

$$2J = \frac{1}{n} \sum_n \frac{\mathcal{A}_n^2}{\beta_{model,n}}. \quad (3.5)$$

Coupling Coupling can be calculated by comparing the amplitude of the tune in the frequency spectrum of a plane to the same tune in the other plane. The coupling RDTs f_{1001} and f_{1010} can be reconstructed with these amplitudes [51, 52],

$$\begin{aligned} |f_{1001}| &= \frac{1}{2} \sqrt{\frac{H(0,1)V(1,0)}{V(0,1)H(1,0)}}, \\ |f_{1010}| &= \frac{1}{2} \sqrt{\frac{H(0,-1)V(0,-1)}{V(0,1)H(1,0)}}, \end{aligned} \quad (3.6)$$

where $H(1, 0)$ is the amplitude of Q_x in the horizontal spectrum while $H(0, 1)$ corresponds to Q_y in the same spectrum. The phases of these RDTs is given by,

$$\begin{aligned} q_{1001} &= \phi_{V(1,0)} - \phi_{H(1,0)} + \frac{\pi}{2}, \\ q_{1010} &= \phi_{H(0,-1)} - \phi_{V(0,1)} + \frac{\pi}{2}. \end{aligned} \quad (3.7)$$

The final expression of the coupling RDTs is then,

$$\begin{aligned} f_{1001} &= |f_{1001}| e^{i \cdot q_{1001}}, \\ f_{1010} &= |f_{1010}| e^{i \cdot q_{1010}}. \end{aligned} \quad (3.8)$$

Amplitude Detuning Amplitude detuning measurements in the LHC are usually taken with varying AC-Dipole kick amplitudes. A linear function is then fitted on the natural tunes Q_x and Q_y versus the action of either planes $2J_x$ or $2J_y$.

Resonance Driving Terms Resonance Driving Terms are measured in the LHC with varying AC-Dipole kick amplitudes. The amplitude of the resonance line of interest in the frequency spectrum can then be fitted to the corresponding action dependence of the RDT, as detailed in Section 2.7.2 and C. As a reminder, the amplitude of the RDT will be given by,

$$|f_{jklm}| = \frac{|H_{f_{jklm}}|}{2j(2I_x)^{\frac{j+k-1}{2}}(2I_y)^{\frac{l+m}{2}}}$$

$$|f_{jklm}| = \frac{|V_{f_{jklm}}|}{2l(2I_x)^{\frac{j+k}{2}}(2I_y)^{\frac{l+m-1}{2}}}.$$

The phase of the RDT can then be reconstructed via the momentum and phase advances. In practice, *forced resonance driving terms* are actually measured, as the oscillations are driven by the AC-Dipole. Simulations are thus always made via tracking with an AC-Dipole to match. Studies linking *forced* RDTs to *free* RDTs is though ongoing to better understand the machine without excitation [53].

3

Lifetime The beam lifetime is a measure of how long the beam can remain circulating without significant losses of particles. It is typically expressed in hours and is related to the rate at which particles are lost from the beam. The beam intensity is measured via the BCTs. The lifetime τ relates then the number N of particles at a time t to its rate of change,

$$\tau = N(t) \cdot \frac{dN^{-1}}{dt}. \quad (3.9)$$

Additionally, Beam Loss Monitors (BLMs) provide local information about beam quality by detecting and localizing particle losses. These losses can as well be integrated to give a lifetime estimate. At injection energy in the LHC, the beam lifetime with a pilot bunch is typically around 3 hours. Sudden particle losses can significantly reduce the measured lifetime, even if the remaining beam stabilizes and does not lose particles as rapidly. This introduces challenges in accurately measuring the lifetime, as the signal needs to stabilize and saturate after any trim to ensure reliable data.

3.2.3. Chromaticity

Contrary to the previously seen observables, chromaticity measurements are performed by varying the RF frequency to induce a change of momentum offset δ , while measuring the tune. The momentum offset δ being related to the RF frequency, the Lorentz factor γ and the momentum compaction factor α_c [27]:

$$\delta = -\left(\frac{1}{\gamma^{-2} + \alpha_c}\right) \cdot \frac{\Delta f_{\text{RF}}}{f_{\text{RF,nominal}}} \quad (3.10)$$

In the LHC, the Lorentz factor γ^{-2} is here negligible, as the energy is large even at injection. At 450GeV, $\gamma^{-2} \approx 10^{-6}$, which is two orders of magnitude smaller than α_c .

During operation, where the linear chromaticity often needs to be measured, a sinusoid function is applied on the RF frequency. This induces a short range of momentum offset, but enough to measure the first order of the chromaticity function. For non-linear measurements, a larger range is required. In order to do so, a new procedure has been developed. Dense frequency scans with steps of 20Hz every 30 seconds are usually taken to compromise between number of data points, precision of the tune estimate, and duration of the measurement. Once beam losses, registered by the BLMs are deemed too high, the frequency is reverted back to its nominal value in larger steps. Attaining the limits of the BLMs ensures a large momentum-offset range. The same procedure is then re-applied in the negative. Figure 3.6 shows a typical RF scan performed to measure chromaticity in the LHC.

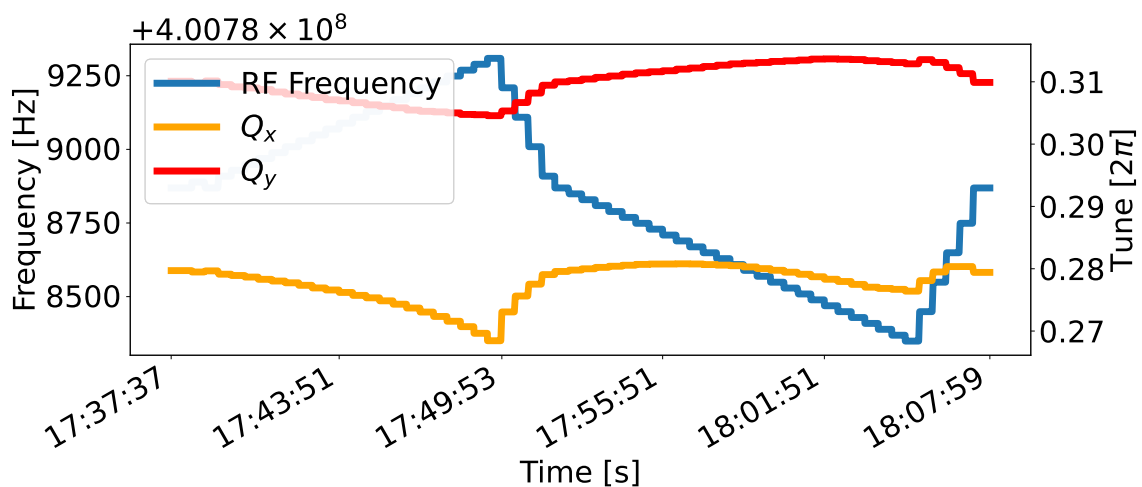


Figure 3.6.: Observation of the tune dependence on momentum offset, created by a shift of RF frequency.

Once the tunes have been acquired and the momentum offset computed via Eq. (3.10), the chromaticity function (see Eq. (2.66)) can be used to fit the measured data and retrieve each order.

As part of the work for this thesis, a new tool, was developed. in order to ease and improve the analysis of chromaticity measurements. The Non-Linear Chromaticity GUI [44] showcases new analysis techniques using the raw signal from the BBQ system along with custom signal cleaning that are detailed later on in Chapter 6. Fits to very high chromaticity orders are also now possible along with their computed corrections and that of resonance driving terms via a combined response matrix approach. Automatic data extraction from the CERN data servers (Timber, NXCAL) is also included.

3.3. Correction Principles

Several ways exist to correct the previous observables. Two common ways to do so are here detailed.

3.3.1. Response Matrix

A response matrix is a linear equation system that describes the change of an observable for a set of individual multipole strengths. By taking the pseudo-inverse of this matrix and multiplying it to the measured observables, a set of corrector strengths if obtained that can replicate the measured value. Taking the opposite sign then gives a correction. This technique is used to correct, amongst others, β -beating, chromaticity as well as Resonance Driving Terms for the first time in the LHC with this thesis. In situations where measurements are taken at each BPM for a particular observable, the corresponding response matrix ends up containing over 500 values per corrector, for a single beam.

Individual MAD-X simulations are run with a single specific circuit powered at a time. The resulting parameter values (e.g. β -beating) are then compared to those obtained from a simulation without any powering, allowing to determine the impact of each circuit on that observable.

A response matrix is thus created following Eq. (3.11), for a matrix of observables O , a reference matrix of observables without any corrector O_R and a fixed multipole strength k . Given measured data M , the set of correctors needed to compensate the values can be obtained by taking the pseudo-inverse of the matrix in Eq. (3.12).

$$R = (O - O_R) \cdot \frac{1}{k} \quad (3.11)$$

$$\begin{bmatrix} k_1 \\ \vdots \\ k_n \end{bmatrix} = -(R^+ \cdot M) \quad (3.12)$$

Response matrices are very versatile and can combine several observables to be corrected by the same multipoles. One example, detailed later in this thesis, is the third order chromaticity and the resonance driving term f_{1004} , both contributed to by decapoles.

Example

In this example, developed for the decapolar corrections presented in Chapter 5, simulations are run with MAD-X PTC to correct the third chromaticity in the LHC. Q'' is taken from `ptc_normal` for each beam and axis, with MCDs, decapole correctors, powered with a fixed strength one at a time. A scaling factor is applied to get the change of chromaticity for one unit of K_5 . 8 correctors are used, which strengths are denoted k_1 through k_8 . Transposes are only used to make the equations easier to display.

The values in Table 3.1 are corrected via Eq. (3.14) after having built the response matrix in Eq. (3.13).

Observable	Value
Q_x'''	-666111
Q_y'''	121557

Table 3.1.: Example chromaticity values to correct via a response matrix

$$R = \left(\text{Individual simulations} \begin{pmatrix} Q_x''' & Q_y''' \\ \underbrace{\begin{bmatrix} -155899 & 122004 \\ -254584 & 138368 \\ -122715 & 106709 \\ -218597 & 110686 \\ -134140 & 106463 \\ -245791 & 118951 \\ -147035 & 116544 \\ -219537 & 112317 \end{bmatrix}}^T & - \underbrace{\begin{bmatrix} 5135 \\ 8470 \end{bmatrix}}_{\text{Reference}} \end{pmatrix} \cdot \underbrace{\frac{1}{-1000}}_{\text{Corrector strength}} \right) \quad (3.13)$$

$$\begin{aligned} k_1 & \begin{pmatrix} -1235 \\ 1032 \end{pmatrix} \\ k_2 & -1394 \\ k_3 & 1449 \\ k_4 & -1043 \\ k_5 & 1864 \\ k_6 & -1187 \\ k_7 & 1369 \end{aligned} = -R^+ \cdot \begin{pmatrix} -666111 \\ 121557 \end{pmatrix} \quad \begin{array}{l} \text{Measured} \\ \text{values} \end{array} \quad (3.14)$$

3.3.2. Global Trims for Chromaticity

As per the placement of the octupolar and decapolar correctors in the LHC layout [54], β -functions at their location are slightly different from arc to arc. This slight imbalance leads theoretically to the possibility of correcting the horizontal and vertical axes of the second and third order chromaticity independently, via a response matrix approach. In practice, the required strength to do so would exceed those of the design of the correctors.

Another way to correct the chromaticity is via a global uniform trim, where every available corrector is powered to the same strength. Simulations are run with MADX-PTC to obtain the response in chromaticity for a given strength. Chromaticity being linear with multipole strength, an affine

3. Optics Measurements and Corrections

function can be determined for each axis. Figure 3.7 shows a simulation with several MCD strengths, highlighting this linear relation between Q''' and K_5 , while Equation (3.15) shows an example of such functions computed at injection energy for the 2022 optics.

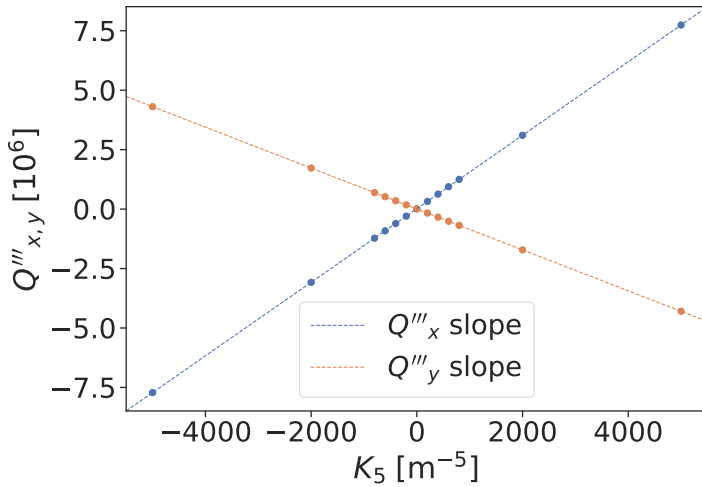


Figure 3.7.: Linear relation between the third order chromaticity and decapole corrector strengths, simulated with MADX-PTC.

$$\begin{aligned} Q'''_x &= 1533 \cdot \Delta K_5 + 6680 \\ Q'''_y &= -860 \cdot \Delta K_5 + 5647 \end{aligned} \quad (3.15)$$

Only the linear part is relevant, as the offset is generated by other multipoles and field errors. It is thus constant for a configuration where only the relevant spool pieces are used.

Corrections involve minimizing both axes, typically where Q'''_x meets Q'''_y :

$$\Delta K_5 = -\frac{(Q'''_x - Q'''_y)}{\text{slope}_{Q'''_x} - \text{slope}_{Q'''_y}} \quad (3.16)$$

Skew Octupolar Fields

4.1. Introduction

Skew-octupolar fields represent an important yet comparatively less-studied aspect of the LHC's non-linear optics. Their impact, although well-understood in simulations, presents unique challenges in real-world operation, especially as we approach closer to the High-Luminosity Large Hadron Collider (HL-LHC), where dynamic aperture is expected to be significantly affected. Unlike quadrupole and sextupole components, which have well-established methods for measurement and correction, skew-octupolar fields pose a significant challenge to measure and quantify.

In contrast to normal octupoles, which have straightforward observables such as amplitude detuning, skew octupolar fields are significantly harder to measure. Historically, these fields have been measured indirectly through feed-down effects on coupling and tune, but this approach has proven unreliable in the presence of other errors [55, 56]. Resonance Driving Terms (RDTs) have shown to be an effective method for measuring skew octupolar fields [53], although obtaining accurate measurements remains challenging due to the high kick amplitudes required.

Previous efforts to correct these resonances using RDT measurements have largely relied on empirical methods, involving extensive numerical simulations and manual adjustments of correctors to identify a combination that reduces the RDTs. While this approach has been functional, it has proven to be time-consuming, labor-intensive, and inadequate for the fast-paced demands of LHC operations. As the machine's performance continues to reach new limits, more efficient and real-time correction techniques are becoming increasingly essential. This need has driven the development of a response matrix based approach to skew-octupolar RDT corrections, offering a quicker and more reliable method for diagnosing and addressing these field errors. These advancements will be needed to facilitate shorter commissioning times and optimize performance in future HL-LHC runs. The RDTs of interest in this chapter are $f_{1012,y}$ and $f_{1210,x}$, with their associated resonances and frequency lines presented in Table 4.1. Given that the working point of the LHC is set near the resonance $Q_x - Q_y$, which is excited by f_{1012} , more detailed studies and corrections of these fields would be beneficial.

RDT	Resonance	H-line	V-line
f_{1012}	$1Q_x - 1Q_y$	$1Q_y$	$-1Q_x + 2Q_y$
f_{1210}	$-1Q_x + 1Q_y$	$2Q_x - 1Q_y$	$1Q_x$

Table 4.1.: Skew octupolar RDTs of interest, their associated resonances and the frequency spectrum lines they contribute to.

Skew octupolar RDTs are primarily expected to arise from skew octupolar errors and their corresponding correctors. However, significant discrepancies have been observed between the LHC’s magnetic and alignment models and the measured RDTs. Normal octupoles, in the presence of coupling, have been identified as contributors to the skew octupolar RDTs. This unexpected contribution amplifies the impact of skew octupolar fields, particularly on beam lifetime and dynamic aperture.

The following sections present the measurements and corresponding corrections performed at top energy, establishing the methods for reliable measurements and corrections of skew-octupolar RDTs. Subsequently, measurements at injection energy, focusing on the unaccounted for contributions of normal octupoles to skew-octupolar RDTs are examined.

4.2. Response Matrix Based RDT Corrections at Top Energy

The first skew octupolar RDT corrections in the LHC were implemented in 2018 during Run 2 [53]. These corrections were calculated by simulating all possible combinations of correctors and selecting the one that best matched the measurements. In practice, this approach proved to be less effective, requiring extensive manual adjustments. Such a method is highly time-consuming and cannot be easily replicated for different optics configurations.

In this section, a different approach is taken, based on response matrices. This type of correction is explained in details in Section 3.3.1. The real and imaginary responses of the RDTs for each corrector at an arbitrary strength are simulated through tracking. These responses are collected into a matrix, allowing the determination of the required strengths to match the RDT level observed in the measurements. Inverting these values result in a correction. This approach has the benefit of being remarkably faster, as only a few simulations are needed. Online corrections in the control room are thus possible in the span of a few hours instead of a whole shift, as no manual adjustments are needed.

4.2.1. Measurement

Initial measurements of the machine at top energy ($\beta^* = 30$ cm) were conducted without any skew octupolar correctors to establish a baseline for the RDTs. Measuring skew octupolar RDTs poses

challenges due to the high amplitude kicks required to distinguish the RDT lines in the frequency spectrum. Consequently, the LHC's working point had to be optimized specifically for these measurements to enhance the forced dynamic aperture, as the lines of interest are not observable at the nominal working point.

Several measurements were conducted at different working points to identify a configuration that enabled high amplitude kicks while maintaining beam losses below the dump threshold. The selection of such a tune combination facilitates repeated kicks and enhances the accuracy of RDT measurements. A summary of the tested working points and the resulting AC-Dipole kick percentages is presented in Table 4.2.

Q_x	Q_y	$\Delta Q_{x,ac}$	$\Delta Q_{y,ac}$	Maximum Kick [%]	
				Beam1	Beam 2
0.310	0.320	-0.008	+0.010	13	16
0.295	0.305	-0.008	+0.010	30	45
0.285	0.292	-0.008	+0.010	55	50

Table 4.2.: Working points tested for skew-octupolar RDT measurements, together with the maximum diagonal kick percentages achieved without reaching the dump threshold.

A suitable configuration was identified that enables high amplitude kicks. Consequently, the measurements were conducted at natural tunes of $Q_x = 0.285$ and $Q_y = 0.292$. The driven tunes were adjusted to $\Delta Q_x = -0.008$ and $\Delta Q_y = 0.01$. This selection of tunes has proven to be the most effective for measuring skew octupolar RDTs while keeping losses under control and is now established as the standard for commissioning activities. Figure 4.1 shows the horizontal frequency spectrum taken with the skew octupolar correctors turned off. In this plane, the line of the RDT f_{1210} is visible at $2Q_x - 1Q_y$, while that of f_{1012} is visible in the vertical one at $-1Q_x + 2Q_y$. The measured RDTs are shown later on, in blue, in Fig. 4.4.

4.2.2. Response Matrix and Corrections

To create a response matrix, simulations were conducted with the tunes and AC-Dipole deltas set to those used for measurements. The natural tunes are $Q_x = 0.285$ and $Q_y = 0.292$ while the driven tunes are $\Delta Q_x = -0.008$ and $\Delta Q_y = 0.01$. Each corrector is then powered individually for each tracking simulation. As measurements near the IP can be quite noisy, those are not utilized in the calculation of the correction. The polar plot of Figure 4.2 illustrates the response of each corrector at a given BPM and can be used to get an intuition of the effect of the correctors.

L5 and R5 having the same angle indicates that either can be used for corrections. Effectively having only two correctors with different angles, it makes computing corrections for four RDTs (two per beam) very challenging. In this context, a response matrix based approach is most effective in determining

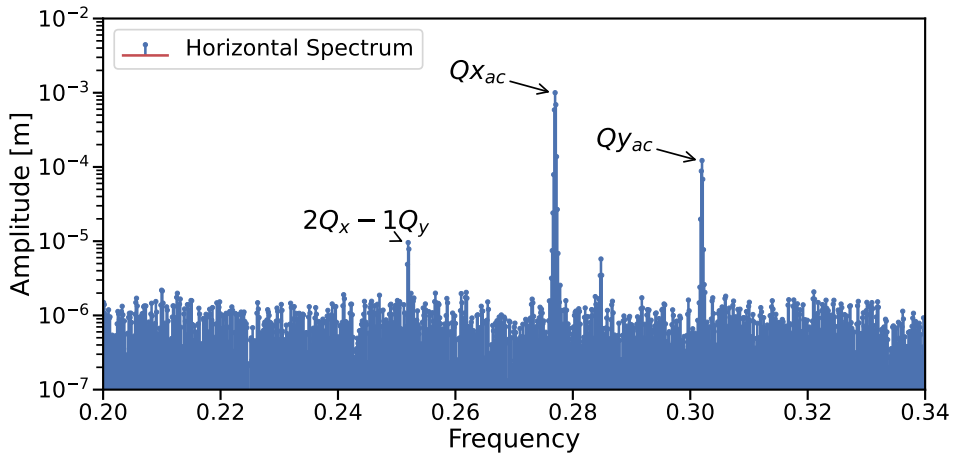


Figure 4.1.: Horizontal spectrum of Beam 1 at top energy before and after application of skew-octupolar RDT corrections. The RDT f_{1210} is seen at $2Q_x - 1Q_y$.

the optimal combination of corrector strengths. Figure 4.3 shows the real part of the RDTs from these simulations for Beam 1. Beam 2 shows a similar level of response for these correctors.

4

Previous simulations with each corrector powered on are compiled into a matrix, as detailed in Section 3.3.1, to capture the RDT response. By inverting this matrix, the appropriate set of correctors needed to replicate the measurement is determined. Finally, multiplying by -1 allows for the computation of the required strengths for the set of correctors. These corrector strengths, for the measured RDTs, are presented in Table 4.3.

These corrections have proven to be effective in reducing the RDT amplitudes and have been applied during 2023's commissioning and later on kept for regular operation. The RDT levels of the bare machine measured previously and with these corrections are shown in Fig. 4.4. It can be observed that both RDT amplitudes are reduced, with the exception of $f_{1210,x}$ for Beam 2, which stays constant, while being at an already low level. The reduction of RDT amplitude is comparable to those obtained in 2018, where the same RDT for Beam 2 did neither improve or worsen.

Corrector	Strength [m^{-4}]
MCOSX3.L1	broken
MCOSX3.R1	-0.50
MCOSX3.L5	0.42
MCOSX3.R5	-0.01

Table 4.3.: Computed corrections for skew octupolar RDTs at top energy. The corrector L1 has been broken for several years and can not be used.

4.2. Response Matrix Based RDT Corrections at Top Energy

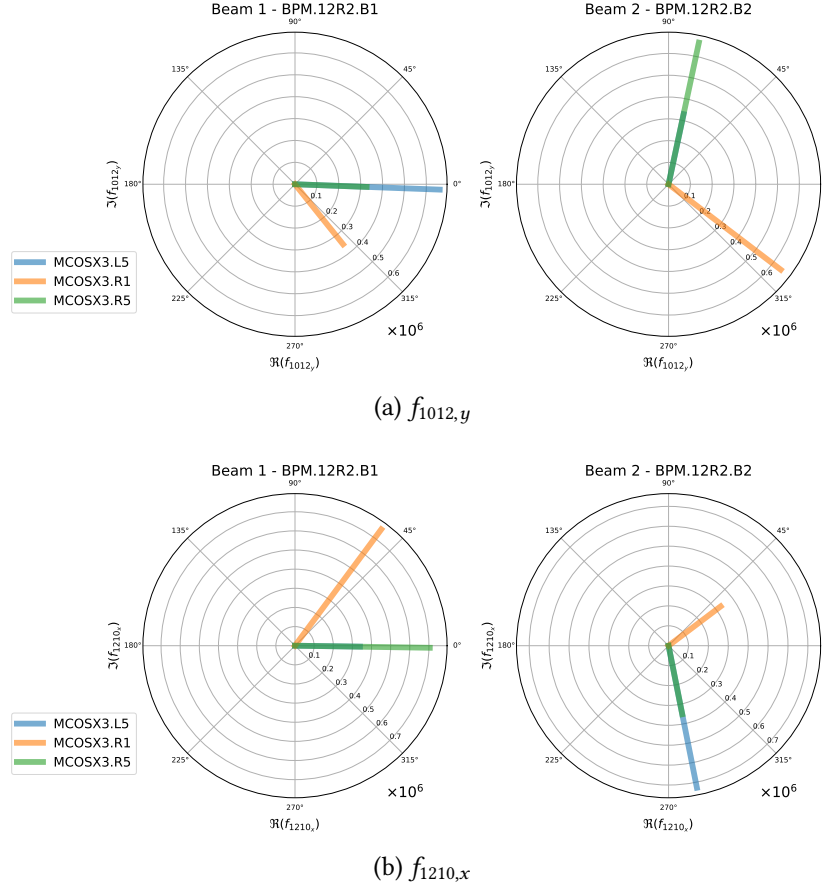


Figure 4.2.: Simulated RDTs response of the available skew octupolar correctors at top energy. Each corrector is powered at $J_4 = 1[\text{m}^{-4}]$. The orthogonality of R1 and L5/R5 allows to independently control the real and imaginary parts.

A improvement in the forced dynamic aperture during AC-Dipole excitation was observed with the earlier skew-octupolar RDTs corrections implemented. Figure 4.5 shows the timeline of the various kicks amplitudes before and after corections. It can clearly seen that skew-octupolar corrections enhance the forced dynamic aperture and allow for higher-amplitude kicks with the same amount of losses.

Skew-octupolar Resonance Driving Terms have, for the first time, been directly corrected using a response matrix-based approach at top energy. This new approach allows for a more efficient use of dedicated machine time compared to the previous empirical approach. Corrections have significantly improved the forced dynamic aperture, enabling the high amplitude kicks necessary for non-linear optics measurements. Furthermore, these corrections can be computed online in the control room, reducing commissioning time and thereby increasing the integrated luminosity of the LHC.

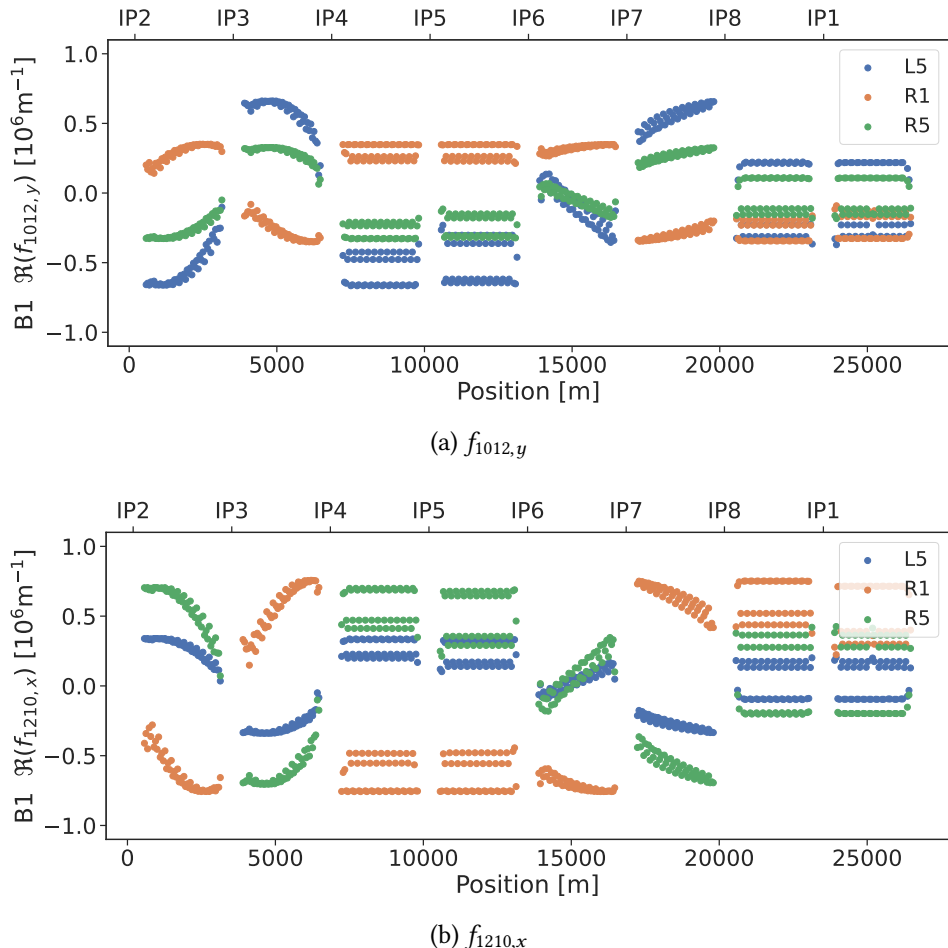


Figure 4.3.: Simulation of the RDT response of the skew octupolar correctors at top energy for Beam 1. Each corrector is powered at $J_4 = 1 \text{ m}^{-4}$.

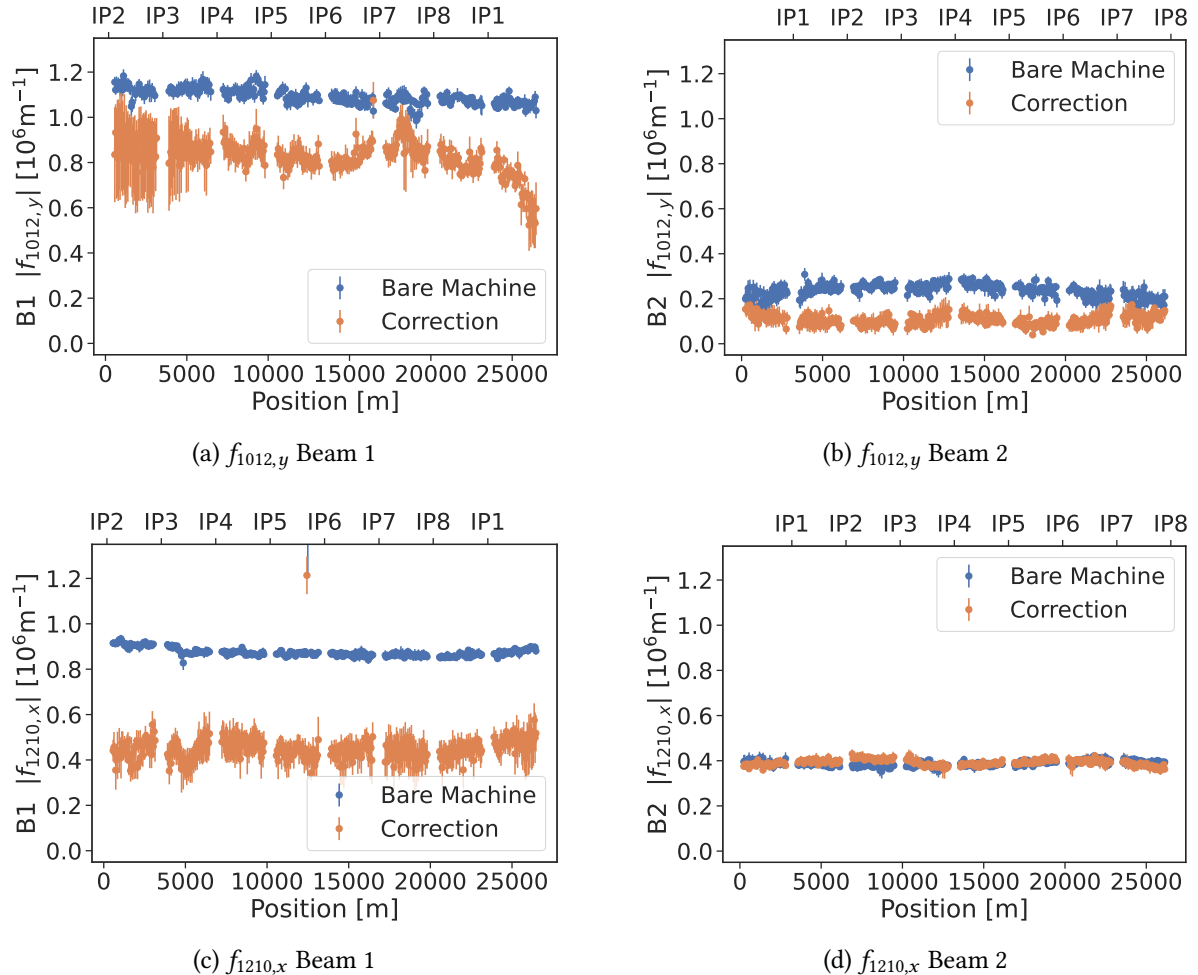


Figure 4.4.: Measured skew octupolar RDTs at top energy and $\beta^* = 30\text{cm}$ before and after correction.
A reduction is observed for all but one RDT in Beam 2.

4. Skew Octupolar Fields

4

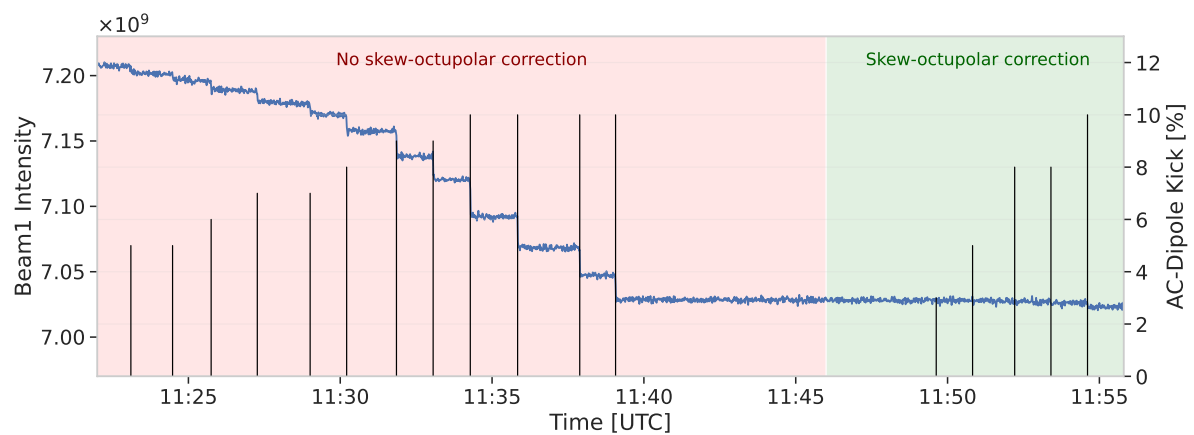


Figure 4.5.: Intensity of Beam 1 related to the kick percentage of the AC-Dipole over time, before and after having applied skew-octupolar RDT corrections.

4.3. Skew-Octupolar RDT driven by Landau Octupoles

The significant progress achieved in understanding skew octupolar RDTs at top energy and their improvement of forced dynamic aperture prompted their study at injection energy, where they had never been studied before. During these studies, large skew octupolar resonances lines were observed when Landau octupoles were powered. These magnets, being normal octupoles, are not expected to contribute to skew octupolar fields. To further understand and characterize the contribution of Landau octupoles to skew octupolar fields, subsequent measurements were conducted. Measurements of the RDTs introduced in Table 4.1, were performed with several strengths of Landau octupoles, ranging from $-2K_4$ to $5K_4$.

The following Fig. 4.6 illustrates the measured amplitude for Beam 1 of the RDT f_{1012} with these varying strengths of Landau octupoles. It can be observed that normal octupoles have a large impact on this RDT at only $K_4 = 5$. This amplitude is expected to increase by an order of magnitude with the nominal powering of Landau octupoles at $K_4 = 18$ and significantly supports the need for their study.

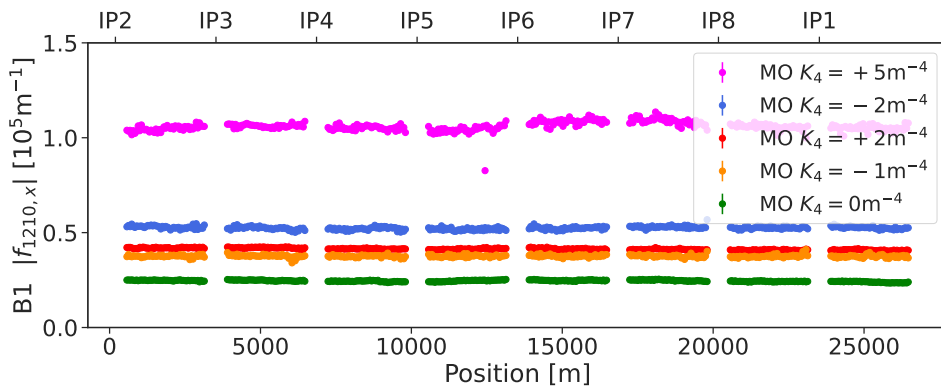


Figure 4.6.: Unexpected amplitude shift of skew-octupolar RDT f_{1210} with varying Landau octupoles strengths.

Simulations conducted with Landau powering of $K_4 = 0$ and $K_4 = 2$, incorporating additional normal and skew field errors, do not replicate the measured shift. The comparison between measurements and simulations is presented in Fig. 4.7, where it is evident that some component is absent from the magnetic model. For conciseness, all figures are shown with respect to Beam 1, although similar results are observed for Beam 2.

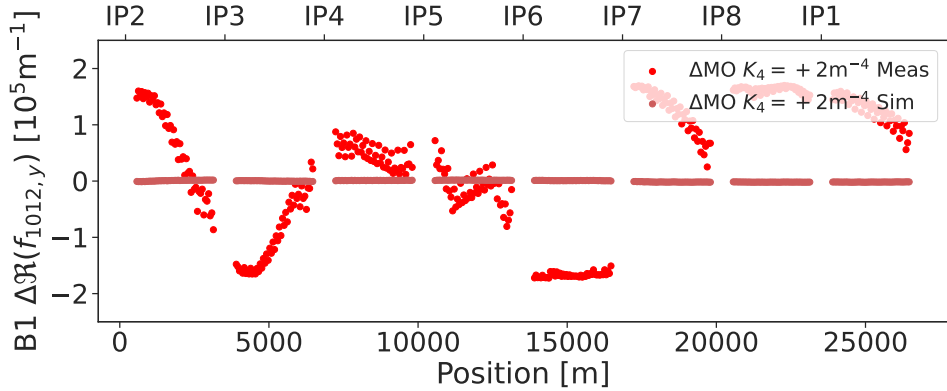


Figure 4.7.: Measured and simulated shift of skew-octupolar RDT after increase of Landau octupoles strength from zero. It is apparent that the shift in measurement is not replicated by the simulation.

4.3.1. Misalignments

Magnet misalignments in the LHC have been previously measured and corrected in several phases [57]. Nevertheless, residual misalignments persist and have been incorporated into the tables used for simulations. These misalignments include horizontal and vertical errors, as well as roll errors. While translation errors may induce feed-down effects, roll errors introduce the skew counterpart of normal magnetic fields, and vice versa.

To assess whether roll errors could explain the behavior observed in measurements, a tracking simulation was conducted with and without roll errors applied to the Landau octupoles, powered at $K_4 = 2$. The amplitude of the RDT f_{1012} is presented in Fig. 4.8, with similar results observed for f_{1210} . These results reveal an imperceptible difference between the two simulations. Roll errors are unable to account for the previously observed shifts. The average roll error of the Landau octupoles is indeed small, approximately 0.08 mrad.

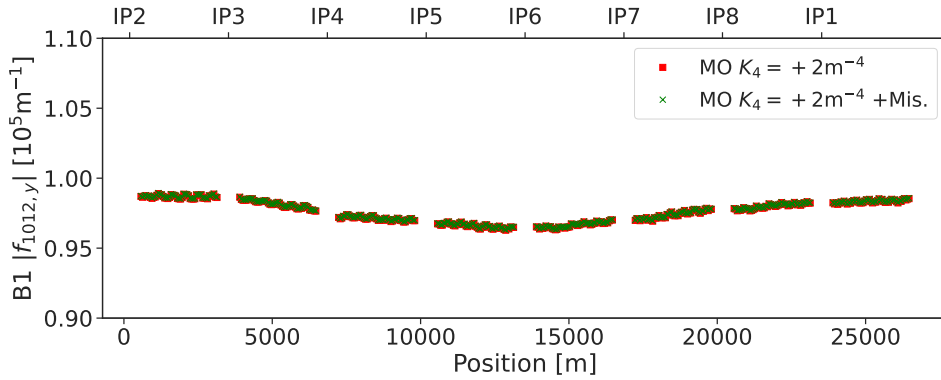


Figure 4.8.: Simulated skew octupolar RDT with normal and skew octupolar errors, and Landau octupoles powered. One simulation includes further roll errors on the Landau octupoles. No significant difference is observed between the two.

4.3.2. Linear Coupling

As misalignments could not explain the discrepancy, it is necessary to consider another source of errors. According to [58], the combination of a normal octupole and a skew quadrupole can yield skew-octupolar-like fields. Linear coupling can effectively be modeled as a skew quadrupole and may be a source of the observed discrepancy. The transfer map for an octupole and a skew quadrupole is detailed in Appendix A.2.4.

To test this hypothesis, simulations were initially conducted with varying values of coupling while maintaining a fixed octupolar strength, allowing for an assessment of the impact of coupling alone. The resulting RDT f_{1012} is shown in Fig. 4.9, with a similar trend observed for f_{1210} . The presented C^- values are commonly encountered in operation and are well within the tolerances established in the LHC design [6]. These results indicate that the skew octupolar RDTs are expected to be significantly altered as coupling increases.

Having established that coupling can significantly contribute to the generation of skew octupolar fields from normal octupoles, further simulations were conducted to match the measured coupling for each set of observations. Initially, local coupling is assessed using coupling RDTs, followed by the definition of a set of correctors linked to a common control knob to globally correct the coupling across the machine. This global knob setting is then applied in simulations to replicate the measured coupling. The measured and simulated shifts in the real part of the RDTs f_{1012} and f_{1210} , resulting from the application of various octupole powerings in the presence of coupling, are shown in Fig. 4.10. A similar trend is observed for the imaginary part.

It can be observed that simulations and measurements for positive strengths ($K_4 = 2$ and $K_4 = 5$) are now in good agreement. This suggests that the primary contribution to the skew octupolar RDTs can

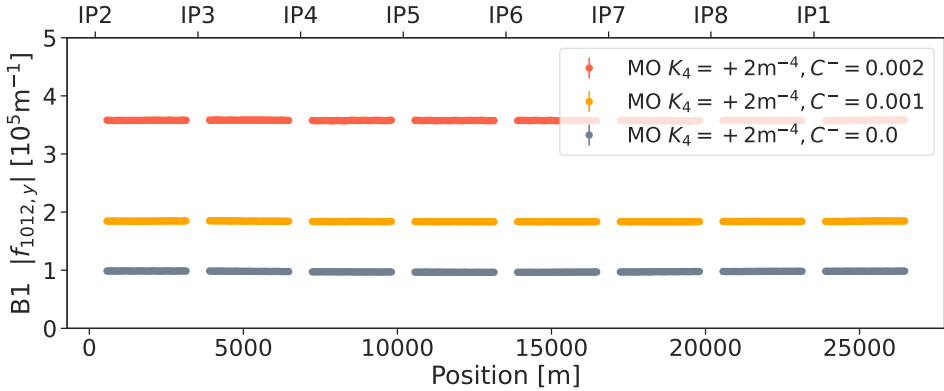


Figure 4.9.: Simulated skew octupolar RDT with fixed Landau octupole strength but varying coupling. Selected coupling values are often seen in operation.

be attributed to the Landau octupoles and coupling. The relative deviation between measurement and simulation can be explained by the sensitivity to the coupling. A difference of 10^{-4} units is enough to be noticeable, making accurate reproduction of skew octupolar RDTs not trivial. It is to be noted that measurements of f_{1012} with *negative* strength exhibit a response that is opposite to the predictions made by simulations, whereas f_{1210} agrees well with the expected results. This behavior may be attributed to magnetic hysteresis. Specifically, the measurements at positive K_4 were taken after a degaussing cycle of the Landau octupoles, while the negative measurements were conducted immediately afterwards the positive ones. Additional measurements, with proper degaussing performed before each test, could help clarify this difference.

As demonstrated in Fig. 4.9, Landau octupoles, along with minor variations in coupling, even at low K_4 strengths, can significantly influence the RDTs f_{1012} and f_{1210} , along with their associated resonances. Furthermore, at their operational powering of $K_4 = 18$, Landau octupoles are anticipated to generate very large skew octupolar RDTs, as simulated in Fig. 4.11, where a realistic operational coupling value is utilized. A difference of two orders of magnitude is observed when powering the octupoles and considering coupling. Such a drastic worsening of the RDTs could prompt for further studies and corrections.

4.3. Skew-Octupolar RDT driven by Landau Octupoles

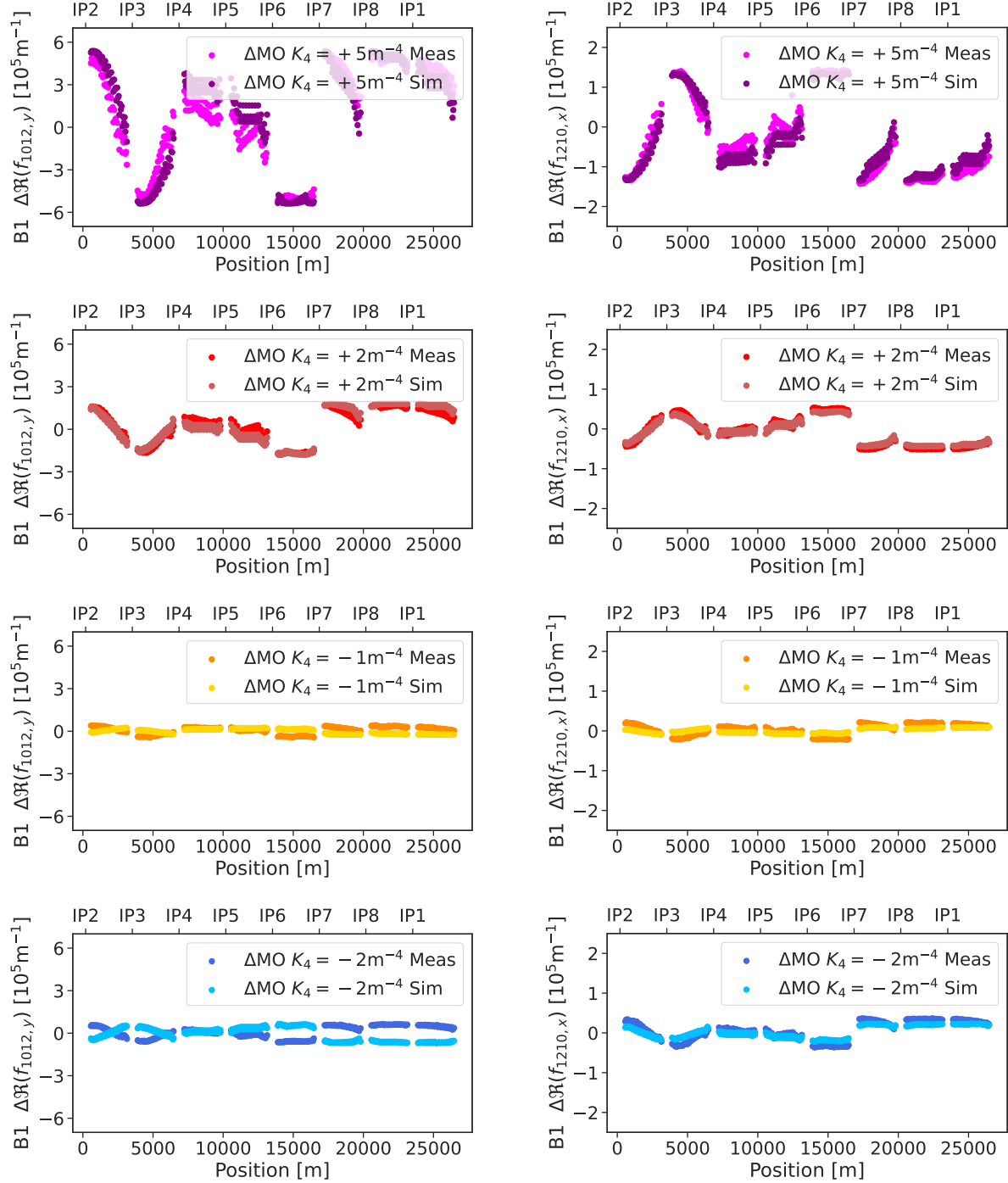


Figure 4.10.: Measured and simulated real part shift of skew octupolar RDTs induced by Landau octupoles in presence of coupling at injection energy. Left column shows f_{1012} while right shows f_{1210} .

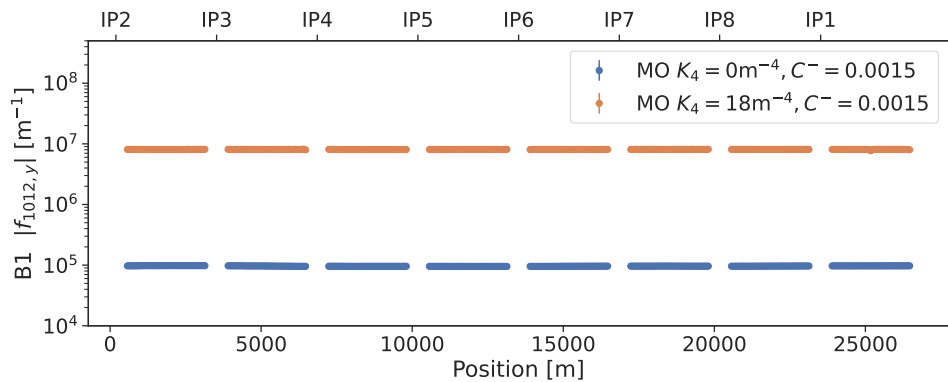


Figure 4.11.: Simulated skew octupolar RDT f_{1012} with Landau octupoles turned off and at their operational powering. Coupling is set to a value commonly seen in operation for both.

4.4. Summary

This chapter investigates the origins of skew-octupolar fields in the LHC and explores methods for measuring and mitigating their effects. The studies demonstrate that these fields significantly contribute to limitations in dynamic aperture, particularly when the beam is kicked with the AC-Dipole.

For the first time, skew-octupolar Resonance Driving Terms have been directly corrected using a response matrix-based approach at top energy. This new method facilitates a more efficient use of dedicated machine time compared to previous empirical approaches. The corrections successfully correct the RDTs f_{1012} and f_{1210} .

Furthermore, the chapter addresses the unexpected influence of Landau octupoles on skew-octupolar RDTs at injection energy. Simulations reveal that misalignments of the Landau octupoles, particularly roll errors, do not have a significant impact. Instead, coupling emerges as a crucial factor. Initial findings indeed suggest that coupling is essential for predicting the behavior of skew-octupolar RDTs in the presence of Landau octupoles. During regular operation, where the Landau octupoles are powered at $K_4 = 18$, significant skew-octupolar RDTs are expected to be generated and degrade the dynamic aperture.

The results presented provide valuable insights into the complex interplay of magnetic fields in the LHC and underscore the importance of accurate modeling for effective corrections. Moreover, the implemented corrections have substantially improved the forced dynamic aperture, enabling the high-amplitude kicks necessary for non-linear optics measurements. These corrections can also be computed online in the control room, thereby reducing commissioning time and increasing the integrated luminosity of the LHC.

Decapolar Fields

5.1. Introduction

Beam-based measurements have been carried in the LHC since Run 1 to better understand the decapolar fields. Those have been carried out via chromaticity measurements [59–61]. The third order of the non-linear chromaticity, Q''' , which is expected to be generated for the most part by decapolar errors in the main dipoles, has shown a consistent discrepancy at injection energy between its expected value from simulations and that observed. Figure 5.1 illustrates this discrepancy, highlighting a factor -2 between the supposedly corrected machine and the corrected model.

The FiDeL model, based on magnetic measurements, is used during operation to correct various multipole errors in the LHC, including octupolar and decapolar. The operational corrections being based on this magnetic model and simulations, the residual Q''' value is expected to be small, which is however not the case. Chromaticity measurements have thus been repeated during LHC's Run 3 and corrections made routine, aimed at correcting the observed discrepancy.

While the study of non-linear chromaticity has proven valuable in identifying the existence of this discrepancy, it does not yet permit alone to understand its exact origins. In an effort to gain deeper insights, additional measurements were performed focusing on novel observables that had not been previously explored. *Bare chromaticity* involves measuring chromaticity with the octupolar and decapolar correctors deactivated ; this approach aims to isolate the machine effects from those of the correctors. *Chromatic amplitude detuning*, evaluates how the tune varies with both the beam's action and the momentum offset ; this method has the benefit of having a different expression from that of the chromaticity, to rule out exclusively momentum dependent effects, such a higher-order dispersion.

In addition to previous measurements, direct measurements of decapolar Resonance Driving Terms (RDTs) were conducted for the first time in the LHC, at injection energy. These high-order RDTs, which influence resonances near the working point, have also benefited from corrections, marking the first instance of directly correcting such high-order terms, using a response matrix-based approach. During the study of these resonances, lower-order multipoles, such as sextupoles and octupoles, were

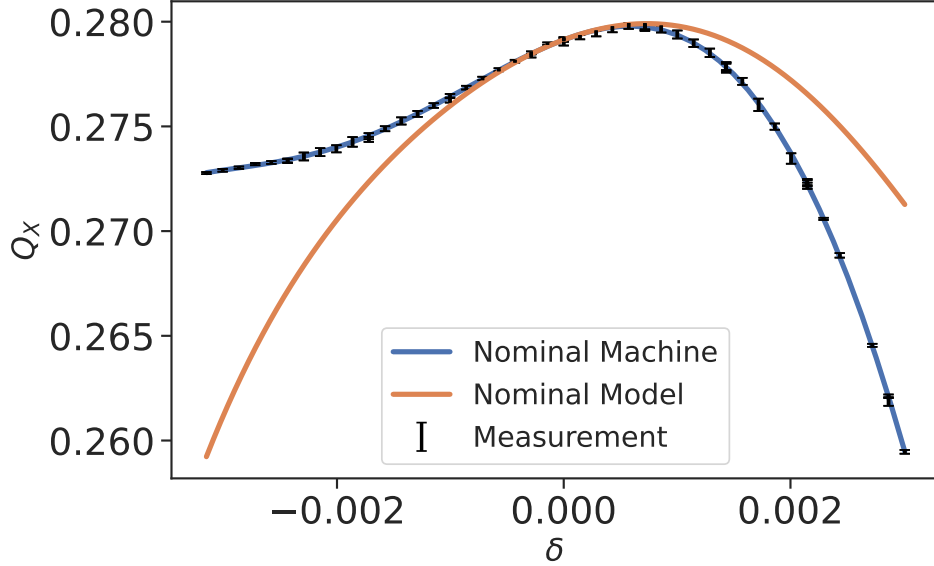


Figure 5.1.: Measured and simulated chromaticity with application of the nominal decapolar corrections from FiDeL. It can be seen that although the corrections should diminish Q''' , it is not well corrected in practice.

found to be significant contributors. Their effects are thoroughly derived and examined, as they are expected to strongly impact the dynamic aperture at injection energy.

While lower-order field errors in the LHC are generally well understood and controlled, this is not the case for higher-order errors such as decapoles and beyond. Precise control of these higher-order non-linearities is expected to be crucial for future colliders like the FCC, where decapolar field corrections will play a large role in maintaining an optimal dynamic aperture. Extending advanced beam-based measurement and correction techniques to higher-order errors is therefore of significant interest. The observed discrepancy in the correction of third-order chromaticity (Q''') points to an incomplete understanding of both the error sources and the magnetic model. Addressing this gap is essential for improving higher-order corrections in the LHC and preparing for the challenges of the next generation of accelerators.

5.2. Response of correctors

As seen in Fig. 2.4, the LHC is equipped with decapole correctors. Those magnets are part of the LHC's design report, aiming at correcting the field errors of the main dipoles. Those correctors, denominated *MCD*, are specific to each beam and are placed after every second dipole, totaling 1232 in number [62]. MCDs are nested with octupolar correctors, *MCO*. The pair of those correctors of often referred to as

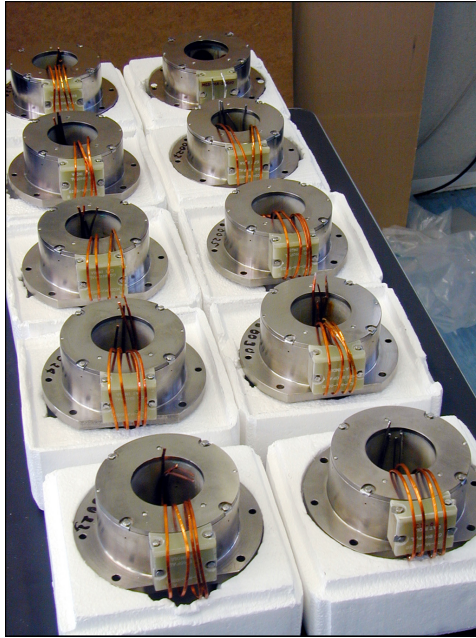


Figure 5.2.: Decapoles on a test bench, being inspected after manufacturing [63].

MCDO. It is not possible to individually power each corrector. Rather, a circuit consists of a whole arc. There are in total 16 circuits to control the correctors of both beams and 8 arcs. Figure 5.2 shows a picture taken of decapoles on a test bench.

The important characteristics of the magnetic fields of correctors are their main field transfer function (or *response*), the field quality and possible crosstalk, as MCOS and MCDs are nested [62]. To resolve the previously stated discrepancy, it is essential to investigate the decapole correctors themselves, to rule them out as the source of this difference.

The full third term of the chromaticity function is highlighted in Eq. (5.1). Details on chromaticity are given in Section 2.6.1.

$$Q(\delta) = Q_0 + Q'\delta + \frac{1}{2!}Q''\delta^2 + \boxed{\frac{1}{3!}Q'''\delta^3} + O(\delta^4). \quad (5.1)$$

This third order, generated by leading order by decapoles in a region of non-zero linear dispersion, is related to the β -function, the dispersion and the normalized strength $K_5[m^{-5}]$ of the decapolar correctors:

$$\begin{aligned}\Delta Q_x''' &= \frac{1}{4\pi} K_5 L \beta_x D_x^3 \\ \Delta Q_y''' &= - \frac{1}{4\pi} K_5 L \beta_x D_x^3.\end{aligned}\tag{5.2}$$

During Run 3's commissioning, the routine measurement and correction of Q'' and Q''' have been established. These corrections provide a valuable opportunity to analyze the response of the decapole correctors, *MCDs*. By studying this response, it is possible to determine whether the source of the Q''' discrepancy originates from a miscalibration of the decapolar correctors or not. Figure 5.3 shows the chromaticity function measured during Run 3's commissioning in 2022 with the nominal FiDeL corrections and with further beam-based corrections computed analytically and applied on top.

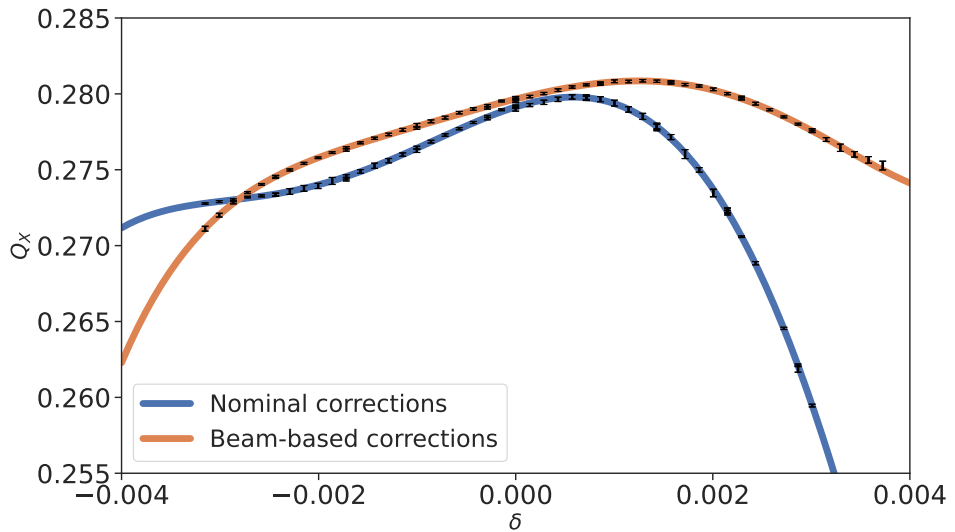


Figure 5.3.: Chromaticity of the horizontal plane of Beam 1 during Run 3's commissioning, with nominal corrections based on the magnetic model and beam-based corrections aimed at correcting Q'' and Q''' .

The nominal and corrected Q''' values are shown in Table 5.1, with the shift in Q''' for each beam and axis. A good agreement between the measurements and simulations can be seen.

The agreement between simulations and measurements confirms that the decapole correctors are functioning as intended. No errors in their calibration or response function (current to strength) have been identified that could explain the observed Q''' discrepancy.

Plane	$Q'''[10^6]$		$\Delta Q'''[10^6]$	
	Nominal	Beam-Based	Meas.	Simulation
Beam 1				
X	-3.36 ± 0.04	-1.02 ± 0.03	2.3 ± 0.1	2.5
Y	1.62 ± 0.05	0.12 ± 0.02	-1.5 ± 0.1	-1.4
Beam 2				
X	-2.72 ± 0.08	-0.64 ± 0.03	2.1 ± 0.1	2.5
Y	1.54 ± 0.06	0.14 ± 0.03	-1.4 ± 0.1	-1.4

Table 5.1.: Third order chromaticity obtained during Run 3 commissioning, with nominal and beam-based corrections aimed at correcting Q'' and Q''' . Response of the correctors between the two configurations is also given for both measurement and simulation.

5.3. Bare Chromaticity

Complementary to the measurements of Q''' shifts with varying decapolar strengths, measurements of the bare machine, without any correctors powered, can provide valuable insights. These measurements help rule out potential crosstalk between the octupolar and decapolar correctors, which are physically nested, and allow for a clearer understanding of the contribution of octupolar correctors to Q''' . Additionally, they offer a direct and clean comparison to the magnetic model. The obtained results are presented in Fig. 5.4.

Simulations have been run with MAD-X and PTC including fields errors from normal sextupole to decahexapole. The expected Q''' values are presented in Table 5.2 and compared to the measured ones along with the ratio between the two.

Quantity	Measured $[10^6]$	Simulated $[10^6]$	Ratio
Beam 1			
Q_x'''	2.95 ± 0.04	6.94 ± 0.02	0.43 ± 0.01
Q_y'''	-1.82 ± 0.04	-4.29 ± 0.01	0.42 ± 0.01
Beam 2			
Q_x'''	3.06 ± 0.07	7.03 ± 0.02	0.44 ± 0.01
Q_y'''	-1.72 ± 0.02	-4.27 ± 0.01	0.42 ± 0.01

Table 5.2.: Measured and simulated third order chromaticity with octupole and decapole correctors turned off. The simulations include field errors from sextupoles to decahexapole (normal sextupole to decahexapole).

The observed discrepancy between the measurements and simulations persists both with the FiDel corrections applied and with the correctors turned off. Similarly, measuring significantly different

5. Decapolar Fields

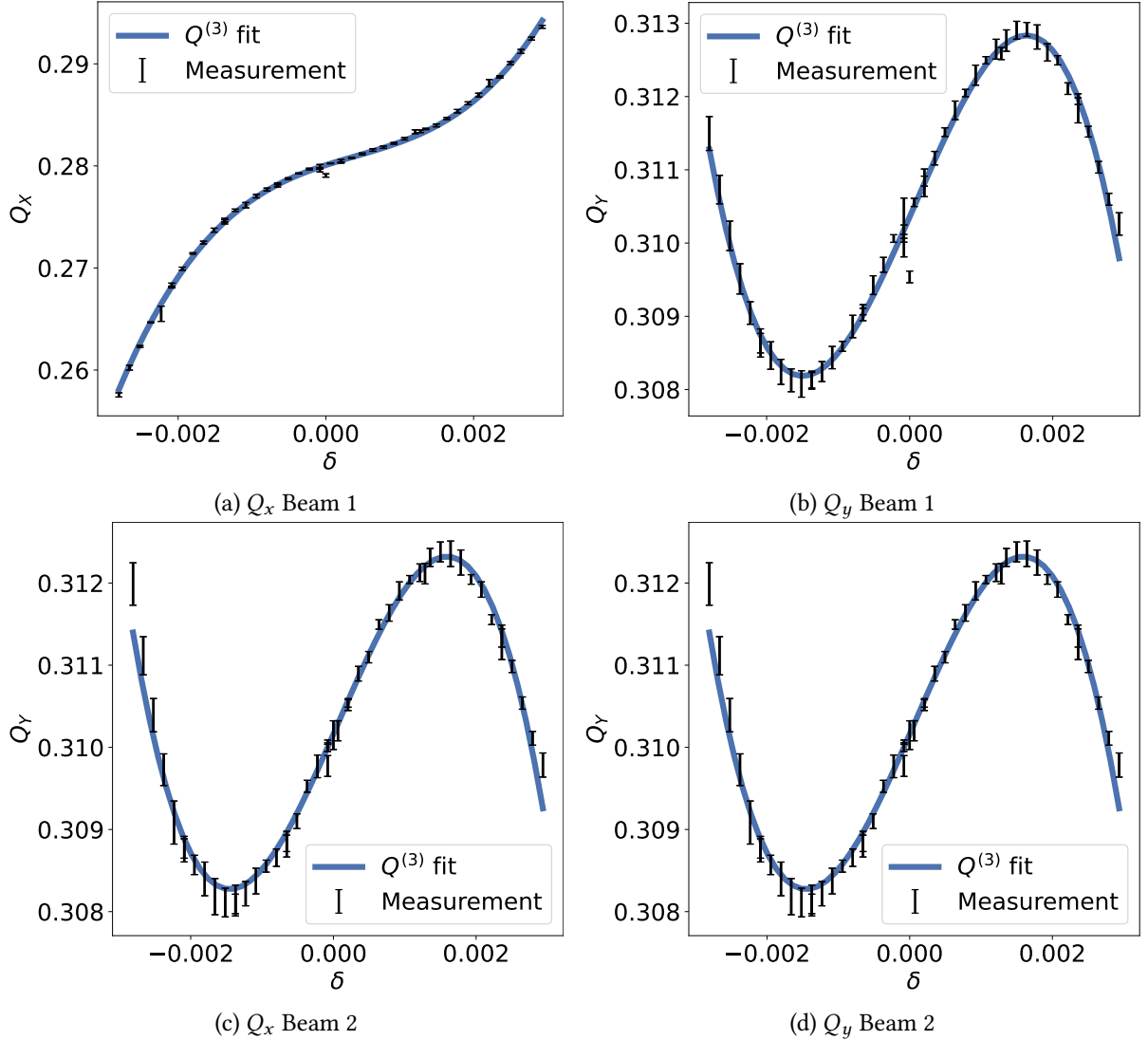


Figure 5.4.: Fit of the chromaticity function for the chromaticity measurement performed with octupole and decapole correctors powered off. The fit includes all orders up to third.

lower-order chromaticities and working points, the discrepancy remains consistently around a factor of 2 between the measured and expected Q'' . This suggests that the source of the discrepancy lies elsewhere. One possible explanation could be an error in the systematic decapolar component of the main dipoles in the magnetic model. However, relying solely on Q'' does not allow for a definitive conclusion, as higher-order effects like non-linear dispersion or non-linear momentum compaction factor could also contribute. To resolve this, additional observables, such as chromatic amplitude detuning, will be required for further investigation.

5.4. Chromatic Amplitude Detuning

The Chromatic Amplitude Detuning is the tune shift dependant on both the actions and the momentum offset, whose decapole contributed terms are described via a Taylor expansion in Eq. (5.3). More information and derivations can be found in Section 2.6.3 and Appendix B.

$$\Delta Q(J_x, J_y, \delta) = \frac{\partial^2 Q}{\partial J_x \partial \delta} \cdot J_x \delta + \frac{\partial^2 Q}{\partial J_y \partial \delta} \cdot J_y \delta + \frac{1}{3!} \frac{\partial^3 Q}{\partial \delta^3} \cdot \delta^3. \quad (5.3)$$

The last term is more commonly referred to as the third order chromaticity, Q''' . Each of those terms depend on the β -functions, the horizontal dispersion D and the normalized decapole field gradient K_5 for a single source of length L ,

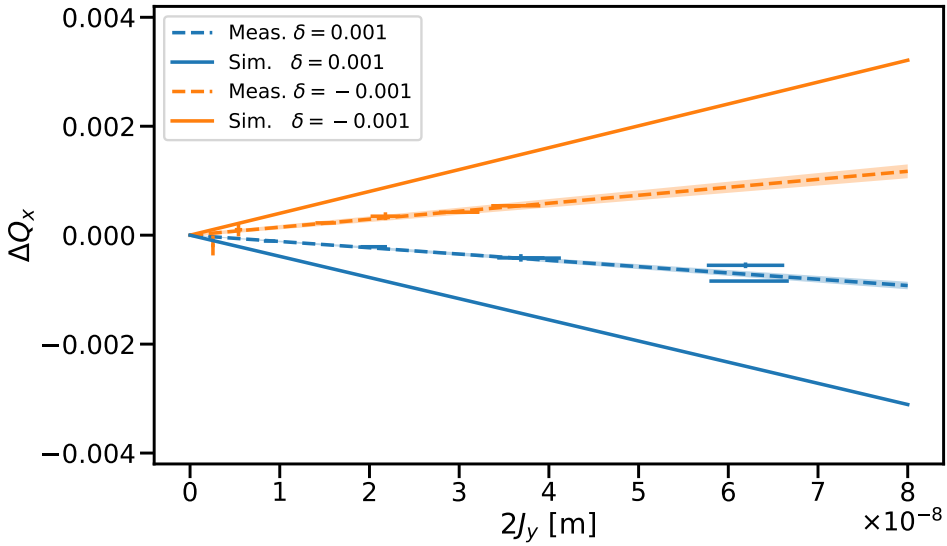
$$\begin{aligned} \frac{\partial^2 Q_x}{\partial J_x \partial \delta} &= \frac{1}{16\pi} K_5 L \beta_x^2 D_x, & \frac{\partial^2 Q_x}{\partial J_y \partial \delta} &= -\frac{1}{8\pi} K_5 L \beta_x \beta_y D_x, \\ \frac{\partial^3 Q_x}{\partial \delta^3} &= \frac{1}{4\pi} K_5 L \beta_x D_x^3, & \frac{\partial^2 Q_y}{\partial J_x \partial \delta} &= -\frac{1}{8\pi} K_5 L \beta_x \beta_y D_x, \\ \frac{\partial^2 Q_y}{\partial J_y \partial \delta} &= \frac{1}{16\pi} K_5 L \beta_y^2 D_x, & \frac{\partial^3 Q_y}{\partial \delta^3} &= -\frac{1}{4\pi} K_5 L \beta_y D_x^3. \end{aligned} \quad (5.4)$$

Notably, while the K_5 dependence is identical to that of Q''' , the β and D_x dependencies differ significantly. In the presence of a systematic error in the magnetic model, one would expect similar ratios for this observable as those observed for Q''' . The action dependant terms can be measured by exciting the beam with an AC-dipole with increasing strengths at different momentum-offsets.

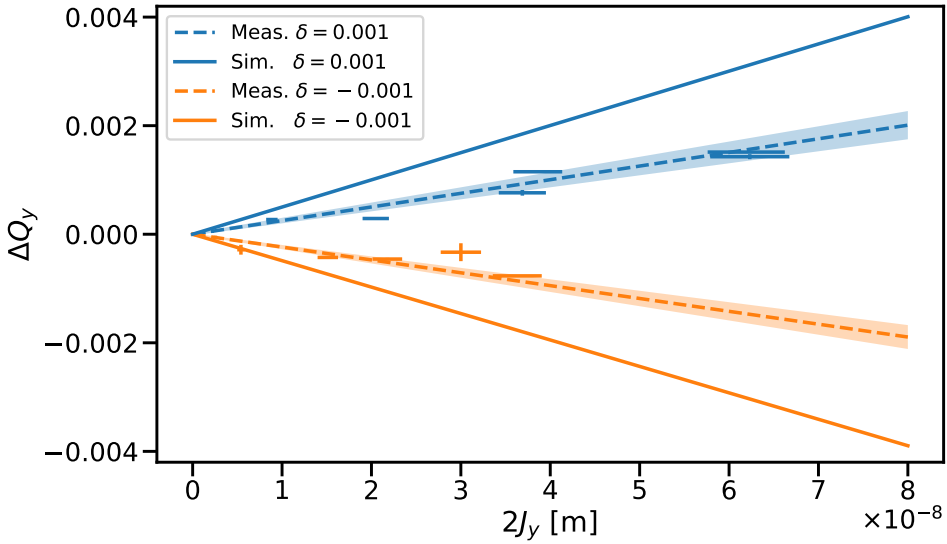
Such a measurement was taken with octupole and decapole correctors turned off to measure the bare machine. The momentum-offsets measured were -0.001 and 0.001 , respectively roughly equal to a trim of $+140\text{Hz}$ and -140Hz of the RF. Some data could not be collected due to machine availability issues, restricting the measurement to low amplitude kicks. Nevertheless, the terms $\frac{\partial^2 Q_x}{\partial J_y \partial \delta}$ and $\frac{\partial^2 Q_y}{\partial J_y \partial \delta}$ for beam 2 were successfully measured for the first time in the LHC.

Figure 5.5a and Fig. 5.5b show a fit of those terms to measured $Q_{x,y}$ vs J_y at two different momentum offsets. Expected shifts from MADX-PTC simulations, that include field errors ranging from sextupoles to decahexapoles (b_3 to b_8 and a_4 to a_8) are shown as a comparison.

5. Decapolar Fields



(a) Horizontal tune shift depending on the vertical action: $\frac{\partial^2 Q_x}{\partial J_y \partial \delta}$.



(b) Vertical tune shift depending on the vertical action: $\frac{\partial^2 Q_y}{\partial J_y \partial \delta}$.

Figure 5.5.: Measured and simulated tune shift due to a change of action via an AC-Dipole at two different momentum offsets. Each fit corresponds to a chromatic amplitude detuning term evaluated at a certain δ .

Type	$\frac{\partial^2 Q_x}{\partial J_y \partial \delta} [10^4 \text{m}^{-1}]$	$\frac{\partial^2 Q_y}{\partial J_y \partial \delta} [10^4 \text{m}^{-1}]$
$\delta = +0.001$		
Meas.	-1.16 ± 0.08	1.26 ± 0.15
Sim.	-3.82 ± 0.01	2.47 ± 0.01
Ratio	0.30 ± 0.02	0.51 ± 0.06
$\delta = -0.001$		
Meas.	1.47 ± 0.12	-1.18 ± 0.13
Sim.	3.92 ± 0.01	-2.41 ± 0.01
Ratio	0.38 ± 0.03	0.49 ± 0.05

Table 5.3.: Comparison of the measured and simulated terms $\frac{\partial^2 Q_x}{\partial J_y \partial \delta}$ and $\frac{\partial^2 Q_y}{\partial J_y \partial \delta}$ via PTC, at two discrete momentum offsets. Simulations include errors from normal sextupole to decahexapole and from skew octupole to decahexapole.

A consistent difference between simulation and measurement is observed. The values and ratios of measurement to model can be found in Table 5.3. The observed ratios of measurements to model for the chromatic amplitude detuning show a good agreement, while not exact, with those of the bare chromaticity. This similarity of the ratios between the chromatic amplitude detuning and Q''' discrepancies suggests an issue with the decapolar error model of the main dipoles, with measurements showing values about half of those predicted by the magnetic model.

5.5. Accounting for Decay

FiDeL, the field model used in operation, aims at correcting the field errors at various energies. Measured field errors but also decay estimates with respect to time are used when computing corrections.

Magnetic decay in superconducting magnets stems from field changes in the strands caused by current redistribution in the superconducting cables. Decay has been shown to be strongly dependent on the magnet powering history [64, 65]. This happens for example when ramping down from an energy of 6.8TeV to 0 and then going back to injection energy at 450GeV. Some components of the magnetic field will persist and gradually change over time until they reach their final value.

While the sextupolar b_3 decay is accounted for during operations, a review of the FiDeL model revealed that the decapolar component b_5 has not been similarly considered. To date, all beam dynamics studies in the LHC have made use of the same set of magnetic measurement error tables, thus neglecting any decapolar decay. It has though be found that during the LHC construction, magnetic measurements were taken for a representative set of main dipoles, and decay measured. The average b_5 field in the main dipoles at $t = 0$, upon reaching the 450 GeV energy, is approximately 1.145 ± 0.5 , based on data

5. Decapolar Fields

from the magnetic reports utilized by FiDeL. For reference, decay measurements of a selection of main dipoles over time are illustrated in Fig. 5.6. Table 5.4 shows the decay expected at injection energy after a typical cycle of machine operation. From this table, it is clear that decay accounts for a large part of the b_5 at injection. $\approx 40\%$ of the compensated b_5 at injection in the main dipoles can indeed be attributed to the decay.

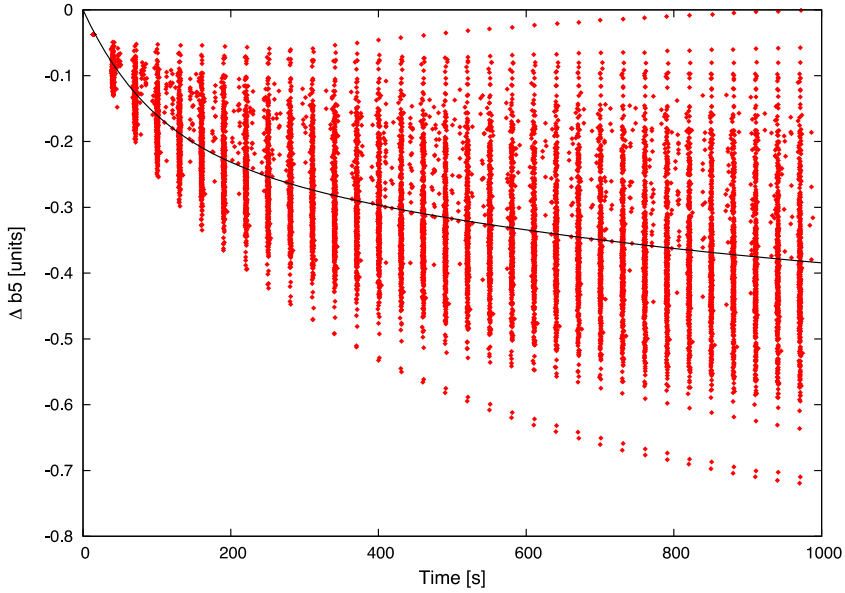


Figure 5.6.: Measured decay of the integrated decapolar field in LHC's main dipoles at injection energy.
The fit is shown in black [15].

5

Time [m]	Δb_5
17	-0.38
33	-0.44
50	-0.46
67	-0.47
83	-0.47
167	-0.47

Table 5.4.: Decay of the b_5 component after injection for long time periods [15].

Unfortunately, individual magnet measurements conducted over 15 years ago could not be recovered. As a result, the b_5 decay in the simulations is implemented as the average decay across all the probed magnets. In the following simulations, each main dipole sees its b_5 component reduced by 0.47 units.

Chromaticity It has been shown in the previous sections, and particularly in Table 5.2 that measurements and simulations were off regarding the third order chromaticity Q''' . New simulations have hence been conducted to evaluate the effect of this decay on chromaticity. Table 5.5 compares simulations with and without the decay of the b_5 component. The simulations use the 100 available error seeds to calculate error bars.

Condition	$Q'''_x [10^6]$	$Q'''_y [10^6]$
No Decay	6.93 ± 0.04	-4.32 ± 0.02
$\Delta b_5 = -0.47$	4.05 ± 0.04	-2.54 ± 0.02

Table 5.5.: Comparison of Q'''_x and Q'''_y for Beam 1 with and without decay of the b_5 component of the main dipoles at injection energy. Fields errors range from normal and skew sextupoles ($n = 3$) to icosapole ($n = 10$).

Implementing the decay of the b_5 component of the main dipoles in the simulations have significantly reduced the discrepancy between beam-based measurement and the magnetic model. Using the values from the bare chromaticity measurement and updating Table 5.2 with the newly obtain data provides a more accurate description of the magnetic model, as shown in Table 5.6.

Quantity	Measured [10^6]	Simulated [10^6]	Ratio
Beam 1			
Q'''_x	2.95 ± 0.04	4.05 ± 0.04	0.73 ± 0.01
Q'''_y	-1.82 ± 0.04	-2.54 ± 0.02	0.72 ± 0.02
Beam 2			
Q'''_x	3.06 ± 0.07	4.27 ± 0.03	0.72 ± 0.02
Q'''_y	-1.72 ± 0.02	-2.55 ± 0.01	0.67 ± 0.01

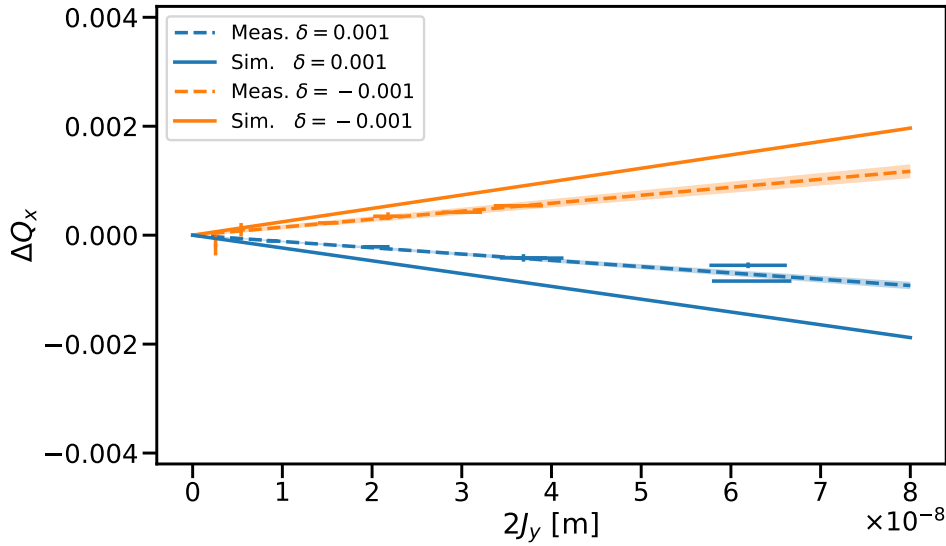
Table 5.6.: Measured and simulated third order chromaticity with octupole and decapole correctors turned off. The simulations include field errors from normal and skew sextupoles to icosapole ($n = 3$ to $n = 10$). The b_5 component of the main dipoles has been updated to include decay.

Chromatic Amplitude Detuning Similar to chromaticity, new simulations have been conducted for chromatic amplitude detuning. Table 5.7 gives an overview of the newly computed values and the related ratios relative to the measurements, while Fig. 5.7 gives a visual clue. A small difference in agreement can be observed between the direct term $\partial^2 Q_y / (\partial J_y \partial \delta)$ and the crossterm. This may arise from the implementation of decay, which only considers the average b_5 across all dipoles and may not fully capture the individual variations. Nevertheless, both terms now demonstrate good agreement with the model, similar to the trend seen with chromaticity.

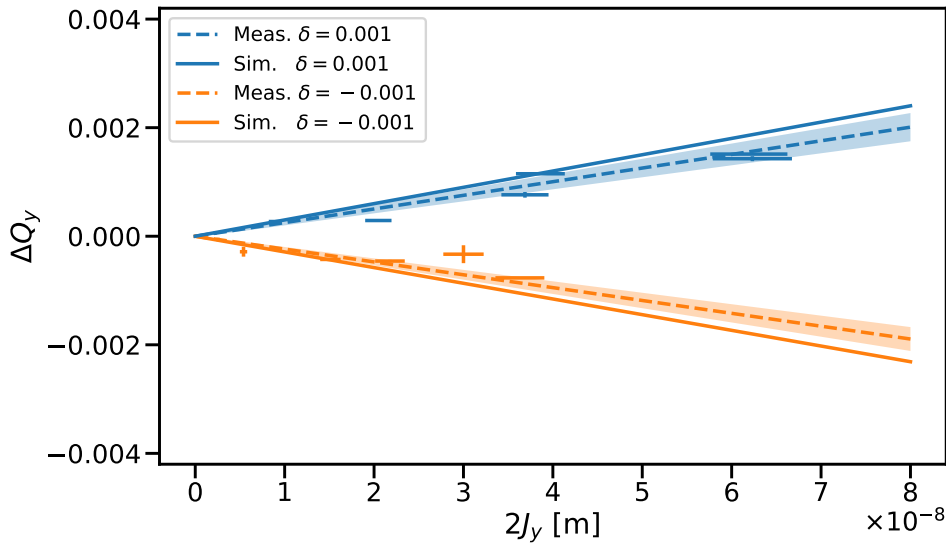
5. Decapolar Fields

Type	$\frac{\partial^2 Q_x}{\partial J_y \partial \delta} [10^4 \text{m}^{-1}]$	$\frac{\partial^2 Q_y}{\partial J_y \partial \delta} [10^4 \text{m}^{-1}]$
$\delta = +0.001$		
Meas.	-1.16 ± 0.08	1.26 ± 0.15
Sim.	-2.35 ± 0.01	1.50 ± 0.01
Ratio	0.49 ± 0.03	0.84 ± 0.10
$\delta = -0.001$		
Meas.	1.47 ± 0.12	-1.18 ± 0.13
Sim.	2.46 ± 0.01	-1.45 ± 0.01
Ratio	0.60 ± 0.05	0.82 ± 0.09

Table 5.7.: Comparison of the measured and simulated terms $\frac{\partial^2 Q_x}{\partial J_y \partial \delta}$ and $\frac{\partial^2 Q_y}{\partial J_y \partial \delta}$ via PTC, at two discrete momentum offsets. Simulations include errors from normal and skew sextupoles to icosapole ($n = 3$ to $n = 10$), as well as the decay of the b_5 component of the main dipoles.



(a) Horizontal tune shift depending on the vertical action: $\frac{\partial^2 Q_x}{\partial J_y \partial \delta}$.



(b) Vertical tune shift depending on the vertical action: $\frac{\partial^2 Q_y}{\partial J_y \partial \delta}$.

Figure 5.7.: Measured and simulated tune shift depending on the action at two different momentum offsets. Each fit corresponds to a chromatic amplitude detuning term evaluated at a certain δ . Estimates from simulations are lowered due to the b_5 decay of the main dipoles.

5.6. Resonance Driving Terms

Decapoles, due to their order, contribute to many RDTs. Indeed, 25 of them can be theoretically observed in simulations and measurements. In practice, the contributions of individual multipoles become indistinguishable as many resonances or lines overlap, making it impossible to isolate certain terms. Some resonances, described in Appendix C, are unique to certain multipoles when considering no too high orders. Those resonances, provided that they are sufficiently strong and the beam close to them, can be measured via their RDTs.

Of interest to the LHC Operation, is the RDT f_{1004} , driving the resonance $1Q_x - 4Q_y$. It can be seen in the horizontal frequency spectrum at $-4Q_y$ with an amplitude dependence on j_y^2 . Figure Fig. 5.8 shows a frequency map [66] of a simulation including decapolar field errors, where their impact on the beam is easily noticeable. The red particles evolving close to the resonance are affected by it and are subject to large tune shifts. Eventually, those particles are lost when their amplitude becomes too large.

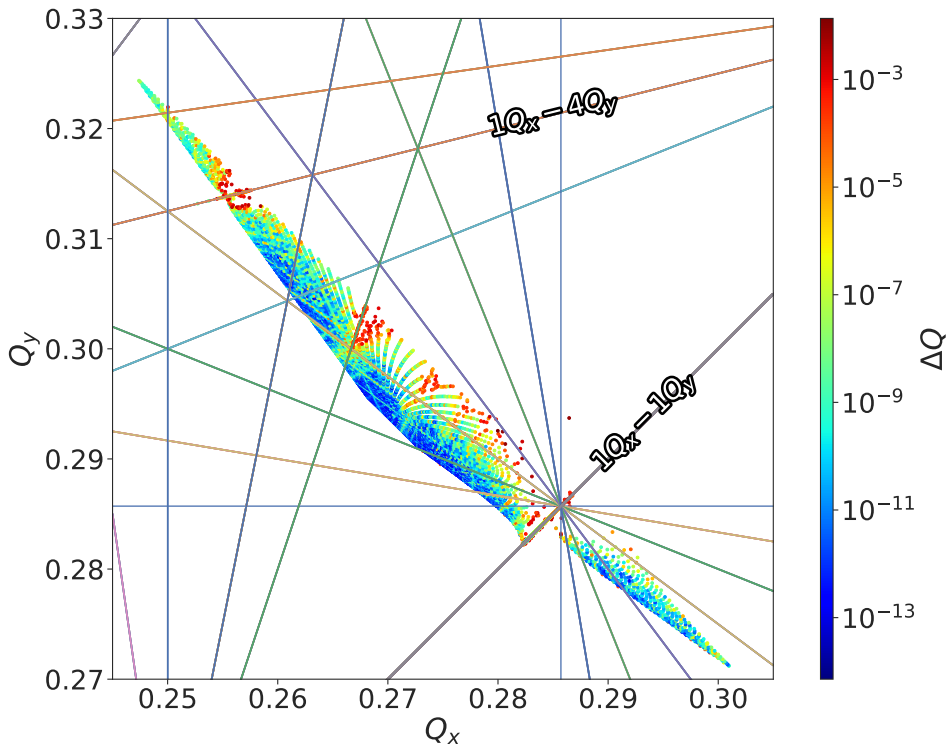


Figure 5.8.: Frequency map at injection energy, with decapolar field errors and nominal settings for landau octupoles. The highlighted resonance $(1,-4)$, excited by decapoles, shows a degradation over 20,000 turns. The tune shift between the start and the end of the simulation is indicated in color.

Measurements were taken for the first time in the LHC to observe the f_{1004} RDT at injection energy. The frequency line of the resonance $1Q_x - 4Q_y$ is seen at $4Q_y$ in the horizontal spectrum, as shows Fig. 5.9.

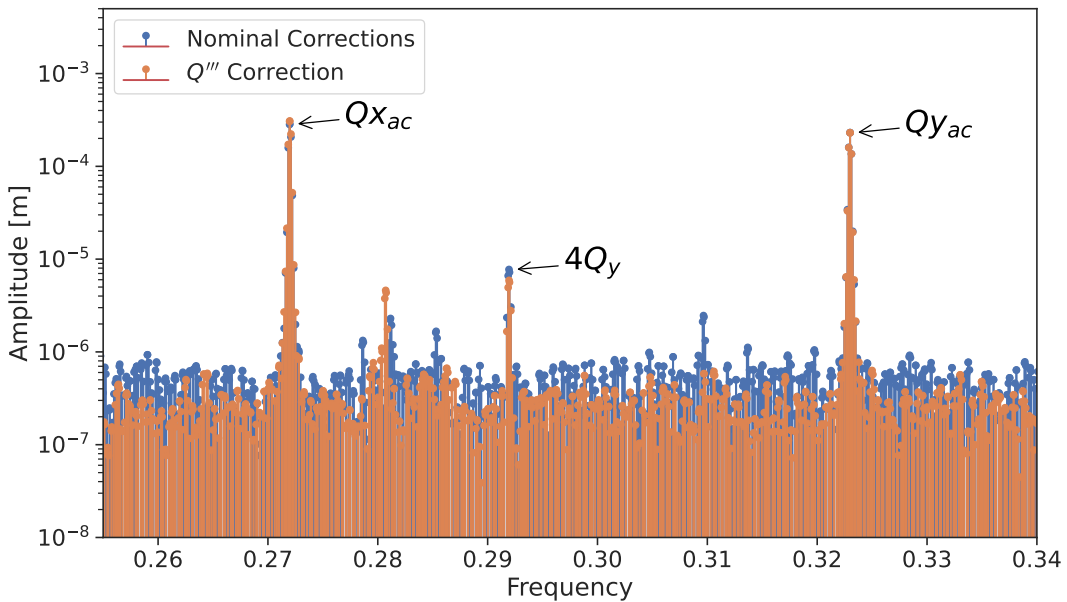


Figure 5.9.: Horizontal frequency spectrum of turn-by-turn data, with nominal and beam-based corrections for the third order chromaticity Q'' . The $1Q_x - 4Q_y$ resonance can be seen at $-4Q_y$ with different amplitudes for each correction scheme.

5.6.1. Measurement and correction

Decapolar fields are expected to be the main contributors to the RDT f_{1004} . As such, powering the decapolar correctors is a good way to correct the related resonances. Being linear with the strength of the correctors, the RDT can be corrected via a response matrix, as previously detailed in Section 3.3.1.

Measurements were conducted to establish a baseline for the amplitude of the RDT without decapolar correctors and with the nominal FiDeL corrections. Although the FiDeL scheme was not intended to correct the RDT but rather only from Q' to Q''' , it would be expected for it to lower the amplitude of the RDT. It can though be seen in Fig. 5.10 that it degrades the resonance compared to the machine with no decapolar correctors. Similar behaviour is seen for Beam 2.

Further corrections were then attempted based on the measurements obtained with the nominal FiDeL settings and were subsequently applied on top of their strengths. The strength of the decapolar correctors is shown in Table 5.8 for the FiDeL settings, the delta applied on top, and the final correctors values.

5. Decapolar Fields

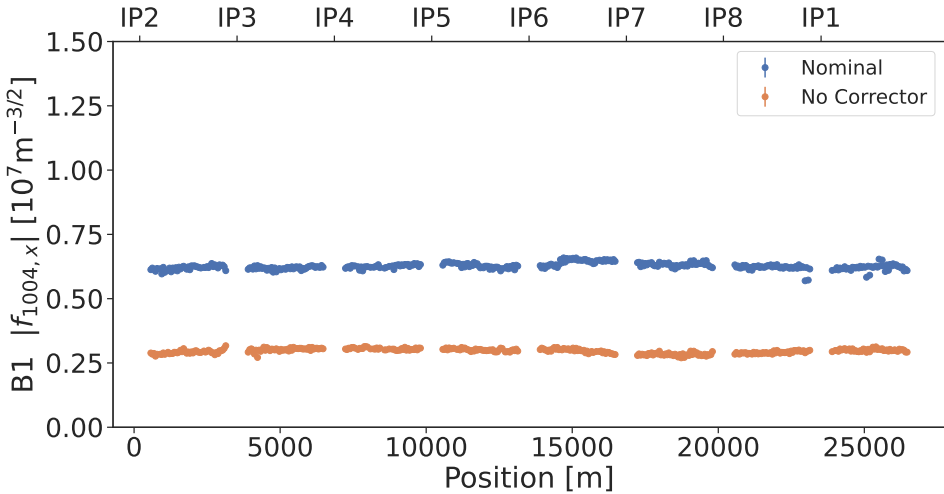


Figure 5.10.: Measured f_{1004} for Beam 1 with decapolar correctors powered off and with nominal corrections for Q''' . Corrections clearly increase the RDT amplitude.

This RDT correction also serves as a partial Q''' correction. To fully correct Q''' indeed approximately requires a strength of $+13,000K_5$ distributed amongst the correctors. Therefore, this new approach also successfully reduces Q''' by about 70% compared to the previous method. The chromatic amplitude detuning terms are also expected to be decreased. The results of these successful corrections, compared to the nominal ones, as well as their inverse, are shown in Fig. 5.11.

To gauge the response of the RDT with the decapolar correctors strengths, simulations were run with decapolar correctors turned off and with the strengths of the RDT correction. The response of the RDT between those two schemes is shown in Fig. 5.12. The difference between their RMS value ratio is $\approx 6\%$, indicating that simulations correctly model the decapolar correctors.

Circuit	$\text{FiDeL } K_5 [\text{m}^{-5}]$	$\Delta K_5 [\text{m}^{-5}]$	$K_5 [\text{m}^{-5}]$
Beam 1			
RCD.A12B1	-4582	6055	1473
RCD.A23B1	-5106	7	-5099
RCD.A34B1	-4855	3827	-1028
RCD.A45B1	-4577	-4746	-9323
RCD.A56B1	-4125	-4903	-9028
RCD.A67B1	-5166	2961	-2205
RCD.A78B1	-6827	3593	-3234
RCD.A81B1	-5500	2380	-3120
Total	-40738	9174	-31564
Beam 2			
RCD.A12B2	-4490	3639	-851
RCD.A23B2	-5155	-1147	-6302
RCD.A34B2	-4825	-1038	-5863
RCD.A45B2	-4619	3986	-633
RCD.A56B2	-4064	2944	-1120
RCD.A67B2	-5066	2357	-2709
RCD.A78B2	-6866	-2952	-9818
RCD.A81B2	-5446	1825	-3621
Total	-40531	9614	-30917

Table 5.8.: Strength of decapolar correctors with nominal FiDeL settings and after application of corrections aiming at reducing both the RDT f_{1004} and Q''' . The total value has a direct incidence on the third order chromaticity Q''' .

5. Decapolar Fields

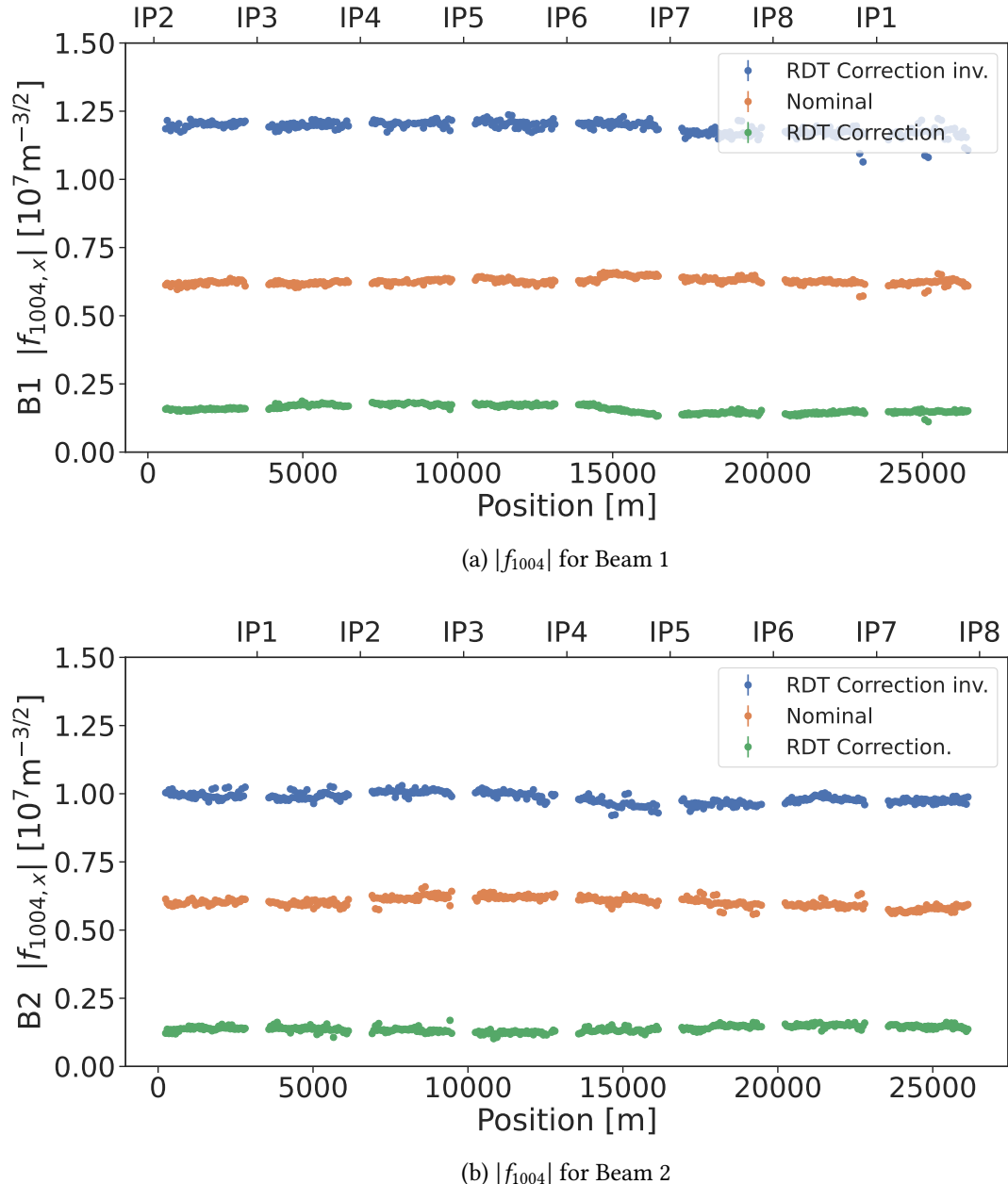


Figure 5.11.: Measured f_{1004} with decapolar correctors powered off, nominal settings, and combined RDT & Q''' correction with normal and opposite signs.

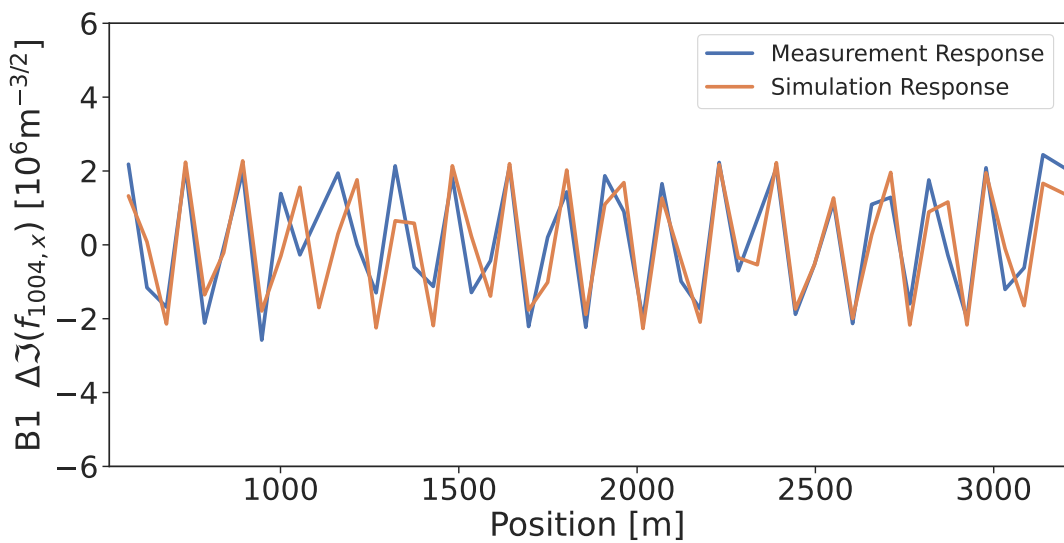


Figure 5.12.: Comparison for measurement and simulation of the response of the imaginary part of f_{1004} upon application on unpowered correctors of the RDT corrections.

5.6.2. Feed-Up Contributions

First Observation

As described in Appendix A, multipoles can combine to create fields that are seen as higher orders when considering higher orders of the BCH expansion. For decapoles, combinations of several sextupoles and sextupoles with octupoles give rise to decapolar-like fields, as described in Table A.3. The following parts of this section will describe those combinations.

This effect was observed in 2022 during Run 3's commissioning. New corrections of the non-linear chromaticity Q'' and Q''' were performed, and RDT measurements taken before and after their correction. As Q''' was corrected, the expectation was that the RDT f_{1004} would also lower with the reduction of the decapolar strengths K_5 . However, an increase of the RDT was observed, as shows Fig. 5.13.

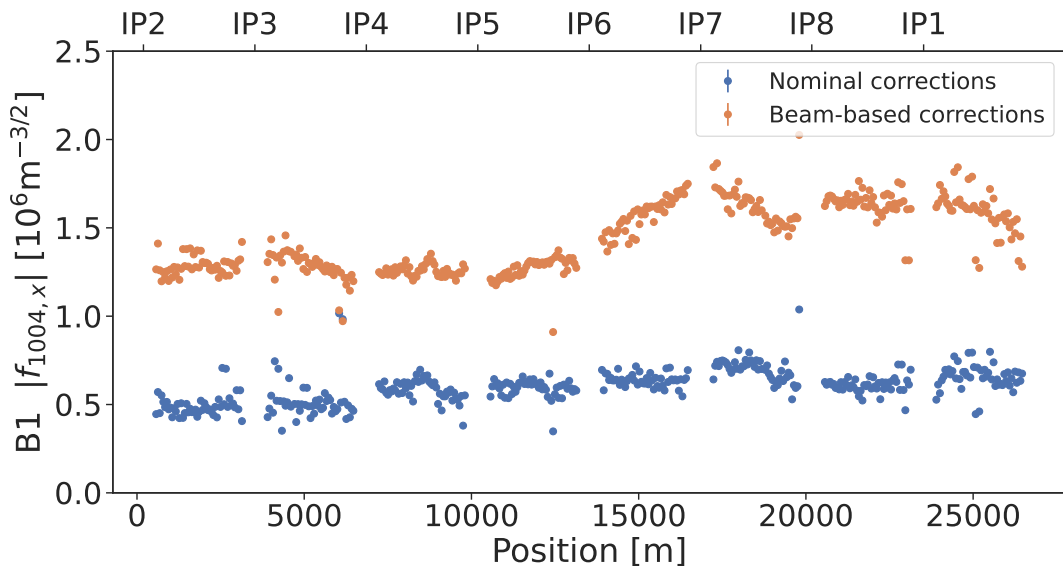


Figure 5.13.: Non intuitive increase of the RDT f_{1004} after application of both the Q'' and Q''' corrections.

Sextupoles

At the third order of the BCH expansion, the combination of two sextupoles yields a decapolar-like expression. This means that, during normal operation of the machine, decapolar observables will be altered when adjusting parameters such as the linear chromaticity Q' . Derivation of such a combination can be found in Appendix A.2.2. The resulting Hamiltonian indeed is similar to the terms of a decapole, dropping the $p_{x,y}$ terms for readability:

$$(H_3)^3 \propto \frac{1}{48} (x^5 - 2x^3y^2 - 3xy^4) \\ \sim x^5 - 10x^3y^2 + 5xy^4. \quad (5.5)$$

To quantify the actual impact of such an equation on the LHC, a simulation was run with injection optics while varying this same linear chromaticity Q' . No higher fields than sextupoles have been included, including field errors. The resulting effect on the RDT f_{1004} can be seen in Fig. 5.14.

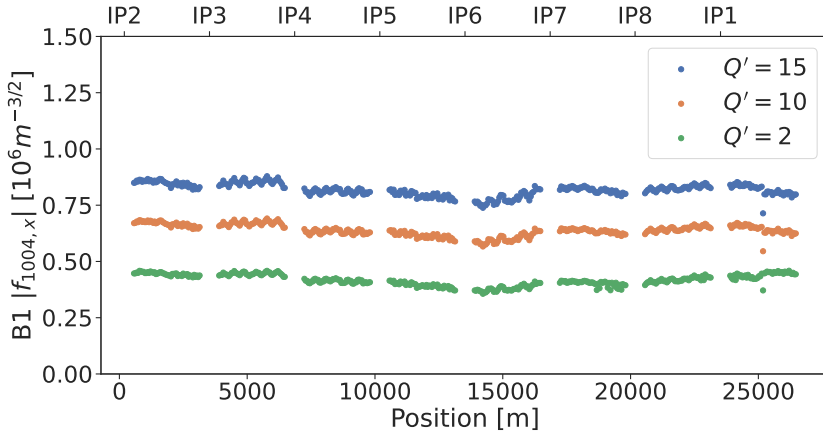


Figure 5.14.: Simulated change of the decapolar RDT f_{1004} with varying linear chromaticity Q' generated by sextupoles. The combination of sextupolar fields clearly shows a increase in decapolar RDT.

As the linear chromaticity increases, the overall K_3 strength of sextupoles actually becomes more negative. Considering the previous Eq. (5.5), a higher chromaticity is expected to increase the amplitude of the RDT f_{1004} , related to the last term xy^4 . Figure 5.15 shows how the RDT is expected to vary, depending on the overall sextupoles strength and the linear chromaticity. It can be noted that although the relation between K_3 and Q' is linear, that of K_3 and the RDT varies with the cubed strength. Using the sum of the cubed strength is possible due to the chromaticity knob being a factor applied on all sextupoles at the same time.

To confirm what is observed in simulations, measurements were performed by varying Q' and kicking the beam with the AC-Dipole. Limited by losses, up to three measurements with distinct Q' were taken, as shows Fig. 5.16.

Like in simulations, it is observed that an increase in Q' translates to an increase in $|f_{1004}|$. The scale of the amplitude is though one order of magnitude higher than that of simulations. An offset for all measurements could be explained by non-included field-errors. The shift between them however should be similar between machine and simulations, this could be due by the interaction of the sextupolar

5. Decapolar Fields

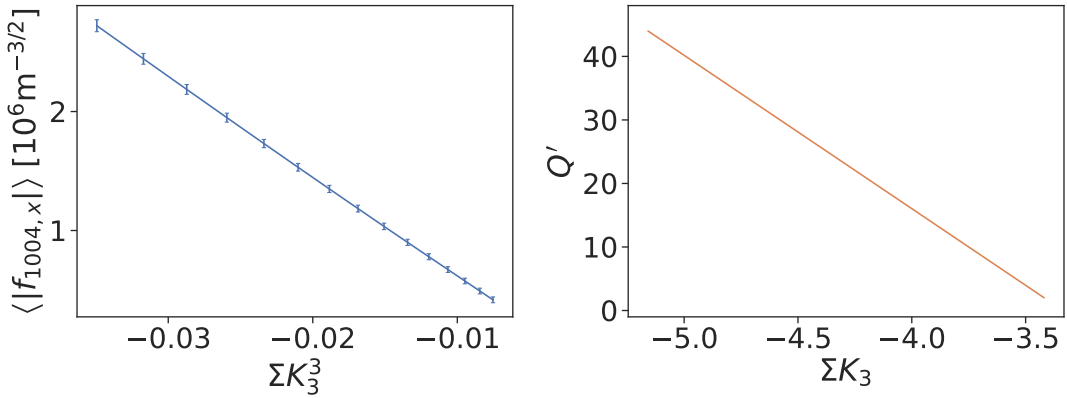


Figure 5.15.: Average amplitude of the decapolar RDT f_{1004} depending on the overall strength of the sextupoles used to control the linear chromaticity Q' . The right plot can be used to relate the RDT amplitude to a specific Q' value.

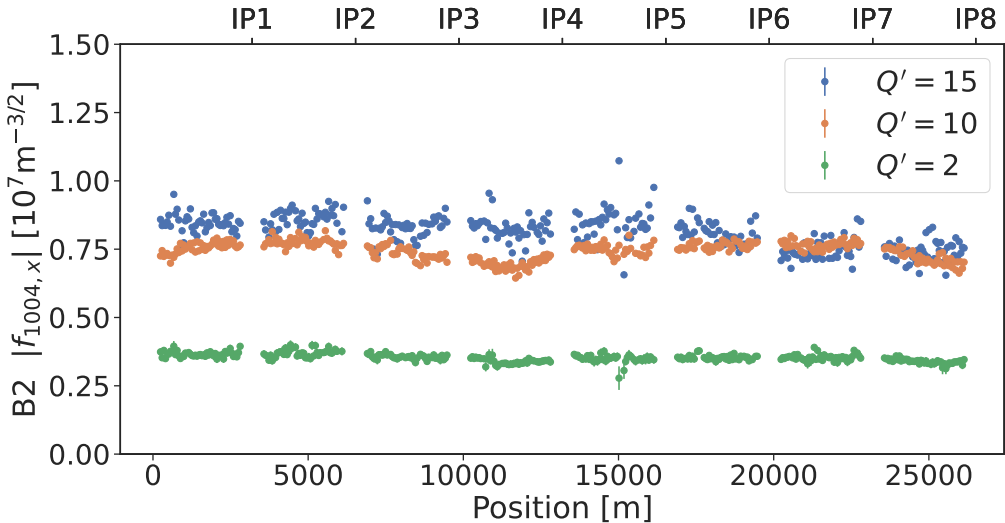


Figure 5.16.: Measured change of the decapolar RDT f_{1004} depending of the desired linear chromaticity Q' generated by sextupoles. It is to be noted that the vertical axis is one order of magnitude higher than the previous simulations' plot.

fields with octupoles, as detailed in the following section. More data points with varying Q' at similar kick amplitudes would be required to further investigate.

Sextupoles and Octupoles

At the second order of the BCH expansion, the combination of a sextupole and an octupole yields a decapolar-like expression. Like sextupoles, octupoles are used in operation, thus contributing to decapolar fields. This happens amongst other when correcting the second order chromaticity Q'' and most importantly with the Landau Octupoles, which are powered to high strengths at injection energy to introduce Landau damping [5]. Derivation of such a combination can be found in Appendix A.2.3. The resulting Hamiltonian indeed is similar to the terms of a decapole, dropping the $p_{x,y}$ terms for readability:

$$\begin{aligned} H_3H_4 &\propto \frac{1}{24} (x^5 + 2x^3y^2 + xy^4) \\ &\sim x^5 - 10x^3y^2 + 5xy^4. \end{aligned} \quad (5.6)$$

In order to assess the previous equation, simulations were run with several configurations. As seen previously, a combination of two sextupoles creates a decapolar-like field, varying their field is thus not needed. Rather, a set of two configurations was run to check the impact of octupoles alone. The first configuration is ran with all sextupoles of the machine turned off, while octupoles are powered. The second configuration turns off all sextupoles and octupoles. Figure 5.17 shows the resulting RDT f_{1004} from these simulations. It is there apparent that varying octupoles without sextupoles does not have any effect on this RDT.

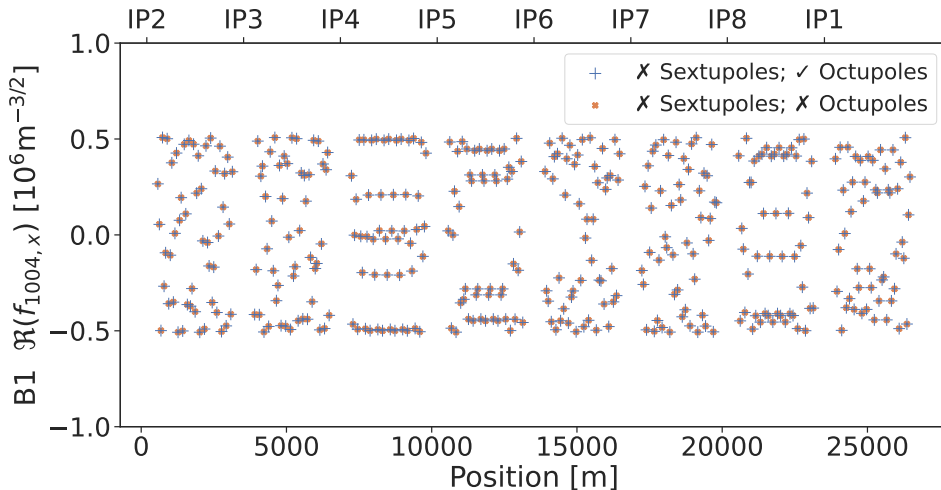


Figure 5.17.: Simulated decapolar RDT f_{1004} with two different schemes. First scheme has lattice sextupoles turned off and octupoles turned on. Second scheme has all sextupoles of the lattice turned off and octupoles turned off as well. No difference is seen, as expected from the equations.

5. Decapolar Fields

The most powerful octupoles used in operation are the lattice octupoles, used for Landau damping. Figure 5.18 shows a simulation ran with varying strengths of those magnets. It can be noted here that the shift of the RDT is almost of an order of magnitude, making octupoles a large contributor to the decapolar fields.

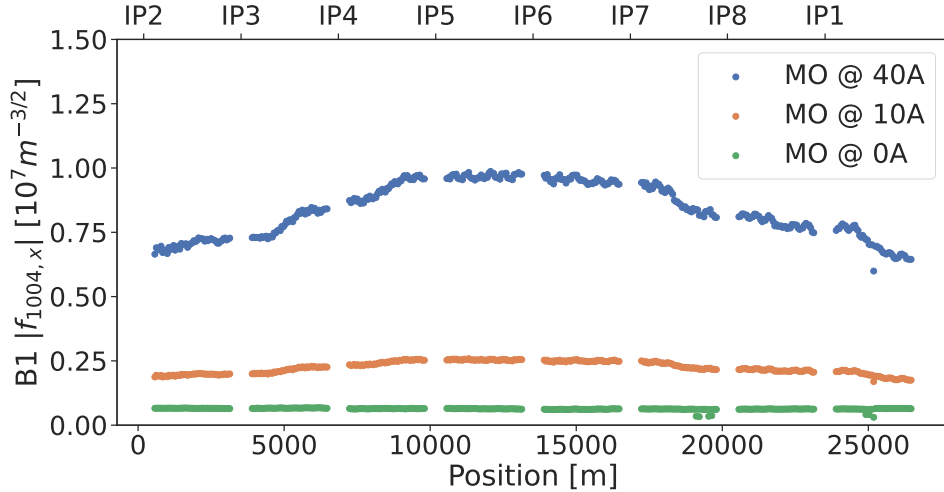


Figure 5.18.: Simulated change of the decapolar RDT f_{1004} depending of the strength of the lattice octupoles used for Landau damping.

While decapoles are expected to be the main contributors to decapolar fields, other strong sources can indeed be identified. Figure 5.19 shows the average amplitude of the RDT f_{1004} depending on the error sources introduced in the simulations. A large contribution comes from the octupolar errors in the main dipoles, being actually larger than the decapolar errors in those magnets.

Measurements were performed to confirm and quantify the effect of octupoles coupled with sextupoles on the decapolar fields. Previous corrections, aimed at correcting the second order chromaticity Q'' , via octupolar correctors MCO, were applied with varying factors. Such corrections apply use a uniform trim on all correctors of $\approx +2.5K_4$. Figure 5.20 shows a comparison of the resulting RDT with those corrections at factors $-10, -4, -1$ and 0 .

Table 5.9 shows the RMS of the amplitude of this RDT for the various configurations. Similar to the shift observed when powering the landau octupoles in simulations, the shift is of one order of magnitude between factors -0 and -10 . Measurements with landau octupoles were also attempted but losses made it impossible to obtain high enough amplitudes to correctly measure the RDT.

Factor	RMS $ f_{1004} $
-10	37,308,159
-4	6,721,270
0	3,533,796
-1	2,333,384

Table 5.9.: RMS of $|f_{1004}|$ depending on the factor of the Q'' corrections.

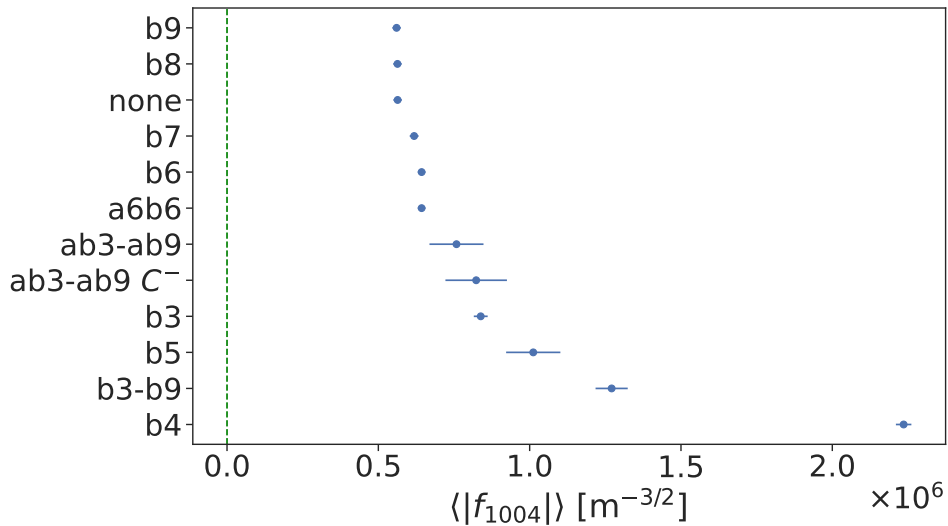


Figure 5.19.: Simulation of the amplitude of the decapolar RDT f_{1004} depending on the field errors applied on main dipoles as well as coupling (C^-). While it is apparent that some multipolar errors drive the resonance higher, some combinations actually seem to cancel each other.

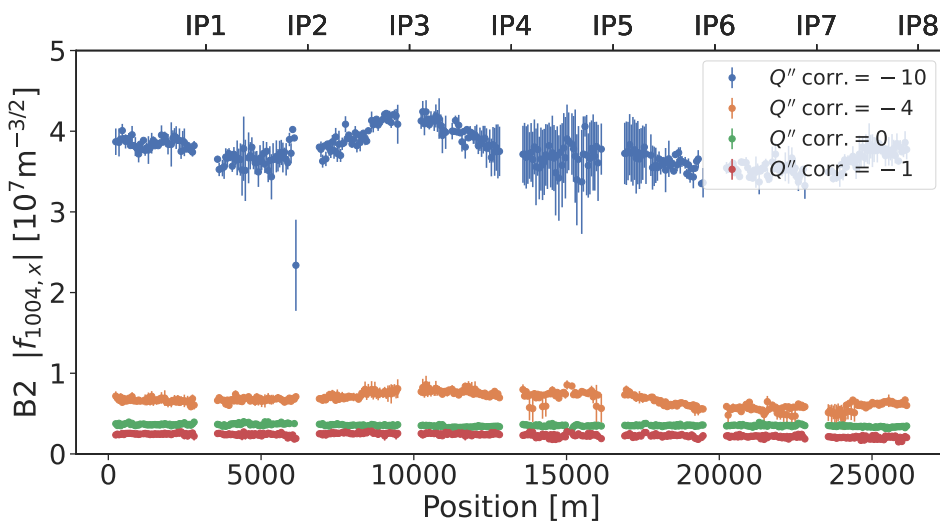


Figure 5.20.: Shift of the decapolar RDT f_{1004} depending on the factor applied on octupolar corrections for Q'' .

Simulated and observed large shifts due to octupoles are relevant to the operation of the LHC, as resonances can be greatly deteriorated, especially when powering landau octupoles. A better understanding of the interaction between Landau octupoles and octupolar correctors could lead to improved corrections in not only octupolar but also decapolar fields in the future.

5.6.3. Feed-Down Contributions

To produce collisions at top energy, *crossing angles* are introduced via the orbit correctors located in the triplets, before the separation dipoles and the matching section of the interaction regions (MCBX, MCBY and MCBC) [67]. Those collisions happen with a small β^* , currently 30cm, requiring strong quadrupolar fields from the triplets.

At such β , those triplets also generate strong dodecapolar field errors. Because of the crossing-angles, feed-down appears and lower-order fields can be observed. Such feed-down to decapolar fields was observed during the first commissioning of Run 3, in 2022 [68]. Figure 5.21 shows how the RDT f_{1004} , normally affected by decapoles, varies with the application of crossing angles.

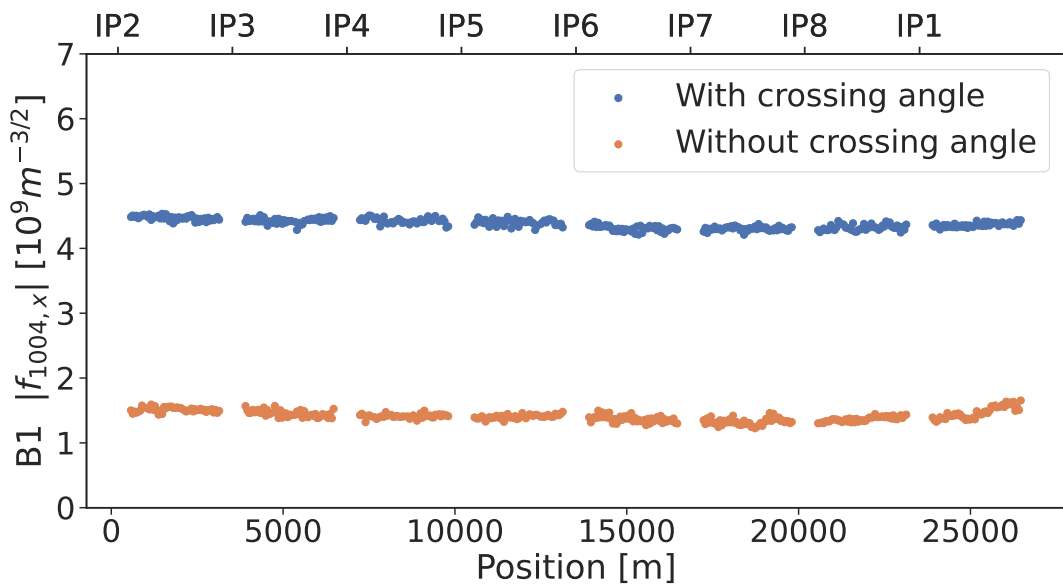


Figure 5.21.: Varying amplitude of the decapolar RDT f_{1004} at top energy depending on the activation or not of the crossing angle at the IP. Offsets in orbit create feed-down from higher orders.

Such a contribution is though not expected at injection energy, as the triplets aren't powered a much as at top energy, β^* being set at around 10m.

5.7. Summary

This chapter examines the role of decapolar perturbations in the Large Hadron Collider (LHC) at injection energy. First is addressed the previously observed discrepancy between measurements and model regarding the third-order chromaticity. To investigate these issues, various measurements and simulations were conducted. By introducing novel observables, such as the bare chromaticity and,

for the first time, chromatic amplitude detuning, a clearer understanding of these discrepancies was achieved. Simulations indicate that the decay of the decapolar component in the main dipoles is a major factor contributing to the discrepancies.

For the first time at injection energy, measurements and corrections of the decapolar Resonance Driving Term (RDT) f_{1004} were carried out. Further simulations and measurements explored how sextupoles and octupoles interact to create decapolar-like fields. The findings revealed that sextupoles, both alone and in combination with Landau octupoles, generate substantial decapolar RDTs during machine operation that could benefit from corrections.

Applying combined corrections for third-order chromaticity, chromatic amplitude detuning, and the RDT f_{1004} led to a 3% improvement in beam lifetime. Additionally, a broader impact of decapolar RDTs on beam stability was investigated. Specifically, intentionally degrading the RDT f_{1004} resulted in a decrease in beam lifetime of about 10%. Furthermore, a significant improvement in the forced dynamic aperture during AC-Dipole excitation was observed when corrections were applied. The earlier corrections for decapolar fields were implemented alongside octupolar corrections for Q'' . Figure 5.22 demonstrates the relative losses encountered when kicking at different amplitudes with the AC-Dipole. This clearly shows that octupolar and decapolar corrections enhance the forced dynamic aperture.

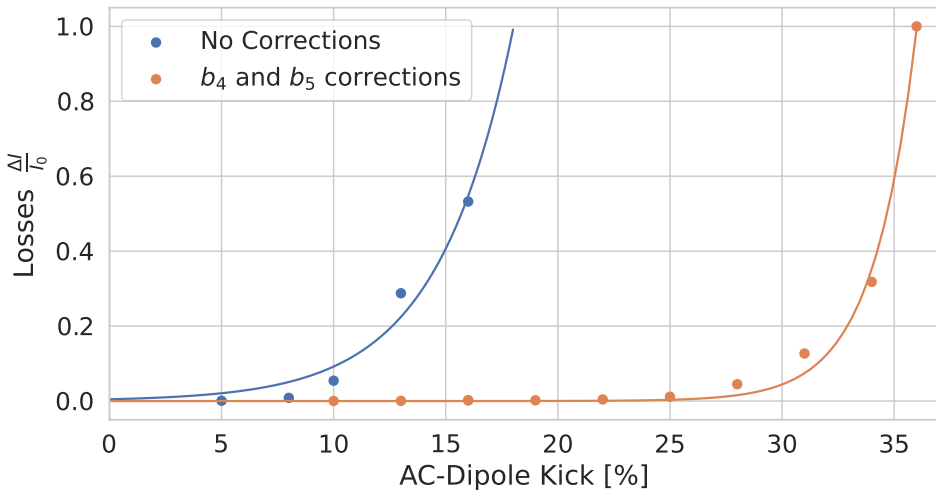


Figure 5.22.: Relative losses experienced with AC-Dipole kick amplitude with and without corrections pertaining to Q'' , Q''' , chromatic amplitude detuning, and RDT f_{1004} .

This underscores the importance of these corrections for stable beam operation and suggests that further advancements in correction methods could lead to even greater improvements.

Higher Order Fields

6.1. Introduction

Beam-based high order field measurements have been carried out in the LHC since its first Run [54, 59], via chromaticity studies. Those measurements, made by varying the RF frequency while observing the resulting tune change, have been performed with a momentum offset of up to $\delta = \pm 2.2 \times 10^{-3}$, which led to the observation of the third order term of the non-linear chromaticity.

During the commissioning of Run 3 in 2022, a new collimator sequence has been introduced, allowing wider momentum offset measurements, within $\delta \in [-3.2 \times 10^{-3}, 3.7 \times 10^{-3}]$. This improved setup led to the observation of the fourth and fifth order terms at injection energy. Those terms, denoted $Q^{(4)}$ and $Q^{(5)}$ respectively in Eq. (6.1), are produced to first order by dodecapoles and decatetrapoles. Dodecapoles being powered off at injection and decatetrapoles being absent from the lattice, those fields originate from the field errors of the various magnets installed in the LHC.

$$Q(\delta) = Q_0 + Q'\delta + \frac{1}{2!}Q''\delta^2 + \frac{1}{3!}Q'''\delta^3 + \frac{1}{4!}Q^{(4)}\delta^4 + \frac{1}{5!}Q^{(5)}\delta^5 + \mathcal{O}(\delta^6). \quad (6.1)$$

In addition to completing the measurements of high-order fields through chromaticity scans, turn-by-turn measurements were also conducted. High amplitude kicks indeed made it possible to observe dodecapolar RDTs in the LHC for the first time. Such fields were never before observed directly, but rather only via feed-down to amplitude detuning [10].

6.2. Chromaticity

6.2.1. Procedure

As described in Section 3.2.3, the momentum offset δ is related to the RF frequency and the momentum compaction factor. This relation is given as a simplified form in Eq. (6.2). The model α_c for the LHC injection optics is 3.48×10^{-4} for beam 1 and 3.47×10^{-4} for beam 2. Via this relation, a change of 140Hz of the RF frequency corresponds to a momentum offset of about -0.001 .

$$\delta = -\frac{1}{\alpha_c} \cdot \frac{\Delta f_{RF}}{f_{RF,nominal}}. \quad (6.2)$$

To properly characterize higher orders of the chromaticity function and ensure quality measurements, several steps are required. The tune measured during chromaticity scans can exhibit jitter and resonance lines may appear, requiring thorough data cleaning to either reject problematic data points or reduce error bars. The simplified Eq. (6.2), describing δ , has been sufficient for reliably measuring up to the third order chromaticity. However, this relation also needs verification.

Noise and Spectral Lines

Noise lines, due to electronics, can be seen in the raw data obtained from the BBQ tune system. Occasionally, when those resonances are strong, their frequency peak can be mistaken as the tune and logged as such by the system. This yield large uncertainties in the measurement when data points can't properly be classified as outliers. A tune measurement presenting this issue is showed in Fig. 6.1.

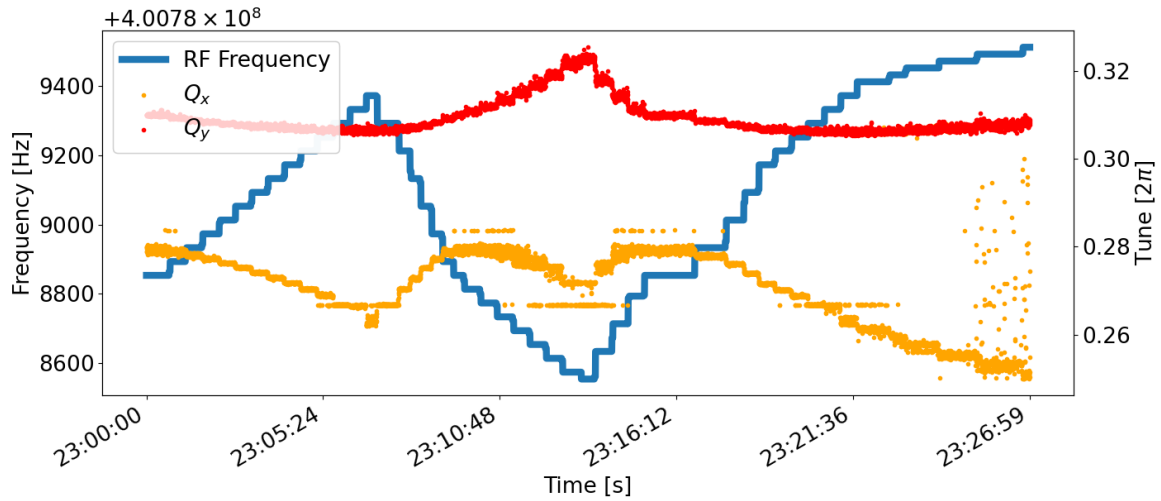


Figure 6.1.: Shift of the tune by variation of the RF. Noise lines can appear in some cases, making the tune error bar large or downright unusable.

A solution to this issue is to use the raw data extracted from the BBQ system. From there, a spectrogram clearly shows the noise lines, as seen in Fig. 6.2. Those lines have been repeatedly identified over several measurements and confirmed to be fixed. The highest peak in the spectrogram can be reliably identified by removing unwanted resonances, resulting in a cleaner measurement. It is also important to note that the BBQ system requires the tune window to be set, which, if overlooked, can lead to erroneous data. By analyzing the raw data, it is ensured that correct data is used, preventing the measurement from inadvertently capturing noise.

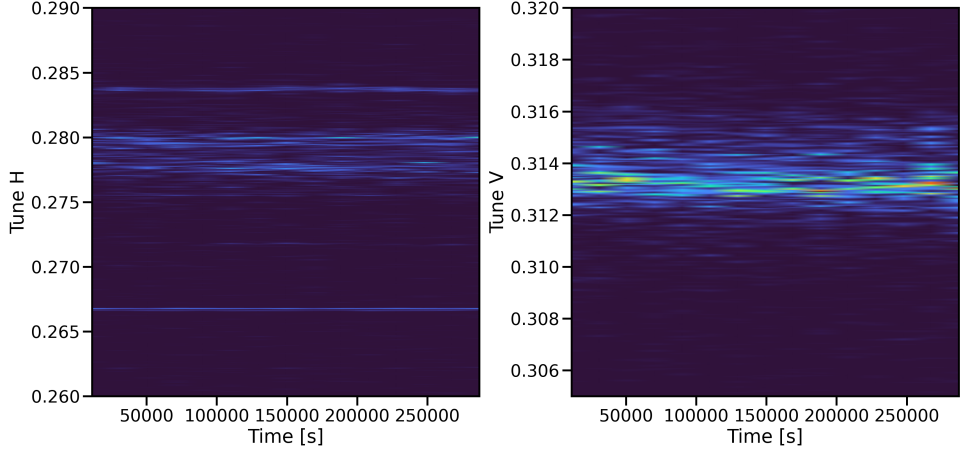


Figure 6.2.: Tune spectrogram obtained via BBQ system. Strong resonance lines can be seen above and below where the tune really is, causing the wrong frequency peak to be identified as the tune.

Momentum Compaction Factor

Rather than a constant, the momentum compaction factor can be expressed as an expansion, as detailed in Section 2.5.1. The first terms are given by the following,

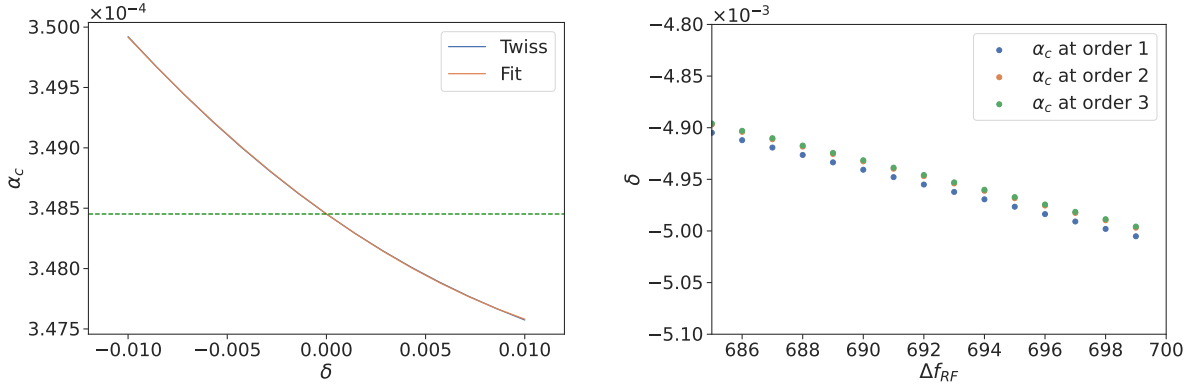
$$\alpha_c = \underbrace{\alpha_{c,0}}_{\text{1st order}} + \underbrace{\alpha_{c,1}\delta}_{\text{2nd order}} + \underbrace{\alpha_{c,2}\delta^2}_{\text{3rd order}}. \quad (6.3)$$

The expression for δ at first and second order then reads,

$$\begin{aligned} \delta &= -\frac{\Delta f_{RF}}{\alpha_0 f_{RF}} && \Rightarrow \text{Order 1} \\ \delta &= \frac{-\alpha_0 f_{RF} + \sqrt{f_{RF} (-4\Delta f_{RF}\alpha_1 + \alpha_0^2 f_{RF})}}{2\alpha_1 f_{RF}} && \Rightarrow \text{Order 2} \end{aligned} \quad (6.4)$$

The momentum compaction factor is computed using MADX at discrete δ values and then fitted, as shown in Fig. 6.3. Its non-linearity is clearly evident. The effect of this non-linearity on the calculated δ via the RF frequency is also presented. Field errors have not been found to have any significant impact on the α_c values.

It is observed that while clearly depending on higher orders, the momentum compaction factor only has a small impact on the calculated δ . Figure 6.4 shows a real-life measurement, comparing the fit of the chromaticity function with various δ , computed up to the third order of α_c .



(a) Non-linear fit of α_c obtained via an evaluation at discrete δ in MAD-X. The green line represents a constant $\alpha_c = \alpha_{c,0}$.

(b) Divergence of the momentum offset when considering higher α_c orders with large RF trims.

Figure 6.3.: Non linearity of α_c and its effect on the computed δ via RF trims. The simulations are done at injection energy of 450GeV.

The fit of the chromaticity function is barely impacted when considering the higher orders of the momentum compaction factor. The different orders of the chromaticity are collected in Table 6.1. The higher order terms of α_c can thus be neglected and are not a source of higher chromaticity orders.

Chromaticity	α_c order		
	1	2	3
$Q^{(1)}$	2.52 ± 0.03	2.53 ± 0.03	2.53 ± 0.03
$Q^{(2)}$	-3.04 ± 0.05	-3.05 ± 0.05	-3.05 ± 0.05
$Q^{(3)}$	-4.75 ± 0.03	-4.75 ± 0.03	-4.75 ± 0.03
$Q^{(4)}$	-0.33 ± 0.07	-0.32 ± 0.07	-0.32 ± 0.07
$Q^{(5)}$	2.33 ± 0.06	2.36 ± 0.06	2.36 ± 0.06

Table 6.1.: Chromaticity values obtained for the same measurement, depending on the order of the momentum compaction factor taken into account.

Momentum Offset from Orbit

During machine operation, the momentum offset, derived from the orbit, used to be logged on the servers. It was then possible to directly compute the chromaticity that way without having to use the RF and the momentum compaction factor. In 2016, measurements of the non-linear chromaticity were performed using the former method. Figure 6.5 shows a comparison of the obtained non-linear chromaticity from both methods, while Table 6.2 shows a numerical comparison. Results being similar,

6. Higher Order Fields

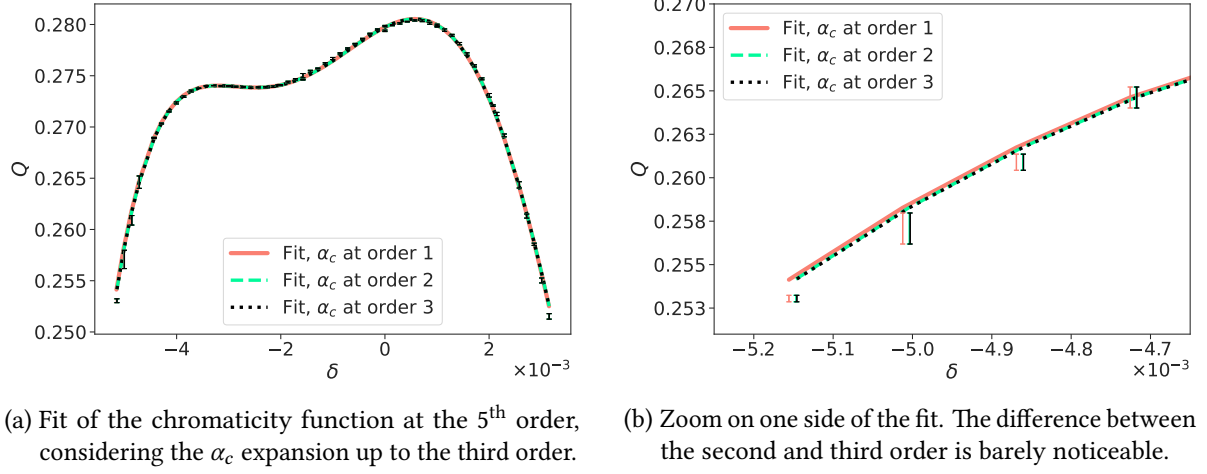


Figure 6.4.: Fit of the chromaticity function considering several α_c orders.

is it deemed that both methods are reliable to measure the non-linear chromaticity in the LHC.

Plane	δ via RF		δ via orbit	
	$Q''[10^3]$	$Q'''[10^6]$	$Q''[10^3]$	$Q'''[10^6]$
Beam 1				
X	-0.64 ± 0.01	3.00 ± 0.04	-0.62 ± 0.01	2.91 ± 0.04
Y	-0.17 ± 0.01	-2.12 ± 0.04	-0.14 ± 0.01	-2.09 ± 0.04
Beam 2				
X	-1.18 ± 0.02	2.89 ± 0.06	-1.23 ± 0.03	3.13 ± 0.11
Y	0.18 ± 0.02	-1.95 ± 0.05	0.20 ± 0.02	-2.02 ± 0.06

Table 6.2.: Comparison of the chromaticity values obtained for the same measurement via two different methods to acquire δ .

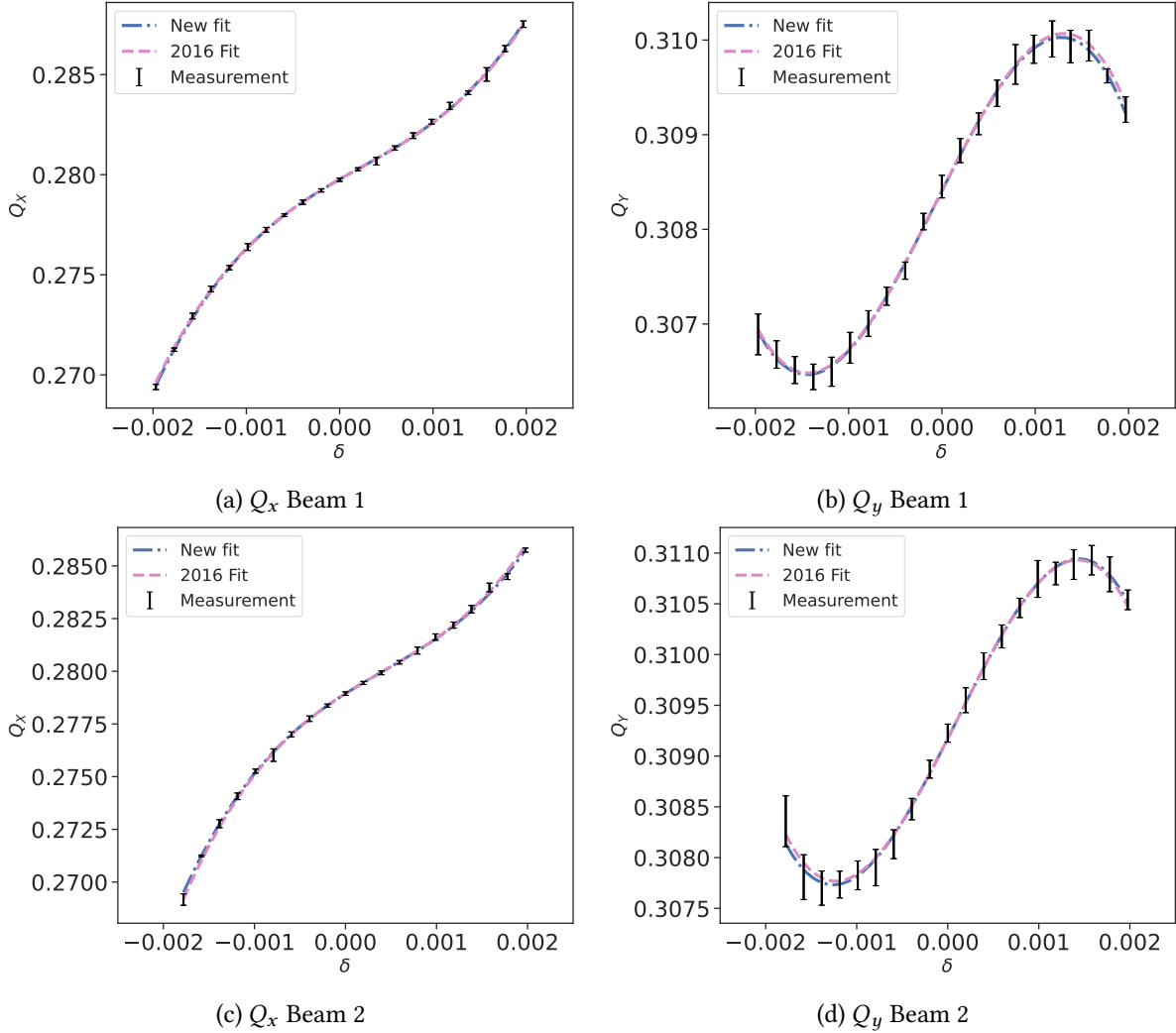


Figure 6.5.: Comparison of the non-linear chromaticity fit obtained from the computed momentum offset via the RF in 2022 and from the logged values in 2016.

6.2.2. Measurements

In order to assess the correctness of the observation of higher chromaticity orders, measurement repeatability is needed. Two measurements were thus taken in 2022, with different configurations pertaining to the correction of the second and third order chromaticities Q'' and Q''' . The first one used the nominal correction strengths for octupole and decapole corrector magnets, derived from magnetic measurements, where the second one used beam-based corrections for the same elements, computed from the previous measurement. More measurements were taken during 2024's commissioning

6. Higher Order Fields

with new optics for the same reasons, to minimize the second and third order chromaticities. Three measurements were taken: with nominal corrections, after having corrected Q''' and then Q'' . The introduced new optics mainly changed the powering of the triplets at the IPs and are not expected to have a considerable impact on the chromaticity.

Table 6.3 shows a summary of those measurements with their respective achieved momentum offset ranges. While the 2024 measurements achieved greater ranges than the previous ones, those were restricted during analysis to allow suitable comparisons.

Number	Year	Corrections	δ min. [$\times 10^{-3}$]	δ max. [$\times 10^{-3}$]
1	2022	Nominal	-3.15	3.01
2	2022	Q'' & Q'''	-3.15	3.72
3	2024	Nominal	-5.15	3.15
4	2024	Q'''	-3.44	4.87
5	2024	Q'' & Q'''	-3.86	4.44

Table 6.3.: Performed chromaticity measurements with their respective momentum offset ranges.

In order to stay consistent, the horizontal and vertical tunes were respectively set to $Q_x = 0.28$ and $Q_y = 0.31$ for both measurements. The linear chromaticity Q' is set to a small value, around 2, to avoid large tune shifts throughout the scan. All measurements were performed during LHC's beam commissioning, as part of the measurements and corrections performed after technical or long shutdowns.

First Observation

The first observation of higher order chromaticity was done with the octupolar and decapolar correctors *MCO* and *MCD* set to their nominal settings. Those are aimed at correcting Q'' and Q''' , as previously described in Chapter 5. Results of this initial measurement are shown in Table 6.4. Lower order chromaticities such as Q' and Q'' are consistent with measurements done during the previous Run [60].

Due to the RF-scan method, the momentum offset crosses zero several times during the measurement. Negligible change in tune at this point makes it possible to determine that the tune drift through the measurement is of no consequence. This measurement was performed after an extended period at injection energy, where the decay of the sextupolar fields is small and not causing any change in the first order chromaticity. The fitted curve for the chromaticity function is shown in Fig. 6.6. It is clear that a higher order polynomial is beneficial to the fit, as discussed further in ??.

Plane	$Q^{(2)} [10^3]$	$Q^{(3)} [10^6]$	$Q^{(4)} [10^9]$	$Q^{(5)} [10^{12}]$
Beam 1				
X	-2.44 ± 0.02	-3.36 ± 0.04	-0.56 ± 0.02	1.20 ± 0.07
Y	0.97 ± 0.02	1.62 ± 0.05	0.15 ± 0.03	-0.88 ± 0.09
Beam 2				
X	-2.45 ± 0.03	-2.72 ± 0.08	-1.00 ± 0.05	0.15 ± 0.14
Y	0.79 ± 0.03	1.54 ± 0.06	0.24 ± 0.04	-0.74 ± 0.13

Table 6.4.: Terms of the high order chromaticity obtained during Run 3's commissioning in 2022, with nominal corrections.

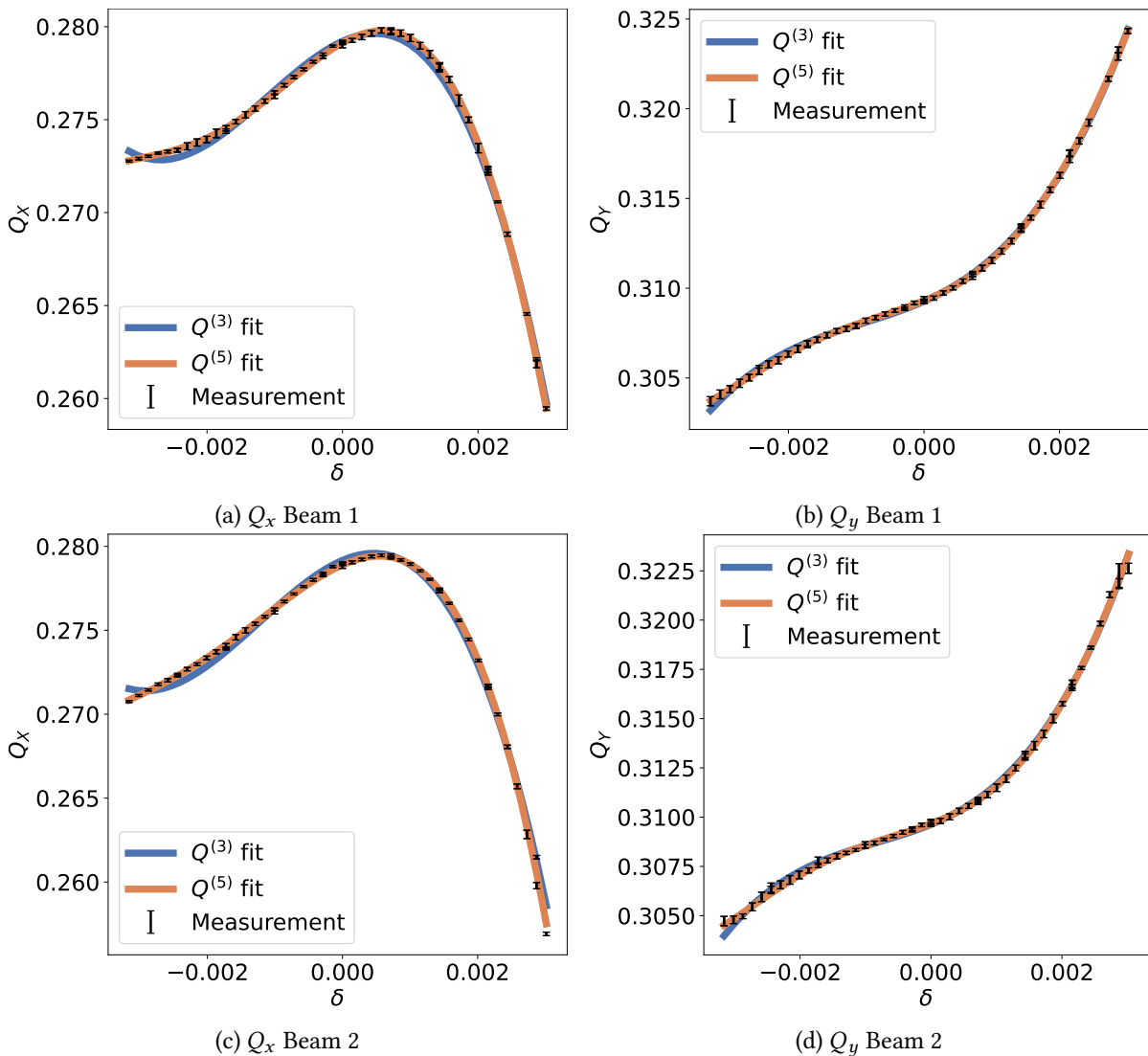


Figure 6.6.: Measurement of higher order chromaticity terms with nominal corrections used during operation. Fits are up to the third and fifth order.

6. Higher Order Fields

Previous studies of chromaticity in the LHC only considered fits up to the third order. Expanding the fits to the fifth order increases the Q''' estimate and improves the fit quality. Accurately measuring the third order chromaticity is essential for its correction, making it important to consider the higher orders.

The reduced chi-square for this measurement of 2022 for each fit order is detailed in Table 6.5. While adding terms to the chromaticity function is beneficial to the fit, it can be seen that the reduced chi-square does not substantially improve above the fifth order, indicating that such further orders are not warranted.

Plane	$Q^{(3)}$	$Q^{(4)}$	χ^2_v	$Q^{(5)}$	$Q^{(6)}$
Beam 1					
X	17.9	12.1	1.8	1.5	
Y	3.0	2.2	0.7	0.7	
Beam 2					
X	17.3	7.1	1.8	1.8	
Y	2.9	2.8	1.0	1.0	

Table 6.5.: Reduced χ^2 values for each order of fit, taken from the second measurement of 2022, with Q'' and Q''' beam-based corrections.

Varying Configurations

The five previously introduced measurements were performed with very different configurations for the octupolar and decapolar correctors. Table 6.6 shows the strengths applied on every circuit for each correction scheme, in 2022. The correction is called *global* as all correctors are trimmed uniformly. The 2024 corrections are similar in order of magnitude. Figure 6.7 shows the measurements and fit of some of these measurements, to highlight their differences.

Beam	$K_4 [\text{m}^{-4}]$	$K_5 [\text{m}^{-5}]$
1	+3.2973	+1610
2	+2.1716	+1618

Table 6.6.: Corrections applied on top of the nominal octupolar and decapolar correctors strengths in 2022 for the Q'' and Q''' corrections.

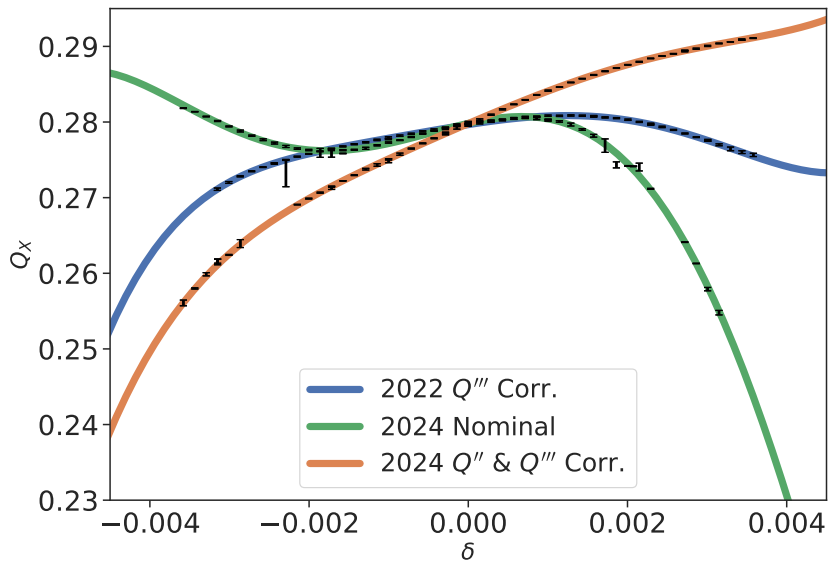


Figure 6.7.: Selection of horizontal chromaticity measurements performed with varying configurations of the octupolar and decapolar correctors for Beam 1 during the commissionings of 2022 and 2024.

A summary of the measured chromaticity orders is given in Table 6.7. The first measurement in the horizontal plane of Beam 2 showed a high correlation between $Q^{(4)}$ and $Q^{(5)}$, making the fit less reliable and is not included. The last measurement for the vertical plane experienced some tune drift, making the fit impossible and is therefore not included for both beams.

6. Higher Order Fields

Axis	Meas.	Q''	Q'''	$Q^{(4)}$	$Q^{(5)}$
Horizontal					
Beam 1	1	-2.44 ± 0.02	-3.37 ± 0.04	-0.56 ± 0.02	1.21 ± 0.07
	2	-0.61 ± 0.01	-1.00 ± 0.03	-0.62 ± 0.02	1.19 ± 0.05
	3	-2.01 ± 0.05	-4.49 ± 0.10	-0.58 ± 0.07	1.34 ± 0.18
	4	-1.46 ± 0.03	-0.29 ± 0.06	-0.43 ± 0.04	1.09 ± 0.10
	5	-0.33 ± 0.01	-0.31 ± 0.03	-0.59 ± 0.01	0.75 ± 0.04
	Avg.			-0.56 ± 0.07	1.12 ± 0.20
Beam 2	2	-0.85 ± 0.01	-0.66 ± 0.03	-0.57 ± 0.02	1.09 ± 0.06
	3	-2.93 ± 0.05	-4.40 ± 0.08	-0.53 ± 0.08	1.66 ± 0.16
	4	-2.21 ± 0.02	-0.00 ± 0.03	-0.46 ± 0.02	1.18 ± 0.05
	5	-0.53 ± 0.02	-0.09 ± 0.03	-0.57 ± 0.02	0.98 ± 0.05
	Avg.			-0.53 ± 0.04	1.23 ± 0.26
Vertical					
Beam 1	1	0.97 ± 0.02	1.62 ± 0.05	0.15 ± 0.03	-0.88 ± 0.09
	2	-0.23 ± 0.01	0.13 ± 0.02	0.09 ± 0.02	-0.60 ± 0.03
	3	0.83 ± 0.02	1.97 ± 0.03	0.29 ± 0.02	-0.68 ± 0.05
	4	0.62 ± 0.01	-0.18 ± 0.03	0.00 ± 0.02	-0.56 ± 0.05
	Avg.			0.13 ± 0.11	-0.68 ± 0.12
Beam 2	1	0.79 ± 0.03	1.54 ± 0.06	0.24 ± 0.04	-0.74 ± 0.13
	2	-0.29 ± 0.01	0.10 ± 0.02	0.13 ± 0.02	-0.58 ± 0.04
	3	0.89 ± 0.02	2.05 ± 0.03	0.32 ± 0.03	-0.73 ± 0.06
	4	0.60 ± 0.02	-0.14 ± 0.03	0.04 ± 0.02	-0.66 ± 0.05
	Avg.			0.18 ± 0.11	-0.68 ± 0.06

Table 6.7.: Summary of the chromaticity values obtained from the measurements presented in Table 6.3.

6.3. Model Estimates

The model of the LHC is based on MADX and magnetic field error tables [16], containing a hundred seeds for the random errors. To compute the chromaticity, simulations are run via PTC, with selected field errors. Field errors are applied to all magnets, with b_2 errors in the main dipoles generating a β -beating of approximately 10%. Coupling is introduced using global knobs to create a C^- value of 0.001, which is commonly observed during operation.

Simulations with various field errors have been run to assess the contribution of individual magnet order and combinations for the fourth and fifth order chromaticity. Normal and skew fields errors ranging from sextupolar (b_3) to decahexapolar (b_8) are added alone or in combination to observe which is the strongest. Quadrupolar field errors (b_2) introduce beta-beating. Coupling is introduced via skew quadrupolar correctors.

Fourth Order Chromaticity

The results from simulations strongly imply that the dodecapolar errors are the main contributors to $Q^{(4)}$, as can be seen in Fig. 6.8. The most notable effect on this chromaticity order is the beta-beating, introducing a very large spread via the various error seeds. Comparing the simulation at the top with most errors added, the b_6 component alone accounts for $\approx 70\%$ of it for both axes on each beam.

6. Higher Order Fields

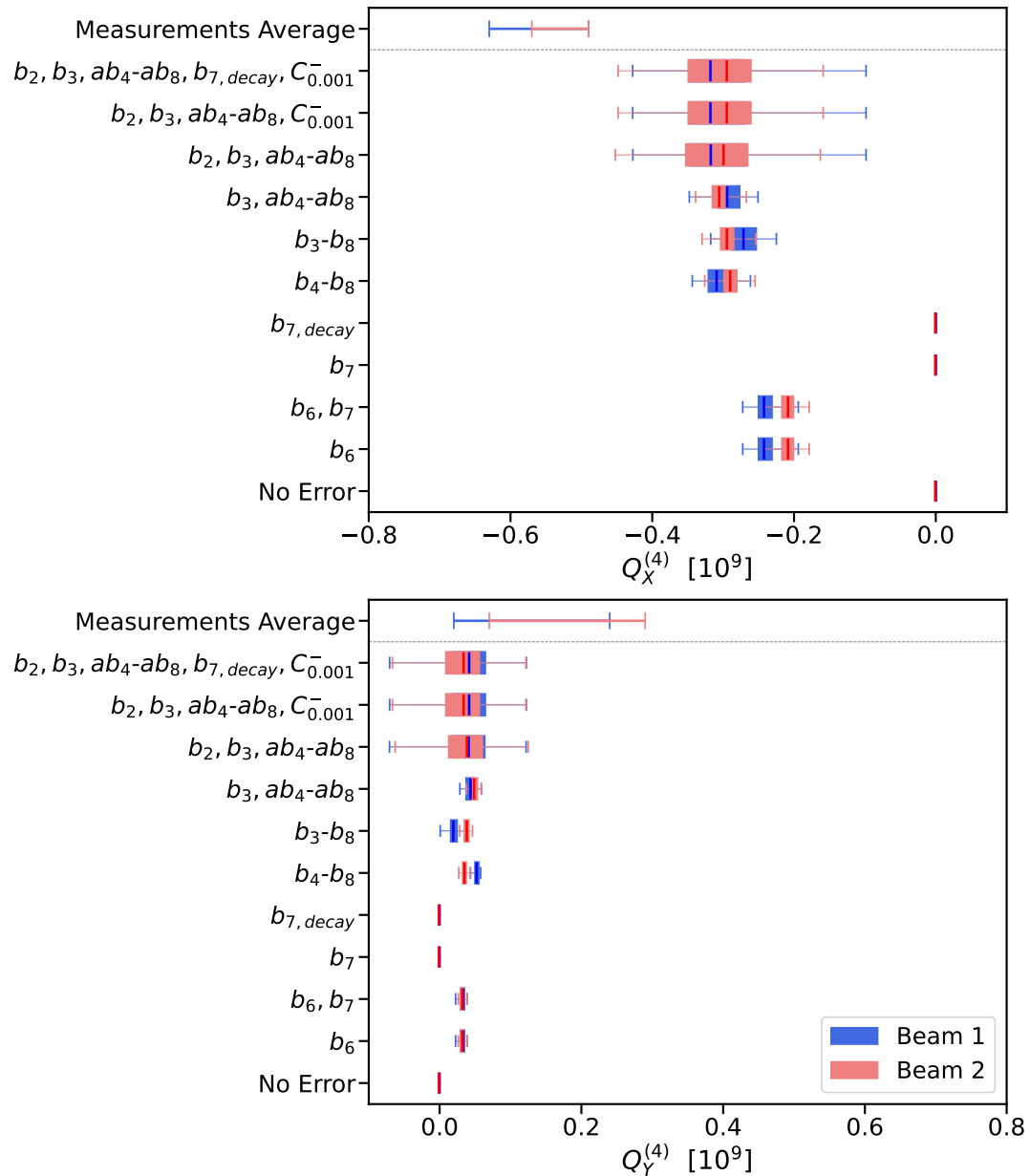


Figure 6.8.: Measured and simulated fourth order chromaticity with different multipole errors. The b_2 errors, applied on dipoles and quadrupoles, generate beta-beating. Coupling is set to a value commonly seen in operation.

Fifth Order Chromaticity

It is seen that the decatetrapolar errors are the main contributors to $Q^{(5)}$, as can be seen in Fig. 6.9. Fringe fields and skew multipoles have been found to have a negligible impact. Beta-beating and coupling are seen to increase by a small amount the chromaticity, while sextupolar errors induce a spread with the different seeds. Comparing the simulation at the top with most errors added, the b_7 component alone accounts for $\approx 70\%$ of it for both axes on each beam of the fifth order chromaticity.

It has been noted in the previous chapter about decapoles (see Section 5.5) that the b_5 component in the main dipoles was large at injection energy, and could explain most of the discrepancy between the measurements and simulations. Such a decay in the main dipoles also exists for the b_7 component [69], and is shown in Fig. 6.10.

Its value is though small and settles around $+0.0351 \pm 0.0007$. The average b_7 of the main dipoles is of 0.32 ± 0.16 . The decay thus increase that value of only about 11%. Simulations done with that decay taken into account are also present in the previous Fig. 6.9.

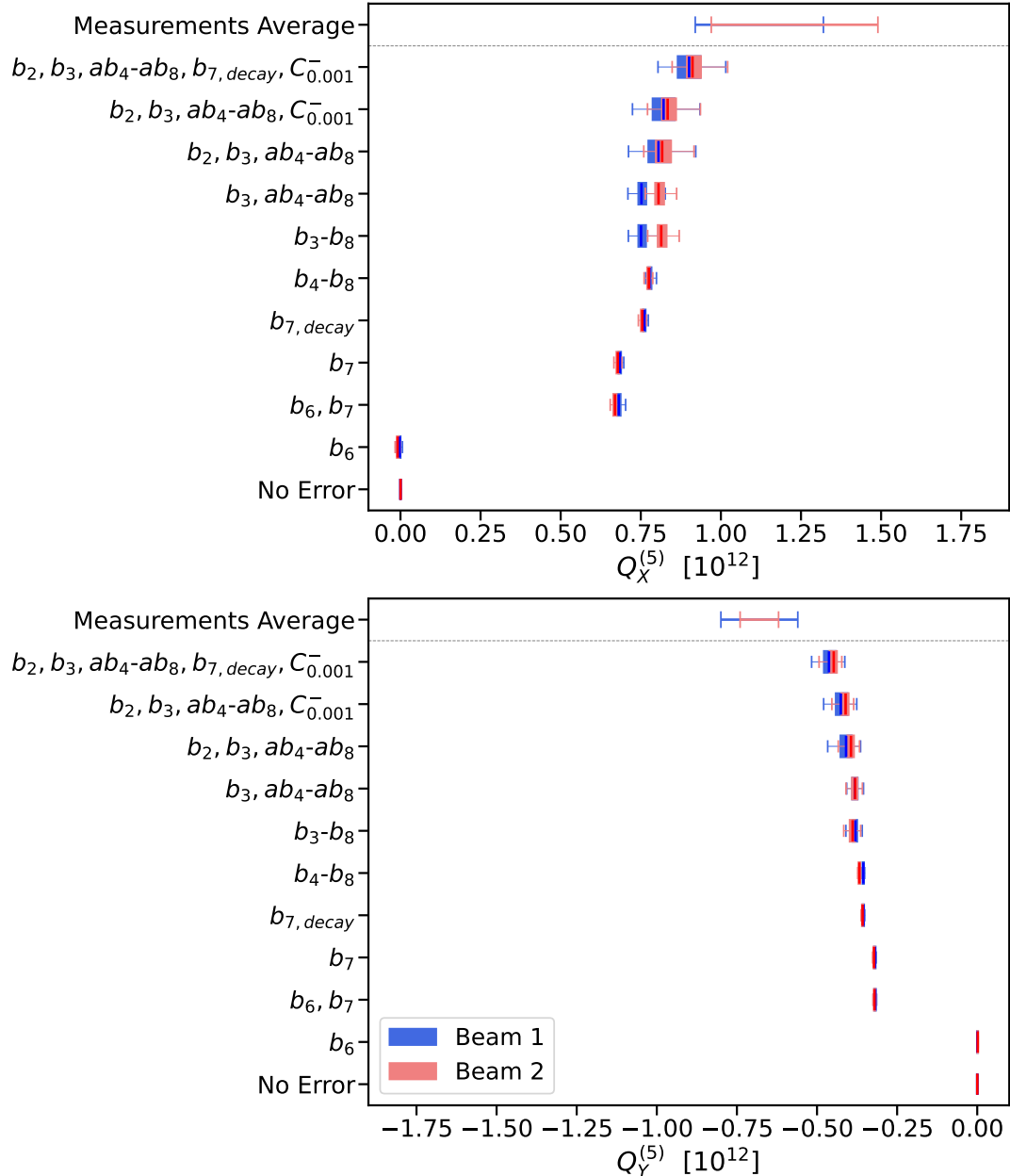


Figure 6.9.: Measured and simulated fifth order chromaticity with different multipole errors. The b_2 errors, applied on dipoles and quadrupoles, generate beta-beating. Coupling is set to a value commonly seen in operation.

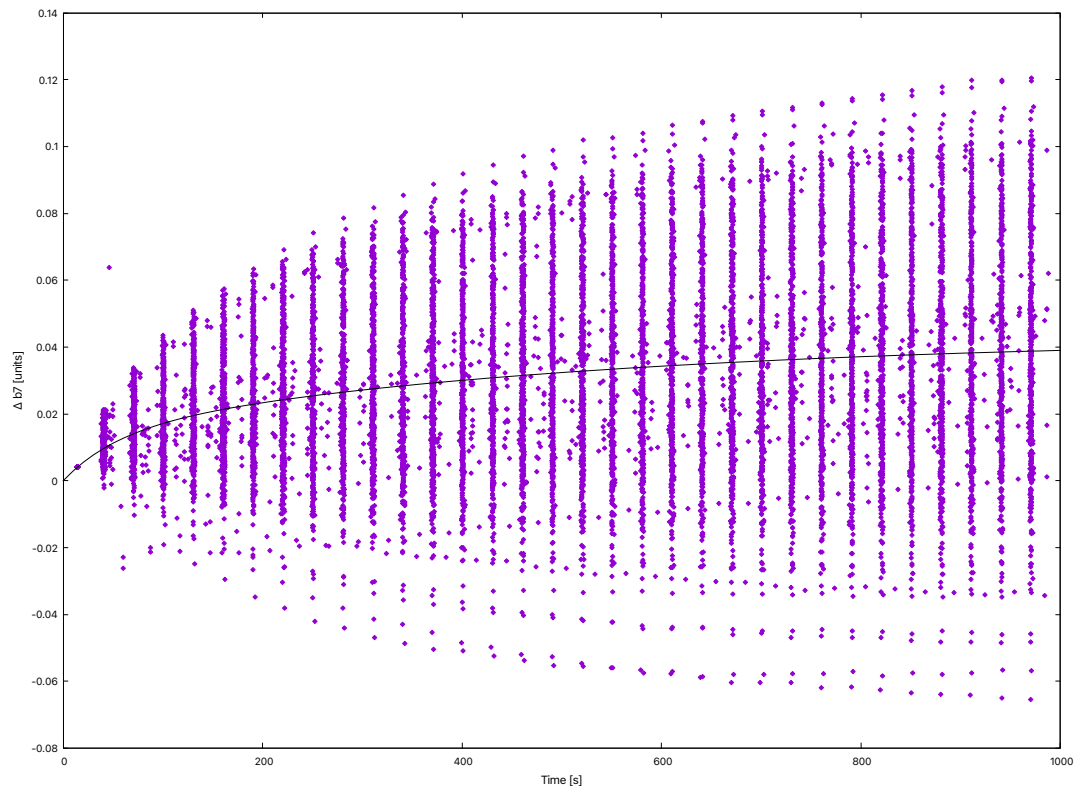


Figure 6.10.: Measured decay of the integrated decatetrapolar field in LHC's main dipoles at injection energy. The fit is shown in black [69] and settles around +0.035.

Agreement with Measurements

Previous simulation results are shown in Table 6.8, taking the values from the simulation including the most effects at the top of the plots. For the fourth order, the beating is not included as the large beating is not yet explained. Table 6.9 shows the ratio between the measured average and simulated chromaticities.

Plane	$Q^{(4)} [10^9]$	$Q^{(5)} [10^{12}]$
Beam 1		
X	-0.29 ± 0.02	0.90 ± 0.05
Y	0.04 ± 0.01	-0.46 ± 0.03
Beam 2		
X	-0.31 ± 0.02	0.92 ± 0.03
Y	0.05 ± 0.00	-0.45 ± 0.01

Table 6.8.: Simulated high order chromaticity terms via PTC at injection energy, including normal and skew sextupolar to decahexapolar field errors. Are also included beta-beating, coupling and decatetrapolar decay. For the fourth order, the values do not include beta-beating as the observed spread is not yet fully understood.

Plane	$Q^{(4)}$ Ratio	$Q^{(5)}$ Ratio
Beam 1		
X	1.91 ± 0.28	1.24 ± 0.23
Y	3.00 ± 2.60	1.47 ± 0.27
Beam 2		
X	1.74 ± 0.16	1.34 ± 0.29
Y	3.70 ± 2.30	1.51 ± 0.14

Table 6.9.: Ratios of the simulated and average measured high-order chromaticity terms. The values are taken from Table 6.7 and Table 6.8.

The similar ratios between planes and beams for the fifth order could indicate a systematic error not modeled. The large differences observed for the fourth order are not yet explained but the difference between planes could be linked to a shift induced by the decapolar corrections in the vertical plane. It indeed seems that the fourth order follows a trend with the third order.

6.4. Dodecapolar RDT

During the commissioning of 2024, resonance driving terms measurements were performed by kicking the beam at various strengths with the AC-Dipole at injection energy. Those measurements were

intended to measure several RDTs with a focus on decapoles and their associated corrections. Kicks were performed using the nominal settings for octupolar and decapolar correctors, first with Q'' corrections and then with additional Q'' corrections applied. A distinct line in the vertical spectrum was observed at $5Q_y$, as shown Fig. 6.11. This line is contributed to by dodecapolar fields (see Appendix C) and is proportional to the vertical oscillation amplitude.

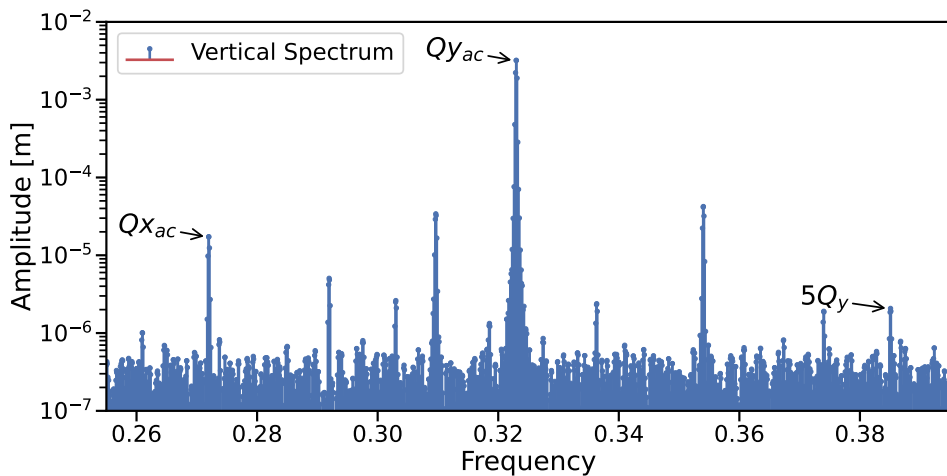


Figure 6.11.: Vertical spectrum of recorded turn-by-turn data for Beam 1 showing the tunes driven by the AC-Dipole along with a line contributed to by dodecapolar fields.

To achieve these measurements, the kick strength of the AC-Dipole was set up to 40% of its maximum, made possible by the newly introduced collimator sequence. The specific excited resonance of the observed line is the $6Q_y$, related to the RDT f_{0060} . Figure 6.12 highlights the real part of this RDT taken with nominal corrections and the repeatability of the measurement at varying kick strengths. The RMS of the amplitude of these kicks is of $3.5 \cdot 10^8$

Similar to the decapoles discussed in Section 5.6.2, the dodecapolar RDTs can be influenced by lower-order components, as shown in Table A.3. At the second-order BCH, a combination of sextupoles and decapoles, as well as a combination of octupoles, generate a decapolar-like field. At the third and fourth orders, these fields are respectively generated by a combination of sextupoles with octupoles and by sextupoles. Several tracking simulations were performed with various combinations of field errors, ranging from normal and skew sextupoles (a, b_3) to decaoctupoles (a, b_9), including as well coupling. Beta-beating is not included as b_2 errors also have an effect on the phase. Figure 6.13 shows the RMS amplitude of the RDT f_{0060} for each of these simulations. As expected from the analytical equations, the lower-order multipoles do contribute to this RDT and seem to cancel the b_6 component. It is though apparent that Beam 1 and Beam 2 do not have the same contributions from the dodecapolar errors. These seem to be compensated by other field errors for Beam 1.

6. Higher Order Fields

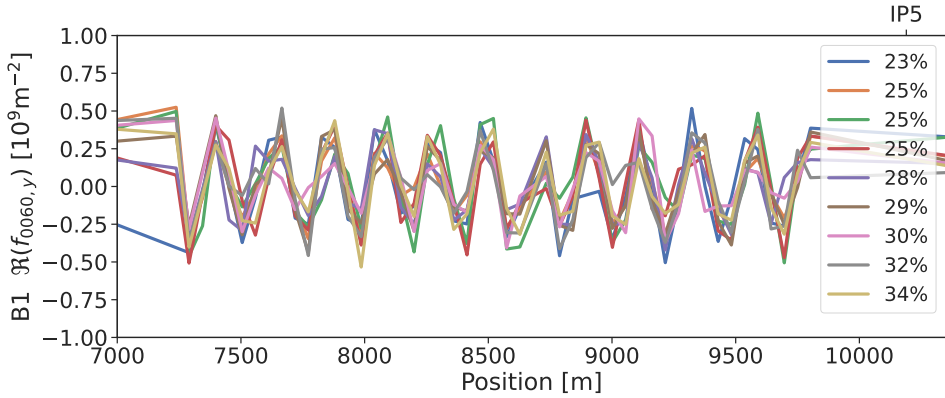


Figure 6.12.: Real part of the dodecapolar RDT f_{0060} measured with several kick strengths. The RMS amplitude is of $3.5 \cdot 10^8$.

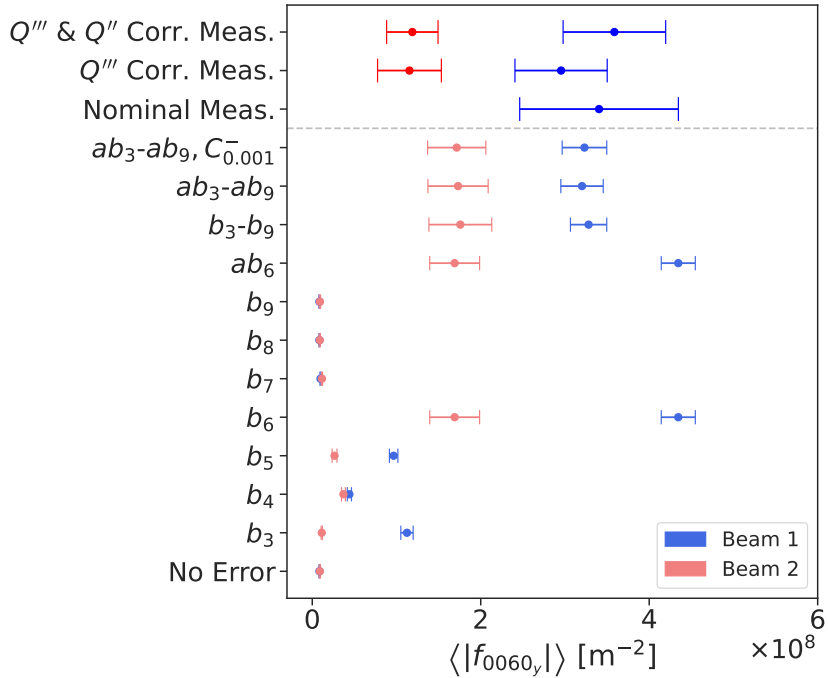


Figure 6.13.: Measured and simulated RDT f_{0060} with various normal and skew field errors. Coupling is set to a common value seen in operation.

The previously referenced measurements are also compared to these simulations. The measurement for Beam 2 with the nominal corrections could not be reliably exploited and is not included. The RDTs from these measurements are similar in amplitude, despite the different configurations for the octupolar and decapolar correctors. This suggests that, at these strength variations, the high-order

correctors do not significantly affect the dodecapolar RDT f_{0060} . It is however important to note that predicting the contributions from lower-order multipoles remains difficult.

6.5. Summary

This chapter explores the measurement and analysis of higher-order fields in the LHC at injection energy, with a focus on dodecapolar and decatetrapolar fields. Leveraging a newly implemented collimation setup and a custom post-processing technique, these higher-order fields have been successfully observed.

Chromaticity measurements were conducted with varying momentum offsets, revealing fourth and fifth-order terms $Q^{(4)}$ and $Q^{(5)}$. The repeated measurements consistently identified these higher-order terms, demonstrating their robustness. Measuring across such extended ranges and including higher orders is essential for accurately characterizing the lower orders. The analysis also shows that the primary contributors to these terms are dodecapolar and decatetrapolar fields, which originate from fields errors of the main dipoles.

For the first time, the dodecapolar Resonance Driving Term f_{0060} was measured. This measurement, repeated for both beams at different configurations, shows a good agreement with the model.

It is then concluded that further investigations could be conducted to address limitations in the measurement range of the chromaticity function and to refine estimates of higher-order chromaticity terms. Dodecapolar RDT studies could benefit from lifetime measurements accompanied by trims of the relevant correctors situated in the Interaction Regions (IRs). Additionally, investigating the impact of lower-order multipoles on the RDT would be valuable. Overall, gaining a thorough understanding of the higher-order field errors is essential for optimizing the LHC's performance.

SuperKEKB Studies

7.1. Introduction

KEK, or the High Energy Accelerator Research Organization (Kō Enerugi Kasokuki Kenkyū Kikō), is a Japanese institution operating the country's largest particle physics laboratory, located in Tsukuba. KEK provides particle accelerators and essential infrastructure for a wide range of research fields, including high-energy physics, material science, structural biology, and radiation science. One of its most notable facilities is SuperKEKB, the world's most advanced electron-positron collider. SuperKEKB is designed to reach an instantaneous luminosity of up to $80 \times 10^{34} \text{ cm}^{-2}\text{s}^{-1}$ and has recently completed its commissioning phase. It stores a 7 GeV electron beam in the High-Energy Ring (HER) and a 4 GeV positron beam in the Low-Energy Ring (LER), which collide at a single interaction point where the Belle II experiment is conducted. SuperKEKB currently holds the world record for instantaneous luminosity at $4.71 \times 10^{34} \text{ cm}^{-2}\text{s}^{-1}$ [70], surpassing the previous record set by the LHC. With a circumference of approximately 3 km, it is the largest lepton collider in operation. Similar to CERN, KEK is a large complex housing multiple accelerators and facilities, as shown in the schematic in Fig. 7.1.

KEK is currently maintaining collaborations with several organizations, including CERN, to facilitate research on various topics of interest. SuperKEKB is especially relevant to FCC-ee as it can act as a prototype for testing innovative manufacturing, measurement, and analysis techniques, whether in mechanical prototyping, elements alignment, or beam dynamics. During my secondment in Japan, the optics measurement techniques utilized at CERN for the LHC, specifically turn-by-turn acquisitions, were tested on the two rings of SuperKEKB. Previous studies have been conducted and are extended in this chapter. Rather than providing an in-depth description, the focus here is on updating the previously employed techniques. For more detailed information, please refer to [27, 72, 73].

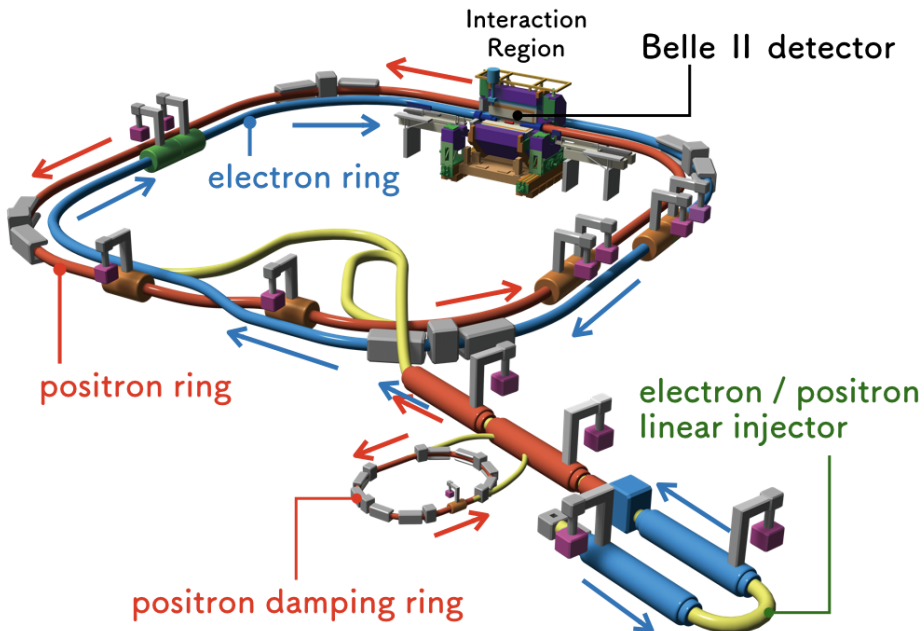


Figure 7.1.: Schematic drawing of the accelerator complex at KEK [71].

7.2. Measurement Techniques for Linear Optics

In SuperKEKB, the beam optics are measured using either Closed Orbit Distortion [74] or turn-by-turn measurements. As fast optics measurements can be achieved with the Tbt method, a measurement campaign has been carried out to improve the measurement quality. This includes investigating various beam excitation techniques and settings. The necessary pre-processing steps for optics measurements have been detailed in [27], and are not covered here.

7.2.1. Closed Orbit Distortion

Optics measurements using the COD method [74–76] are well established and routinely performed at SuperKEKB. In COD measurements, the beam is excited using six corrector magnets, and the centroid orbit is recorded by 466 BPMs for the HER and 444 BPMs for the LER, respectively. The measured orbits, averaged over several turns, are stored in a matrix that contains a large number of elements. The optics of both transverse planes are then reconstructed using analytical formulas. Since the correctors must be powered one at a time, the COD method is relatively time-consuming. Since the average particle orbit is observed, the BPM readings are highly dependent on precise calibration. One significant

advantage of COD measurements at SuperKEKB is that approximately 6.5 times more BPMs can be used compared to the TbT data.

7.2.2. Turn-by-Turn

In SuperKEKB, 68 and 70 BPMs in the HER and LER rings are capable of recording turn-by-turn (TbT) orbit data, typically capturing several thousand turns in both transverse planes. TbT measurements are usually performed with a single bunch, with currents ranging from 0.2 mA to 1.5 mA. The beam can be excited using three different methods.

First, an Injection Kicker (IK) delivers a single horizontal kick, causing the beam motion to damp due to synchrotron radiation. The damping times for the positron and electron rings are 46 ms and 53 ms, corresponding to 4600 and 5300 turns, respectively [27]. However, the IK only provides horizontal kicks, limiting the precision of vertical optics measurements.

In contrast, the Phase-Locked Loop (PLL) method allows continuous excitation of the beam in both horizontal and vertical planes. The PLL tracks the natural tune of the beam and drives it at the corresponding frequency. A key advantage of the PLL system is that it can excite both planes simultaneously, enabling measurements of transverse coupling and other resonance-driving terms (RDTs). The PLL is currently the only method capable of performing vertical TbT measurements, although data acquisition must be started manually, and a minimum bunch current of 0.5 mA is required. This method was not used for the data discussed in this thesis.

The third method is not strictly an excitation. To induce oscillations in the vertical plane, the beam can be injected with an orbit offset. This vertical offset causes the beam to oscillate as if it had received a single kick. The oscillations then damp, and a new beam must be injected to repeat the measurement. This method has been successfully used for the first time to measure vertical optics using turn-by-turn data.

Once the TbT data is recorded, the standard analysis procedures outlined in Section 3.2 are applied. Specifically, the frequency spectrum is calculated before reconstructing the optics. The model used for this analysis is generated with the SAD (Strategic Accelerator Design) software [77]. A typical turn-by-turn signal is depicted in Fig. 7.2.

7.2.3. OMC3 Graphical User Interface

The graphical user interface (GUI) used for optics analysis on the LHC, based on OMC3 [78], has been updated to support the HER and LER rings of SuperKEKB. This tool is essential for the rapid and efficient cleaning of bad kicks, BPMs, and for detecting resonance lines. Utilizing the latest version of the GUI provides access to recent bug fixes and improvements, enhancing usability and functionality.

7. SuperKEKB Studies

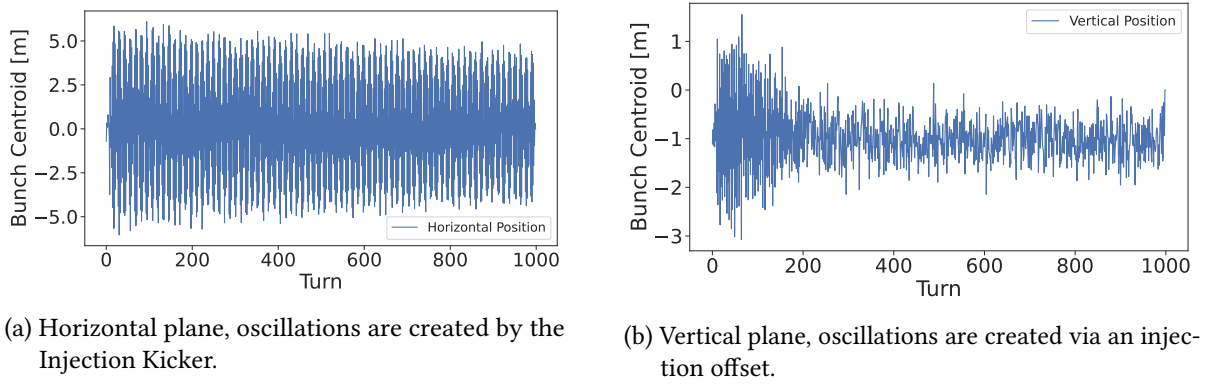


Figure 7.2.: Typical horizontal and vertical recorded turn-by-turn signals.

A typical use case is illustrated in Fig. 7.3, where BPMs that provide erroneous data across multiple measurements can be easily identified.

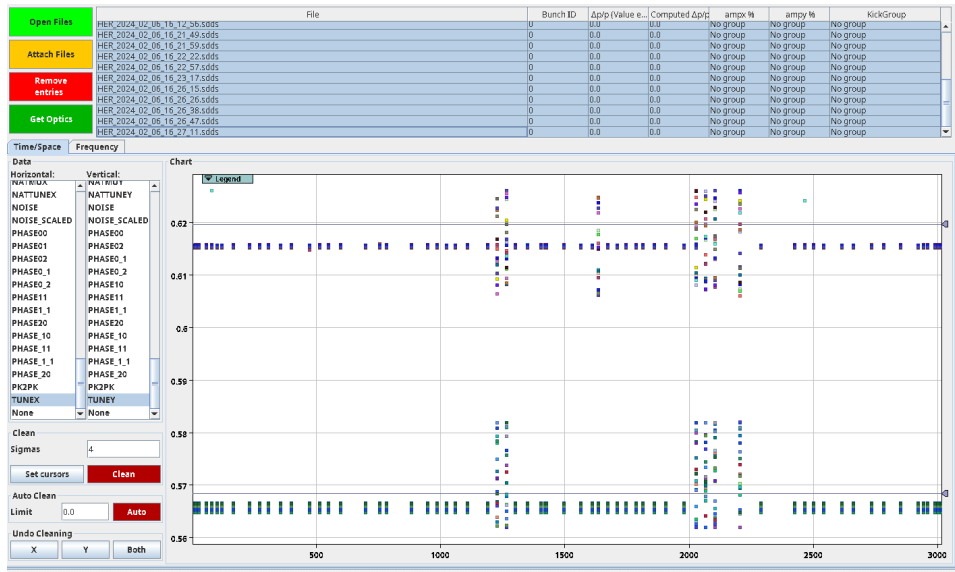


Figure 7.3.: The identification of bad BPMs across measurements is easily done with the GUI.

7.3. Optics Observations

7

All the measurements presented in this section have been performed in February 2024, during the commissioning phase of SuperKEKB.

Ring	Day	β_x^* [mm]	β_y^* [mm]	Q_x	Q_y	Kicks
LER	06	384	48.6	44.556	46.635	H & V
	09	384	48.6	44.553	46.621	H
	20	200	8	44.527	46.604	H
	22	200	8	44.535	46.590	H
HER	06	400	81	45.572	43.616	H & V
	20	200	8	45.530	43.595	H
	22	200	8	45.535	43.596	V
	26	200	8	45.535	43.596	V

Table 7.1.: Configurations of the HER and LER rings for measurements performed via turn-by-turn acquisition.

7.3.1. Beta-Beating

Several configurations of the machine were measured using turn-by-turn acquisitions, as detailed in Table 7.1. The configurations with $\beta_y^* = 48.6$ mm in LER and $\beta_y^* = 81$ mm in HER are referred to as *detuned*. Multiple kicks were performed for each configuration to increase measurement precision. Although additional measurements were taken, insufficient kick amplitude in some cases made it challenging to extract reliable linear optics data and are thus here not included. Specifically, vertical measurements are challenging to perform as oscillation amplitudes are often low due to the limited achievable injection offset. The low vertical action often makes measurements noisy.

Both the *detuned* and 8mm squeezed optics are reliably measured for both rings. However, the vertical plane for the squeezed optics could not be measured in LER due to the absence of injection offset. Figure 7.4 and Fig. 7.6 show the measurements taken with *detuned* optics for LER and HER. For the squeezed optics, at 8mm, a comparison to the measurements performed via COD is done in Fig. 7.5 and Fig. 7.7, for LER and HER respectively. The agreement between the COD and the TbT techniques is a good indication of their robustness. The agreement found during these measurements is similar to that obtained in previous studies [27].

A summary of the performed measurements and the RMS β -beating is given in Table 7.2.

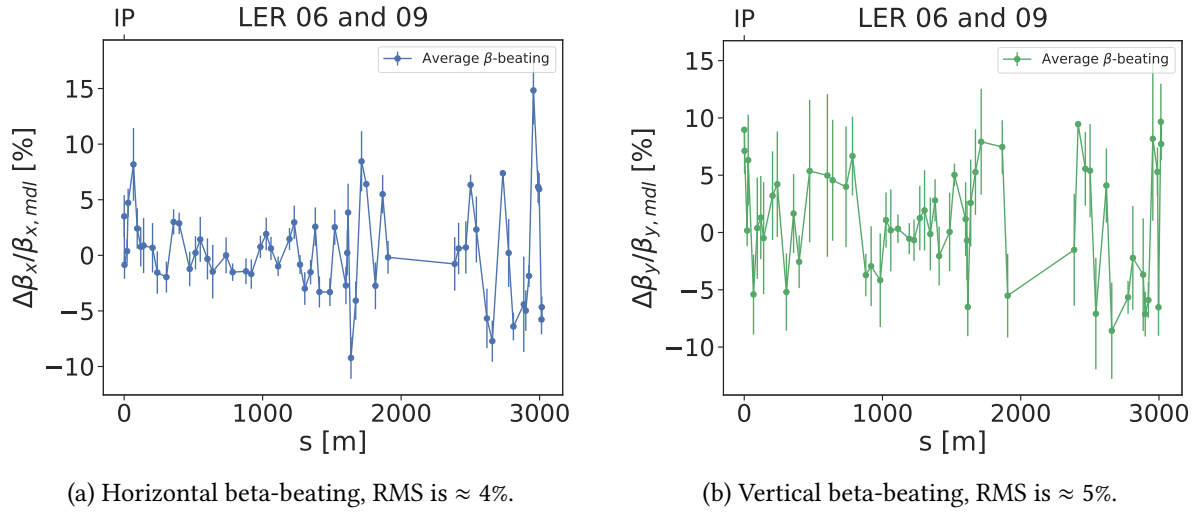


Figure 7.4.: LER horizontal and vertical beta-beating for *detuned* optics, reliably measured during two different days. The vertical plane is noticeably noisier as oscillation amplitudes are smaller.

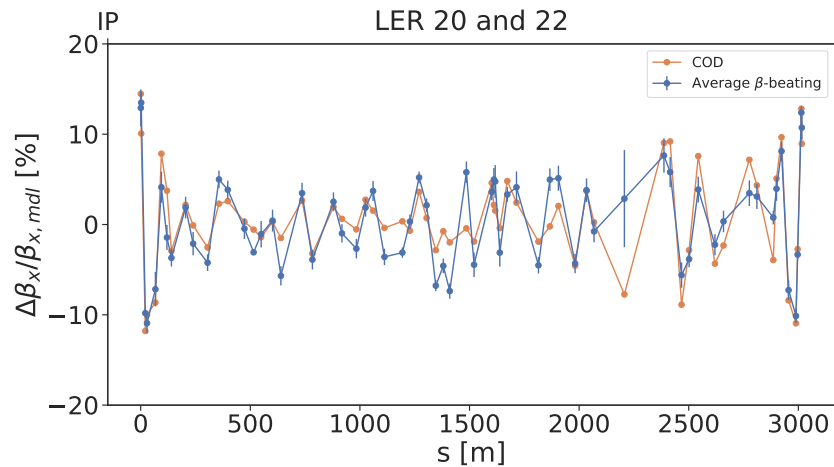


Figure 7.5.: LER horizontal beta-beating for *8mm squeezed* optics, reliably measured during two different days. The vertical plane is absent due to amplitudes being too low to reconstruct linear optics. A comparison to the beating measured via COD is made. RMS is ≈ 6

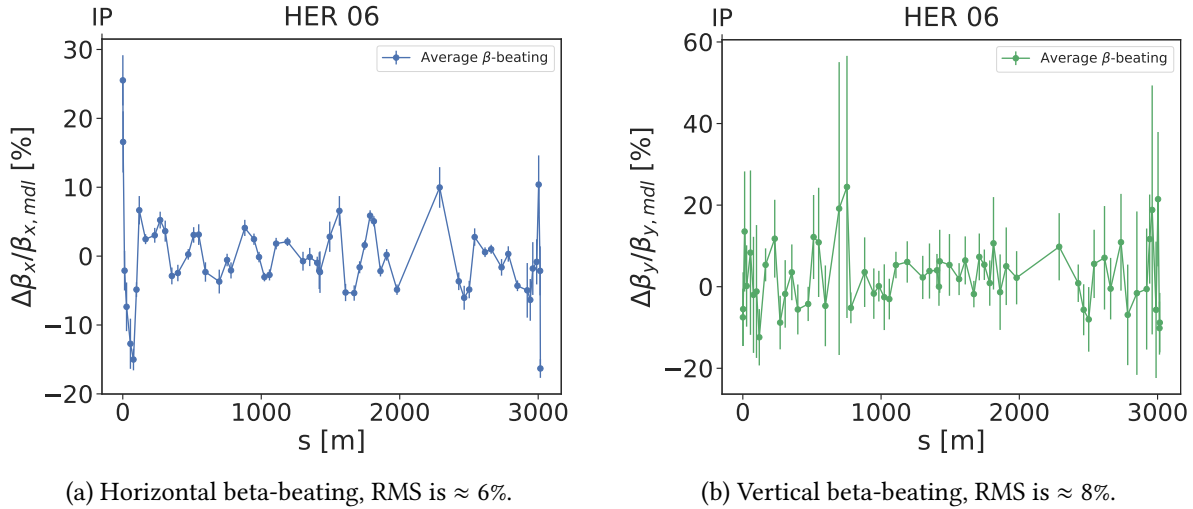


Figure 7.6.: HER horizontal and vertical beta-beating for *detuned* optics. The vertical plane is noticeably noisier as oscillation amplitudes are smaller.

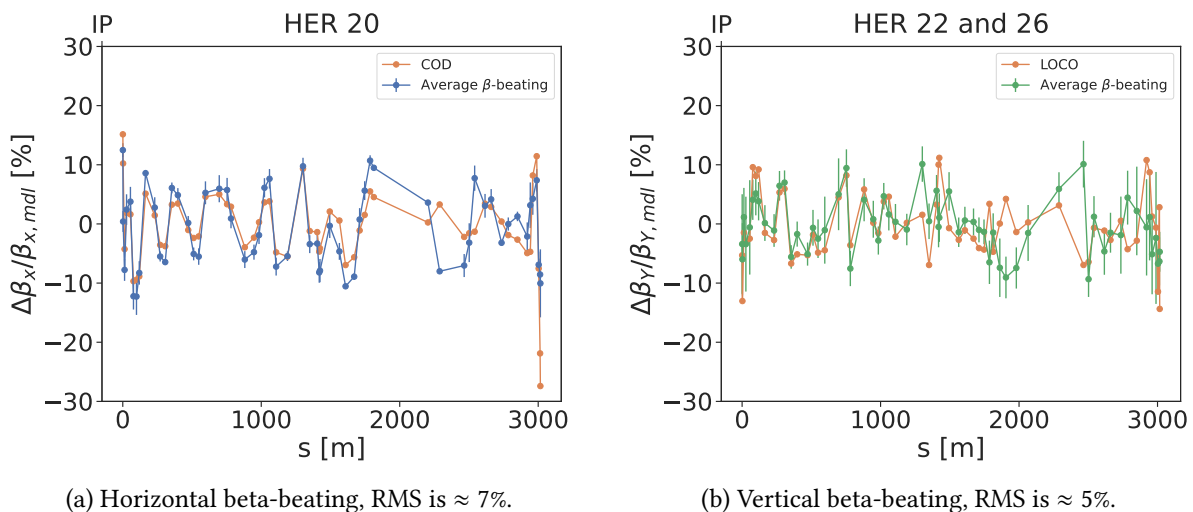


Figure 7.7.: HER horizontal and vertical beta-beating for *8mm squeezed* optics. The vertical plane is noticeably noisier as oscillation amplitudes are smaller. A comparison to the beating measured via COD is made.

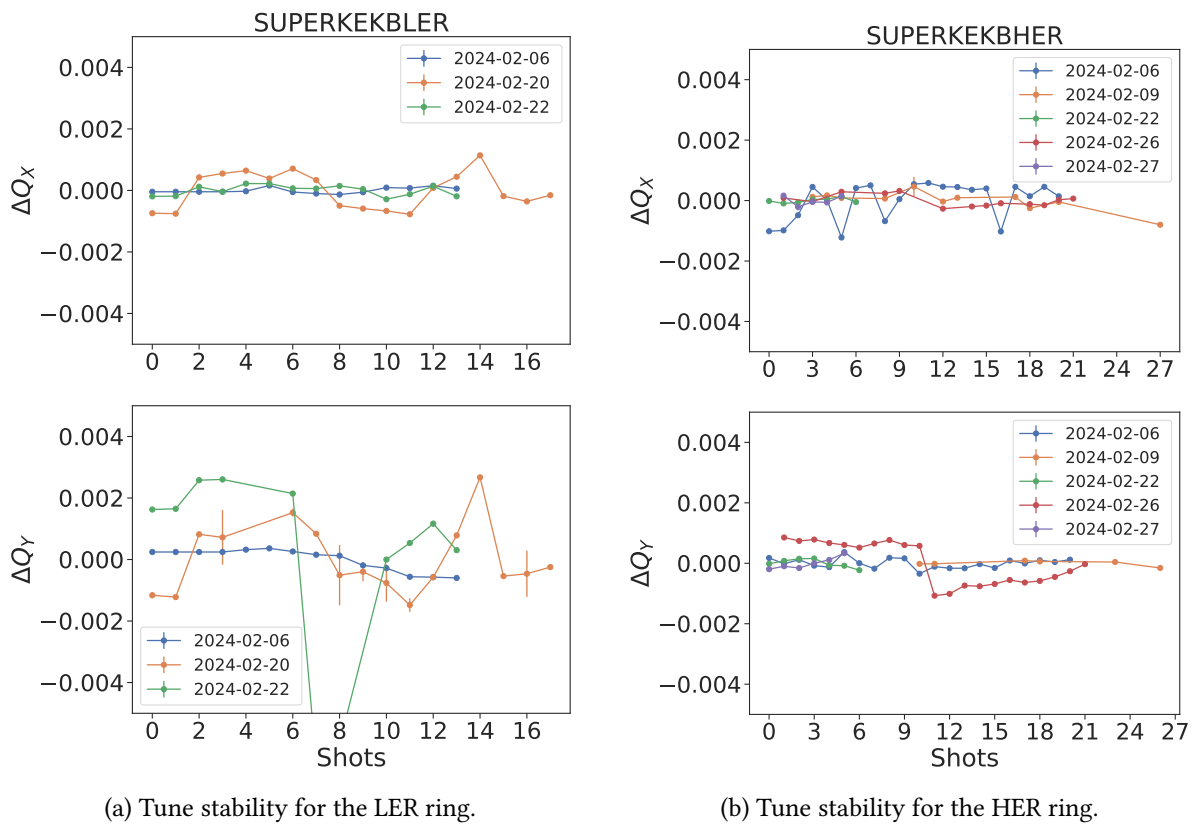
Ring	Configuration	β -b. rms H	β -b. rms V
LER	Detuned	4%	5%
	Squeezed 8mm	6%	
HER	Detuned	6%	8%
	Squeezed 8mm	7%	5%

Table 7.2.: Summary of the measured β -beating with squeezed and detuned optics in the HER and LER rings.

7.3.2. Amplitude Detuning

Tune Stability

To accurately measure non-linear optics, reliable measurement of the tune is essential. Ensuring tune stability across consecutive kicks is needed to minimize measurement uncertainties and reflects the reproducibility of the machine. With an appropriate kicker in the horizontal plane, this plane is expected to be easier to measure, and is reflected by the tune stability across kicks. Figure 7.8 illustrates the variation in tune from the first kick compared to subsequent kicks for both rings and planes. While reproducibility is poor in the vertical plane of the LER, all other measurements agree within few 10^{-3} .



Amplitude Detuning in LER

Particularly notable measurements have been conducted in the LER ring with *detuned* optics. These measurements stand out due to their larger action range compared to others. Figure 7.9 illustrates

the various kicks performed and their corresponding action. The tune is computed across each kick using a window of 200 turns, every 50 turns. A clear trend emerges with the tune increasing with the amplitude of the kicks. Over time, the oscillations gradually dampen due to synchrotron radiation, and the tune reduces accordingly.

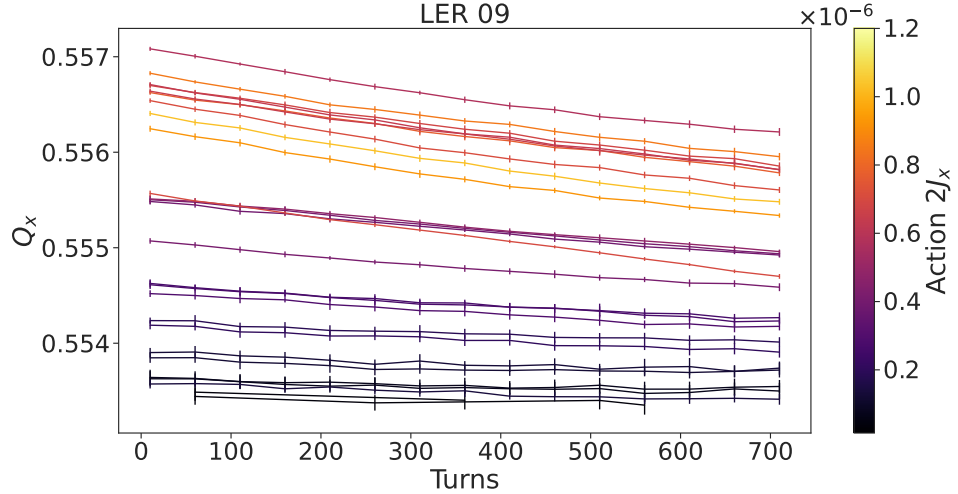


Figure 7.9.: Correlation between the measured tune with the action of the kick. The tune is computed via a running window over 200 turns, every 50 turns.

The variation of the horizontal tune with the horizontal kick amplitude is related to the amplitude detuning term $\frac{\partial Q_x}{\partial J_x}$. Its value can be retrieved by fitting the tune to the action. Figure 7.10 shows the various kicks along with a fit and a comparison to the model. The measured value, 6500 ± 500 is one order of magnitude higher than that simulated, of 600. This observed discrepancy indicates possible un-modeled octupolar-like sources. Such a discrepancy, although not as large, already has been observed with different optics [27].

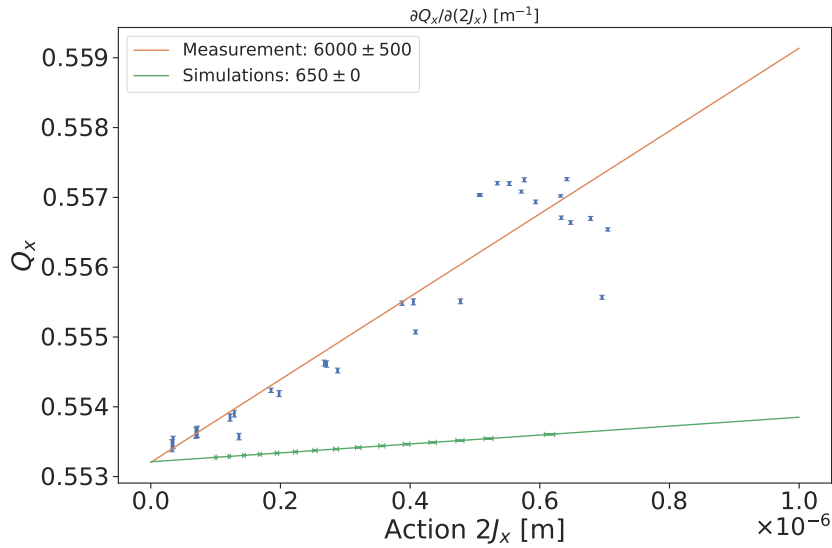


Figure 7.10.: Amplitude dependence of the tune in the LER ring. The slope of the fitted line corresponds to the amplitude detuning term $\partial Q_x / \partial 2J_x$. For comparison, the tune computed from the model is shown in green.

7.3.3. Resonance Driving Terms

Resonance Driving Terms, coefficients linked to the strength of a resonance, can be measured via their associated line amplitude in the frequency spectrum. To reliably measure RDTs, these line amplitudes must be clearly distinguishable and above the noise level for every BPM. This can be challenging to achieve and often requires high amplitude kicks. For example, lines in the vertical spectrum, attributed to octupoles, were previously observed [27] but could not lead to a successful RDT measurement due to kick amplitudes.

However, new measurements were taken with a different working point in order to be closer to the resonances with the hope of increasing their impact on particle motion. A resonance diagram, illustrating those resonances and the typical working point of LER is shown in Fig. 7.11. Although several working points were tested, no clear correlation between them and successful RDTs measurements could be established. The main determining factor remained the kick amplitude. A typical frequency spectrum from a successful measurement in HER for the vertical plane is shown in Fig. 7.12. The line $-1Q_x - 1Q_y$ is seen at each BPM. Additionally, lines near the vertical tune are attributed to the synchrotron tune.

Successful measurements of sextupolar RDTs were indeed obtained. Specifically, the RDTs $f_{3000,x}$ in LER and $f_{1020,y}$ in HER were measured using the *detuned* optics configuration. While additional sextupolar lines were clearly visible in both the horizontal and vertical spectra, no clear RDT measurements could be extracted. The measured amplitudes, along with comparisons to the model, are

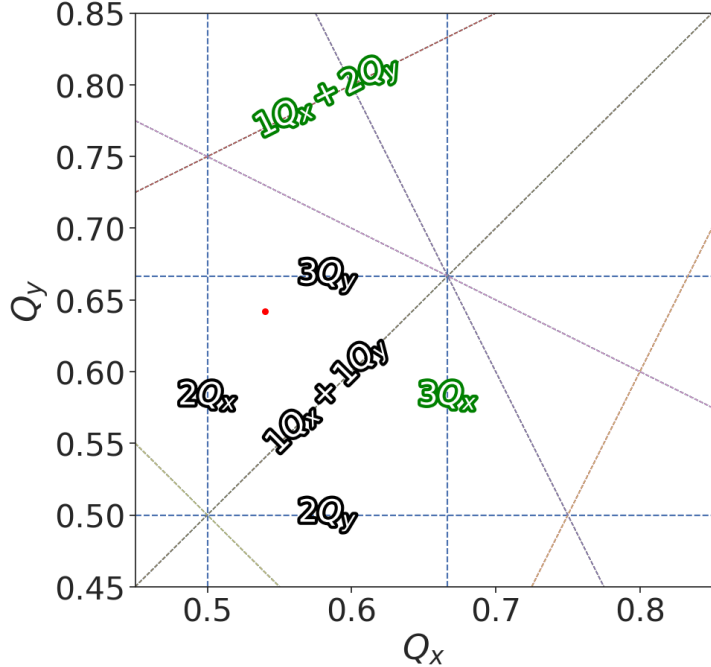


Figure 7.11.: Resonance diagram highlighting the resonances close to the HER working point, in red, and those often visible in the frequency spectra, in green.

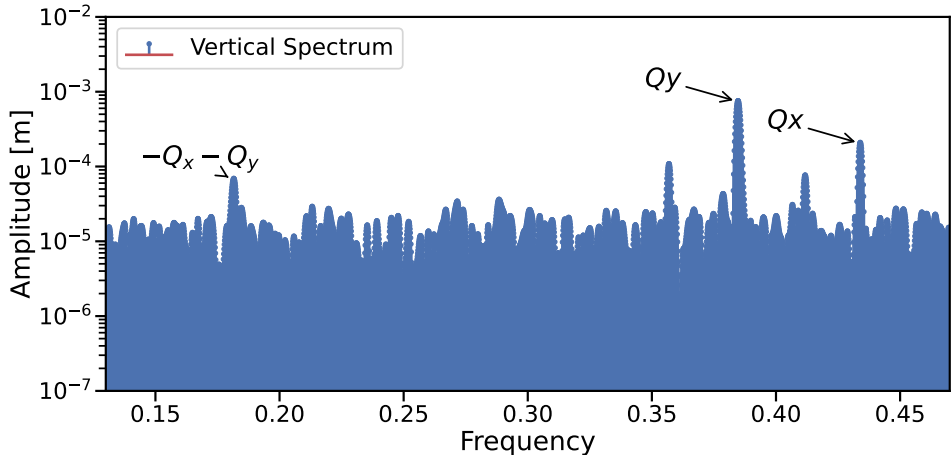


Figure 7.12.: Vertical frequency spectrum of HER, showing the natural tunes as well as a line excited by the sextupolar RDT f_{1020} .

presented in Fig. 7.14 and Fig. 7.13. Notably, both measurements exhibit discrepancies with the model. The average amplitude of f_{1020} in the vertical plane for HER is measured at 21, compared to a modeled amplitude of 7. Similarly, for f_{3000} , the average values measured in the horizontal plane for LER are 2

and 1.3. These discrepancies remain largely unexplored and may arise from decoherence effects that were not accounted for in the analysis software. Additionally, these could also arise from contributions from other multipoles through feed-down or feed-up, as observed in the LHC. The measured spikes in the LER RDT are not yet explained, but could come from a badly reconstructed phase space due to non-optimal phase advances between BPMs in that region, inverted BPM plane signal or absent from the model [79].

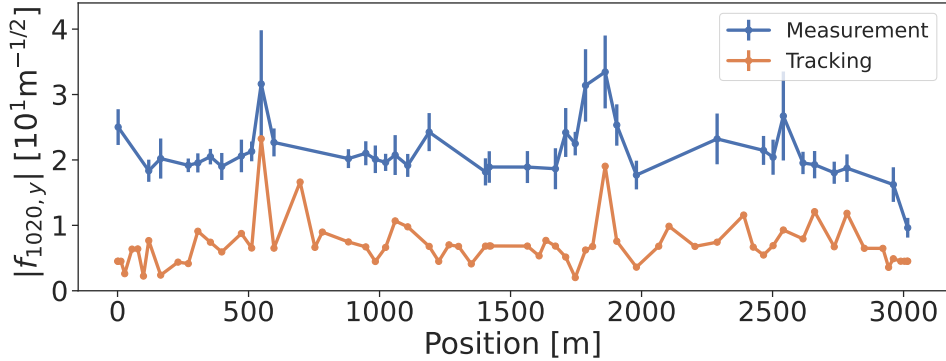


Figure 7.13.: Sextupolar RDT $f_{1020,y}$ measured in HER with *detuned* optics and compared to the model.

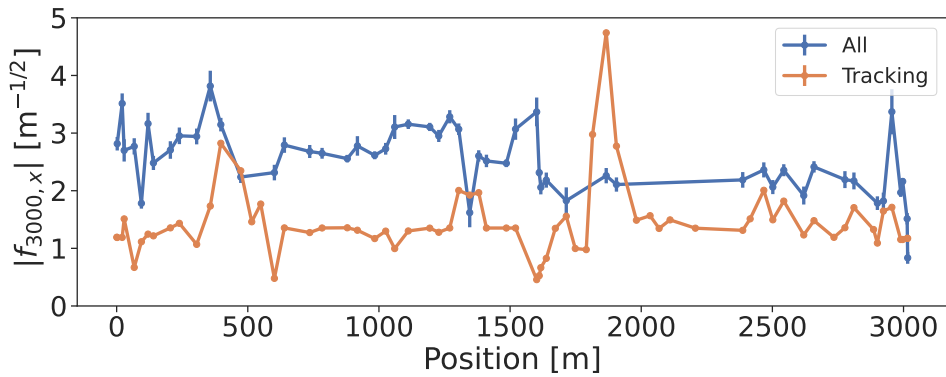


Figure 7.14.: Sextupolar RDT $f_{3000,x}$ measured in LER with *detuned* optics and compared to the model.

7.3.4. Chromaticity

Chromaticity measurements were performed using the method of varying the RF frequency, as described in Section 3.2.3. While this method is standard at the LHC, it is not regularly used on the SuperKEKB rings. However, it provides the ability to measure the tune over a broader range of momentum offsets. Chromaticity can also be computed using the Injection Kicker [27]. Similar to the LHC at injection energy, the Lorentz factor γ^{-2} is small compared to the momentum compaction

7. SuperKEKB Studies

factor α_c and can therefore be neglected. Figure 7.15 illustrates the RF frequency method.

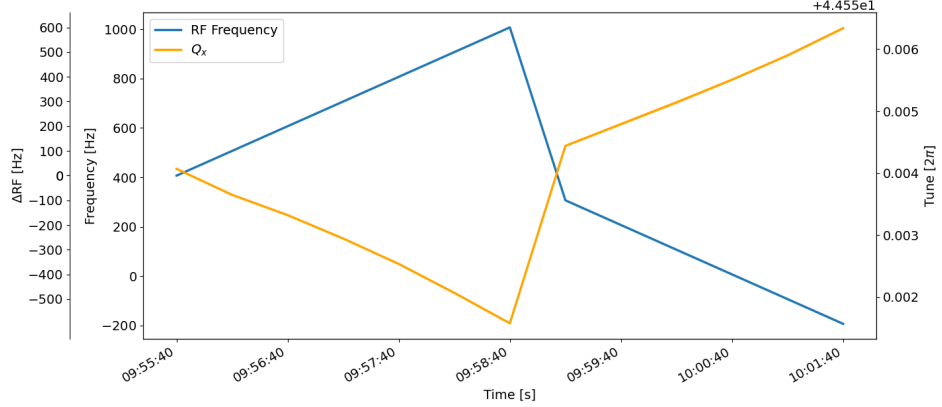


Figure 7.15.: Horizontal tune change relative to the change in RF Frequency at SuperKEKB.

Two measurements were taken with *detuned* optics for the HER and LER rings and are shown in Fig. 7.16 and Fig. 7.17. The values of the fitted chromaticity function are given in Table 7.3 and Table 7.4 for HER and LER respectively. In order to allow for a better comparison the tune and the linear chromaticity taken from the the measurements.

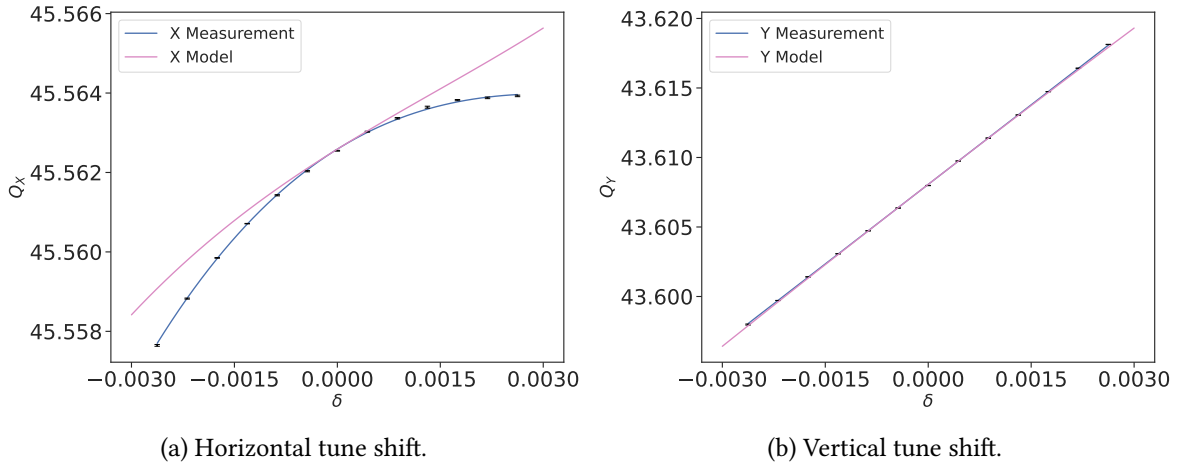
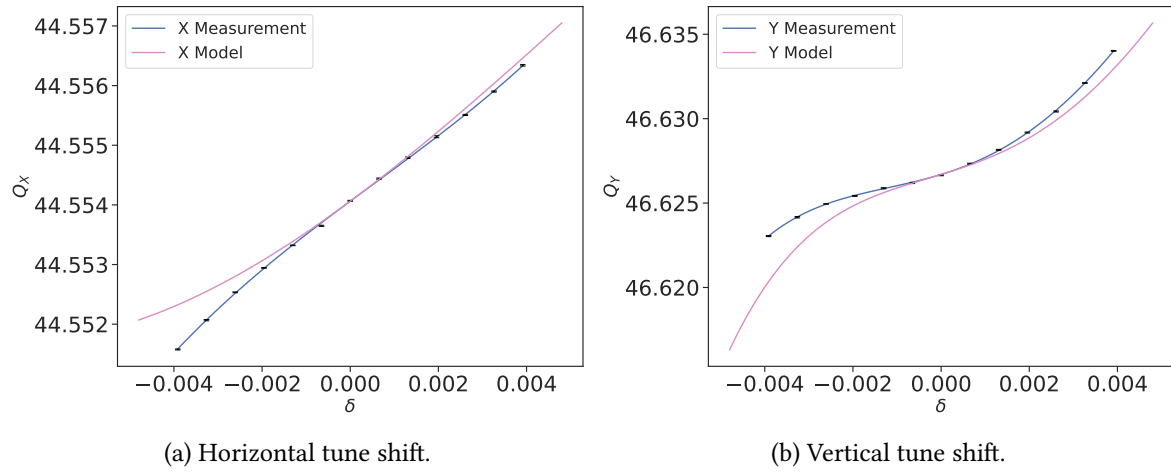


Figure 7.16.: HER chromaticity measurements with *detuned* optics.

It can be noted that most of the measured third and fourth-order chromaticities agree well with the model, whereas the second-order chromaticity appears to deviate. Discrepancies in Q'' were already observed in 2022 with different optics [27]. This discrepancy could arise from octupolar sources and higher-order contributions from sextupoles.

Figure 7.17.: LER chromaticity measurements with *detuned* optics.

		$Q'' [\times 10^3]$	$Q''' [\times 10^6]$
X	Meas.	-0.51 ± 0.01	0.11 ± 0.02
	Model	-0.12 ± 0.00	0.09 ± 0.00
Y	Meas.	0.00 ± 0.0	
	Model	-0.04 ± 0.0	

Table 7.3.: Measured and modeled chromaticity in the HER ring with *detuned* optics in both planes.

		$Q'' [\times 10^3]$	$Q''' [\times 10^6]$	$Q^{(4)} [\times 10^9]$
X	Meas.	-0.01 ± 0.0	0.02 ± 0.0	
	Model	0.04 ± 0.0	-0.01 ± 0.0	
Y	Meas.	0.35 ± 0.01	0.25 ± 0.01	-0.09 ± 0.01
	Model	0.10 ± 0.00	0.32 ± 0.00	-0.09 ± 0.00

Table 7.4.: Measured and modeled chromaticity in the LER ring with *detuned* optics in both planes.

7.4. Summary

The measurements reveal excellent reproducibility of linear optics, with notable improvements in the horizontal plane when a kicker is used. This consistency has been observed over multiple days and across different shots. Sextupolar Resonance Driving Term (RDT) measurements have been carried out in both rings for the first time, though some measurements were challenging to achieve, and certain discrepancies remain unresolved. Chromaticity measurements for both rings were generally satisfactory, but some inconsistencies in Q'' were observed in both the HER and LER.

7. SuperKEKB Studies

Amplitude detuning for the LER was measured with detuned optics, and the model comparison showed an order of magnitude difference. Combined with the chromaticity results, this suggests potential errors due to higher-order effects of sextupoles and octupoles. Further investigations are needed to clarify these discrepancies.

Overall, the measurements are consistent with those obtained using different methods at KEK. This suggests that the techniques employed at CERN are effective and could enhance our understanding of the machine and its modeling.

Conclusions

This thesis has provided a comprehensive analysis of higher-order magnetic fields in the Large Hadron Collider (LHC) and their significant impact on beam dynamics and stability. The research underscores the critical importance of understanding and correcting skew octupolar, decapolar, dodecapolar, and decatetrapolar fields to ensure optimal performance of the LHC, particularly at injection energy.

The investigation into skew octupolar fields made use a response matrix approach for correcting resonance driving using corrector magnets. The research further identified the interplay between Landau octupoles and skew octupolar RDTs, highlighting the essential role of accurate coupling modeling.

The study of decapolar fields addressed discrepancies between measured and predicted third-order chromaticity, pinpointing the decay of decapolar components in the main dipoles as a key factor. The development of new correction strategies led to tangible improvements in beam lifetime and stability, demonstrating the effectiveness of these approaches.

Finally, the thesis introduced innovative measurement techniques for higher-order chromaticity terms, revealing the contribution of dodecapolar and decatetrapolar fields errors. Furthermore, first measurements of dodecapolar resonance driving terms were made. These findings reinforce the need for further exploration of higher-order fields to enhance the LHC's operational efficiency.

Overall, the research provides valuable insights into the complex interplay of magnetic fields within the LHC and lays the groundwork for future advancements in collider performance and stability.

List of Figures

2.1.	Schematic illustration of the accelerator complex at CERN. Most accelerators are both used as injectors for the LHC or to provide beams to fixed target experiments [3].	4
2.2.	3D cut of a main LHC dipole [4]. Both beam pipes can be seen surrounded by the coils, strongly clamped by the yokes.	5
2.3.	Schematic of the LHC layout.	6
2.4.	Schematic of an LHC Arc cell [6].	7
2.5.	Simplified illustration of a standard LHC cycle. Adapted from [9].	8
2.6.	Schematics of magnetic multipoles. In black the magnetic field lines, which extend also to the inner part of the magnets, but drawing them there has been omitted for clarity of the figure. Red arrows indicate the direction of force on a positive charge moving out of the page towards the reader. Courtesy of Joschua Dilly [10].	9
2.7.	Magnetic field in a dipole magnet [15].	13
2.8.	Frenet-Serret coordinate system, commonly used in accelerator physics. The system moves along the reference orbit.	14
2.9.	Line composed of FoDo cells, a basic cell present in most accelerators, composed of a Focusing and a Defocusing quadrupole. The envelope is a factor of the β -function and the action J	15
2.10.	Phase-space ellipse of a linear machine, parametrized by the Courant-Snyder parameters α , β and γ	15
2.11.	Phase space described in both regular and normalized coordinates	17
2.12.	Exaggerated phase space distorted by non-linearities described in regular (left), normalized (middle) and normal form (right) coordinates.	22
2.13.	A one turn map from turn N to N+1 solved using a generating function F , transforming to normal form coordinates ζ , applying the linear rotation R and transforming back to normalized coordinates.	22
2.14.	Particles with a momentum offset will be deflected differently by dipoles. This offset in position can be described by the dispersion function.	28

2.15. Evolution of the β -function along the lattice. Horizontal and vertical beatings are usually opposite given the focusing and defocusing properties of quadrupoles in each plane.	29
2.16. Tune diagram with resonance lines excited by different multipole orders. The working point is chosen in an area where few lines are present. When considering higher orders, it becomes apparent that the beam will inevitably hit several resonances.	35
3.2. Beam Loss Monitors (BLM), in yellow, on the LHC [33].	38
3.3. Graphical interface used in the CERN Control Center (CCC) for instantaneous losses in the LHC [33]. Different parts of the accelerator have varying dump thresholds.	39
3.4. Simulated turn by turn data with an AC-Dipole first ramping up then down.	40
3.5. Horizontal frequency spectrum of a turn-by-turn measurement in the LHC. The <i>driven</i> tunes of the AC-Dipoles have the highest amplitudes while the natural tune can be seen close to it. Other lines are often created by resonances.	41
3.6. Observation of the tune dependence on momentum offset, created by a shift of RF frequency.	45
3.7. Linear relation between the third order chromaticity and decapole corrector strengths, simulated with MADX-PTC.	48
4.1. Horizontal spectrum of Beam 1 at top energy before and after application of skew-octupolar RDT corrections. The RDT f_{1210} is seen at $2Q_x - 1Q_y$	52
4.2. Simulated RDTs response of the available skew octupolar correctors at top energy. Each corrector is powered at $J_4 = 1[\text{m}^{-4}]$. The orthogonality of R1 and L5/R5 allows to independently control the real and imaginary parts.	53
4.3. Simulation of the RDT response of the skew octupolar correctors at top energy for Beam 1. Each corrector is powered at $J_4 = 1[\text{m}^{-4}]$	54
4.4. Measured skew octupolar RDTs at top energy and $\beta^* = 30\text{cm}$ before and after correction. A reduction is observed for all but one RDT in Beam 2.	55
4.5. Intensity of Beam 1 related to the kick percentage of the AC-Dipole over time, before and after having applied skew-octupolar RDT corrections.	56
4.6. Unexpected amplitude shift of skew-octupolar RDT f_{1210} with varying Landau octupoles strengths.	57
4.7. Measured and simulated shift of skew-octupolar RDT after increase of Landau octupoles strength from zero. It is apparent that the shift in measurement is not replicated by the simulation.	58
4.8. Simulated skew octupolar RDT with normal and skew octupolar errors, and Landau octupoles powered. One simulation includes further roll errors on the Landau octupoles. No significant difference is observed between the two.	59

4.9.	Simulated skew octupolar RDT with fixed Landau octupole strength but varying coupling. Selected coupling values are often seen in operation.	60
4.10.	Measured and simulated real part shift of skew octupolar RDTs induced by Landau octupoles in presence of coupling at injection energy. Left column shows f_{1012} while right shows f_{1210}	61
4.11.	Simulated skew octupolar RDT f_{1012} with Landau octupoles turned off and at their operational powering. Coupling is set to a value commonly seen in operation for both.	62
5.1.	Measured and simulated chromaticity with application of the nominal decapolar corrections from FiDeL. It can be seen that although the corrections should diminish Q''' , it is not well corrected in practice.	66
5.2.	Decapoles on a test bench, being inspected after manufacturing [63].	67
5.3.	Chromaticity of the horizontal plane of Beam 1 during Run 3's commissioning, with nominal corrections based on the magnetic model and beam-based corrections aimed at correcting Q'' and Q'''	68
5.4.	Fit of the chromaticity function for the chromaticity measurement performed with octupole and decapole correctors powered off. The fit includes all orders up to third.	70
5.5.	Measured and simulated tune shift due to a change of action via an AC-Dipole at two different momentum offsets. Each fit corresponds to a chromatic amplitude detuning term evaluated at a certain δ	72
5.6.	Measured decay of the integrated decapolar field in LHC's main dipoles at injection energy. The fit is shown in black [15].	74
5.7.	Measured and simulated tune shift depending on the action at two different momentum offsets. Each fit corresponds to a chromatic amplitude detuning term evaluated at a certain δ . Estimates from simulations are lowered due to the b_5 decay of the main dipoles.	77
5.8.	Frequency map at injection energy, with decapolar field errors and nominal settings for landau octupoles. The highlighted resonance (1,-4), excited by decapoles, shows a degradation over 20,000 turns. The tune shift between the start and the end of the simulation is indicated in color.	78
5.9.	Horizontal frequency spectrum of turn-by-turn data, with nominal and beam-based corrections for the third order chromaticity Q''' . The $1Q_x - 4Q_y$ resonance can be seen at $-4Q_y$ with different amplitudes for each correction scheme.	79
5.10.	Measured f_{1004} for Beam 1 with decapolar correctors powered off and with nominal corrections for Q''' . Corrections clearly increase the RDT amplitude.	80
5.11.	Measured f_{1004} with decapolar correctors powered off, nominal settings, and combined RDT & Q''' correction with normal and opposite signs.	82
5.12.	Comparison for measurement and simulation of the response of the imaginary part of f_{1004} upon application on unpowered correctors of the RDT corrections.	83

5.13. Non intuitive increase of the RDT f_{1004} after application of both the Q'' and Q''' corrections.	84
5.14. Simulated change of the decapolar RDT f_{1004} with varying linear chromaticity Q' generated by sextupoles. The combination of sextupolar fields clearly shows a increase in decapolar RDT.	85
5.15. Average amplitude of the decapolar RDT f_{1004} depending on the overall strength of the sextupoles used to control the linear chromaticity Q' . The right plot can be used to relate the RDT amplitude to a specific Q' value.	86
5.16. Measured change of the decapolar RDT f_{1004} depending of the desired linear chromaticity Q' generated by sextupoles. It is to be noted that the vertical axis is one order of magnitude higher than the previous simulations' plot.	86
5.17. Simulated decapolar RDT f_{1004} with two different schemes. First scheme has lattice sextupoles turned off and octupoles turned on. Second scheme has all sextupoles of the lattice turned off and octupoles turned off as well. No difference is seen, as expected from the equations.	87
5.18. Simulated change of the decapolar RDT f_{1004} depending of the strength of the lattice octupoles used for Landau damping.	88
5.19. Simulation of the amplitude of the decapolar RDT f_{1004} depending on the field errors applied on main dipoles as well as coupling (C^-). While it is apparent that some multipolar errors drive the resonance higher, some combinations actually seem to cancel each other.	89
5.20. Shift of the decapolar RDT f_{1004} depending on the factor applied on octupolar corrections for Q''	89
5.21. Varying amplitude of the decapolar RDT f_{1004} at top energy depending on the activation or not of the crossing angle at the IP. Offsets in orbit create feed-down from higher orders.	90
5.22. Relative losses experienced with AC-Dipole kick amplitude with and without corrections pertaining to $Q'', Q''',$ chromatic amplitude detuning, and RDT f_{1004}	91
6.1. Shift of the tune by variation of the RF. Noise lines can appear in some cases, making the tune error bar large or downright unusable.	95
6.2. Tune spectrogram obtained via BBQ system. Strong resonance lines can be seen above and below where the tune really is, causing the wrong frequency peak to be identified as the tune.	96
6.3. Non linearity of α_c and its effect on the computed δ via RF trims. The simulations are done at injection energy of 450GeV.	97
6.4. Fit of the chromaticity function considering several α_c orders.	98
6.5. Comparison of the non-linear chromaticity fit obtained from the computed momentum offset via the RF in 2022 and from the logged values in 2016.	99

6.6. Measurement of higher order chromaticity terms with nominal corrections used during operation. Fits are up to the third and fifth order.	101
6.7. Selection of horizontal chromaticity measurements performed with varying configurations of the octupolar and decapolar correctors for Beam 1 during the commissionings of 2022 and 2024.	103
6.8. Measured and simulated fourth order chromaticity with different multipole errors. The b_2 errors, applied on dipoles and quadrupoles, generate beta-beating. Coupling is set to a value commonly seen in operation.	106
6.9. Measured and simulated fifth order chromaticity with different multipole errors. The b_2 errors, applied on dipoles and quadrupoles, generate beta-beating. Coupling is set to a value commonly seen in operation.	108
6.10. Measured decay of the integrated decatetrapolar field in LHC's main dipoles at injection energy. The fit is shown in black [69] and settles around +0.035.	109
6.11. Vertical spectrum of recorded turn-by-turn data for Beam 1 showing the tunes driven by the AC-Dipole along with a line contributed to by dodecapolar fields.	111
6.12. Real part of the dodecapolar RDT f_{0060} measured with several kick strengths. The RMS amplitude is of $3.5 \cdot 10^8$	112
6.13. Measured and simulated RDT f_{0060} with various normal and skew field errors. Coupling is set to a common value seen in operation.	112
 7.1. Schematic drawing of the accelerator complex at KEK [71].	116
7.2. Typical horizontal and vertical recorded turn-by-turn signals.	118
7.3. The identification of bad BPMs across measurements is easily done with the GUI.	118
7.4. LER horizontal and vertical beta-beating for <i>detuned</i> optics, reliably measured during two different days. The vertical plane is noticeably noisier as oscillation amplitudes are smaller.	120
7.5. LER horizontal beta-beating for <i>8mm squeezed</i> optics, reliably measured during two different days. The vertical plane is absent due to amplitudes being too low to reconstruct linear optics. A comparison to the beating measured via COD is made. RMS is ≈ 6	120
7.6. HER horizontal and vertical beta-beating for <i>detuned</i> optics. The vertical plane is noticeably noisier as oscillation amplitudes are smaller.	121
7.7. HER horizontal and vertical beta-beating for <i>8mm squeezed</i> optics. The vertical plane is noticeably noisier as oscillation amplitudes are smaller. A comparison to the beating measured via COD is made.	121
7.8. Difference in tune between consecutive measurements, across several days.	123
7.9. Correlation between the measured tune with the action of the kick. The tune is computed via a running window over 200 turns, every 50 turns.	124

List of Figures

7.10. Amplitude dependence of the tune in the LER ring. The slope of the fitted line corresponds to the amplitude detuning term $\partial Q_x / \partial 2J_x$. For comparison, the tune computed from the model is shown in green.	125
7.11. Resonance diagram highlighting the resonances close to the HER working point, in red, and those often visible in the frequency spectra, in green.	126
7.12. Vertical frequency spectrum of HER, showing the natural tunes as well as a line excited by the sextupolar RDT f_{1020}	126
7.13. Sextupolar RDT $f_{1020,y}$ measured in HER with <i>detuned</i> optics and compared to the model.	127
7.14. Sextupolar RDT $f_{3000,x}$ measured in LER with <i>detuned</i> optics and compared to the model.	127
7.15. Horizontal tune change relative to the change in RF Frequency at SuperKEKB.	128
7.16. HER chromaticity measurements with <i>detuned</i> optics.	128
7.17. LER chromaticity measurements with <i>detuned</i> optics.	129

List of Tables

2.1.	Relation between the field indices used in this thesis and multipoles.	8
3.1.	Example chromaticity values to correct via a response matrix	47
4.1.	Skew octupolar RDTs of interest, their associated resonances and the frequency spectrum lines they contribute to.	50
4.2.	Working points tested for skew-octupolar RDT measurements, together with the maximum diagonal kick percentages achieved without reaching the dump threshold.	51
4.3.	Computed corrections for skew octupolar RDTs at top energy. The corrector L1 has been broken for several years and can not be used.	52
5.1.	Third order chromaticity obtained during Run 3 commissioning, with nominal and beam-based corrections aimed at correcting Q'' and Q''' . Response of the correctors between the two configurations is also given for both measurement and simulation. .	69
5.2.	Measured and simulated third order chromaticity with octupole and decapole correctors turned off. The simulations include field errors from sextupoles to decahexapole (normal sextupole to decahexapole).	69
5.3.	Comparison of the measured and simulated terms $\frac{\partial^2 Q_x}{\partial J_y \partial \delta}$ and $\frac{\partial^2 Q_y}{\partial J_y \partial \delta}$ via PTC, at two discrete momentum offsets. Simulations include errors from normal sextupole to decahexapole and from skew octupole to decahexapole.	73
5.4.	Decay of the b_5 component after injection for long time periods [15].	74
5.5.	Comparison of Q'_x and Q'_y for Beam 1 with and without decay of the b_5 component of the main dipoles at injection energy. Fields errors range from normal and skew sextupoles ($n = 3$) to icosapole ($n = 10$).	75
5.6.	Measured and simulated third order chromaticity with octupole and decapole correctors turned off. The simulations include field errors from normal and skew sextupoles to icosapole ($n = 3$ to $n = 10$). The b_5 component of the main dipoles has been updated to include decay.	75

5.7. Comparison of the measured and simulated terms $\frac{\partial^2 Q_x}{\partial J_y \partial \delta}$ and $\frac{\partial^2 Q_y}{\partial J_y \partial \delta}$ via PTC, at two discrete momentum offsets. Simulations include errors from normal and skew sextupoles to icosapole ($n = 3$ to $n = 10$), as well as the decay of the b_5 component of the main dipoles.	76
5.8. Strength of decapolar correctors with nominal FiDeL settings and after application of corrections aiming at reducing both the RDT f_{1004} and Q''' . The total value has a direct incidence on the third order chromaticity Q'''	81
5.9. RMS of $ f_{1004} $ depending on the factor of the Q'' corrections.	88
6.1. Chromaticity values obtained for the same measurement, depending on the order of the momentum compaction factor taken into account.	97
6.2. Comparison of the chromaticity values obtained for the same measurement via two different methods to acquire δ	98
6.3. Performed chromaticity measurements with their respective momentum offset ranges.	100
6.4. Terms of the high order chromaticity obtained during Run 3's commissioning in 2022, with nominal corrections.	101
6.5. Reduced χ^2 values for each order of fit, taken from the second measurement of 2022, with Q'' and Q''' beam-based corrections.	102
6.6. Corrections applied on top of the nominal octupolar and decapolar correctors strengths in 2022 for the Q'' and Q''' corrections.	102
6.7. Summary of the chromaticity values obtained from the measurements presented in Table 6.3.	104
6.8. Simulated high order chromaticity terms via PTC at injection energy, including normal and skew sextupolar to decahexapolar field errors. Are also included beta-beating, coupling and decatetrapolar decay. For the fourth order, the values do not include beta-beating as the observed spread is not yet fully understood.	110
6.9. Ratios of the simulated and average measured high-order chromaticity terms. The values are taken from Table 6.7 and Table 6.8.	110
7.1. Configurations of the HER and LER rings for measurements performed via turn-by-turn acquisition.	119
7.2. Summary of the measured β -beating with squeezed and detuned optics in the HER and LER rings.	122
7.3. Measured and modeled chromaticity in the HER ring with <i>detuned</i> optics in both planes.	129
7.4. Measured and modeled chromaticity in the LER ring with <i>detuned</i> optics in both planes.	129
A.1. Normal and skew Hamiltonians of multipoles up to order 8.	146

A.2. Resulting multipole orders arising from the Poisson brackets of a given BCH order for two multipoles A and B of order m and n . At order 7, the Poisson brackets are not given as duplicates grow the list significantly.	148
A.3. Correspondence of a combination of multipoles from a BCH order to multipole-like fields. The exponents indicate the order of the BCH for individual components.	149
C.1. Number of valid RDTs for a given multipole order	161
C.2. Correspondence of Resonance Driving Terms to the lines seen in the horizontal or vertical frequency spectrum, up to dodecapoles ($n = 6$).	164
C.3. Amplitude dependence, associated resonance and spectrum correspondence of Resonance Driving Terms up to dodecapoles ($n = 6$).	169

Appendices

Hamiltonians and Transfer Maps

This appendix is intended to gather and explicit the Hamiltonians of the elements used in this thesis. Non-linear transfer maps are also described for some of those elements from the first to the second order.

A.1. Hamiltonians of Elements

The Hamiltonian of a *multipole* is the following [25, 27, 80]:

$$H = \Re \left[\sum_{n>1} (K_n + iJ_n) \frac{(x+iy)^n}{n!} \right]. \quad (\text{A.1})$$

From this, normal and skew fields can be separated:

$$\begin{aligned} N_n &= \frac{1}{n!} K_n \Re [(x+iy)^n] \\ S_n &= -\frac{1}{n!} J_n \Im [(x+iy)^n], \end{aligned} \quad (\text{A.2})$$

where K and J are the normalized strength of the multipole and x, y the transverse coordinates. Table A.1 explicits the normal and skew Hamiltonians of multipoles up to order 8.

A. Hamiltonians and Transfer Maps

Name	Order	Normal and Skew Hamiltonians
Drift	-	$H = \frac{1}{2}(p_x^2 + p_y^2)$
Quadrupole	2	$N_2 = \frac{1}{2!}K_2(x^2 - y^2)$ $S_2 = -J_2xy$
Sextupole	3	$N_3 = \frac{1}{3!}K_3(x^3 - 3xy^2)$ $S_3 = -\frac{1}{3!}J_3 \cdot (3x^2y - y^3)$
Octupole	4	$N_4 = \frac{1}{4!}K_4(x^4 - 6x^2y^2 + y^4)$ $S_4 = -\frac{1}{4!}J_4 \cdot (4x^3y - 4xy^3)$
Decapole	5	$N_5 = \frac{1}{5!}K_5(x^5 - 10x^3y^2 + 5xy^4)$ $S_5 = -\frac{1}{5!}J_5 \cdot (5x^4y - 10x^2y^3 + y^5)$
Dodecapole	6	$N_6 = \frac{1}{6!}K_6(x^6 - 15x^4y^2 + 15x^2y^4 - y^6)$ $S_6 = -\frac{1}{6!}J_6 \cdot (6x^5y - 20x^3y^3 + 6xy^5)$
Decatetrapole	7	$N_7 = \frac{1}{7!}K_7(x^7 - 21x^5y^2 + 35x^3y^4 - 7xy^6)$ $S_7 = -\frac{1}{7!}J_7 \cdot (7x^6y - 35x^4y^3 + 21x^2y^5 - y^7)$
Decahexapole	8	$N_8 = \frac{1}{8!}K_8(x^8 - 28x^6y^2 + 70x^4y^4 - 28x^2y^6 + y^8)$ $S_8 = -\frac{1}{8!}J_8 \cdot (8x^7y - 56x^5y^3 + 56x^3y^5 - 8xy^7)$

Table A.1.: Normal and skew Hamiltonians of multipoles up to order 8.

A.2. Transfer Maps

This section goes more in depth regarding the derivation of the examples of transfer maps introduced in Section 2.4.

As a reminder, the BCH of two elements up to order 3 is given below,

$$Z = \underbrace{H_2 + H_1}_{\text{First order}} + \underbrace{\frac{[H_2, H_1]}{2}}_{\text{Second order}} + \underbrace{\frac{[H_2, [H_2, H_1]]}{12}}_{\text{Third order}} - \underbrace{\frac{[H_1, [H_2, H_1]]}{12}}_{\text{Third order}}. \quad (\text{A.3})$$

A.2.1. Generic Effective Hamiltonian of Two Elements

In order not to have to derive every combination of multipoles, a generic approach can be taken. Two elements of orders n and m can indeed be combined together via the BCH. Their hamiltonians is thus the one from Eq. (A.1) with orders m and n . A drift is put in between the two multipoles to change the coordinates. This results in non-zero Poisson brackets as the momentum is propagated,

$$[H_2, H_1] \rightarrow [H_2, D \cdot H_1]. \quad (\text{A.4})$$

Higher orders will arise with derivations when applying the Poisson brackets. Those orders can be found by counting the number of Poisson brackets, and which operators are implicated. A Poisson bracket implicating H_2 will increase the resulting order by m , and likewise for H_1 and n . The resulting order is then decreased by the number of poisson brackets times 2. Equation (A.5) gives how this can be calculated when considering the written form of the Poisson brackets (eg. $[H_2, [H_2, H_1]]$).

$$\text{resulting order} = \text{count}(“H_2”) \cdot m + \text{count}(“H_1”) \cdot n - 2 \cdot \text{count}(“[“]) \quad (\text{A.5})$$

Although this formula is quite helpful, it is not trivial to compute which orders will arise from each BCH order. Indeed, not all combinations of H_1 and H_2 appear, as explained in details in [23]. Table A.2 shows the Poisson brackets corresponding to each order of the BCH, up to order 6, along with the resulting multipole order. To keep the table readable, Poisson Brackets are not shown above that order, as duplicates of resulting orders become quite frequent. Similarly, Table A.3 shows how fields can be generated depending on the orders of multipoles and that of the BCH.

A. Hamiltonians and Transfer Maps

BCH Order	Poisson Brackets	Resulting Order
1	A	m
	B	n
2	$\frac{[A,B]}{2}$	$m+n-2$
3	$-\frac{[B,[A,B]]}{12}$ $\frac{[A,[A,B]]}{12}$	$m+2n-4$ $2m+n-4$
4	$-\frac{[B,[A,[A,B]]]}{24}$	$2m+2n-6$
5	$-\frac{[A,[B,[A,[A,B]]]]}{120}$ $-\frac{[B,[A,[A,[A,B]]]]}{180}$ $-\frac{[A,[B,[B,[A,B]]]]}{360}$ $-\frac{[A,[A,[A,[A,B]]]]}{720}$ $-\frac{[B,[B,[A,[A,B]]]]}{180}$ $-\frac{[B,[B,[B,[A,B]]]]}{720}$	$3m+2n-8$ $3m+2n-8$ $2m+3n-8$ $4m+n-8$ $2m+3n-8$ $m+4n-8$
6	$-\frac{[A,[A,[B,[A,B]]]]}{240}$ $-\frac{[A,[B,[A,[A,B]]]]}{240}$ $-\frac{[B,[B,[A,[A,B]]]]}{360}$ $-\frac{[A,[B,[B,[A,B]]]]}{720}$ $-\frac{[B,[A,[A,[A,B]]]]}{1440}$ $-\frac{[B,[B,[A,[A,B]]]]}{1440}$	$3m+3n-10$ $3m+3n-10$ $3m+3n-10$ $2m+4n-10$ $4m+2n-10$ $2m+4n-10$
7	\dots	$2m+5n-12$ $m+6n-12$ $3m+4n-12$ $5m+2n-12$ $6m+n-12$ $4m+3n-12$

Table A.2.: Resulting multipole orders arising from the Poisson brackets of a given BCH order for two multipoles A and B of order m and n . At order 7, the Poisson brackets are not given as duplicates grow the list significantly.

BCH Order						
Field	1	2	3	4	5	6
3	H_3					
4	H_4	$(H_3)^2$				
5	H_5	$H_3 H_4$	$(H_3)^3$			
6	H_6	$H_3 H_5,$ $(H_4)^2$	$(H_3)^2 H_4$	$(H_3)^4$		
7	H_7	$H_3 H_6,$ $H_4 H_5$	$(H_3)^2 H_5,$ $H_3 (H_4)^2$		$(H_3)^5$	
8	H_8	$(H_5)^2,$ $H_3 H_7,$ $H_4 H_6$	$(H_3)^2 H_6,$ $(H_4)^3$	$(H_3)^2 (H_4)^2$	$(H_3)^4 H_4$	$(H_3)^6$
9	H_9	$H_4 H_7,$ $H_3 H_8,$ $H_5 H_6$	$(H_3)^2 H_7,$ $(H_4)^2 H_5,$ $H_3 (H_5)^2$		$(H_3)^3 (H_4)^2,$ $(H_3)^4 H_5$	
10	H_{10}	$H_4 H_8,$ $H_5 H_7,$ $H_3 H_9,$ $(H_6)^2$	$(H_3)^2 H_8,$ $H_4 (H_5)^2,$ $(H_3)^2 (H_5)^2$	$(H_4)^4,$ $(H_3)^2 (H_5)^2$	$(H_3)^2 (H_4)^3,$ $(H_3)^4 H_6$	$(H_3)^4 (H_4)^2$
11	H_{11}	$H_4 H_9,$ $H_3 H_{10},$ $H_6 H_7,$ $H_5 H_8$	$(H_4)^2 H_7,$ $H_3 (H_6)^2,$ $(H_5)^3,$ $(H_3)^2 H_9$		$(H_3)^4 H_7,$ $H_3 (H_4)^4,$ $(H_3)^3 (H_5)^2$	$(H_3)^3 (H_4)^3$
12	H_{12}	$H_6 H_8,$ $(H_7)^2,$ $H_5 H_9,$ $H_3 H_{11},$ $H_4 H_{10}$	$H_4 (H_6)^2,$ $(H_4)^2 H_8,$ $(H_5)^2 H_6,$ $(H_4)^2 (H_5)^2$	$(H_3)^2 (H_6)^2,$ $(H_4)^2 (H_5)^2$	$(H_3)^4 H_8,$ $(H_4)^5$	$(H_3)^4 (H_5)^2,$ $(H_3)^2 (H_4)^4$

Table A.3.: Correspondence of a combination of multipoles from a BCH order to multipole-like fields.
The exponents indicate the order of the BCH for individual components.

A.2.2. Transfer Map of Two Sextupoles

The transfer map of two sextupoles H_1 and H_2 of strength K_1 and K_2 , separated by a drift to introduce a change of coordinates in H_1 is the following,

$$\mathcal{M} = e^{\cdot Z \cdot} = e^{\cdot H_2 \cdot} \cdot e^{D \cdot H_1 \cdot}, \quad (\text{A.6})$$

After such application of the drift on H_1 , the two hamiltonians read,

$$\begin{aligned} H_1 &= \frac{1}{3!} K_1 L_1 \left((L_D p_x + x)^3 - 3 (L_D p_x + x) (L_D p_y + y)^2 \right) \\ H_2 &= \frac{1}{3!} K_2 L_2 (x^3 - 3xy^2). \end{aligned} \quad (\text{A.7})$$

Below are detailed each term of the BCH. Each term should be added together in order to obtain the whole effective Hamiltonian Z .

First Order

$$K_1 L_1 L_D \left(\begin{array}{l} \left(\frac{L_D^2 p_x^3}{6} - \frac{L_D^2 p_x p_y^2}{2} + \frac{L_D p_x^2 x}{2} - L_D p_x p_y y \right) \\ \left(-\frac{L_D p_y^2 x}{2} + \frac{p_x x^2}{2} - \frac{p_x y^2}{2} - p_y x y \right) \\ + K_1 L_1 \left(\frac{x^3}{6} - \frac{x y^2}{2} \right) + K_2 L_2 \left(\frac{x^3}{6} - \frac{x y^2}{2} \right) \end{array} \right) \text{ sextupolar} \quad (\text{A.8})$$

Second Order

$$K_1 K_2 L_1 L_2 L_D \left(\begin{array}{l} \left(\frac{L_D^2 p_x^2 x^2}{8} - \frac{L_D^2 p_x^2 y^2}{8} + \frac{L_D^2 p_x p_y x y}{2} - \frac{L_D^2 p_y^2 x^2}{8} \right) \\ \left(+ \frac{L_D^2 p_y^2 y^2}{8} + \frac{L_D p_x x^3}{4} + \frac{L_D p_x x y^2}{4} + \frac{L_D p_y x^2 y}{4} \right) \\ + \frac{L_D p_y y^3}{4} + \frac{x^4}{8} + \frac{x^2 y^2}{4} + \frac{y^4}{8} \end{array} \right) \text{ octupolar-like} \quad (\text{A.9})$$

Third Order

$$\begin{aligned}
& K_1^2 K_2 L_1^2 L_2 L_D \left(\begin{array}{l} \frac{L_D^5 p_x^4 x}{48} + \frac{L_D^5 p_x^3 p_y y}{12} - \frac{L_D^5 p_x^2 p_y^2 x}{8} - \frac{L_D^5 p_x p_y^3 y}{12} \\ + \frac{L_D^5 p_y^4 x}{48} + \frac{L_D^4 p_x^3 x^2}{12} + \frac{L_D^4 p_x^3 y^2}{12} - \frac{L_D^4 p_x p_y^2 x^2}{4} \\ - \frac{L_D^4 p_x p_y^2 y^2}{4} + \frac{L_D^3 p_x^2 x^3}{8} + \frac{L_D^3 p_x^2 x y^2}{8} - \frac{L_D^3 p_x p_y x^2 y}{4} \\ - \frac{L_D^3 p_x p_y y^3}{4} - \frac{L_D^3 p_y^2 x^3}{8} - \frac{L_D^3 p_y^2 x y^2}{8} + \frac{L_D^2 p_x x^4}{12} \\ - \frac{L_D^2 p_x y^4}{12} - \frac{L_D^2 p_y x^3 y}{6} - \frac{L_D^2 p_y x y^3}{6} + \frac{L_D x^5}{48} \\ - \frac{L_D x^3 y^2}{24} - \frac{L_D x y^4}{16} \end{array} \right) \\
& + K_1 K_2^2 L_1 L_2^2 L_D \left(\begin{array}{l} \frac{L_D^2 p_x x^4}{48} - \frac{L_D^2 p_x x^2 y^2}{8} + \frac{L_D^2 p_x y^4}{48} + \frac{L_D^2 p_y x^3 y}{12} \\ - \frac{L_D^2 p_y x y^3}{12} + \frac{L_D x^5}{48} - \frac{L_D x^3 y^2}{24} - \frac{L_D x y^4}{16} \end{array} \right)
\end{aligned} \quad \left. \right\} \text{decapolar-like} \quad (\text{A.10})$$

A.2.3. Transfer Map of a Sextupole and Octupole

The transfer map of a sextupole H_1 and octupole H_2 of strength K_1 and K_2 , separated by a drift like in the previous example is given by

$$\mathcal{M} = e^{:Z:} = e^{:H_2:} \cdot e^{D:H_1:} \quad (\text{A.11})$$

with H_1 and H_2 having as final expressions,

$$\begin{aligned}
H_1 &= \frac{1}{3!} K_{3,h1} L_1 \left((L_D p_x + x)^3 - 3 (L_D p_x + x) (L_D p_y + y)^2 \right) \\
H_2 &= \frac{1}{4!} K_2 L_2 (x^4 - 6x^2 y^2 + y^4).
\end{aligned} \quad (\text{A.12})$$

The first two orders of the BCH of those two elements is given below.

First Order

$$\begin{aligned}
K_3 & \left(\begin{array}{l} \frac{L_D^3 p_x^3}{6} - \frac{L_D^3 p_x p_y^2}{2} + \frac{L_D^2 p_x^2 x}{2} - L_D^2 p_x p_y y - \frac{L_D^2 p_y^2 x}{2} \\ + \frac{L_D p_x x^2}{2} - \frac{L_D p_x y^2}{2} - L_D p_y x y + \frac{x^3}{6} - \frac{x y^2}{2} \end{array} \right) \left. \right\} \text{sextupolar} \\
& + K_4 \left(\frac{x^4}{24} - \frac{x^2 y^2}{4} + \frac{y^4}{24} \right) \left. \right\} \text{octupolar}
\end{aligned} \quad (\text{A.13})$$

Second Order

$$K_3 K_4 L_D \left(\begin{array}{l} \left(\frac{L_D^2 p_x^2 x^3}{24} - \frac{L_D^2 p_x^2 x y^2}{8} + \frac{L_D^2 p_x p_y x^2 y}{4} - \frac{L_D^2 p_x p_y y^3}{12} \right) \\ - \frac{L_D^2 p_y^2 x^3}{24} + \frac{L_D^2 p_y^2 x y^2}{8} + \frac{L_D p_x x^4}{12} - \frac{L_D p_x y^4}{12} \\ + \frac{L_D p_y x^3 y}{6} + \frac{L_D p_y x y^3}{6} + \frac{x^5}{24} + \frac{x^3 y^2}{12} + \frac{x y^4}{24} \end{array} \right) \text{ decapolar-like} \quad (\text{A.14})$$

A.2.4. Transfer Map of a Skew Quadrupole and Octupole

The transfer map of a skew quadrupole H_1 and octupole H_2 of strength K_1 and K_2 , separated by a drift like in the previous examples is given by

$$\mathcal{M} = e^{Z:} = e^{H_2:} \cdot e^{D:H_1:} \quad (\text{A.15})$$

with H_1 and H_2 having as final expressions,

$$\begin{aligned} H_1 &= -J_1 L_1 (L_D p_x + x) (L_D p_y + y) \\ H_2 &= \frac{1}{4!} K_2 L_2 (x^4 - 6x^2 y^2 + y^4). \end{aligned} \quad (\text{A.16})$$

The first two orders of the BCH of those two elements is given below.

First Order

$$\begin{aligned} J_1 L_1 \left(-L_D^2 p_x p_y - L_D p_x y - L_D p_y x - x y \right) \} &\text{ skew quadrupolar} \\ + K_2 L_2 \left(\frac{x^4}{24} - \frac{x^2 y^2}{4} + \frac{y^4}{24} \right) \} &\text{ octupolar} \end{aligned} \quad (\text{A.17})$$

Second Order

$$J_1 K_2 L_1 L_2 L_D \left(\begin{array}{l} \left(\frac{L_D p_x x^2 y}{4} - \frac{L_D p_x y^3}{12} - \frac{L_D p_y x^3}{12} \right) \\ + \frac{L_D p_y x y^2}{4} + \frac{x^3 y}{6} + \frac{x y^3}{6} \end{array} \right) \text{ skew octupolar-like} \quad (\text{A.18})$$

Chromatic Amplitude Detuning

This appendix details the derivations of chromatic amplitude detuning from sextupoles up to dodecapoles. *Chromatic Amplitude Detuning*, being detuning coming from both the action and the momentum offset, only starts appearing with decapoles. Below that order, only amplitude detuning and chromaticity can be observed. As those are part of the derivations, they will also be detailed here.

B.1. Derivations

In this section, the terms of the chromatic amplitude detuning are given up to dodecapoles. Derivations are given only for sextupoles and octupoles, as the process remains fairly similar for higher orders. Vertical offsets will be neglected, as horizontal dispersion is dominant. The reasoning remains the same.

Up to the third order, the expression of the Taylor expansion of the Chromatic Amplitude Detuning around ϵ_x , ϵ_y and δ , for a tune Q_z , $z \in \{x, y\}$ reads:

$$\begin{aligned}
 Q_z(\epsilon_x, \epsilon_y, \delta) = & Q_{z0} + \left[\frac{\partial Q_z}{\partial \epsilon_x} \epsilon_x + \frac{\partial Q_z}{\partial \epsilon_y} \epsilon_y + \frac{\partial Q_z}{\partial \delta} \delta \right] \\
 & + \frac{1}{2!} \left[\frac{\partial^2 Q_z}{\partial \epsilon_x^2} \epsilon_x^2 + \frac{\partial^2 Q_z}{\partial \epsilon_y^2} \epsilon_y^2 + \frac{\partial^2 Q_z}{\partial \delta^2} \delta^2 \right. \\
 & \quad \left. + 2 \frac{\partial^2 Q_z}{\partial \epsilon_x \partial \epsilon_y} \epsilon_x \epsilon_y + 2 \frac{\partial^2 Q_z}{\partial \epsilon_x \partial \delta} \epsilon_x \delta + 2 \frac{\partial^2 Q_z}{\partial \delta \partial \epsilon_y} \delta \epsilon_y \right] \\
 & + \frac{1}{3!} \left[\frac{\partial^3 Q_z}{\partial \delta^3} \delta^3 + \frac{\partial^3 Q_z}{\partial \epsilon_x^3} \epsilon_x^3 + \frac{\partial^3 Q_z}{\partial \epsilon_y^3} \epsilon_y^3 \right. \\
 & \quad \left. + 3 \frac{\partial^3 Q_z}{\partial \epsilon_x \partial \delta^2} \delta^2 \epsilon_x + 3 \frac{\partial^3 Q_z}{\partial \epsilon_y \partial \delta^2} \delta^2 \epsilon_y + 3 \frac{\partial^3 Q_z}{\partial \epsilon_x^2 \partial \delta} \delta \epsilon_x^2 \right. \\
 & \quad \left. + 3 \frac{\partial^3 Q_z}{\partial \epsilon_y^2 \partial \delta} \delta \epsilon_y^2 + 3 \frac{\partial^3 Q_z}{\partial \epsilon_y \partial \epsilon_x^2} \epsilon_x^2 \epsilon_y + 3 \frac{\partial^3 Q_z}{\partial \epsilon_y^2 \partial \epsilon_x} \epsilon_x \epsilon_y^2 \right. \\
 & \quad \left. + 6 \frac{\partial^3 Q_z}{\partial \epsilon_y \partial \epsilon_x \partial \delta} \delta \epsilon_x \epsilon_y \right] + \dots
 \end{aligned} \tag{B.1}$$

B

B.1.1. Principle

From [28], the detuning caused by a magnet of length L can be described by its hamiltonian with

$$\Delta Q_z = \frac{1}{2\pi} \int_L \frac{\partial \langle H \rangle}{\partial J_z} ds. \tag{B.2}$$

The usual variables x and y of Eq. (2.13) can be replaced by *action-angle* variables to introduce the action:

$$\begin{aligned}
 x &\rightarrow \sqrt{2J_x \beta_x} \cos \phi_x \\
 y &\rightarrow \sqrt{2J_y \beta_y} \cos \phi_y
 \end{aligned} \tag{B.3}$$

A momentum dependence can be introduced for a particle with a different orbit (Δz) [81] via dispersion. Combined with Eq. (B.3), a dependence on all required components is achieved:

$$\begin{aligned}
 x + \Delta x &\rightarrow \sqrt{2J_x \beta_x} \cos \phi_x + D_x \delta \\
 y + \Delta y &\rightarrow \sqrt{2J_y \beta_y} \cos \phi_y + D_y \delta
 \end{aligned} \tag{B.4}$$

After averaging over the phase variable, all that is left is to compute the partial derivatives.

B.1.2. Sextupole

Taken from Table A.1, the normal field of a sextupole is $N_3 = \frac{1}{3!}K_3(x^3 - 3xy^2)$. Introducing δ via an orbit offset and changing the variables to action-angle, as given in Eq. (B.4), leads to the following expression:

$$N_3 = \frac{1}{6}K_3 \left[-3 \left(\delta D_x + \sqrt{2J_x\beta_x} \cos \phi_x \right) \left(\sqrt{2J_y\beta_y} \cos \phi_y \right)^2 + \left(\delta D_x + \sqrt{2J_x\beta_x} \cos \phi_x \right)^3 \right] \quad (\text{B.5})$$

Averaging over the cosines means integrating over $[0, \pi]$ and dividing by π :

$$\begin{aligned} \langle N_3 \rangle &= \frac{1}{\pi} \int_0^\pi N_3 \\ &= \frac{1}{6\pi^2} K_3 \cdot (3\pi^2 J_x \beta_x \delta D_x - 3\pi^2 J_y \beta_y \delta D_x + \pi^2 \delta^3 D_x^3) \end{aligned} \quad (\text{B.6})$$

Differentiating by either J_x or J_y gives the tune shift induced by a single sextupole:

$$\begin{aligned} \Delta Q_x &= -\frac{1}{4\pi} K_3 \beta_x D_x \delta L \\ \Delta Q_y &= -\frac{1}{4\pi} K_3 \beta_y D_x \delta L \end{aligned} \quad (\text{B.7})$$

From now on, differentiating by the action would give amplitude detuning, and by δ the chromaticity. Cross-terms exist but evidently depend on the expression of the multipole. For a sextupole, differentiating by the action does not have an effect, as no action is present in the tune shift equation. Rather, sextupoles are known to contribute to the first order chromaticity Q' . The following gives a recap of those operations:

$$\begin{aligned} \frac{\partial Q_x}{\partial J_x} &= 0 & ; & \frac{\partial Q_x}{\partial J_y} = 0 & ; & \frac{\partial Q_x}{\partial \delta} = -\frac{1}{4\pi} K_3 \beta_x D_x L \\ \frac{\partial Q_y}{\partial J_x} &= 0 & ; & \frac{\partial Q_y}{\partial J_y} = 0 & ; & \frac{\partial Q_y}{\partial \delta} = -\frac{1}{4\pi} K_3 \beta_y D_x L \end{aligned} \quad (\text{B.8})$$

The overall contribution of sextupoles to the Chromatic Amplitude Detuning is then highlighted in the following:

$$Q_z(\epsilon_x, \epsilon_y, \delta) = Q_{z0} + \left[\frac{\partial Q_z}{\partial \epsilon_x} \epsilon_x + \frac{\partial Q_z}{\partial \epsilon_y} \epsilon_y + \frac{\partial Q_z}{\partial \delta} \delta \right] \quad (\text{B.9})$$

B.1.3. Octupole

With the normal hamiltonian of octupoles being $N_4 = \frac{1}{4!} K_4 (x^4 - 6x^2y^2 + y^4)$, applying an orbit offset and changing for action-angle variables gives the following:

$$\begin{aligned}
 N_4 = & \frac{1}{24} K_4 \left[\left(\sqrt{2J_x\beta_x} \cos \phi_x \right)^4 \right. \\
 & + 4 \left(\sqrt{2J_x\beta_x} \cos \phi_x \right)^3 D_x \delta \\
 & + 6 \left(\sqrt{2J_x\beta_x} \cos \phi_x \right)^2 D_x^2 \delta^2 \\
 & + 4 \left(\sqrt{2J_x\beta_x} \cos \phi_x \right) D_x^2 \delta \\
 & + D_x^4 \delta^4 \\
 & - 6 \left(\sqrt{2J_x\beta_x} \cos \phi_x \right)^2 \left(\sqrt{2J_y\beta_y} \cos \phi_y \right)^2 \\
 & - 6 \left(\sqrt{2J_y\beta_y} \cos \phi_y \right)^2 \cdot 2 \left(\sqrt{2J_x\beta_x} \cos \phi_x \right) D_x \delta \\
 & - 6 \left(\sqrt{2J_y\beta_y} \cos \phi_y \right)^2 D_x^2 \delta^2 \\
 & \left. + \left(\sqrt{2J_y\beta_y} \cos \phi_y \right)^4 \right] \tag{B.10}
 \end{aligned}$$

Average over the phase variables gives the following:

$$\begin{aligned}
 \langle N_4 \rangle &= \frac{1}{\pi} \int_0^\pi N_4 \\
 &= \frac{1}{48} K_4 \left[3J_x^2 \beta_x^2 + 12J_x \beta_x D_x^2 \delta^2 + 2D_x^4 \delta^4 \right. \\
 &\quad \left. - 12J_y \beta_y (J_x \beta_x + D_x^2 \delta^2) + 3J_y^2 \beta_y^2 \right] \tag{B.11}
 \end{aligned}$$

Differentiating by either J_x or J_y gives the tune shift induced by a single octupole. Contrary to sextupoles, it can be noted that some action terms $J_{x,y}$ remain in the expression.

$$\begin{aligned}
 \Delta Q_x &= \frac{1}{48\pi} K_4 L \left[3J_x \beta_x^2 + 6\beta_x D_x^2 \delta^2 - 6\beta_x J_y \beta_y \right] \\
 \Delta Q_y &= \frac{1}{48\pi} K_4 L \left[-6J_x \beta_x \beta_y - 6\beta_y D_x^2 \delta^2 + 3J_y \beta_y^2 \right] \tag{B.12}
 \end{aligned}$$

Differentiating by the action $J_{x,y}$ yields amplitude detuning, while differentiating by the momentum offset yields the second order chromaticity Q'' :

$$\begin{aligned}\frac{\partial Q_x}{\partial J_x} &= \frac{1}{16\pi} K_4 \beta_x^2 L & ; \frac{\partial Q_x}{\partial J_y} &= -\frac{1}{8\pi} K_4 \beta_x \beta_y L & ; \frac{\partial^2 Q_x}{\partial \delta^2} &= \frac{1}{4\pi} K_4 \beta_x D_x^2 L \\ \frac{\partial Q_y}{\partial J_x} &= -\frac{1}{8\pi} K_4 \beta_x \beta_y L & ; \frac{\partial Q_y}{\partial J_y} &= \frac{1}{16\pi} K_4 \beta_y^2 L & ; \frac{\partial^2 Q_y}{\partial \delta^2} &= -\frac{1}{4\pi} K_4 \beta_y D_x^2 L\end{aligned}\quad (\text{B.13})$$

The overall contribution of octupoles to the Chromatic Amplitude Detuning is then highlighted in the following:

$$\begin{aligned}Q_z(\epsilon_x, \epsilon_y, \delta) &= Q_{z0} + \left[\frac{\partial Q_z}{\partial \epsilon_x} \epsilon_x + \frac{\partial Q_z}{\partial \epsilon_y} \epsilon_y + \frac{\partial Q_z}{\partial \delta} \delta \right] \\ &\quad + \frac{1}{2!} \left[\frac{\partial^2 Q_z}{\partial \epsilon_x^2} \epsilon_x^2 + \frac{\partial^2 Q_z}{\partial \epsilon_y^2} \epsilon_y^2 + \frac{\partial^2 Q_z}{\partial \delta^2} \delta^2 \right. \\ &\quad \left. + 2 \frac{\partial^2 Q_z}{\partial \epsilon_x \partial \epsilon_y} \epsilon_x \epsilon_y + 2 \frac{\partial^2 Q_z}{\partial \epsilon_x \partial \delta} \epsilon_x \delta + 2 \frac{\partial^2 Q_z}{\partial \delta \partial \epsilon_y} \delta \epsilon_y \right]\end{aligned}\quad (\text{B.14})$$

B.1.4. Decapole

Skipping the first steps detailed previously, the tune shift induced by a normal decapole is given by the following:

$$\begin{aligned}\Delta Q_x &= \frac{1}{240\pi} K_5 L \left[10D_x^3 \delta^3 \beta_x + 15D_x \delta J_x \beta_x^2 - 30J_y \beta_y \beta_x D_x \delta \right] \\ \Delta Q_y &= \frac{1}{240\pi} K_5 L \left[-10D_x^3 \delta^3 \beta_y + 15D_x \delta J_y \beta_y^2 - 30J_x \beta_y \beta_x D_x \delta \right]\end{aligned}\quad (\text{B.15})$$

The terms of the chromatic amplitude detuning can now be computed. Unlike sextupoles and octupoles, cross-terms between δ and the action now appear, giving rise to *chromatic amplitude detuning* and the third order chromaticity Q''' :

$$\begin{aligned}\frac{\partial^2 Q_x}{\partial J_x \partial \delta} &= \frac{1}{16\pi} K_5 \beta_x^2 D_x L & ; \frac{\partial^2 Q_x}{\partial J_y \partial \delta} &= \frac{1}{8\pi} K_5 \beta_x \beta_y D_x L & ; \frac{\partial^3 Q_x}{\partial \delta^3} &= \frac{1}{4\pi} K_5 \beta_x D_x^3 L \\ \frac{\partial^2 Q_y}{\partial J_x \partial \delta} &= -\frac{1}{8\pi} K_5 \beta_x \beta_y D_x L & ; \frac{\partial^2 Q_y}{\partial J_y \partial \delta} &= \frac{1}{16\pi} K_5 \beta_y^2 D_x L & ; \frac{\partial^3 Q_y}{\partial \delta^3} &= -\frac{1}{4\pi} K_5 \beta_y D_x^3 L\end{aligned}\quad (\text{B.16})$$

The contribution of decapoles to Chromatic Amplitude Detuning is then the following:

B. Chromatic Amplitude Detuning

$$\begin{aligned}
Q_z(\epsilon_x, \epsilon_y, \delta) = Q_{z0} + & \left[\frac{\partial Q_z}{\partial \epsilon_x} \epsilon_x + \frac{\partial Q_z}{\partial \epsilon_y} \epsilon_y + \frac{\partial Q_z}{\partial \delta} \delta \right] \\
& + \frac{1}{2!} \left[\frac{\partial^2 Q_z}{\partial \epsilon_x^2} \epsilon_x^2 + \frac{\partial^2 Q_z}{\partial \epsilon_y^2} \epsilon_y^2 + \frac{\partial^2 Q_z}{\partial \delta^2} \delta^2 \right. \\
& \quad \left. + 2 \frac{\partial^2 Q_z}{\partial \epsilon_x \partial \epsilon_y} \epsilon_x \epsilon_y + 2 \frac{\partial^2 Q_z}{\partial \epsilon_x \partial \delta} \epsilon_x \delta + 2 \frac{\partial^2 Q_z}{\partial \delta \partial \epsilon_y} \delta \epsilon_y \right] \\
& + \frac{1}{3!} \left[\frac{\partial^3 Q_z}{\partial \delta^3} \delta^3 + \dots \right]
\end{aligned} \tag{B.17}$$

B.1.5. Dodecapole

The tune shift induced by a normal dodecapole is given by the following:

$$\begin{aligned}
Q_x = & \frac{1}{720\pi} K_6 L \left[15 J_x^2 \beta_x^3 + 30 \beta_x D_x^4 \delta^4 + 90 J_x \beta_x^2 D_x^2 \delta^2 \right. \\
& \quad \left. - 180 J_y \beta_y \beta_x D_x^2 \delta^2 - 90 J_y \beta_y J_x \beta_x^2 + 90 J_y^2 \beta_y^2 \beta_x \right] \\
Q_y = & \frac{1}{720\pi} K_6 L \left[-30 \beta_y D_x^4 \delta^4 - 180 \beta_y J_x \beta_x D_x^2 \delta^2 - 90 \beta_y J_x^2 \beta_x^2 \right. \\
& \quad \left. + 90 J_y \beta_y^2 J_x \beta_x + 45 J_y \beta_y^2 D_x^2 \delta^2 - 15 J_y^2 \beta_y^3 \right]
\end{aligned} \tag{B.18}$$

The terms of the chromatic amplitude detuning can now be computed. Like for decapoles, chromatic amplitude detuning terms appear, as well as the third order chromaticity $Q^{(4)}$:

$$\begin{aligned}
\frac{\partial^2 Q_x}{\partial J_x^2} = & \frac{1}{96\pi} K_6 \beta_x^3 L \quad ; \quad \frac{\partial^2 Q_y}{\partial J_y^2} = -\frac{1}{96\pi} K_6 \beta_y^3 L \\
\frac{\partial^3 Q_x}{\partial J_x \partial \delta^2} = & \frac{1}{16\pi} K_6 \beta_x^2 D_x^2 L \quad ; \quad \frac{\partial^3 Q_y}{\partial J_y \partial \delta^2} = \frac{1}{16\pi} K_6 \beta_y^2 D_x^2 L \\
\frac{\partial^2 Q_x}{\partial J_y^2} = & \frac{1}{32\pi} K_6 \beta_y^2 \beta_x L \quad ; \quad \frac{\partial^2 Q_y}{\partial J_x^2} = -\frac{1}{32\pi} K_6 \beta_y \beta_x^2 L \\
\frac{\partial^3 Q_x}{\partial J_y \partial \delta^2} = & -\frac{1}{8\pi} K_6 \beta_y \beta_x D_x^2 L \quad ; \quad \frac{\partial^3 Q_y}{\partial J_x \partial \delta^2} = -\frac{1}{8\pi} K_6 \beta_y \beta_x D_x^2 L \\
\frac{\partial^2 Q_x}{\partial J_x \partial J_y} = & -\frac{1}{32\pi} K_6 \beta_y \beta_x^2 L \quad ; \quad \frac{\partial^2 Q_y}{\partial J_y \partial J_x} = \frac{1}{32\pi} K_6 \beta_y^2 \beta_x L \\
\frac{\partial^4 Q_x}{\partial \delta^4} = & \frac{1}{4\pi} K_6 \beta_x D_x^4 L \quad ; \quad \frac{\partial^4 Q_y}{\partial \delta^4} = -\frac{1}{4\pi} K_6 \beta_y D_x^4 L
\end{aligned} \tag{B.19}$$

The contribution of dodecapoles to Chromatic Amplitude Detuning is then the following:

$$\begin{aligned}
 Q_z(\epsilon_x, \epsilon_y, \delta) = Q_{z0} + & \left[\frac{\partial Q_z}{\partial \epsilon_x} \epsilon_x + \frac{\partial Q_z}{\partial \epsilon_y} \epsilon_y + \frac{\partial Q_z}{\partial \delta} \delta \right] \\
 & + \frac{1}{2!} \left[\frac{\partial^2 Q_z}{\partial \epsilon_x^2} \epsilon_x^2 + \frac{\partial^2 Q_z}{\partial \epsilon_y^2} \epsilon_y^2 + 2 \frac{\partial^2 Q_z}{\partial \epsilon_x \partial \epsilon_y} \epsilon_x \epsilon_y + \dots \right] \\
 & + \frac{1}{3!} \left[3 \frac{\partial^3 Q_z}{\partial \epsilon_x \partial \delta^2} \delta^2 \epsilon_x + 3 \frac{\partial^3 Q_z}{\partial \epsilon_y \partial \delta^2} \delta^2 \epsilon_y + \dots \right] \\
 & + \frac{1}{4!} \left[\frac{\partial^4 Q_z}{\partial \delta^4} \delta^4 \right]
 \end{aligned} \tag{B.20}$$

B

B.2. PTC Validation

A simulation has been done with PTC to assess that those equations are correct. A dodecapole has been added to the lattice with a strength $KL = 1e^6$. Here are the results, confirming PTC works as intended.

The ANH numbers refer to the partial derivative relative to J_x, J_y and δ . So ANHX 021 would for example be $\frac{\partial^3 Q_x}{\partial J_y^2 \partial \delta}$.

Term	Analytical	Simulation	Rel. Diff [%]
ANH X 200	4782639.96971	4782639.97	0.0
ANH X 102	86945.930342	86945.93	-0.0
ANH X 020	593469879.552116	593469880.01	0.0
ANH X 012	-1118366.433407	-1118366.433	-0.0
ANH X 110	-92277073.535598	-92277073.6	0.0
ANH X 004	1053.754809	1053.7548	-0.000001
ANH Y 200	-92277073.535598	-92277073.6	0.0
ANH Y 102	-1118366.433407	-1118366.433	-0.0
ANH Y 020	-1272278817.264865	-1272278818.913	0.0
ANH Y 012	3596325.539479	3596325.543	0.0
ANH Y 110	593469879.552116	593469880.01	0.0
ANH Y 004	-6777.108503	-6777.1085	-0.0

B

Resonance Driving Terms

This appendix intends to clarify where Resonance Driving Terms can be seen in the frequency spectrum, what resonance they contribute to and what their action dependance is.

C.1. Expressions

The number of valid RDTs indeed grows rapidly with the magnet order n , as shows Table C.1, and is given by the following combinations:

$$C(n+3, 3) - C(n+1, 1) - [(n+1) \bmod 2] \cdot C\left(\left\lfloor \frac{n}{2} \right\rfloor + 1, 1\right). \quad (\text{C.1})$$

Multipole	Order	Number of poles	Number of RDTs
Quadrupole	2	4	5
Sextupole	3	6	16
Octupole	4	8	27
Decapole	5	10	50
Dodecapole	6	12	73
Decatetrapole	7	14	112
Decahexapole	8	16	151
Hectopole	50	100	23349
Kilopole	500	1000	2.1×10^7

Table C.1.: Number of valid RDTs for a given multipole order

Several different RDTs can contribute to the same line, which can be observed in the horizontal or vertical spectrum. The tables below describe which RDTs contribute to a specific combination of line

C. Resonance Driving Terms

and plane. All tables have been computed up to the order 6, for octopoles. The line columns represents (Q_x, Q_y) . For example $(-1, 2)$ is $-1Q_x + 2Qy$.

As a reminder, for a given RDT f_{jklm} , we will observe:

$$\begin{aligned} (j - k)Q_x + (l - m)Q_y = p \in \mathbb{N} & \quad \text{excited resonance} \\ H(1 - j + k, m - l) & \quad \text{horizontal line, if } j \neq 0 \\ V(k - j, 1 - l + m) & \quad \text{vertical line, if } l \neq 0. \end{aligned} \quad (C.2)$$

The amplitude of each line is given by:

$$\begin{aligned} |H_{f_{jklm}}| &= 2j(2I_x)^{\frac{j+k-1}{2}}(2I_y)^{\frac{l+m}{2}}|f_{jklm}| \\ |V_{f_{jklm}}| &= 2l(2I_x)^{\frac{j+k}{2}}(2I_y)^{\frac{l+m-1}{2}}|f_{jklm}|. \end{aligned} \quad (C.3)$$

According to Eq. (C.2) and Eq. (C.3), it can be seen that many RDTs will not contribute to any line and thus can not be observed.

C.2. Frequency Spectrum Lines

The following Table C.2 shows which RDTs can be seen at a factor $Q_x \pm Q_y$ in the vertical or horizontal spectrums. This table is mostly useful when trying to identify which multipole or RDT contributes to a specific line that can appear during measurements.

Q_x	Q_y	H-jklm	V-jklm
-5	0	6000	5010
-4	-1	5010	4020
-4	0	5000	4010
-4	1	5001	4011
-3	-2	4020	3030
-3	-1	4010	3020
-3	0	4000, 4011, 5100	3010, 3021, 4110
-3	1	4001	3011
-3	2	4002	3012
-2	-3	3030	2040
-2	-2	3020	2030
-2	-1	3010, 3021, 4110	2020, 2031, 3120
-2	0	3000, 3011, 4100	2010, 2021, 3110
-2	1	3001, 3012, 4101	2011, 2022, 3111
-2	2	3002	2012

Q_x	Q_y	H-jklm	V-jklm
-2	3	3003	2013
-1	-4	2040	1050
-1	-3	2030	1040
-1	-2	2020, 2031, 3120	1030, 1041, 2130
-1	-1	2010, 2021, 3110	1020, 1031, 2120
-1	0	2000, 2011, 3100, 2022, 3111, 4200	1010, 1021, 2110, 1032, 2121, 3210
-1	1	2001, 2012, 3101	1011, 1022, 2111
-1	2	2002, 2013, 3102	1012, 1023, 2112
-1	3	2003	1013
-1	4	2004	1014
0	-5	1050	0060
0	-4	1040	0050
0	-3	1030, 1041, 2130	0040, 0051, 1140
0	-2	1020, 1031, 2120	0030, 0041, 1130
0	-1	1010, 1021, 2110, 1032, 2121, 3210	0020, 0031, 1120, 0042, 1131, 2220
0	0	1011, 2100, 1022, 2111, 3200	0021, 1110, 0032, 1121, 2210
0	1	1001, 1012, 2101, 1023, 2112, 3201	
0	2	1002, 1013, 2102	0012, 0023, 1112
0	3	1003, 1014, 2103	0013, 0024, 1113
0	4	1004	0014
0	5	1005	0015
1	-4	1140	0150
1	-3	1130	0140
1	-2	1120, 1131, 2220	0130, 0141, 1230
1	0		0110, 0121, 1210, 0132, 1221, 2310
1	-1	1110, 1121, 2210	0120, 0131, 1220
1	1	1101, 1112, 2201	0111, 0122, 1211
1	2	1102, 1113, 2202	0112, 0123, 1212
1	3	1103	0113
1	4	1104	0114
2	-3	1230	0240
2	-2	1220	0230
2	-1	1210, 1221, 2310	0220, 0231, 1320
2	0	1200, 1211, 2300	0210, 0221, 1310
2	1	1201, 1212, 2301	0211, 0222, 1311
2	2	1202	0212
2	3	1203	0213
3	-2	1320	0330
3	-1	1310	0320
3	0	1300, 1311, 2400	0310, 0321, 1410
3	1	1301	0311
3	2	1302	0312

C. Resonance Driving Terms

Q_x	Q_y	H-jklm	V-jklm
4	-1	1410	0420
4	0	1400	0410
4	1	1401	0411
5	0	1500	0510

Table C.2.: Correspondence of Resonance Driving Terms to the lines seen in the horizontal or vertical frequency spectrum, up to dodecapoles ($n = 6$).

C.3. Amplitude, Resonances and Lines

This part focuses on individual Resonance Drivings Terms, detailing what magnet they originate from, what resonance they excite, how they can be observed and what kicks are needed in order to measure them. The amplitude columns implicitly omits the term $|f_{jklm}|$, which depends on K and J . The color coding helps quickly identifying dependences:

- I_x : depends only on horizontal amplitude
- I_y : depends only on vertical amplitude
- $I_x I_y$: depends on both horizontal and vertical amplitudes

n	jklm	Type	Resonance	H-line	V-line	Amplitude H	Amplitude V
2	0020	normal	(0, 2)		(0, -1)		$4(2I_y)^{1/2}$
2	2000	normal	(2, 0)	(-1, 0)		$4(2I_x)^{1/2}$	
2	0110	skew	(-1, 1)		(1, 0)		$2(2I_x)^{1/2}$
2	1001	skew	(1, -1)	(0, 1)		$2(2I_y)^{1/2}$	
2	1010	skew	(1, 1)	(0, -1)	(-1, 0)	$2(2I_y)^{1/2}$	$2(2I_x)^{1/2}$
3	0111	normal	(-1, 0)		(1, 1)		$2(2I_x)^{1/2}(2I_y)^{1/2}$
3	0120	normal	(-1, 2)		(1, -1)		$4(2I_x)^{1/2}(2I_y)^{1/2}$
3	1002	normal	(1, -2)	(0, 2)		$2(2I_y)$	
3	1011	normal	(1, 0)	(0, 0)	(-1, 1)	$2(2I_y)$	$2(2I_x)^{1/2}(2I_y)^{1/2}$
3	1020	normal	(1, 2)	(0, -2)	(-1, -1)	$2(2I_y)$	$4(2I_x)^{1/2}(2I_y)^{1/2}$
3	1200	normal	(-1, 0)	(2, 0)		$2(2I_x)$	
3	2100	normal	(1, 0)	(0, 0)		$4(2I_x)$	
3	3000	normal	(3, 0)	(-2, 0)		$6(2I_x)$	
3	0012	skew	(0, -1)		(0, 2)		$2(2I_y)$
3	0021	skew	(0, 1)		(0, 0)		$4(2I_y)$
3	0030	skew	(0, 3)		(0, -2)		$6(2I_y)$
3	0210	skew	(-2, 1)		(2, 0)		$2(2I_x)$

n	jklm	Type	Resonance	H-line	V-line	Amplitude H	Amplitude V
3	1101	skew	(0, -1)	(1, 1)		$2(2I_x)^{1/2}(2I_y)^{1/2}$	
3	1110	skew	(0, 1)	(1, -1)	(0, 0)	$2(2I_x)^{1/2}(2I_y)^{1/2}$	$2(2I_x)$
3	2001	skew	(2, -1)	(-1, 1)		$4(2I_x)^{1/2}(2I_y)^{1/2}$	
3	2010	skew	(2, 1)	(-1, -1)	(-2, 0)	$4(2I_x)^{1/2}(2I_y)^{1/2}$	$2(2I_x)$
4	0013	normal	(0, -2)		(0, 3)		$2(2I_y)^{3/2}$
4	0031	normal	(0, 2)		(0, -1)		$6(2I_y)^{3/2}$
4	0040	normal	(0, 4)		(0, -3)		$8(2I_y)^{3/2}$
4	0211	normal	(-2, 0)		(2, 1)		$2(2I_x)(2I_y)^{1/2}$
4	0220	normal	(-2, 2)		(2, -1)		$4(2I_x)(2I_y)^{1/2}$
4	1102	normal	(0, -2)	(1, 2)		$2(2I_x)^{1/2}(2I_y)$	
4	1120	normal	(0, 2)	(1, -2)	(0, -1)	$2(2I_x)^{1/2}(2I_y)$	$4(2I_x)(2I_y)^{1/2}$
4	1300	normal	(-2, 0)	(3, 0)		$2(2I_x)^{3/2}$	
4	2002	normal	(2, -2)	(-1, 2)		$4(2I_x)^{1/2}(2I_y)$	
4	2011	normal	(2, 0)	(-1, 0)	(-2, 1)	$4(2I_x)^{1/2}(2I_y)$	$2(2I_x)(2I_y)^{1/2}$
4	2020	normal	(2, 2)	(-1, -2)	(-2, -1)	$4(2I_x)^{1/2}(2I_y)$	$4(2I_x)(2I_y)^{1/2}$
4	3100	normal	(2, 0)	(-1, 0)		$6(2I_x)^{3/2}$	
4	4000	normal	(4, 0)	(-3, 0)		$8(2I_x)^{3/2}$	
4	0112	skew	(-1, -1)		(1, 2)		$2(2I_x)^{1/2}(2I_y)$
4	0121	skew	(-1, 1)		(1, 0)		$4(2I_x)^{1/2}(2I_y)$
4	0130	skew	(-1, 3)		(1, -2)		$6(2I_x)^{1/2}(2I_y)$
4	0310	skew	(-3, 1)		(3, 0)		$2(2I_x)^{3/2}$
4	1003	skew	(1, -3)	(0, 3)		$2(2I_y)^{3/2}$	
4	1012	skew	(1, -1)	(0, 1)	(-1, 2)	$2(2I_y)^{3/2}$	$2(2I_x)^{1/2}(2I_y)$
4	1021	skew	(1, 1)	(0, -1)	(-1, 0)	$2(2I_y)^{3/2}$	$4(2I_x)^{1/2}(2I_y)$
4	1030	skew	(1, 3)	(0, -3)	(-1, -2)	$2(2I_y)^{3/2}$	$6(2I_x)^{1/2}(2I_y)$
4	1201	skew	(-1, -1)	(2, 1)		$2(2I_x)(2I_y)^{1/2}$	
4	1210	skew	(-1, 1)	(2, -1)	(1, 0)	$2(2I_x)(2I_y)^{1/2}$	$2(2I_x)^{3/2}$
4	2101	skew	(1, -1)	(0, 1)		$4(2I_x)(2I_y)^{1/2}$	
4	2110	skew	(1, 1)	(0, -1)	(-1, 0)	$4(2I_x)(2I_y)^{1/2}$	$2(2I_x)^{3/2}$
4	3001	skew	(3, -1)	(-2, 1)		$6(2I_x)(2I_y)^{1/2}$	
4	3010	skew	(3, 1)	(-2, -1)	(-3, 0)	$6(2I_x)(2I_y)^{1/2}$	$2(2I_x)^{3/2}$
5	0113	normal	(-1, -2)		(1, 3)		$2(2I_x)^{1/2}(2I_y)^{3/2}$
5	0122	normal	(-1, 0)		(1, 1)		$4(2I_x)^{1/2}(2I_y)^{3/2}$
5	0131	normal	(-1, 2)		(1, -1)		$6(2I_x)^{1/2}(2I_y)^{3/2}$
5	0140	normal	(-1, 4)		(1, -3)		$8(2I_x)^{1/2}(2I_y)^{3/2}$

C. Resonance Driving Terms

n	jklm	Type	Resonance	H-line	V-line	Amplitude H	Amplitude V
5	0311	normal	(-3, 0)		(3, 1)		$2(2I_x)^{3/2}(2I_y)^{1/2}$
5	0320	normal	(-3, 2)		(3, -1)		$4(2I_x)^{3/2}(2I_y)^{1/2}$
5	1004	normal	(1, -4)	(0, 4)		$2(2I_y)^2$	
5	1013	normal	(1, -2)	(0, 2)	(-1, 3)	$2(2I_y)^2$	$2(2I_x)^{1/2}(2I_y)^{3/2}$
5	1022	normal	(1, 0)	(0, 0)	(-1, 1)	$2(2I_y)^2$	$4(2I_x)^{1/2}(2I_y)^{3/2}$
5	1031	normal	(1, 2)	(0, -2)	(-1, -1)	$2(2I_y)^2$	$6(2I_x)^{1/2}(2I_y)^{3/2}$
5	1040	normal	(1, 4)	(0, -4)	(-1, -3)	$2(2I_y)^2$	$8(2I_x)^{1/2}(2I_y)^{3/2}$
5	1202	normal	(-1, -2)	(2, 2)		$2(2I_x)(2I_y)$	
5	1211	normal	(-1, 0)	(2, 0)	(1, 1)	$2(2I_x)(2I_y)$	$2(2I_x)^{3/2}(2I_y)^{1/2}$
5	1220	normal	(-1, 2)	(2, -2)	(1, -1)	$2(2I_x)(2I_y)$	$4(2I_x)^{3/2}(2I_y)^{1/2}$
5	1400	normal	(-3, 0)	(4, 0)		$2(2I_x)^2$	
5	2102	normal	(1, -2)	(0, 2)		$4(2I_x)(2I_y)$	
5	2111	normal	(1, 0)	(0, 0)	(-1, 1)	$4(2I_x)(2I_y)$	$2(2I_x)^{3/2}(2I_y)^{1/2}$
5	2120	normal	(1, 2)	(0, -2)	(-1, -1)	$4(2I_x)(2I_y)$	$4(2I_x)^{3/2}(2I_y)^{1/2}$
5	2300	normal	(-1, 0)	(2, 0)		$4(2I_x)^2$	
5	3002	normal	(3, -2)	(-2, 2)		$6(2I_x)(2I_y)$	
5	3011	normal	(3, 0)	(-2, 0)	(-3, 1)	$6(2I_x)(2I_y)$	$2(2I_x)^{3/2}(2I_y)^{1/2}$
5	3020	normal	(3, 2)	(-2, -2)	(-3, -1)	$6(2I_x)(2I_y)$	$4(2I_x)^{3/2}(2I_y)^{1/2}$
5	3200	normal	(1, 0)	(0, 0)		$6(2I_x)^2$	
5	4100	normal	(3, 0)	(-2, 0)		$8(2I_x)^2$	
5	5000	normal	(5, 0)	(-4, 0)		$10(2I_x)^2$	
5	0014	skew	(0, -3)		(0, 4)		$2(2I_y)^2$
5	0023	skew	(0, -1)		(0, 2)		$4(2I_y)^2$
5	0032	skew	(0, 1)		(0, 0)		$6(2I_y)^2$
5	0041	skew	(0, 3)		(0, -2)		$8(2I_y)^2$
5	0050	skew	(0, 5)		(0, -4)		$10(2I_y)^2$
5	0212	skew	(-2, -1)		(2, 2)		$2(2I_x)(2I_y)$
5	0221	skew	(-2, 1)		(2, 0)		$4(2I_x)(2I_y)$
5	0230	skew	(-2, 3)		(2, -2)		$6(2I_x)(2I_y)$
5	0410	skew	(-4, 1)		(4, 0)		$2(2I_x)^2$
5	1103	skew	(0, -3)	(1, 3)		$2(2I_x)^{1/2}(2I_y)^{3/2}$	
5	1112	skew	(0, -1)	(1, 1)	(0, 2)	$2(2I_x)^{1/2}(2I_y)^{3/2}$	$2(2I_x)(2I_y)$
5	1121	skew	(0, 1)	(1, -1)	(0, 0)	$2(2I_x)^{1/2}(2I_y)^{3/2}$	$4(2I_x)(2I_y)$
5	1130	skew	(0, 3)	(1, -3)	(0, -2)	$2(2I_x)^{1/2}(2I_y)^{3/2}$	$6(2I_x)(2I_y)$
5	1301	skew	(-2, -1)	(3, 1)		$2(2I_x)^{3/2}(2I_y)^{1/2}$	
5	1310	skew	(-2, 1)	(3, -1)	(2, 0)	$2(2I_x)^{3/2}(2I_y)^{1/2}$	$2(2I_x)^2$

C.3. Amplitude, Resonances and Lines

n	jklm	Type	Resonance	H-line	V-line	Amplitude H	Amplitude V
5	2003	skew	(2, -3)	(-1, 3)		$4(2I_x)^{1/2}(2I_y)^{3/2}$	
5	2012	skew	(2, -1)	(-1, 1)	(-2, 2)	$4(2I_x)^{1/2}(2I_y)^{3/2}$	$2(2I_x)(2I_y)$
5	2021	skew	(2, 1)	(-1, -1)	(-2, 0)	$4(2I_x)^{1/2}(2I_y)^{3/2}$	$4(2I_x)(2I_y)$
5	2030	skew	(2, 3)	(-1, -3)	(-2, -2)	$4(2I_x)^{1/2}(2I_y)^{3/2}$	$6(2I_x)(2I_y)$
5	2201	skew	(0, -1)	(1, 1)		$4(2I_x)^{3/2}(2I_y)^{1/2}$	
5	2210	skew	(0, 1)	(1, -1)	(0, 0)	$4(2I_x)^{3/2}(2I_y)^{1/2}$	$2(2I_x)^2$
5	3101	skew	(2, -1)	(-1, 1)		$6(2I_x)^{3/2}(2I_y)^{1/2}$	
5	3110	skew	(2, 1)	(-1, -1)	(-2, 0)	$6(2I_x)^{3/2}(2I_y)^{1/2}$	$2(2I_x)^2$
5	4001	skew	(4, -1)	(-3, 1)		$8(2I_x)^{3/2}(2I_y)^{1/2}$	
5	4010	skew	(4, 1)	(-3, -1)	(-4, 0)	$8(2I_x)^{3/2}(2I_y)^{1/2}$	$2(2I_x)^2$
6	0015	normal	(0, -4)		(0, 5)		$2(2I_y)^{5/2}$
6	0024	normal	(0, -2)		(0, 3)		$4(2I_y)^{5/2}$
6	0042	normal	(0, 2)		(0, -1)		$8(2I_y)^{5/2}$
6	0051	normal	(0, 4)		(0, -3)		$10(2I_y)^{5/2}$
6	0060	normal	(0, 6)		(0, -5)		$12(2I_y)^{5/2}$
6	0213	normal	(-2, -2)		(2, 3)		$2(2I_x)(2I_y)^{3/2}$
6	0222	normal	(-2, 0)		(2, 1)		$4(2I_x)(2I_y)^{3/2}$
6	0231	normal	(-2, 2)		(2, -1)		$6(2I_x)(2I_y)^{3/2}$
6	0240	normal	(-2, 4)		(2, -3)		$8(2I_x)(2I_y)^{3/2}$
6	0411	normal	(-4, 0)		(4, 1)		$2(2I_x)^2(2I_y)^{1/2}$
6	0420	normal	(-4, 2)		(4, -1)		$4(2I_x)^2(2I_y)^{1/2}$
6	1104	normal	(0, -4)	(1, 4)		$2(2I_x)^{1/2}(2I_y)^2$	
6	1113	normal	(0, -2)	(1, 2)	(0, 3)	$2(2I_x)^{1/2}(2I_y)^2$	$2(2I_x)(2I_y)^{3/2}$
6	1131	normal	(0, 2)	(1, -2)	(0, -1)	$2(2I_x)^{1/2}(2I_y)^2$	$6(2I_x)(2I_y)^{3/2}$
6	1140	normal	(0, 4)	(1, -4)	(0, -3)	$2(2I_x)^{1/2}(2I_y)^2$	$8(2I_x)(2I_y)^{3/2}$
6	1302	normal	(-2, -2)	(3, 2)		$2(2I_x)^{3/2}(2I_y)$	
6	1311	normal	(-2, 0)	(3, 0)	(2, 1)	$2(2I_x)^{3/2}(2I_y)$	$2(2I_x)^2(2I_y)^{1/2}$
6	1320	normal	(-2, 2)	(3, -2)	(2, -1)	$2(2I_x)^{3/2}(2I_y)$	$4(2I_x)^2(2I_y)^{1/2}$
6	1500	normal	(-4, 0)	(5, 0)		$2(2I_x)^{5/2}$	
6	2004	normal	(2, -4)	(-1, 4)		$4(2I_x)^{1/2}(2I_y)^2$	
6	2013	normal	(2, -2)	(-1, 2)	(-2, 3)	$4(2I_x)^{1/2}(2I_y)^2$	$2(2I_x)(2I_y)^{3/2}$
6	2022	normal	(2, 0)	(-1, 0)	(-2, 1)	$4(2I_x)^{1/2}(2I_y)^2$	$4(2I_x)(2I_y)^{3/2}$
6	2031	normal	(2, 2)	(-1, -2)	(-2, -1)	$4(2I_x)^{1/2}(2I_y)^2$	$6(2I_x)(2I_y)^{3/2}$
6	2040	normal	(2, 4)	(-1, -4)	(-2, -3)	$4(2I_x)^{1/2}(2I_y)^2$	$8(2I_x)(2I_y)^{3/2}$
6	2202	normal	(0, -2)	(1, 2)		$4(2I_x)^{3/2}(2I_y)$	

C. Resonance Driving Terms

n	jklm	Type	Resonance	H-line	V-line	Amplitude H	Amplitude V
6	2220	normal	(0, 2)	(1, -2)	(0, -1)	$4(2I_x)^{3/2}(2I_y)$	$4(2I_x)^2(2I_y)^{1/2}$
6	2400	normal	(-2, 0)	(3, 0)		$4(2I_x)^{5/2}$	
6	3102	normal	(2, -2)	(-1, 2)		$6(2I_x)^{3/2}(2I_y)$	
6	3111	normal	(2, 0)	(-1, 0)	(-2, 1)	$6(2I_x)^{3/2}(2I_y)$	$2(2I_x)^2(2I_y)^{1/2}$
6	3120	normal	(2, 2)	(-1, -2)	(-2, -1)	$6(2I_x)^{3/2}(2I_y)$	$4(2I_x)^2(2I_y)^{1/2}$
6	4002	normal	(4, -2)	(-3, 2)		$8(2I_x)^{3/2}(2I_y)$	
6	4011	normal	(4, 0)	(-3, 0)	(-4, 1)	$8(2I_x)^{3/2}(2I_y)$	$2(2I_x)^2(2I_y)^{1/2}$
6	4020	normal	(4, 2)	(-3, -2)	(-4, -1)	$8(2I_x)^{3/2}(2I_y)$	$4(2I_x)^2(2I_y)^{1/2}$
6	4200	normal	(2, 0)	(-1, 0)		$8(2I_x)^{5/2}$	
6	5100	normal	(4, 0)	(-3, 0)		$10(2I_x)^{5/2}$	
6	6000	normal	(6, 0)	(-5, 0)		$12(2I_x)^{5/2}$	
6	0114	skew	(-1, -3)		(1, 4)		$2(2I_x)^{1/2}(2I_y)^2$
6	0123	skew	(-1, -1)		(1, 2)		$4(2I_x)^{1/2}(2I_y)^2$
6	0132	skew	(-1, 1)		(1, 0)		$6(2I_x)^{1/2}(2I_y)^2$
6	0141	skew	(-1, 3)		(1, -2)		$8(2I_x)^{1/2}(2I_y)^2$
6	0150	skew	(-1, 5)		(1, -4)		$10(2I_x)^{1/2}(2I_y)^2$
6	0312	skew	(-3, -1)		(3, 2)		$2(2I_x)^{3/2}(2I_y)$
6	0321	skew	(-3, 1)		(3, 0)		$4(2I_x)^{3/2}(2I_y)$
6	0330	skew	(-3, 3)		(3, -2)		$6(2I_x)^{3/2}(2I_y)$
6	0510	skew	(-5, 1)		(5, 0)		$2(2I_x)^{5/2}$
6	1005	skew	(1, -5)	(0, 5)		$2(2I_y)^{5/2}$	
6	1014	skew	(1, -3)	(0, 3)	(-1, 4)	$2(2I_y)^{5/2}$	$2(2I_x)^{1/2}(2I_y)^2$
6	1023	skew	(1, -1)	(0, 1)	(-1, 2)	$2(2I_y)^{5/2}$	$4(2I_x)^{1/2}(2I_y)^2$
6	1032	skew	(1, 1)	(0, -1)	(-1, 0)	$2(2I_y)^{5/2}$	$6(2I_x)^{1/2}(2I_y)^2$
6	1041	skew	(1, 3)	(0, -3)	(-1, -2)	$2(2I_y)^{5/2}$	$8(2I_x)^{1/2}(2I_y)^2$
6	1050	skew	(1, 5)	(0, -5)	(-1, -4)	$2(2I_y)^{5/2}$	$10(2I_x)^{1/2}(2I_y)^2$
6	1203	skew	(-1, -3)	(2, 3)		$2(2I_x)(2I_y)^{3/2}$	
6	1212	skew	(-1, -1)	(2, 1)	(1, 2)	$2(2I_x)(2I_y)^{3/2}$	$2(2I_x)^{3/2}(2I_y)$
6	1221	skew	(-1, 1)	(2, -1)	(1, 0)	$2(2I_x)(2I_y)^{3/2}$	$4(2I_x)^{3/2}(2I_y)$
6	1230	skew	(-1, 3)	(2, -3)	(1, -2)	$2(2I_x)(2I_y)^{3/2}$	$6(2I_x)^{3/2}(2I_y)$
6	1401	skew	(-3, -1)	(4, 1)		$2(2I_x)^2(2I_y)^{1/2}$	
6	1410	skew	(-3, 1)	(4, -1)	(3, 0)	$2(2I_x)^2(2I_y)^{1/2}$	$2(2I_x)^{5/2}$
6	2103	skew	(1, -3)	(0, 3)		$4(2I_x)(2I_y)^{3/2}$	
6	2112	skew	(1, -1)	(0, 1)	(-1, 2)	$4(2I_x)(2I_y)^{3/2}$	$2(2I_x)^{3/2}(2I_y)$
6	2121	skew	(1, 1)	(0, -1)	(-1, 0)	$4(2I_x)(2I_y)^{3/2}$	$4(2I_x)^{3/2}(2I_y)$

C.3. Amplitude, Resonances and Lines

n	jklm	Type	Resonance	H-line	V-line	Amplitude H	Amplitude V
6	2130	skew	(1, 3)	(0, -3)	(-1, -2)	$4(2I_x)(2I_y)^{3/2}$	$6(2I_x)^{3/2}(2I_y)$
6	2301	skew	(-1, -1)	(2, 1)		$4(2I_x)^2(2I_y)^{1/2}$	
6	2310	skew	(-1, 1)	(2, -1)	(1, 0)	$4(2I_x)^2(2I_y)^{1/2}$	$2(2I_x)^{5/2}$
6	3003	skew	(3, -3)	(-2, 3)		$6(2I_x)(2I_y)^{3/2}$	
6	3012	skew	(3, -1)	(-2, 1)	(-3, 2)	$6(2I_x)(2I_y)^{3/2}$	$2(2I_x)^{3/2}(2I_y)$
6	3021	skew	(3, 1)	(-2, -1)	(-3, 0)	$6(2I_x)(2I_y)^{3/2}$	$4(2I_x)^{3/2}(2I_y)$
6	3030	skew	(3, 3)	(-2, -3)	(-3, -2)	$6(2I_x)(2I_y)^{3/2}$	$6(2I_x)^{3/2}(2I_y)$
6	3201	skew	(1, -1)	(0, 1)		$6(2I_x)^2(2I_y)^{1/2}$	
6	3210	skew	(1, 1)	(0, -1)	(-1, 0)	$6(2I_x)^2(2I_y)^{1/2}$	$2(2I_x)^{5/2}$
6	4101	skew	(3, -1)	(-2, 1)		$8(2I_x)^2(2I_y)^{1/2}$	
6	4110	skew	(3, 1)	(-2, -1)	(-3, 0)	$8(2I_x)^2(2I_y)^{1/2}$	$2(2I_x)^{5/2}$
6	5001	skew	(5, -1)	(-4, 1)		$10(2I_x)^2(2I_y)^{1/2}$	
6	5010	skew	(5, 1)	(-4, -1)	(-5, 0)	$10(2I_x)^2(2I_y)^{1/2}$	$2(2I_x)^{5/2}$

Table C.3.: Amplitude dependence, associated resonance and spectrum correspondence of Resonance Driving Terms up to dodecapoles ($n = 6$).

C

Bibliography

- [1] P.J. Bryant. “A brief history and review of accelerators”. In: *CAS - CERN Accelerator School : 5th General Accelerator Physics Course* (1994). DOI: [10.5170/CERN-1994-001.1](https://doi.org/10.5170/CERN-1994-001.1). URL: <https://cds.cern.ch/record/261062>.
- [2] Bryant Philip and Kurt Hübner. “CERN’s ISR: the world’s first hadron collider”. In: (2011). URL: <https://cerncourier.com/a/cerns-isr-the-worlds-first-hadron-collider/>.
- [3] *The CERN accelerator complex, layout in 2022*. 2022. URL: <https://cds.cern.ch/record/2800984>.
- [4] *CERN Resources Website*. URL: <https://home.cern/resources>.
- [5] J Gareyte, J P Koutchouk, and F Ruggiero. *Landau Damping, Dynamic Aperture and Octupoles in LHC*. LHC Project Report 91. CERN, 1997. URL: <https://cds.cern.ch/record/321824>.
- [6] Oliver Sim Brüning et al. *LHC Design Report*. 2004. DOI: [10.5170/CERN-2004-003-V-1](https://doi.org/10.5170/CERN-2004-003-V-1).
- [7] Jorg Wenniger. *LHC Modes*. Tech. rep. LHC-OP-ES-0022. 2019. URL: <https://edms.cern.ch/ui/file/1070479/2.1/LHC-OP-ES-0022-V2.1.pdf>.
- [8] L Bottura et al. *Pre-Cycles of the LHC Magnets during Operation*. Tech. rep. CERN-ATS-2010-174. 2010. URL: <https://cds.cern.ch/record/1283477>.
- [9] Félix Soubelet. “Local Interaction Region Coupling Correction for the LHC”. PhD thesis. 2023. URL: <https://cds.cern.ch/record/2891759>.
- [10] Joschua Dilly. “Corrections of High-Order Nonlinear Errors in the LHC and HL-LHC Beam Optics”. To Be Submitted. Humboldt University of Berlin, 2022.
- [11] Helmut Wiedemann. *Particle Accelerator Physics*. 4th. Graduate Texts in Physics. Cham: Springer International Publishing, 2015. DOI: [10.1007/978-3-319-18317-6](https://doi.org/10.1007/978-3-319-18317-6). URL: <http://link.springer.com/10.1007/978-3-319-18317-6>.
- [12] Rob Wolf. *Engineering Specification: Field Error Naming Conventions for LHC Magnets*. Tech. rep. LHC-M-ES-001.00. CERN, 2001. URL: <https://lhc-div-mms.web.cern.ch/lhc-div-mms/tests/MAG/FiDeL/Documentation/lhc-m-es-0001-30-00.pdf>.

Bibliography

- [13] B. J. Holzer et al. “Design and Principles of Synchrotrons and Circular Colliders”. In: *Particle Physics Reference Library : Volume 3: Accelerators and Colliders*. Ed. by Stephen Myers and Herwig Schopper. Cham: Springer International Publishing, 2020. doi: [10.1007/978-3-030-34245-6_6](https://doi.org/10.1007/978-3-030-34245-6_6). URL: https://doi.org/10.1007/978-3-030-34245-6_6.
- [14] Andrzej Wolski. *Beam Dynamics in High Energy Particle Accelerators*. London : Singapore ; Hackensack, NJ: Imperial College Press ; Distributed by World Scientific, 2014.
- [15] Laurent Deniau. *Magnetic model of Main Dipoles*. Technology Department. CERN, 2009.
- [16] P. Hagen et al. *Wise: An adaptive simulation of the LHC optics*. Tech. rep. 2006. URL: <https://cds.cern.ch/record/977794/files/lhc-project-report-971.pdf>.
- [17] *FiDeL - the magnetic model of the LHC*. 2021. URL: <https://lhc-div-mms.web.cern.ch/tests/MAG/Fidel/>.
- [18] E. D Courant and H. S Snyder. “Theory of the Alternating-Gradient Synchrotron”. In: *Annals of Physics* 3.1 (1958). doi: [10.1016/0003-4916\(58\)90012-5](https://doi.org/10.1016/0003-4916(58)90012-5). URL: <http://www.sciencedirect.com/science/article/pii/0003491658900125>.
- [19] S. Y. Lee. *Accelerator Physics*. Second. Hackensack, N.J: World Scientific, 2004.
- [20] A J Dragt. “An Overview of Lie Methods for Accelerator Physics”. In: *Proceedings of PAC*. Pasadena, CA USA: JACoW, 2013.
- [21] Ghislain J Roy. “Analysis of the optics of the Final Focus Test Beam using Lie algebra based techniques”. PhD thesis. 1992.
- [22] Etienne Forest. *Beam dynamics: a new attitude and framework*. The physics and technology of particle and photon beams 8. Amsterdam: Harwood Academic, 1998.
- [23] Fernando Casas and Ander Murua. “An efficient algorithm for computing the Baker-Campbell-Hausdorff series and some of its applications”. In: *Journal of Mathematical Physics* 50.3 (2009). doi: [10.1063/1.3078418](https://doi.org/10.1063/1.3078418). URL: <http://arxiv.org/abs/0810.2656>.
- [24] Felix Simon Carlier. “A Nonlinear Future: Measurements and Corrections of Nonlinear Beam Dynamics Using Forced Transverse Oscillations”. PhD Thesis. 2020. URL: <http://cds.cern.ch/record/2715765/>.
- [25] Andrea Franchi. “Studies and Measurements of Linear Coupling and Nonlinearities in Hadron Circular Accelerators”. Doctoral Thesis. Johann Wolfgang Goethe-Universität, 2006. URL: <https://publikationen.ub.uni-frankfurt.de/frontdoor/index/index/year/2006/docId/2270>.
- [26] Werner Herr. *Mathematical and Numerical Methods for Non-linear Beam Dynamics*. Tech. rep. CERN Accelerator School, 2018. URL: <http://arxiv.org/abs/2006.09052>.
- [27] Keintzel Jacqueline. “Beam Optics Design, Measurement and Correction Strategies for Circular Colliders at the Energy and Luminosity Frontier”. PhD thesis. 2022.

- [28] Joschua Dilly and Mael Le Garrec. *On the derivation of Amplitude Detuning and Chromaticity Formulas for Particle Accelerators*. 2023. URL: <http://arxiv.org/abs/2301.09132>.
- [29] Jacqueline Keintzel et al. “Second-Order Dispersion Measurement in LHC”. In: *IPAC’19*. Melbourne, Australia, 2019. doi: [10.18429/JACoW-IPAC2019-MOPMP027](https://doi.org/10.18429/JACoW-IPAC2019-MOPMP027).
- [30] R. Bartolini and F. Schmidt. “Normal Form via Tracking or Beam Data”. In: *Part. Accel.* 59.LHC-Project-Report-132 (1997).
- [31] M. Wendt. “BPM Systems: A Brief Introduction to Beam Position Monitoring”. In: *ArXiv200514081 Phys.* (2020). URL: <http://arxiv.org/abs/2005.14081>.
- [32] S Redaelli et al. “LHC Collimator Controls for a Safe LHC Operation”. In: vol. C111010. Grenoble, France, 2011. URL: <https://cds.cern.ch/record/1562636>.
- [33] R Schmidt. *Machine Protection*. 2014. doi: [10.5170/CERN-2014-009.221](https://doi.org/10.5170/CERN-2014-009.221). URL: <https://cds.cern.ch/record/1982423>.
- [34] P Odier, M Ludwig, and S Thoulet. “The DCCT for the LHC Beam Intensity Measurement”. In: Basel, Switzerland, 2009. URL: <https://epaper.kek.jp/d09/papers/mopd45.pdf>.
- [35] A. Boccardi et al. *First Results from the LHC BBQ Tune and Chromaticity Systems*. 2009. URL: <https://cds.cern.ch/record/1156349/>.
- [36] M. Gasior and R. Jones. *High Sensitivity Tune Measurement by Direct Diode Detection*. Tech. rep. CERN-AB-2005-060. 2005. URL: <https://cds.cern.ch/record/895142>.
- [37] R. Miyamoto et al. “Parametrization of the driven betatron oscillation”. In: *Physical Review Special Topics - Accelerators and Beams* 11.8 (2008). doi: [10.1103/PhysRevSTAB.11.084002](https://doi.org/10.1103/PhysRevSTAB.11.084002). URL: <https://link.aps.org/doi/10.1103/PhysRevSTAB.11.084002>.
- [38] Javier Serrano and Matthieu Cattin. *The LHC AC Dipole system: an introduction*. 2010.
- [39] R. Tomás. “Normal Form of Particle Motion under the Influence of an Ac Dipole”. In: *Phys. Rev. ST Accel. Beams* 5.5 (2002). doi: [10.1103/PhysRevSTAB.5.054001](https://doi.org/10.1103/PhysRevSTAB.5.054001). URL: <https://link.aps.org/doi/10.1103/PhysRevSTAB.5.054001>.
- [40] S. White, Ewen Hamish Maclean, and R. Tomás. “Direct Amplitude Detuning Measurement with Ac Dipole”. In: *Phys. Rev. ST Accel. Beams* 16.7 (2013). doi: [10.1103/PhysRevSTAB.16.071002](https://doi.org/10.1103/PhysRevSTAB.16.071002). URL: <https://link.aps.org/doi/10.1103/PhysRevSTAB.16.071002>.
- [41] Laurent Deniau et al. *MAD-X User Guide*. URL: <http://cern.ch/madx/releases/last-rel/madxuguide.pdf>.
- [42] Laurent Deniau, Joschua Gray, and Riccardo De Maria. *MAD-NG*. 2020. URL: <https://github.com/MethodicalAcceleratorDesign/MAD-NG>.
- [43] G. Iadarola et al. *Xsuite*. URL: <https://github.com/xsuite/xsuite>.
- [44] M. Le Garrec. *Non-linear Chromaticity GUI*. 2022. URL: <https://gitlab.cern.ch/mlegarre/nl-chroma-gui>.

Bibliography

- [45] OMC-Team et al. *PyLHC v0.3.0*. 2021. doi: [10.5281/ZENODO.5705041](https://doi.org/10.5281/ZENODO.5705041).
- [46] N. Catalan-Lasheras, Stéphane David Fartoukh, and Jean-Pierre Koutchouk. *Linear Optics Measurements Using an AC-Dipole Excitation*. Tech. rep. 2004. URL: <http://cds.cern.ch/record/712136>.
- [47] Michiko G. Minty and Frank Zimmermann. *Measurement and Control of Charged Particle Beams*. Particle Acceleration and Detection. Berlin, Heidelberg: Springer Berlin Heidelberg, 2003. doi: [10.1007/978-3-662-08581-3](https://doi.org/10.1007/978-3-662-08581-3). URL: <http://link.springer.com/10.1007/978-3-662-08581-3>.
- [48] A. Langner et al. “Utilizing the N Beam Position Monitor Method for Turn-by-Turn Optics Measurements”. In: *Phys. Rev. Accel. Beams* 19.9 (2016). doi: [10.1103/PhysRevAccelBeams.19.092803](https://doi.org/10.1103/PhysRevAccelBeams.19.092803). URL: <https://link.aps.org/doi/10.1103/PhysRevAccelBeams.19.092803>.
- [49] A. Wegscheider et al. “Analytical N beam position monitor method”. In: *Physical Review Accelerators and Beams* 20.11 (2017). doi: [10.1103/PhysRevAccelBeams.20.111002](https://doi.org/10.1103/PhysRevAccelBeams.20.111002). URL: <https://link.aps.org/doi/10.1103/PhysRevAccelBeams.20.111002>.
- [50] Ana García-Tabarés Valdivieso and Rogelio Tomás. “Optics-Measurement-Based Beam Position Monitor Calibrations in the LHC Insertion Regions”. In: *Phys. Rev. Accel. Beams* 23.4 (2020). doi: [10.1103/PhysRevAccelBeams.23.042801](https://doi.org/10.1103/PhysRevAccelBeams.23.042801). URL: <https://link.aps.org/doi/10.1103/PhysRevAccelBeams.23.042801>.
- [51] A. Franchi, Rogelio Tomás, and G. Vanbavinkhove. *Computation of the Coupling Resonance Driving Term F1001 and the Coupling Coefficient C from Turn-by-Turn Single-BPM Data*. Tech. rep. 2010. URL: <http://cds.cern.ch/record/1264111>.
- [52] R. Tomás et al. “CERN Large Hadron Collider Optics Model, Measurements, and Corrections”. In: *Phys. Rev. ST Accel. Beams* 13.12 (2010). doi: [10.1103/PhysRevSTAB.13.121004](https://doi.org/10.1103/PhysRevSTAB.13.121004). URL: <https://link.aps.org/doi/10.1103/PhysRevSTAB.13.121004>.
- [53] Félix Simon Carlier. “A nonlinear future: measurements and corrections of nonlinear beam dynamics using forced transverse oscillations”. PhD thesis. 2020.
- [54] Ewen Hamish Maclean et al. *Commissioning of the nonlinear chromaticity at injection for LHC Run II*. Accelerators & Technology Sector Note 2016-0013. 2016. URL: <https://cds.cern.ch/record/2121333>.
- [55] E. H. Maclean et al. “New Approach to LHC Optics Commissioning for the Nonlinear Era”. In: *Phys. Rev. Accel. Beams* 22.6 (2019). doi: [10.1103/PhysRevAccelBeams.22.061004](https://doi.org/10.1103/PhysRevAccelBeams.22.061004). URL: <https://link.aps.org/doi/10.1103/PhysRevAccelBeams.22.061004>.
- [56] E. H. Maclean et al. “First Measurement and Correction of Nonlinear Errors in the Experimental Insertions of the CERN Large Hadron Collider”. In: *Phys. Rev. ST Accel. Beams* 18 (2015). doi: [10.1103/PhysRevSTAB.18.121002](https://doi.org/10.1103/PhysRevSTAB.18.121002). URL: <https://doi.org/10.1103/PhysRevSTAB.18.121002>.
- [57] D Missiaen et al. “The Final Alignment of the LHC”. In: KEK, Tsukuba, Japan, 2008.

- [58] Armando Bazzani et al. *A Normal Form Approach to the Theory of Nonlinear Betatronic Motion*. CERN Yellow Reports: Monographs. Geneva: CERN, 1994. URL: <http://cds.cern.ch/record/262179>.
- [59] E H Maclean et al. “Non-linear Chromaticity Studies of the LHC at Injection”. In: *Proc. IPAC’11*. San Sebastian, Spain, Sep. 2011: JACoW Publishing, Geneva, Switzerland, 2011. URL: <https://jacow.org/IPAC2011/papers/WEPC078.pdf>.
- [60] Ewen Hamish Maclean, Felix Simon Carlier, and Jaime Coello de Portugal. “Commissioning of Non-linear Optics in the LHC at Injection Energy”. In: *Proc. IPAC*. Busan, Korea, 2016. doi: [10.18429/JACoW-IPAC2016-THPMR039](https://doi.org/10.18429/JACoW-IPAC2016-THPMR039). URL: <https://cds.cern.ch/record/2207446>.
- [61] Ewen Hamish Maclean et al. “Measurement of Nonlinear Observables in the Large Hadron Collider Using Kicked Beams”. In: *Phys. Rev. ST Accel. Beams* 17.8 (2014). doi: [10.1103/PhysRevSTAB.17.081002](https://doi.org/10.1103/PhysRevSTAB.17.081002). URL: <https://link.aps.org/doi/10.1103/PhysRevSTAB.17.081002>.
- [62] W. Venturini Delsolaro and R Wolf. *Magnetic Behavior of LHC Superconducting Correctors: Issues for Machine Operation*. Tech. rep. 2005. URL: <https://cds.cern.ch/record/987834/>.
- [63] *Ten out of ten for LHC decapole magnets*. Tech. rep. BUL-NA-2001-041. 2001. URL: <https://cds.cern.ch/record/45154>.
- [64] N J Sammut and L Bottura. “The Dependence of the Field Decay on the Powering History of the LHC Superconducting Dipole Magnets”. In: Edinburgh, Scotland, 2006.
- [65] M Haverkamp, L Bottura, and M Schneider. *Studies of Decay and Snapback Effects on LHC Dipole Magnets*. Tech. rep. 1999.
- [66] Yannis Papaphilippou. “Detecting chaos in particle accelerators through the frequency map analysis method”. In: *arXiv:1406.1545* (2014). doi: <https://doi.org/10.48550/arXiv.1406.1545>. URL: <https://cds.cern.ch/record/1708155/>.
- [67] Riccardo de Maria. “LHC Interaction region upgrade”. PhD thesis. 2008. URL: <https://cds.cern.ch/record/1127611>.
- [68] Ewen H. Maclean et al. “Prospects for beam-based study of dodecapole nonlinearities in the CERN High-Luminosity Large Hadron Collider”. In: *The European Physical Journal Plus* 137.11 (2022). doi: [10.1140/epjp/s13360-022-03367-2](https://doi.org/10.1140/epjp/s13360-022-03367-2). URL: <https://link.springer.com/10.1140/epjp/s13360-022-03367-2>.
- [69] Laurent Deniau. *Private communication*. 2024.
- [70] Demin Zhou et al. *Luminosity performance of SuperKEKB*. 2023. URL: <http://arxiv.org/abs/2306.02692>.
- [71] *Operation of the SuperKEKB accelerator restarted after upgrades*. 2024. URL: <https://www.kek.jp/en/topics/202402291200>.

Bibliography

- [72] Jacqueline Keintzel et al. “SuperKEKB Optics Measurements Using Turn-by-Turn Beam Position Data”. In: *Proceedings of the 12th International Particle Accelerator Conference IPAC2021* (2021). doi: [10.18429/JACOW-IPAC2021-TUPAB009](https://doi.org/10.18429/JACOW-IPAC2021-TUPAB009). URL: <https://jacow.org/ipac2021/doi/JACoW-IPAC2021-TUPAB009.html>.
- [73] Jacqueline Keintzel et al. “Impact of Bunch Current on Optics Measurements in SuperKEKB”. In: *Proceedings of the 12th International Particle Accelerator Conference IPAC2021* (2021). doi: [10.18429/JACOW-IPAC2021-TUPAB010](https://doi.org/10.18429/JACOW-IPAC2021-TUPAB010). URL: <https://jacow.org/ipac2021/doi/JACoW-IPAC2021-TUPAB010.html>.
- [74] Y Ohnishi et al. “Optics Correction in KEKB Commissioning”. In: (1999).
- [75] M Harrison and S Peggs. “GLOBAL BETA MEASUREMENT FROM TWO PERTURBED CLOSED ORBITS”. In: (1987).
- [76] Y. Chung, G. Decker, and K. Evans. “Measurement of beta-function and phase using the response matrix”. In: *Proceedings of International Conference on Particle Accelerators*. Washington, DC, USA: IEEE, 1993. doi: [10.1109/pac.1993.308986](https://doi.org/10.1109/pac.1993.308986). URL: <http://ieeexplore.ieee.org/document/308986/>.
- [77] *SAD Home Page – Strategic Accelerator Design*. URL: <https://acc-physics.kek.jp/SAD/>.
- [78] OMC-Team et al. *OMC3*. 2021. doi: [10.5281/ZENODO.5705625](https://doi.org/10.5281/ZENODO.5705625). URL: <https://github.com/pylhc/omc3>.
- [79] Frank Zimmermann. *Private communication*. 2024.
- [80] Rogelio Tomás. “Direct Measurement of Resonance Driving Terms in the Super Proton Synchrotron (SPS) of CERN Using Beam Position Monitors”. PhD Thesis. 2003. URL: <http://cds.cern.ch/record/615164>.
- [81] Helmut Wiedemann. *Particle accelerator physics*. 2nd ed. Berlin ; New York: Springer, 1999.
- [82] Joschua Dilly et al. “First operational dodecapole correction in the LHC”. In: *Physical Review Accelerators and Beams* 26.12 (2023). doi: [10.1103/PhysRevAccelBeams.26.121001](https://doi.org/10.1103/PhysRevAccelBeams.26.121001). URL: <https://link.aps.org/doi/10.1103/PhysRevAccelBeams.26.121001>.
- [83] Mael Le Garrec et al. “Measurement and modelling of decapole errors in the LHC from beam-based studies”. In: *IPAC’23*. Venice, Italy, 2023. doi: [10.18429/JACOW-IPAC2023-MOPL024](https://doi.org/10.18429/JACOW-IPAC2023-MOPL024). URL: <https://jacow.org/ipac2023/doi/jacow-ipac2023-mopl024>.
- [84] Mael Le Garrec et al. “First measurement of fourth and fifth order chromaticity in the LHC”. In: *IPAC’23*. Venice, Italy, 2023. doi: [10.18429/JACOW-IPAC2023-MOPL027](https://doi.org/10.18429/JACOW-IPAC2023-MOPL027). URL: <https://jacow.org/ipac2023/doi/jacow-ipac2023-mopl027>.
- [85] Tobias Persson et al. “LHC Optics Commissioning in 2023 and 2024”. In: *IPAC’24*. Nashville, Tennessee, USA, 2024.

- [86] Vittorio Ferrentino et al. “LHC 2023 Ion Optics Commissioning”. In: *IPAC’24*. Nashville, Tennessee, USA, 2024.
- [87] Sasha J. Horney et al. “Sextupole RDTs in The LHC at Injection and in the Ramp”. In: *IPAC’24*. Nashville, Tennessee, USA, 2024.
- [88] Tuuli Nissinen et al. “LHC Optics Measurements from Transverse Damper for the High Intensity Frontier”. In: 2023. doi: [10.18429/JACOW-HB2023-THBP14](https://doi.org/10.18429/JACOW-HB2023-THBP14). URL: <https://jacow.org/hb2023/doi/JACoW-HB2023-THBP14.html>.
- [89] Rogelio Tomás García et al. “Optics for Landau Damping with Minimized Octupolar Resonances in the LHC”. In: 2023. doi: [10.18429/JACOW-HB2023-THBP20](https://doi.org/10.18429/JACOW-HB2023-THBP20). URL: <https://jacow.org/hb2023/doi/JACoW-HB2023-THBP20.html>.
- [90] Jacqueline Keintzel et al. “60° phase advance optics measurements in the Large Hadron Collider at CERN”. In: *IPAC’23*. Venice, Italy, 2023. doi: [10.18429/JACOW-IPAC2023-MOPL026](https://doi.org/10.18429/JACOW-IPAC2023-MOPL026). URL: <https://jacow.org/ipac2023/doi/jacow-ipac2023-mopl026>.
- [91] Felix Carlier et al. “Challenges of K-modulation measurements in the LHC Run 3”. In: *IPAC’23*. Venice, Italy, 2023. doi: [10.18429/JACOW-IPAC2023-MOPL014](https://doi.org/10.18429/JACOW-IPAC2023-MOPL014). URL: <https://jacow.org/ipac2023/doi/jacow-ipac2023-mopl014>.
- [92] Felix Carlier et al. “LHC Run 3 optics corrections”. In: *IPAC’23*. Venice, Italy, 2023. doi: [10.18429/JACOW-IPAC2023-MOPL015](https://doi.org/10.18429/JACOW-IPAC2023-MOPL015). URL: <https://jacow.org/ipac2023/doi/jacow-ipac2023-mopl015>.
- [93] Elena Fol et al. “Experimental Demonstration of Machine Learning Application in LHC Optics Commissioning”. In: *Proc. 13th Int. Part. Accel. Conf. IPAC22*. Vol. IPAC2022. Bangkok, Thailand: JACoW, 2022. doi: [10.18429/JACOW-IPAC2022-MOPOPT047](https://doi.org/10.18429/JACOW-IPAC2022-MOPOPT047).
- [94] Tobias Persson et al. “Optics Correction Strategy for Run 3 of the LHC”. In: *Proc. 13th Int. Part. Accel. Conf. IPAC22*. Vol. IPAC2022. Bangkok, Thailand: JACoW, 2022. doi: [10.18429/JACOW-IPAC2022-WEPOST008](https://doi.org/10.18429/JACOW-IPAC2022-WEPOST008).
- [95] Tobias Persson et al. “Optics Measurements and Correction Plans for the HL-LHC”. In: *IPAC’21*. Campinas, Brazil: JACoW Publishing, Geneva, Switzerland, 2021. doi: [10.18429/JACoW-IPAC2021-WEPAB026](https://doi.org/10.18429/JACoW-IPAC2021-WEPAB026). URL: <https://accelconf.web.cern.ch/ipac2021/doi/JACoW-IPAC2021-WEPAB026.html>.
- [96] Tobias Persson et al. “Optics Correction Strategy for Run 3 of the LHC”. In: *IPAC’21*. Campinas, Brazil: JACoW Publishing, Geneva, Switzerland, 2021. doi: [10.18429/JACoW-IPAC2021-WEPAB027](https://doi.org/10.18429/JACoW-IPAC2021-WEPAB027). URL: <https://accelconf.web.cern.ch/ipac2021/doi/JACoW-IPAC2021-WEPAB027.html>.
- [97] Ewen Maclean et al. “Optics Measurement by Excitation of Betatron Oscillations in the CERN PSB”. In: *IPAC’21*. Campinas, Brazil: JACoW Publishing, Geneva, Switzerland, 2021. doi: [10.18429/JACoW-IPAC2021-THPAB168](https://doi.org/10.18429/JACoW-IPAC2021-THPAB168).

Bibliography

- [98] Maël Le Garrec et al. *MD6864 – Decapole studies at injection*. Accelerators & Technology Sector Note CERN-ACC-NOTE-2023-0018. CERN, 2023. URL: <https://cds.cern.ch/record/2879070>.
- [99] Xavier Buffat et al. *Optics Measurement and Correction Strategies for HL-LHC*. Accelerators & Technology Sector Note CERN-ACC-2022-0004. CERN, 2022. URL: <https://cds.cern.ch/record/2808650>.
- [100] O. Aberle et al. *High-Luminosity Large Hadron Collider (HL-LHC): Technical Design Report*. CERN Yellow Reports: Monographs CERN-2020-010. Geneva: CERN, 2020. doi: [10.23731/CYRM-2020-0010](https://doi.org/10.23731/CYRM-2020-0010). URL: <https://cds.cern.ch/record/2749422>.
- [101] Maël Le Garrec. *Correction of Decapolar Resonances in the LHC*. Goethe Universität, Frankfurt, 2023.
- [102] Maël Le Garrec. *Les champs décapolaires du LHC*. Roscoff, France, 2023. URL: <https://indico.ijclab.in2p3.fr/event/9312/contributions/30982/>.

List of Publications

Journal Publications (co-author)

- (1) Ewen H. Maclean et al. “Prospects for beam-based study of dodecapole nonlinearities in the CERN High-Luminosity Large Hadron Collider”. In: *The European Physical Journal Plus* 137.11 (2022). doi: [10.1140/epjp/s13360-022-03367-2](https://doi.org/10.1140/epjp/s13360-022-03367-2). URL: <https://link.springer.com/10.1140/epjp/s13360-022-03367-2>
- (2) Joschua Dilly et al. “First operational dodecapole correction in the LHC”. in: *Physical Review Accelerators and Beams* 26.12 (2023). doi: [10.1103/PhysRevAccelBeams.26.121001](https://doi.org/10.1103/PhysRevAccelBeams.26.121001). URL: <https://link.aps.org/doi/10.1103/PhysRevAccelBeams.26.121001>

Conference Proceedings

- (1) Mael Le Garrec et al. “Measurement and modelling of decapole errors in the LHC from beam-based studies”. In: *IPAC’23*. Venice, Italy, 2023. doi: [10.18429/JACOW-IPAC2023-MOPL024](https://doi.org/10.18429/JACOW-IPAC2023-MOPL024). URL: <https://jacow.org/ipac2023/doi/jacow-ipac2023-mopl024>
- (2) Mael Le Garrec et al. “First measurement of fourth and fifth order chromaticity in the LHC”. in: *IPAC’23*. Venice, Italy, 2023. doi: [10.18429/JACOW-IPAC2023-MOPL027](https://doi.org/10.18429/JACOW-IPAC2023-MOPL027). URL: <https://jacow.org/ipac2023/doi/jacow-ipac2023-mopl027>

Conference Proceedings (co-author)

- (1) Tobias Persson et al. “LHC Optics Commissioning in 2023 and 2024”. In: *IPAC’24*. Nashville, Tennessee, USA, 2024

- (2) Vittorio Ferrentino et al. “LHC 2023 Ion Optics Commissioning”. In: *IPAC’24*. Nashville, Tennessee, USA, 2024
- (3) Sasha J. Horney et al. “Sextupole RDTs in The LHC at Injection and in the Ramp”. In: *IPAC’24*. Nashville, Tennessee, USA, 2024
- (4) Tuuli Nissinen et al. “LHC Optics Measurements from Transverse Damper for the High Intensity Frontier”. In: 2023. doi: [10.18429/JACOW-HB2023-THBP14](https://doi.org/10.18429/JACOW-HB2023-THBP14). URL: <https://jacow.org/hb2023/doi/JACoW-HB2023-THBP14.html>
- (5) Rogelio Tomás García et al. “Optics for Landau Damping with Minimized Octupolar Resonances in the LHC”. in: 2023. doi: [10.18429/JACOW-HB2023-THBP20](https://doi.org/10.18429/JACOW-HB2023-THBP20). URL: <https://jacow.org/hb2023/doi/JACoW-HB2023-THBP20.html>
- (6) Jacqueline Keintzel et al. “60° phase advance optics measurements in the Large Hadron Collider at CERN”. in: *IPAC’23*. Venice, Italy, 2023. doi: [10.18429/JACOW-IPAC2023-MOPL026](https://doi.org/10.18429/JACOW-IPAC2023-MOPL026). URL: <https://jacow.org/ipac2023/doi/jacow-ipac2023-mopl026>
- (7) Felix Carlier et al. “Challenges of K-modulation measurements in the LHC Run 3”. In: *IPAC’23*. Venice, Italy, 2023. doi: [10.18429/JACOW-IPAC2023-MOPL014](https://doi.org/10.18429/JACOW-IPAC2023-MOPL014). URL: <https://jacow.org/ipac2023/doi/jacow-ipac2023-mopl014>
- (8) Felix Carlier et al. “LHC Run 3 optics corrections”. In: *IPAC’23*. Venice, Italy, 2023. doi: [10.18429/JACOW-IPAC2023-MOPL015](https://doi.org/10.18429/JACOW-IPAC2023-MOPL015). URL: <https://jacow.org/ipac2023/doi/jacow-ipac2023-mopl015>
- (9) Elena Fol et al. “Experimental Demonstration of Machine Learning Application in LHC Optics Commissioning”. In: *Proc. 13th Int. Part. Accel. Conf. IPAC22*. Vol. IPAC2022. Bangkok, Thailand: JACoW, 2022. doi: [10.18429/JACOW-IPAC2022-MOPOT047](https://doi.org/10.18429/JACOW-IPAC2022-MOPOT047)
- (10) Tobias Persson et al. “Optics Correction Strategy for Run 3 of the LHC”. in: *Proc. 13th Int. Part. Accel. Conf. IPAC22*. Vol. IPAC2022. Bangkok, Thailand: JACoW, 2022. doi: [10.18429/JACOW-IPAC2022-WEPOST008](https://doi.org/10.18429/JACOW-IPAC2022-WEPOST008)
- (11) Tobias Persson et al. “Optics Measurements and Correction Plans for the HL-LHC”. in: *IPAC’21*. Campinas, Brazil: JACoW Publishing, Geneva, Switzerland, 2021. doi: [10.18429/JACoW-IPAC2021-WEPAB026](https://doi.org/10.18429/JACoW-IPAC2021-WEPAB026). URL: <https://accelconf.web.cern.ch/ipac2021/doi/JACoW-IPAC2021-WEPAB026.html>
- (12) Tobias Persson et al. “Optics Correction Strategy for Run 3 of the LHC”. in: *IPAC’21*. Campinas, Brazil: JACoW Publishing, Geneva, Switzerland, 2021. doi: [10.18429/JACoW-IPAC2021-WEPAB027](https://doi.org/10.18429/JACoW-IPAC2021-WEPAB027). URL: <https://accelconf.web.cern.ch/ipac2021/doi/JACoW-IPAC2021-WEPAB027.html>
- (13) Ewen Maclean et al. “Optics Measurement by Excitation of Betatron Oscillations in the CERN PSB”. in: *IPAC’21*. Campinas, Brazil: JACoW Publishing, Geneva, Switzerland,

Notes and Reports

- (1) Maël Le Garrec et al. *MD6864 – Decapole studies at injection*. Accelerators & Technology Sector Note CERN-ACC-NOTE-2023-0018. CERN, 2023. url: <https://cds.cern.ch/record/2879070>
- (2) Joschua Dilly and Mael Le Garrec. *On the derivation of Amplitude Detuning and Chromaticity Formulas for Particle Accelerators*. 2023. url: <http://arxiv.org/abs/2301.09132>
- (3) Xavier Buffat et al. *Optics Measurement and Correction Strategies for HL-LHC*. Accelerators & Technology Sector Note CERN-ACC-2022-0004. CERN, 2022. url: <https://cds.cern.ch/record/2808650>
- (4) O. Aberle et al. *High-Luminosity Large Hadron Collider (HL-LHC): Technical Design Report*. CERN Yellow Reports: Monographs CERN-2020-010. Geneva: CERN, 2020. doi: [10.23731/CYRM-2020-0010](https://doi.org/10.23731/CYRM-2020-0010). url: <https://cds.cern.ch/record/2749422>

Seminars and Conferences

- (1) Maël Le Garrec. *Correction of Decapolar Resonances in the LHC*. Goethe Universität, Frankfurt, 2023
- (2) Maël Le Garrec. *Les champs décapolaires du LHC*. Roscoff, France, 2023. url: <https://indico.ijclab.in2p3.fr/event/9312/contributions/30982/>



Maël Le Garrec

CS ENGINEER · ACCELERATOR PHYSICS PHD STUDENT

298 Route de Gex, 01170 Crozet, France

□ (+33) 6 48 38 93 04 | ☎ mael@legarrec.org | 🌐 https://mael.legarrec.org | Born 06/1995

Experience



KEK

VISITING SCIENTIST

- Measurement of linear optics of SuperKEKB
- First observations of higher chromaticity non-linear orders
- First observations of sextupolar Resonance Driving Terms

Tsukuba, JP

2024



CERN

PHD STUDENT - ACCELERATORS AND BEAM PHYSICS

- Measurements and corrections during LHC's commissioning
 - Linear optics: β -beating, dispersion, energy, coupling
 - Non-linear optics via chromaticity: Q'' and Q'''
- Measurement, modelling and correction of decapole fields via Chromatic Amplitude Detuning, Q''' and RDTs.
- Observation and modelling of higher order fields (dodecapole and decatetrapole).
- Measurement and correction of skew octupole fields via RDTs.
- Analytical calculations from Hamiltonians.

Geneva, CH

2021 — 2024

TRAINEE - ACCELERATORS AND BEAM PHYSICS

- Software development for Optics Measurements and Corrections for LHC Run III commissioning.
- Particle tracking simulations ; dev in Python and Java.

Geneva, CH

2019 — 2021



Scaleway

DEVOPS

- Maintenance of Python APIs, server images and system software.
- Administration of thousand of hypervisors and servers.

Paris, FR

2018 — 2019

Education

Gothe Universität Frankfurt

Frankfurt am Main, DE

2021 - 2024

DOCTORAL CANDIDATE

- Thesis: LHC Effective Model for Optics Corrections
- Under the supervision of Apl. Prof. Dr. Giuliano Franchetti and Dr. Ewen H. Maclean

CERN Accelerator School

Chavanne de Bogis, CH / Sévrier, FR

2021-2022

ACCELERATOR PHYSICS COURSES - [HTTPS://CAS.WEB.CERN.CH](https://cas.web.cern.ch)

- Introduction to Accelerator Physics, 2 weeks focused on basic accelerator physics subjects.
- Advanced Accelerator Physics, continuation of previous school, focused on advanced subjects.

EPITA

Paris, FR

2013 - 2019

COMPUTER SCIENCE ENGINEERING

- Focus on systems and network security
- Low-level development and system administration

Skills and Interests

Coding Python, C/C++, Java, bash, LaTeX, Rust

Web Flask, HTML, CSS, Apache

Others Archlinux, Debian, Git, pgSQL, Scipy, Sympy, Numpy, Pandas, Matplotlib

Languages French, English (C1), German (A2)

Interests Electronics, CAD Design & 3D Printing, Automotive Mechanics, Climbing, Paragliding

Professional Knowledge

Particle Tracking and Analysis

MAD-X, MAD-NG, OMC3, XSUITE

2019-

- LHC single particle tracking with field errors.
- Frequency and Optics analysis for beta-beating, dispersion, RDTs, etc.
- Correction of Optics based on response matrices (Chromaticity, RDTs)
- Modelling of machine errors.
- Dynamic Aperture simulations with XSuite.

Contests

FRANCE

2017 37th/700, *Meilleur Développeur de France* (Best French Developer), algorithms contest

Paris